UNIVERSITÀ DEGLI STUDI DI PALERMO

Dottorato in Ingegneria Chimica, Gestionale, Meccanica, Informatica

Indirizzo “Ingegneria Chimica e dei Materiali”

Dipartimento di Ingegneria Chimica, Gestionale, Meccanica, Informatica

Settore Scientifico Disciplinare ING/IND 26

COMPUTATIONAL FLUID DYNAMICS OF REVERSE ELECTRODIALYSIS SYSTEMS

IL DOTTORE

LUIGI GURRERI

IL COORDINATORE

Prof. Ing. SALVATORE GAGLIO

IL TUTOR

Prof. Ing. GIORGIO MICALE

I CO TUTORS

Dr. Ing. ANDREA CIPOLLINA

Prof. Ing. MICHELE CIOFALO

Prof. Ing. ENRICO NAPOLI

CICLO XXV

ANNO CONSEGUIMENTO TITOLO 2015

This work was performed within the REAPower (Reverse Electrodialysis Alternative Power production) project (http://www.reapower.eu) funded by the EU-FP7 programme (Project Number: 256736).

CONTENTS

INTRODUCTION

One of the most important challenges in the 21st century is the development of technologies for the utilization of alternative energy sources. This is necessary due to (i) the increasing energy demand, (ii) the progressive depletion of the conventional fossil resources and (iii) the environmental issues, i.e. pollution phenomena and global warming. Therefore, in the last decades research has been prompted towards renewable energies based on renewable resources, that could be also economically competitive. In this framework, the *salinity gradient power* (SGP) can play a crucial role. It was estimated that a significantly high theoretical global potential is available from the mixing of seawater and river water, totalling a power value of 2.6 TW. Moreover, unlike wind and solar energy, this form of energy is less subjected to time fluctuations.

Reverse Electrodialysis (RED) is a very promising technology that converts SGP directly into electric energy. In RED two salt solutions flow in alternating channels, separated by an alternated series of anion and cation exchange membranes. The chemical potential difference between the two solutions generates an electric potential difference over the membranes and thus a selective ion transport across themselves, from the concentrated channels towards the dilute ones. At the electrodes, the ionic transport is converted by redox reactions into a current of electrons supplying an external load. In the last years, the technological advancement and the reduction of the membranes cost have strongly enhanced the efficiency of the RED process, making it the most promising SGP-based technology. Further improvements are still necessary, but in the near future they may well be achieved, so that RED could start to be commercialized at the industrial scale.

The process performance depends on a number of phenomena interacting at various scales. The key aspects of the process are: theoretical driving force, Ohmic resistances, non-Ohmic resistances (due to concentration changes) and pumping power. All parameters identifying the stack configuration affect in a complex way these aspects. However, fluid dynamics represents a fundamental major feature and can be identified as the flow and concentration fields occurring in the system. They are established by the interaction of stack geometry, flow rate and feeds properties, and determine a strong influence on all the key aspects, except the theoretical driving force.

Due to the complex influence on the process performance, fluid dynamics is crucial in RED systems, thus needs to be thoroughly investigated. To this aim, modelling can be very helpful. On the other hand, the mathematical description of the RED process by a thorough model is a hard task, due to the complexity of phenomena involved and geometry. An integrated model conceived by a hierarchical strategy of analysis with separation of scales can address effectively the full simulation problem.

This work is carried out within the REAPower (*Reverse Electrodialysis Alternative Power Production*) project, which focuses on RED processes using seawater or brackish water as dilute solution and brine as concentrated solution. The project is aimed at optimizing the system by a multi-scale modelling tool and experimental tests. The Computational Fluid Dynamics (CFD) simulations at small scale are the basis of this model. CFD is the technique to study fluid dynamics and associated phenomena by means of numerical methods in computer-based simulations. Therefore CFD is a powerful predictive tool to test a number of cases by requiring fewer equipment and time compared to the experimental investigation and to do detailed analyses at small scale.

This work focuses on fluid dynamics and mass transport phenomena in RED systems, by a suitable CFD model. The general aim is building up a predictive tool for the stack design and optimization and the evaluation of the most effective operating conditions, which represent crucial aspects for efficiency and economic competitiveness.

With the purpose to fill some major gaps in the literature, the specific objectives pursued and the activities performed are identified. A suitable 3D CFD model to investigate effectively channels for RED systems at low scale has been developed. Fluid dynamics and mass transfer phenomena have been studied by solving the fluid flow governing equations (Navier–Stokes and continuity) and a transport equation suitable also for concentrated solutions, of a binary electrolyte (NaCl), derived from the Stefan–Maxwell equations by assuming the local electroneutrality. The periodic domain of a single channel has been simulated with suitable boundary conditions (membranes are not simulated). Spacer-filled channels and profiled-membrane channels have been investigated, comprising geometries not simulated so far. Woven spacers are commonly adopted and offer some potential benefits, such as better mixing and lower shadow effect. Profiled-membrane channels represent a promising alternative to the spacers. In this work, these kinds of geometries are simulated in CFD environment for the first time. Moreover, the analysis has been carried out at low Reynolds numbers (*Re*) typical of

RED stacks, while usually higher *Re* pertinent to other membrane processes are investigated. The simulations provide the local distribution of the variables of fluid dynamics and mass transfer. The effects of channel geometry, *Re* and feeds features on concentration polarization and pumping power are evaluated by means of process parameters, i.e. dimensionless numbers as Sherwood number and power number. Thus, the features that a high performance RED channel should possess can be identified.
The validation of pressure drop results for a couple of spacers has been done. Also, simulation results were compared with experimental and CFD data on pressure drop and mass transfer from literature.
A different scale has been also investigated, in order to assess the effect of the features of the entire hydraulic circuit of a stack on the fluid dynamics performance. An improved design of manifolds devised in rectangular geometry has been simulated. The influence of manifolds and stack lay-out on the pressure loss and on the flow rate distribution within the channels has been evaluated.
Finally, the results provide input data for the process simulator (higher levels of modelling) in order to identify the optimal channel configuration and operating conditions.

In the following an outline of the present thesis is reported.
Chapter 1 reports fundamentals and review of the pertinent literature.
Chapter 2 describes the CFD model developed.
Chapter 3 is devoted to the fluid dynamics investigation in spacer-filled channels with different slip condition imposed, the validation with experimental results on pressure drop, the evaluation of porous fibrous media and the simulation of the whole hydraulic circuit of stack.
Chapter 4 focuses on commercial spacer-filled channels, with particular attention to the concentration polarization and the various quantities on which it depends.
Chapter 5 completes the previous chapter by a thorough investigation of geometries in a parametric analysis of woven and non-woven spacers, and a comparison with CFD and experimental data from the literature.
Chapter 6 investigates profiled-membrane channels in another parametric analysis.

1 FUNDAMENTALS, STATE OF THE ART AND LITERATURE REVIEW

Abstract

Reverse electrodialysis (RED) is a promising technology for electric power generation by converting the chemical potential difference of a salinity gradient, within a stack equipped by selective ion-exchange membranes. The process performance depends on some crucial aspects, which are influenced in a complex way by various factors identifying the stack configuration. Fluid dynamics within the system is a prominent factor affecting the power producible.

The theoretical driving force depends mostly on the ratio between the activities of the two salt solutions. The voltage generated is reduced by the internal resistance, due to Ohmic and non-Ohmic resistances. The Ohmic resistances are due to the contribution of membranes, diluted channels, concentrated channels and electrodic compartments. The non-Ohmic resistances represent losses of voltage due (i) to the streamwise concentration change in the bulk of the solution, and (ii) to the concentration polarization in the boundary layers. When river water and seawater are used, they are comparable to the Ohmic resistances, and at low flow rates can be the dominant ones; when concentrated solutions are used (as seawater and brine) they can be negligible, as the relative concentration changes are lower when the concentration increases. The net power obtainable depends on the pumping power consumption. The reduction in power output due to the pumping power amounts normally to ~10-20% at the flow rate that maximizes the net power; also, the pressure drops in the manifolds can represent an important contribution or even the main contribution to the overall hydraulic loss if they are not properly designed.

Stack geometry, flow rate and feeds properties represent fundamental factors for the process performance. In order to maximize the gross power, a dilute solution as river water or brackish water (0.02-0.1 M) and a concentrated brine (5 M) should be used. The inter-membrane distance and the channel shape should be suitable for minimizing the pressure drop; on the other hand, they affect Ohmic and non-Ohmic resistances, as well as the mechanical stability of the channels. Therefore, the identification of the optimal channel configuration must take into account the complex influence on all these aspects.

Net spacers are usually adopted as mechanical support within the channels and as mixing promoters (reduction of the boundary layer resistance). On the other hand, a non-conducting spacer exhibits the drawback of higher Ohmic resistances and pressure drop. As an alternative, profiled membranes can be used, with the benefits of reduced Ohmic resistances and hydraulic loss, although they are less effective in the mixing promotion.
The geometry of the distribution/collection system can affect significantly pressure drop, flow rate distribution among the channels and flow rate distribution along the width of each channel, with a consequent influence on pumping power, leakage issues, non-Ohmic resistances and thus on the net power achievable.
Modelling of the RED process is an arduous challenge, and the numerical models are based on simplifying assumptions on the domain simulated and on the mathematical description of the phenomena involved. The REAPower project focuses on the power production by RED technology using seawater or brackish water as dilute solution and brine as concentrated solution. Among the activities carried out in four years, the development of a simulation tool was achieved. A multi-scale model was built, based on the Computational Fluid Dynamics (CFD) analysis at low scale. The project ended with the installation of the first prototype RED plant to generate electricity from brine at the salt works of Marsala, which also produced the maximum gross power achieved so far from a RED stack.

1.1 Introduction

In the XXI century, the depletion of energy sources and environmental problems, as pollution phenomena and global warming, have prompted research towards renewable energy sources that can be sustainable and economically competitive. Renewable energies based on inexhaustible resources as sun and water, are the most attractive. In this regard, the *Salinity Gradient Power* (SGP) is a renewable energy form which can be drawn by the chemical potential difference between two different salt-concentrated aqueous solutions. It was estimated that the global potential power from the mixing of seawater and river water is 2.6 TW [1]. As well as the typical benefits of renewable energy technologies, SGP is less subject to issues related to time fluctuations in power production, which in contrast are unavoidable in wind and solar energy due to variations in wind speed and sunshine.

Different technologies have been proposed in order to exploit this energy source: Reverse Electrodialysis (RED), Pressure Retarded Osmosis, Capacitive Double Layer Expansion and Mixing Entropy Battery. In RED a controlled mixing between two differently concentrated solutions is obtained by means of selective ionic exchange membranes. The consequent ions transport generates an electric potential difference which can be drawn as electric power [2]. In 1954 Pattle [3] introduced the concept of energy from mixing of fresh and seawater and demonstrated it through an apparatus named "hydroelectric pile", now known as RED. For several years the scientific community has not been very interested in this field, but in the last decade, several research efforts have been devoted to RED process. Nowadays RED is the most promising process among the technologies based on the SGP, since it exhibits the best performance thanks to the technological advances and the cost abatement of the membranes. For the optimization of the process and thus for the commercialization in large scale of RED plants, further improvements are still necessary.

Pressure drop and polarization phenomena can reduce significantly the efficiency of membrane processes. In fact, pressure drop is responsible of an energy consumption increase, while polarization phenomena lead to higher power consumption in non-spontaneous processes and lower driving force in spontaneous processes [4-14]. In the specific case of RED, pressure drop and concentration polarization can affect strongly the power output obtainable: the former reduces the net power produced; the latter decreases the gross power. Also, a certain "spacer" separating the membranes is compulsory (i.e. the empty channel should be regarded only as an ideal condition). The channel geometry optimization should take into account several aspects related to mechanical stability, mass transfer, electrical resistance and hydraulic friction.

This chapter is focused on the state of the art, with particular reference to the aspects investigated in the present PhD work, such as fluid dynamics and mass transport phenomena. In particular, it is aimed at:

i) Analysing the working principle and the key issues of the RED process;

ii) Reviewing the pertinent literature;

iii) Briefly describing the REAPower project, in which the present PhD work is carried out.

1.2 Principle of Reverse Electrodialysis (RED)

Reverse Electrodialysis is a technology to draw electric energy from the mixing of solutions at different salt concentrations (*Salinity Gradient Power*, SGP). In particular, RED allows the production of electricity harvesting energy from the difference in chemical potential between two saline solutions flowing in alternate channels separated by selective ion exchange membranes (IEMs) [3]. A stack contains several repeating units (*cell pairs*), each consisting of a cationic exchange membrane (CEM), a compartment fed by a more concentrated salt solution (e.g. seawater), an anionic exchange membrane (AEM) and a compartment fed by a more dilute salt solution (e.g. river water). Spacers are usually employed in order to (i) separate the membranes, thus creating the channels and (ii) promote fluid mixing. The classical plate and frame configuration is usually adopted.

The chemical potential difference between the two salt solutions generates an ion transport from the concentrated solution towards the dilute one in each cell pair: cations move selectively through the CEMs and anions through the AEMs, towards the cathode and the anode, respectively. In particular, continuity of the electrochemical potential through the system causes the chemical potential difference to generate an electric potential difference at each membrane-solution interface, referred as Donnan potential; as the membrane is in contact with two solutions of different concentration, a potential difference between the two solutions is established, referred to as membrane potential [15]. The sum of the voltages generated over all the membranes is the overall difference of electrical potential available at the electrodes. At the electrodic compartments (end compartments), the ionic transport is converted by reversible redox reactions into a current of electrons supplying an external load. When the circuit is open and thus no current is circulating, the maximum voltage across the stack is established at the electrodes. This is named Open Circuit Voltage and represents the electromotive force of the RED generator. A schematic representation of a RED stack is reported in Figure 1.1; more details on the principle of working and on the features of a RED typical system can be found in the literature [3, 16-18].

The open circuit voltage, i.e. the electromotive force arising from the chemical potential difference between the solutions separated by the membranes, can be evaluated as the sum of the Nernst potential difference over the CEMs and over the AEMs due to the

cations and anions respectively [13, 19]. For the case of a monovalent binary electrolyte, the open circuit voltage is [14]

$$E_{OCV} = N_m \alpha_m \frac{RT}{zF} \ln\left(\frac{C^{conc}\gamma^{conc}}{C^{dil}\gamma^{dil}}\right) \tag{1.1}$$

where α_m is the mean apparent permselectivity of the membranes (ratio between the obtained membrane voltage and the theoretical voltage), N_m is the total number of membranes, R is the universal gas constant (8.31 J/(mol·K)), T is the absolute temperature, z is the valence of the ions (z = 1 for monovalent electrolyte), F is the Faraday constant (96485 C/mol), C is the electrolyte concentration, γ is the activity coefficient (the product $C{\cdot}\gamma$ is the activity of the electrolyte), and the superscripts *conc* and *dil* refer to the concentrated and diluted channel respectively.

When the circuit is closed by an external load, the voltage obtained over the electrodes (U) produces an electrical current (i (A/m^2)) and is reduced due to the internal resistance of the stack itself (R_{int} (Ωm^2))

$$U = E_{OCV} - iR_{int} \tag{1.2}$$

Following Vermaas et al. [14], the potential drop due to the internal resistance can be written as the sum of the voltage drop due to Ohmic resistances and two non-Ohmic voltage drops, as expressed by the following equation

$$U = E_{OCV} - \eta_{\Delta C} - \eta_{BL} - iR_{ohm} \tag{1.3}$$

where $\eta_{\Delta C}$ is a loss of voltage due to the streamwise concentration change (i.e. along the compartment length) in the bulk of the solution, η_{BL} is a loss of voltage due to the concentration polarization in the boundary layers, R_{ohm} is the standard Ohmic areal resistance. This last term takes into account for the resistance of: AEMs, CEMs, diluted channels, concentrated channels and electrodic compartments [14, 17].

The losses due to non-Ohmic effects can be compared to the Ohmic loss when are divided by the current density, so that are expressed as non-Ohmic resistances

$$U = E_{OCV} - \left(R_{\Delta C} + R_{BL} + R_{ohm}\right) i \tag{1.4}$$

Therefore, the total resistance inside the stack has been split into three different contributions.

The voltage and the current density depend on the resistance of the external load; in fact, from the Ohm's law the current density is

$$i = \frac{E_{OCV}}{R_{int} + R_{load}} \tag{1.5}$$

The power density per membrane unit area (W/m^2) can be found from Kirchhoff's law as

$$P_d = \frac{i^2 R_{load}}{N_m} = \frac{iU}{N_m} = \frac{E_{OCV}^2 R_{load}}{N_m \left(R_{int} + R_{load}\right)^2} \tag{1.6}$$

The maximum power density is obtained when R_{load} is equal to R_{int}

$$P_{d,max} = \frac{E_{OCV}^2}{4 N_m R_{int}} \tag{1.7}$$

The power efficiency (η_{power}) represents the thermodynamic efficiency of the process and is the fraction of total power extracted by an external load with respect to the total power consumed (the latter term corresponds to the exergy decrease per second) [18, 19]

$$\eta_{power} = \frac{i^2 R_{load} / N_m}{\left(i^2 R_{int} + i^2 R_{load}\right) / N_m} = \frac{R_{load}}{R_{int} + R_{load}} \tag{1.8}$$

When the power density is maximum ($R_{load} = R_{int}$), the power efficiency is theoretically equal to 50%. A higher efficiency can be achieved at lower power densities ($R_{load} > R_{int}$). The energy efficiency is the ratio of the extracted energy and the incoming exergy [18, 20, 21].

Finally, it is important to highlight that a consumption of energy is required for pumping the feed solutions through the stack, which can reduce dramatically the net power. In other words, the net power obtained is given by subtracting the pumping power to the gross power produced [13] and in terms of density per membrane area is

$$P_{d,net} = P_d - \frac{P_{pump}}{N_m A_m} \tag{1.9}$$

where the pumping power consumption can be obtained from the pressure drop over the inlet and outlet of the feed solutions, their flow rate and the pump efficiency as [13]

$$P_{pump} = \frac{\Delta p^{conc} Q^{conc} + \Delta p^{dil} Q^{dil}}{\eta_{pump}} \tag{1.10}$$

Finally, the net energy efficiency is the ratio of the net energy and the incoming exergy [18, 20].

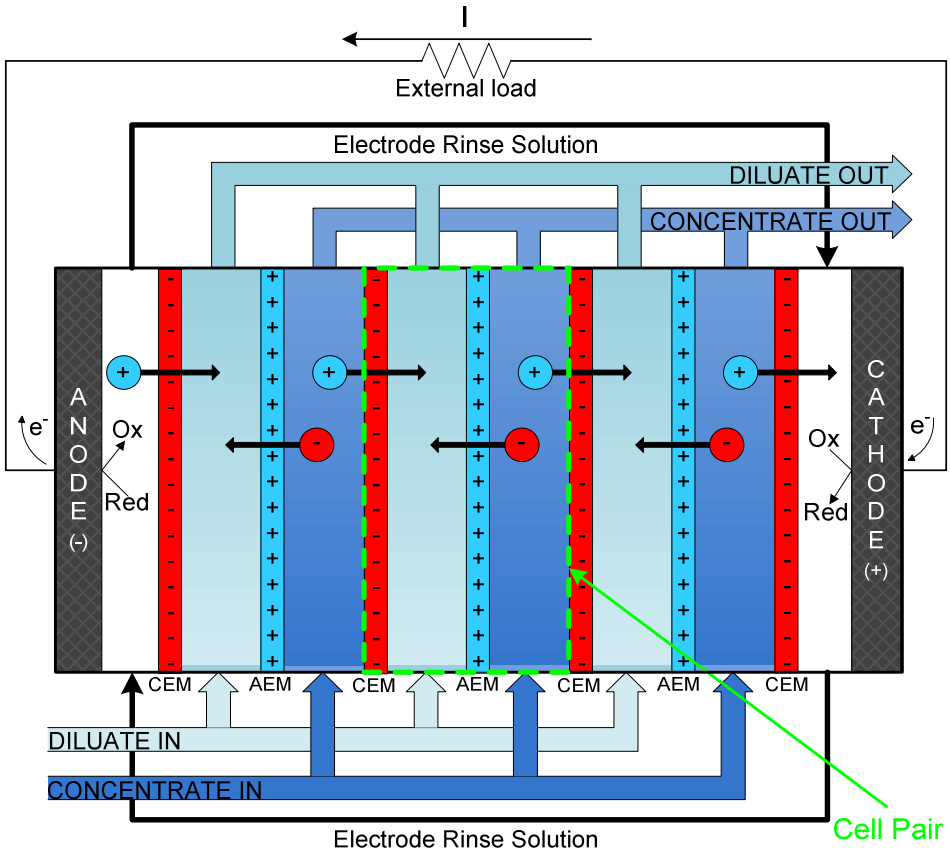

Figure 1.1. Schematic representation of a reverse electrodialysis stack. The sketch highlights one cell pair including the spacer-filled channel.

1.3 Key aspects and critical issues of the RED process

The process performance depends on a number of phenomena occurring at various scales and interacting with each other. According to the previous section, the power production of the RED process depends on the following key aspects: (i) theoretical driving force, (ii) Ohmic resistances, (iii) non-Ohmic resistances and (iv) pumping power consumption. Many factors affect in a complex way these aspects and thus the performance of the RED process [16, 21-24]: properties of components such as membranes, spacers and electrodic systems, but also stack geometry, operating conditions and feeds properties. Table 1.1 summarizes schematically the key aspects of the process and the factors affecting them.

A parameter can determine his effect directly and independently on the other parameters (e.g. the spacer affecting the Ohmic resistances, and the ionic species influencing the electromotive force) and/or combined with other factors. Fluid dynamics is identified as the flow and concentration fields occurring within the system. They are established by the interaction of various factors, and determine combined effects on three key aspects: Ohmic resistances, non-Ohmic resistances and pumping power. In this PhD work, the aspects analysed are (i) non-Ohmic resistances due to boundary layer and (ii) pumping power, and the parameters investigated are stack geometry, flow rate and feed properties. In Table 1.1 the "✓" symbol indicates the fields of interest relevant to this thesis. Ohmic resistances are related to fluid dynamics in terms of solutions conductivity and are not considered in the modelling developed in this work.

The electrodic system is important mainly for the environmental and economic point of view and is less significant for the power production [22, 23]; thus is not considered in this analysis. The stack geometry includes the geometry of the channels and also the geometry of the distributor and collector. The feeding mode indicates the relative direction of the two feed solutions in the channels and can be co-current, counter-current, cross-flow. The feeds properties and the other operating conditions comprise: ions present, concentrations, density, viscosity, salt diffusivity, temperature. Finally, phenomena of osmotic flux, electro-osmotic flux, short-cut currents and solution leakage are not considered in the simplified scheme of Table 1.1 and the subsequent analysis.

Table 1.1. Key aspects of the RED process and factors that affect them.

		Theoretical driving	Ohmic resistances	Non-Ohmic resistances	Pumping power
	Membranes properties	■	■	■	-
Fluid dynamics	*Stack geometry*	-	■	✓	✓
	Flow rate	-	■	✓	✓
	Feeding mode	-	■	■	-
	Feeds properties & Other operating conditions	■	■	✓	✓

✓ *indicates that the factor affects the key aspect and is analysed in this work*

■ *indicates that the factor affects the key aspect, but is not analysed in this work*

- indicates that the factor does not affect the key aspect

1.3.1 Theoretical driving force

The theoretical electromotive force (E_{OCV}) depends on the *ratio* between the salt activity in the concentrated channel and the dilute one (Eq.(1.1)). Usually, standard solutions are considered solutions of NaCl 0.017 M (river water) and 0.5 M (river water), because in the industrial applications a RED stack could operate in the coastal areas near the mouth of a river. The use of more concentrated solutions, useful to reduce the internal resistances, could decrease the E_{OCV}, although the salinity *gradient* is increased. As an example, if the dilute channel is fed by seawater 0.5 M and the concentrated by brine 5 M, neglecting the influence of the activity coefficients, the ratio between the concentrations and thus E_{OCV} are reduced with respect to the case of river water and seawater [25]. Also, E_{OCV} depends on the valence of the ions.

The open circuit voltage is proportional to the membranes permselectivity, which is often close to 1, but when concentrated solutions are adopted, it can undergo a not negligible reduction [13, 25].

1.3.2 Ohmic resistances

The Ohmic resistances are due to the various contributions of membranes (AEMs and CEMs), diluted channels, concentrated channels and electrodic compartments. The resistance of the electrodic compartments begins negligible when the stack contains several cell pairs. The resistance of the channels depends on the conductivity of the solutions and the inter-membrane distance. When the dilute compartment is fed by a low concentration solution as river water, often it gives the main contribution to the Ohmic resistances [17, 21, 26]. On the contrary, when more concentrated solutions are used, the Ohmic resistances are dominated by the membranes resistance [25].

The Ohmic resistances are also influenced by the presence of a spacer. Non-conductive spacers cover part of the membrane area (spacer shadow effect) and impose a tortuous path for the ions in the feeds compartments [14, 17]. The Ohmic resistances can be increased more than 50% by the spacer [17, 21, 25-27]. A spacer with a more open structure can decrease significantly the Ohmic resistance of the channel [28]. Ion conductive spacers can almost completely eliminate the spacer shadow effect, thus

obtaining a significant decrease in the Ohmic resistances [29]. This effect is achieved also by adopting profiled membranes instead of the traditional non-conducting net spacers; the conducting profiles offer a path for the ionic flow, so that the shadow effect is eliminated. Therefore, the Ohmic resistances can be reduced with respect to stacks equipped with spacers; for example, Vermaas et al. [30] report a reduction of 30%, confirmed by similar findings in a subsequent work [28].

Fluid dynamics can have an effect on the Ohmic resistances when they are dominated by the resistance of the dilute channels, as it occurs normally when the stack operates with river water-seawater solutions. In fact, the conductivity of the river water increases due to the ions transfer through membranes from the seawater compartment; this increment is larger as the flow rate decreases, i.e. the residence time increases, because of the higher quantity of ions transported. As a consequence, the Ohmic resistances can be lower at low flow rates [21, 28].

1.3.3 Non-Ohmic resistances

The non-Ohmic resistances are reductions of the driving force due to concentration changes that result in a voltage lower than the theoretical one. For convenience, these voltage losses due to non-Ohmic effects are quantified in terms of resistances in order to be compared to the Ohmic ones.

They are given by two contributions to the reduction of the driving force: (i) along the fluid flow direction due to the streamwise concentration change in the bulk of the two solutions (caused by the ions transport from the concentrated channel to the diluted channel) ($R_{\Delta C}$); (ii) at the membrane-solution interfaces due to the concentration polarization in the boundary layers (R_{BL}).

Concentration polarization phenomena consist of concentration gradients in the boundary layer between the membrane surface and the fluid bulk, due to the mass flux through the ion exchange membranes, accompanied by a difference between ions mobility in the membrane and solution phases [15]. In RED, concentration polarization phenomena result in an increased salt concentration at the membrane surface in the dilute channel and a decreased salt concentration at the membrane surface in the concentrate channel [2, 31]. As a consequence, the concentration difference at the membrane-solution interfaces becomes smaller than the concentration difference

between the bulk solutions, the resulting electromotive force becomes lower than the theoretical value, and a lower voltage over the stack is obtained [21].

The non-Ohmic resistances are determined in a complicated manner by all the factors which identify the configuration of the stack. Clearly, the non-Ohmic effects are linked to the ionic flux across the membranes, i.e. to the current density. In a stack where the current density tends to increase by using less resistant membranes, $R_{\Delta C}$ and R_{BL} are increased, but with a negative feedback that mitigates the current density itself. However, the effect of the membranes resistance is only indirect. In general, since the non-Ohmic resistances are actually loss of voltage, every factor affecting the Ohmic resistances has an indirect influence on the non-Ohmic ones. Moreover, stack geometry, flow rate and solutions properties have also significant direct effects on the non-Ohmic resistances.

As well as on the ionic fluxes, $R_{\Delta C}$ is dependent on the channel geometry and the flow velocity, i.e. it is determined by the residence time within the channels [21], and it depends strongly on the solutions concentrations [25]. In standard condition where river water and seawater are used, at low flow rates $R_{\Delta C}$ can represents the highest term of the stack resistance; at higher flow rates it can be significantly decreased, but at the flow rates in which the maximum net power is obtained it can play still an important role, being comparable to the other resistances [21, 25, 30]. Conversely, when higher concentration solutions are adopted, the streamwise concentration changes relative to the inlet concentration are lower and their effects in terms of $R_{\Delta C}$ decrease (notice that the voltage over the membranes is given by the *ratio* of the solutions activities); therefore $R_{\Delta C}$ can begin negligible [25].

Concentration polarization phenomena are determined by the mixing within the channel between the fluid bulk and the membrane-solution interface. The concentration field in the channel and thus R_{BL} are established by channel geometry, flow rate and solution properties. In dimensionless terms, the Sherwood number (*Sh*) depends on the geometrical features of the channel, the Reynolds number (*Re*) and the Schmidt number (*Sc*). Also, the bulk concentration has a strong influence on the effects due to polarization (as in the case of $R_{\Delta C}$). When river water and seawater are used, R_{BL} is an important contribution to the overall stack resistance, and decreases by increasing the flow rate [4, 21, 26, 30]. At the flow rates that allow gaining the maximum net power, R_{BL} is lower than the Ohmic resistances, but is comparable with them [21, 25, 30].

In the case of higher concentration solutions, the concentration change in the boundary layer relative to the bulk concentration is lower and R_{BL} decreases till to begin even negligible at high concentrations, as the voltage over the membranes depends on the *ratio* of the solutions activities [25]. The effect of *Sc* on the concentration change in the boundary layers is of minor importance.

Sizes and shape of the channel can affect significantly R_{BL}. A spacer-filled channel reduces R_{BL} with respect to an empty channel [27]. A small inter-membrane distance and a more effective spacer in promoting mixing, restricts the boundary layer thickness, thus reducing R_{BL} [21, 28]. Usually, profiled membranes have geometries that enhance less mixing, therefore lead to higher R_{BL} than spacers [28, 30].

More details on the boundary layer resistance for spacer-filled channels and profiled-membrane channels are reported in section 1.4 and 1.5.

1.3.4 Pumping power and net power

The energy consumption for pumping the feed solutions can reduce considerably the net power achievable (see Eqs. (1.9) and (1.10)). The pumping power is obtained by multiplying the flow rate times the pressure drop. The pressure drop through the stack is influenced by the stack geometry, flow rate and properties of the feed solution. In dimensionless terms, the power number (*Pn*) depends on the Reynolds number (*Re*) and the friction factor (*f*), which in turn depends on the geometrical features and *Re*. Also, the hydraulic loss is due to various contributions: localized drop in the manifolds and distributed loss along the channels.

As the flow rate increases, the non-Ohmic resistances are reduced and thus the gross power density increases asymptotically till the maximum value. On the other hand, higher flow rates lead to increased pressure drop. As a consequence of these opposite effects, the net power density has a maximum value at an optimal flow rate of the feed solutions which depends on the specific configuration of the stack [2, 14, 18, 20, 21, 28, 30]. The reduction in power output due to the pumping power (pumping power/gross power) reported in literature amounts normally to ~10-20% at the flow rate that maximizes the net power. Moreover the maximum (asymptotic) gross power is reached at higher flow rates by consuming a pumping power much higher of it, thus a negative net power is obtained. The loss of power with respect to the maximum value of gross

power ((maximum gross power-maximum net power)/maximum gross power) is much higher. This parameter quantifies the loss with respect to the theoretical maximum achievable, and from literature data is estimated to be usually ~25-45% [18, 20, 21, 28, 30, 32].

Very thin channels are used in RED stacks. The channel thickness is usually ~100-500 μm, and the typical linear flow velocities at which the maximum net power is obtained are around 1 cm/s, corresponding to very low Reynolds numbers (lower than 5) [17, 18, 20, 21, 25, 28, 30, 32]. Therefore, the fluid flow regime is perfectly laminar.

Overall pressure drop depends strongly on the geometry (shape and sizes) of channels and manifolds. The hydraulic loss per unit length is much higher compared to that one in an empty channel of infinite streamwise and spanwise extend, with increments of one/two orders of magnitude [14, 19, 21, 28, 30, 33]. Notice that the pressure drops localized in the manifolds distributing and collecting the feed solutions can represent an important contribution or even the main contribution to the overall hydraulic loss [14, 18, 20, 28, 30, 33, 34]. Nevertheless, an improved geometry of the distribution system can reduce dramatically this localized loss, but the increment of pressure drop along the channel due to a spacer remain quite higher with respect to the empty channel [28].

The experimental works on RED stacks show that the spacer features have a significant impact on hydraulic loss [21, 28, 32] and that profiled membranes can have geometries which reduce significantly the friction with respect to the net spacers [14, 28, 30]. The inter-membrane distance and the channel shape should be suitable for minimizing the pressure drop; on the other hand, they affect Ohmic and non-Ohmic resistances (as seen in the previous sections), as well as the mechanical stability of the channels. Therefore an optimal configuration depending on the other features of the stack should be found. Conversely, the flow path length should be as short as possible, for minimizing both pressure drop and $R_{\Delta C}$.

Finally, the influence of the solution properties should not be neglected. In particular, for highly concentrated solutions (i.e. brine 5 M) density and, especially, viscosity can increase significantly, thus determining an important increase in pressure drop.

More details on pressure drop and pumping power are reported in section 1.4, 1.5 and 1.6.

1.3.5 Optimization strategies and key aspects analysed in this work

On the basis of the analysis carried out in the previous sections, the main optimization strategies for the RED process can be identified.

The ion exchange membranes are an essential element (not investigated in this work), thus their properties play an important role, mainly because of the effects of selectivity and electrical resistance on power density [13, 16, 25, 35]. The technological improvement in the membrane manufacturing should allow the development of cost effective membranes (very important to make economical the process) with low resistance and high permselectivity also when in contact with highly concentrated solutions.

The feed properties have a strong influence on process performance, since they affect all the key aspects. A larger salinity gradient increases the open circuit voltage. On the other hand, both Ohmic and non-Ohmic resistances are reduced drastically when high concentration feeds are used [25, 31]. Also, the membranes permselectivity is sensitive to the concentration of the solutions, but his reduction is of minor importance with respect to the decrease of the internal resistances. Clearly, the optimum concentrations for the two solutions are dependent on these different effects and on the other several parameters that define the stack configuration, such as the membrane resistance, the intermembrane distance, etc. Nevertheless, for maximizing the gross power output the couple of solutions of NaCl was identified as: a dilute solution with concentration close to river water concentration (0.02 M) [25] or a brackish water 0.1 M [13], and a concentrated brine close to the saturation (5 M) [13, 25]. The potentialities of application are linked to the availability of the feed solutions. Applications with natural concentrated solutions (i.e. from salt ponds) or artificial concentrated solutions (i.e. from industrial processes) are possible. Also, a closed loop, where the solutions are regenerated from low grade heat in a range of temperature between 50 °C and 100 °C (e.g. solar and geothermal energy or waste heat), may be promising.

However, the use of one diluted solution is unavoidable. Therefore, the issues relevant the Ohmic and non-Ohmic resistances stemming from the presence of a low concentration solution in the stack should be addressed. Moreover, the “real” power obtained is given by the net power, thus the optimization of the process must take into account for the pressure drop, which in addition can increase a lot for the concentrated

solution (effect of density and viscosity). Ultimately, stack geometry, flow rate and feeds properties represent crucial factors for Ohmic resistances, non-Ohmic resistances and pumping power, which play a fundamental influence on the system performance; thus fluid dynamics of the system needs to be thoroughly investigated in order to optimize the RED process.

The optimal channel geometry in terms of inter-membrane distance and shape is one that maximizes the net power. This does not mean simply reducing pressure drop. If a channel configuration exhibits lower pressure drop, the pumping power decreases. Hence the net power *would* tend to approach the gross power. Also, a lower pressure drop *would* enable higher flow rates, which *would* reduce the non-Ohmic resistances thus enhancing the gross power. Therefore, the net power *would* approach even more the maximum gross power (as a function of the flow rate). Nevertheless, the channel configuration has an influence also on the gross power, determined by means of the internal resistances (Ohmic and non-Ohmic). Therefore, the identification of the optimal channel configuration must take into account the complex influence on all these aspects. As an example, a higher channel thickness increases the resistances, but reduces pressure drop; as a consequence, an optimum channel thickness exists. The same applies to the channel shape [21, 28].

In this regard, net spacers are usually adopted as mechanical support within the channels and as mixing promoters. A spacer-filled channel reduces R_{BL} with respect to an empty channel [27], with an influence that depends on the spacer features [21, 28]. On the other hand, a non-conducting spacer exhibits the drawback of higher Ohmic resistances [17, 21, 25-28] and pressure drop [14, 19, 21, 28, 30]. As an alternative, profiled membranes can be used, with the benefits of reduced Ohmic resistances and hydraulic loss, although they are less effective in the mixing promotion (higher R_{BL}) [28, 30]. Among the few examples of channel configurations tested up to now, the net power densities have been found higher for stacks equipped with profiled membranes [28, 30], although a thorough investigation on the various spacer geometries has not been carried out.

As concerns the channel length, it should be as short as possible in order to minimize $R_{\Delta C}$ and pressure drop, and thus maximize the net power. An example of the impact of the channel length can be found in the theoretical calculations of Vermaas et al. [14], which show a remarkable increase in net power density for small cell lengths. Moreover, the drastic reduction of pressure drop in short channels would allow higher flow rates

and lower inter-membrane distances, resulting in lower polarization phenomena (R_{BL}) and Ohmic resistances. Another benefit can be achieved in short empty channels, where the entry effects could reduce R_{BL} [27]. Nevertheless, the possibility to achieve very short channels poses issues of mechanical stability for the typical plate-and-frame or spiral wound stacks, especially for large scale unit with hundreds of cells. A new stack concept is required, but none has been tested before. Only Veerman et al. [19] proposing a new design with "fractal profiled membranes". In this system, deep feed channels and thin reactor channels with a cell length of ~1 mm are pressed in the membranes.

In the optimization of the RED process, other important hydrodynamics aspects to be reckoned are the pressure drops contribution of the distributor and collector channels, and the flow rates distribution within the channels of the stack. Wide manifolds are able (i) to reduce significantly the pressure drop localized in the distribution/collection system and (ii) to ensure a uniform fluid flow within the channel, which reduces the non-Ohmic resistances [28, 36].

Summarizing, various factors interact in a complex way influencing the key aspects that determine the net power output. The identification of the optimal configuration of the stack should take into account many parameters. With respect to the issues investigated in this work, the study is focused on the analysis of the three factors identifying the fluid dynamics of the system and affecting the process performance, by means of Computational Fluid Dynamics (CFD) modelling: stack geometry, flow rate and feeds features. The effects on concentration polarization phenomena (R_{BL}) and pumping power is evaluated.

1.4 Spacer-filled channels for membrane processes

Net spacers represent an essential element of RED stacks and in general of many other membrane processes in flat sheet and spiral wound modules as: electrodialysis, reverse osmosis, ultra-filtration, nano-filtration, membrane distillation, etc. A spacer consists of a net of polymeric filaments and can be made with varying geometrical features. For example, commercial net spacers can be either with woven or non-woven wires. Spacers are adopted as mechanical support for the membranes, giving dimensional stability to the channel, but they can also promote fluid mixing thus reducing polarization phenomena. On the other hand, the presence of a spacer implies disadvantages, as increased pressure

drop and reduced membrane active area, as well as increased electrical (Ohmic) resistance in RED.

As regards mass transport in spacer-filled channels for membrane processes, experiments and simulations provide average and/or local values at the wall of the mass transfer coefficient or Sheerwood number, which give an indirect quantification of the actual effects that would occur in a RED process in terms of reduction of the voltage achievable. Moreover, there exist measurement techniques for the evaluation of the boundary layer resistance (R_{BL}) in RED stacks. The next two sub-sections are purposely devoted to a literature review of these two topics, reporting also the relevant analysis of fluid dynamics for spacer-filled channels (in general) and net power in RED stacks with spacer-filled channels, respectively.

However there exist also various techniques of visualization of the concentration profile. They are not discussed thoroughly here because not pertinent this work. Only some examples are mentioned in the following. Choi et al. [37] measured the potential drops, corresponding to the applied currents, at various distances from a cation exchange membrane (two compartments cell), obtaining the concentration profile in the depleted side, by using a mobile micro-electrode. Tanaka [38] obtained the electrolyte concentration near the ion-exchange membrane by using the Schlieren-diagonal method, i.e. by measuring the refractive index, in a three-compartment optical glass cell. Grigorchuk et al. [39] and Shaposhinik et al. [40-42] employed laser interferometery in an electrodialyzer. Experiments in empty channel and ion conducting spacers were done, highlighting that the local boundary layer thickness can vary significantly due to the presence of the spacer.

1.4.1 Fluid flow, pressure drop and mass transfer in spacer-filled channels

Several works can be found in the literature on the experimental characterization and modelling of spacer-filled channels, aiming to investigate the effect of spacer geometry (filament spacing, filament diameter, filament shape, angle between crossing filaments, flow attack angle) on fluid dynamics features such as flow pattern, recirculation, shear rate distribution, flow regime, pressure drops and mass transport phenomena. Performance in terms of mass transfer in spacer-filled channels for membrane processes

is often evaluated by the limiting current density on electrodes or ion exchange membranes [7, 37, 43-47], from which the Sherwood number can be obtained. Also, experimental works on pressure driven processes can provide data on mass transfer.

In the analysis of spacer-filled channels for membrane processes, computational fluid dynamics (CFD) is a very effective predictive method for a detailed evaluation at small scale and for testing a number of different cases. The Navier-Stokes equations and the continuity equation are solved as governing equations for fluid dynamics; when mass transfer is analysed too, the convective-diffusive transport equation is added to the equations system.

Isaacson and Sonin [48] carried out limiting current measurements in an six channels electrodialyzer (one cell pair, two guard channels and the two electrodic compartments) in order to investigate the spacer performance. Correlations among Sherwood number (*Sh*), friction factor (*f*) and Reynolds number (*Re*) were found for strip-type eddy promoters at various spacings. The optimal spacing was about four times channel thickness, and it exhibited performance comparable with traditional spacers.

Schock and Miquel [49] carried out tests of some commercial spacers, collecting experimental data on pressure drop and mass transfer in spiral wound modules for pressure driven processes. Correlations among the dimensionless numbers before mentioned were obtained, and a performance calculation aiming at optimizing spiral wound elements was addressed.

Da Costa et al. [50] analysed in more detail the spacer characteristics developping a semi-empirical model which permits the evaluation of spacer performance (specifically for ultrafiltration). The angle between the filaments was found to be the most important parameter and the optimal value was 90°, because it leads to the maximum mass transfer coefficient along with low pressure drop.

Schwinge et al. examined fluid flow [51] and mass transfer [52] for cylindrical spacer filaments that were orientated transverse to the main flow direction, by a two-dimensional CFD modelling. The effect of different spacer configurations was evaluated. Recirculation regions were found before and after each filament. A pressure loss increase was found by increasing the Reynolds number and the filament diameter and by decreasing the mesh length. A large mesh length allowed redevelopment of the boundary layer between the filaments. Mass transfer increased with the filament

diameter; however, at a smaller filament diameter, the overall spacer performance increased, as indicated by a high mass transfer enhancement to pressure loss ratio.

Karode and Kumar [53] applied the 3D-CFD simulation on several commercial spacers. The dependence of the total drag coefficient on *Re* was found in agreement with the experimental data. Simulations showed that for spacers with a low mesh length, the fluid bulk flows parallel to the filaments and the pressure drop was found to be largely caused by an abrupt change in the direction of the velocity vectors across the plane of intersection of the spacer filaments; for high values of mesh length, the fluid bulk flows parallel to the channel axis. It was also observed that symmetric spacers (equal filament diameters) typically lead to higher pressure drops and more uniform shear rate distribution at the walls. Finally, the influence of spacer geometry on the average shear rate was found higher by increasing the fluid velocity.

Li et al. [54] carried out CFD simulations to determine mass transfer coefficients and power consumption of net spacers. The mesh length, the angle between the filaments and the flow attack angle were the geometric parameter investigated. They introduced a dimensionless power number (*Pn*) in order to quantify the pumping power consumption. The optimal spacer geometry was with the filament spacing divided by the channel height equal to 4, the angle between filament of 120° and flow direction bisecting this angle. The same authors validated experimentally these simulations in a subsequent paper [55], obtaining mass transfer coefficients by the limiting current method. This is also the only paper where spacers with woven filaments are investigated. The entry length in the channels was found equivalent to about three to five repeating flow cells along the mean flow direction.

Tanaka [56] performed limiting current density measurements on anion and cation exchange membranes in a six channel electrodialyzer. A diamond spacer with overlapped filaments was used in the measuring channel. Results showed that the spacer adopted did not increase the limiting current density, probably because of the dead spaces between the spacer and the membrane; thus a spacer could eventually not have effects on mixing enhancement.

Balster et al. [57] tested performance of different spacer configurations by limiting current density measurements in a six compartment electrodialysis stack. Conventional non-woven, modified, twisted, and multi-layer spacers were tested. The presence of a spacer clearly enhanced mass transfer respect to the empty channel. Results showed that

twisted rectangular filaments can provide better mixing than round filaments due to swirling flows, although channel performance is affected too by the angle between filaments and the flow attack angle. At the same *Pn* the best multi-layer spacer tested showed a 20% increment in mass transfer with respect to a conventional spacer. In the multi-layer configuration, the middle spacer moves the flow from the bulk towards the channel walls; here, the thin spacers decrease the boundary layer thickness by creating vortices near the membrane.

Ranade and Kumar [58] showed that a "unit cell" approach can be used successfully in CFD simulations, allowing to resolve in detail small-scale flow features. Also, the contributions of form drag and viscous drag to the overall pressure drop were quantified and spacers with different cross-sections were studied.

Santos et al. [59] investigated spacers made of rectangular cross-section filaments, by means of CFD direct numerical simulations on periodic cells and experiments, finding that all the fluid dynamics variables were determined mainly by the transverse filaments. Results showed that the transition from laminar to transitional flow regime can be rigorously determined by the slope of the friction factor-Reynolds number curve.

Koutsou et al. [60] carried out CFD direct numerical simulations in a periodic unit cell and experimental tests on diamond spacers, by changing the mesh length and angle between the crossing filaments (β). As expected, pressure drop tends to decrease by increasing the mesh length and reducing β; the smallest values of wall shear stresses were near the contacts spacer filaments/walls. The same authors published a systematic study (CFD simulations and experiments by limiting current) on mass transfer [61]. Lower values of *Sh* were obtained as the mesh length was increased, and as β was increased. *Sh* and time/space-averaged shear stresses exhibited very similar dependences on *Re*. Also the *Sh* dependence on the Schmidt number (*Sc*) was studied, finding a power law with exponent near 0.4.

Shakaib et al. [62] analyzed by CFD the effects of spacer geometry in terms of spacing and thickness of the two sets of filaments, flow attack angle and angle between the filaments, on pressure drop and shear stress. The same authors investigated also mass transfer [63]. A comparison between shear stress distribution and mass transfer coefficient distribution was done. Also, the average mass transfer coefficient was found

to increase in (i) spacers with increased transverse filament thickness and (ii) spacers with filaments inclined towards channel axis which involve zigzag nature of flow.

Li and Tung [64] have evaluated different cell types for periodic boundary conditions in CFD simulations of overlapped spacer-filled channels, showing that for symmetric spacers all the possible cell types reported in literature are suitable, while for asymmetric spacers the best cell type is when the filaments overlap at the centre of its lateral faces, because only in this case the lateral areas are equivalent.

Some papers have been devoted to study the unsteady flow regime [65, 66], other ones have been focused on multi-layer or non-conventional spacers [57, 67-71] and some papers addressed the CFD modelling of pressure driven membrane processes [72-74].

1.4.2 Boundary layer resistance and net power in RED stacks with spacer-filled channels

Literature data on boundary layer resistance and net power in RED stacks equipped with spacer-filled channels are reported and analysed in this section. The measurement techniques for the evaluation of R_{BL} in RED stacks are (i) chronopotentiometry and (ii) electrochemical impedance spectroscopy coupled with direct current measurements.

Jagur-Grodzinski and Kramer [32] carried out experiment by investigating the effect of a modified spacer. The surface of a commercial spacer was modified by chlorosulfonation and subsequent hydrolysis to make it less frictional and cation conducting. The hydraulic loss was considerably reduced and the gross power was increased when the modified spacer was adopted, by obtaining an increase of net power of ~55%. Only ~10% and ~4% of the energy produced was spent for pumping solutions, for the case of the unmodified spacer and the modified spacer respectively, at the flow rate that maximizes the net power. These percentages were low due to the high thickness of the channels, equal to 0.85 mm and 0.65 mm.

Post et al. [17] employed the chronopotentiometric technique for the case of a stack provided with spacer-filled channels either 0.5 mm or 0.2 mm thick, concluding that the stack resistance was mainly Ohmic, but a non-Ohmic resistance of 6% and 16% respectively was also present.

Długołęcki et al. [26] employed direct current measurements coupled with electrochemical impedance spectroscopy in a stack with the same spacers used by Post et

al. [17]. From these experiments, it is highlighted that: (i) at low flow rates, concentration polarization phenomena can account for the dominant resistance; (ii) the spacer shadow effect (which contributes to the Ohmic resistance) is significant.

Długołęcki et al. [29] employed the same technique for investigating the effects of ion conductive spacers. Results show a reduction of the overall stack resistance by a factor ~2 and an increase in power density of a factor 3-4 compared to the stack with non-conductive spacers with the same open area and shape. This performance improvement is due to a significant reduction of the Ohmic resistance by eliminating the spacer shadow effect. On the other hand, an increase in R_{BL} was found when ion conductive spacers are used, due to the contribution of the spacer-solution interface to concentration polarization phenomena.

Długołęcki et al. [4] carried out experiments by the same technique in a two compartments cell (without spacers), in order to measure all the contributions to the resistance across an ion exchange membrane: pure membrane resistance, diffusion boundary layer resistance and double layer resistance. Experimental data reveal that, at very low salt concentration (0.017 M NaCl), the dominant resistance is the diffusion boundary layer resistance, while the other two contributions are of minor importance. At higher salt concentration (0.5 M NaCl), the pure membrane resistance is the dominant one, the diffusion boundary layer plays a considerable role and the double layer resistance is not significant. Note that in these comparisons, the Ohmic resistance of the solution (which depends on the distance of the measuring electrodes) is not considered. Also, the beneficial effect of the flow rate in reducing R_{BL} is shown.

Veerman et al. [18] carried out experiments on a 50 cells stack with spacers 200 μm thick. The maximal net power is reached at a linear flow velocity of ~0.7 cm/s. At this optimum the pumping power reduces the power output by 25%, while the reduction of the maximum gross power can be estimated to be ~38%. The pressure drop as a function of the flow rate is fitted by a parabolic curve, mainly due to the contribution of the manifolds (80% of the total [34]). This emphasizes that the design of the manifolds is crucial.

Veerman et al. [20] compared the same stack of [18] with a large stack with 50 cells 25 × 75 cm^2. At the maximal net power density, the energy loss in hydrodynamic friction is 13% and 16% for the small stack and for the large stack, respectively. Also, the authors

concluded that the main contribution to the hydraulic resistance is due to the spacer-filled part of the compartments just around the supply and drain holes. With respect to an infinite wide and long empty channel, the total pressure drop per unit length is incremented of 715 times, as highlighted in [19].

Vermaas et al. [21] performed experiments by chronopotentiometry for evaluating the performance of four different spacers with thickness of 60, 100, 200, 485 μm. The Ohmic resistances (mainly due to the resistance of the river water compartment) were predominant at high flow rates, as the non-Ohmic resistances were decreased. For a given flow rate, R_{BL} increases as the spacer thickness increases (as expected). At the flow rates that give the maximum values of net power, R_{BL} is comparable with $R_{\Delta C}$ and R_{ohm}, and it is comprised from ~16% to ~25% of the total internal resistance. The maximal net power is obtained at Reynolds numbers lower than 1. The reduction of the gross power due to the pumping power is about 44%, 18%, 14% and 6% for the spacers in ascending order of thickness, while the difference between the maximum net power obtained and the maximum gross power achievable is >50% (not easy to evaluate from available data), ~47%, ~28% and ~25%. The total pressure drop per unit length through the stack is ~35 times the pressure drop per unit length in an empty channel with infinite streamwise and spanwise extend, (inversely proportional to the cubic power of the thickness).

Vermaas et al. [14] proposed a method to predict R_{BL} from design parameters only: they assumed that the degree of mixing in the boundary layers depends on the velocity shear at the membrane-solution interface. Also, the effect of the channel length was evaluated, showing that a very short path length can increase significantly the net power, especially if low resistance membranes are used.

In [28] experiments were performed using various channel configurations. In particular, a standard woven spacer (245 μm) and a twisted spacer (223 μm) made by single wires as a weft and two twisted wires as a warp, were used. The twisted spacer shows the following performance with respect to the woven spacer: significantly lower ohmic resistance (decrease of 15%), due to the more open area and porosity, which reduce the spacer shadow effect; slightly higher non-Ohmic resistances, but at the flow rates that maximise the net power ($Re \approx 3$ vs 2.5) they are practically equal and consist of ~18% vs ~22% of the total resistance; higher gross power density, due to the reduction of the Ohmic resistances, which were the dominant ones; lower pressure drop (~3/4) due to the

more voidage; higher net power density, with a reduction of the gross power due to the pumping power of ~10% for both spacers, and a difference between the maximal net power obtained and the maximum gross power of ~30% for both spacers, with values slightly lower for the twisted one. To the authors, low non-Ohmic resistances were found, due to a uniform feed flow distribution over the whole width of the channels that avoid the presence of dead zones ([36]). This was achieved by means of wide manifolds for the distribution in the stack used for these experiments. Also, a tremendous reduction of the pressure drop localized in the manifolds was obtained, but the overall hydraulic loss for the normal spacer was ~10 times higher compared to a profiled-membrane channel, although large standard errors occurred in the measurements.

Up to now, Daniilidis et al. [25] have carried out the only work addressing the evaluation of the performance of a RED stack fed by different concentrated solutions. NaCl concentrations ranging from 0.01 M to 5 M were used. The spacer adopted had a thickness of 100 μm. The membrane resistance is dominant at high concentrations, while the Ohmic resistance of the channel and the non-Ohmic resistances are reduced significantly at high concentrations. On one hand, the higher conductivity reduces the Ohmic resistance; on the other hand, the effects of the non-Ohmic phenomena are affected strongly by the solution concentration. In fact, the streamwise concentration change relative to the inlet concentration and the concentration change in the boundary layer relative to the bulk concentration are lower as the average concentration increases. Since the voltage established over the membrane depends on the *ratio* of the solutions concentrations, the lower relative reductions of concentrations reduce $R_{\Delta C}$ and R_{BL}, which at high concentrations (for example 0.5 M - 5 M) begin negligible. The maximum gross power output was found for the couple 0.02 M - 5 M.

Pawlowski et al. [27] carried out measurements in limiting current conditions and chronopotentiometric measurements in under-limiting current conditions, in a stack with either spacer-filled or empty channels 800 μm thick. Limiting current density measurements showed that the double layer thickness does not depend on the NaCl concentration within the investigated range (1, 5 and 30 g/l solutions). The presence of spacers reduced the boundary layer thickness by 25% at the lowest linear flow velocity investigated (~0.2 mm/s) and 60% at the highest one (~3.5 cm/s). Also the entry effects in the empty channel were studied. The concentration field becomes fully developed at a

certain distance from the channel inlet (~10 cm or more), i.e. the Sherwood number (*Sh*) reduces up to an asymptotic value, although the slope of the curve is much higher near the entrance; also, as the linear flow velocity increases, *Sh* settles at a longer channel length. In a spacer-filled channel, convective transport favours mixing, but also reduces drastically the entrance effects, which are confined in a small region near the inlet [55, 63]. Therefore, the use of short empty channels (e.g. 0.5 cm) could even reduce R_{BL}, as the entry effects could enhance mass transfer more than the convective motions induced by spacers. Chronopotentiometric measurements of Ohmic and non-Ohmic resistances for the two channel configurations were performed. The spacer increased the Ohmic resistances and reduced the non-Ohmic resistances compared to the empty channel, while at higher concentrations and higher flow velocities the two contributions to the resistance were decreased. The following data were obtained below 1 cm/s of linear flow velocity, which is the range of major interest for RED (in terms of maximum net power): (i) at the concentration of 1 g/l (0.017 M) the non-Ohmic resistances accounted for ~14% and ~32% for spacer-filled channel and empty channel, respectively, with a reduction of the total resistance in the empty channel of ~35%; (ii) at 5 g/l (0.085 M) the non-Ohmic resistances were of ~8% and ~21% for spacer-filled and empty channel, respectively, with a reduction of the total resistance in the empty channel of ~54%; (iii) at 30 g/l (0.511 M) the resistances were significantly lower and the non-Ohmic resistances had the relative influence further reduced.

1.5 Profiled membranes

Profiled membranes represent a valid alternative to the traditional net spacers. The profiles, present either on one or on both sides of each membrane, can be obtained by hot pressing and perform the function of spacers separating the membranes and thus generating the channels for the feed solutions, while maintaining good chemical and mechanical characteristics [75]. The use of profiles made by ion-conductive material reduces the Ohmic resistances of the stack, as the undesired spacer shadow effect is avoided, and the membrane active area can be increased. Another important advantage is the reduction of the friction factor compared to a spacer-filled channel; this fact allows operating either with lower power consumption for pumping, or at higher Reynolds numbers thus promoting mixing and reducing the residence time. On the other hand, at a

given flow rate the net spacers provide enhanced convective transport which improves mixing. Finally, cost savings should not be forgotten.

In the next two sub-sections a literature review on performance of profiled membranes is reported. Section 1.5.1 is devoted to the analysis of fluid dynamics and mass transfer in profiled-membrane channels, while section 1.5.2 reports data from the few works found in the literature on RED stacks with profiled membranes.

1.5.1 Fluid flow, pressure drop and mass transfer in profiled-membrane channels

In the literature, some examples of profiled membrane applications in electrodialysis experiments can be found. Measurements at limiting current density and overlimiting current densities provide mass transfer coefficient or Sherwood number for the characterization of mass transport phenomena.

Scott and Lobato [76] carried out limiting current density measurements, and proposed an experimental correlation relating the Sherwood, Reynolds and Schmidt numbers for a cross-corrugated module, valid in the range Re = 50-1000. A flow regime with an irregular flow path was caused by the membrane corrugations (which disturb and break the boundary layers), thereby enhancing mass transfer and providing flow features typical of a turbulent flow [77].

Nikonenko et al. [78] suggested a semi-empirical approach to predict mass transfer characteristics of electrodialysis and electrodeionization stacks used for the desalination of dilute solutions in overlimiting current modes: a higher increase in the mass transfer coefficient due to mixing promotion was obtained for channels with profiled membranes, as compared to spacer-filled channels (and of course empty channels).

In the work of Larchet et al. [79], a stack with profiled membranes exhibited a lower hydraulic resistance and a higher mass transfer rate than a stack with spacer-filled channels. Also, profiled membranes were effective in the overall range of concentrations investigated, while non-conducting spacers were effective only at feed solution concentrations higher than 0.002 M.

Balster et al. [80] prepared and characterized a novel membrane design, referred as “membrane with integrated spacer”, where the profiles were obtained by capillary forces of a drying polymer solution in contact with a net spacer. This membrane was tested in

an electrodialysis stack, showing (i) an enhanced mass transfer and (ii) a reduced electrical resistance of the stack compared to the corresponding flat membrane.

Strathmann [10] carried out experiments of ED with profiled membranes, obtaining lower stack resistance and higher limiting current densities than in a stack provided with flat membranes and net spacers.

Moreover, several papers can be found in the literature on hydrodynamics and heat transfer predictions via CFD in corrugated channels, mainly with reference to heat exchangers [81-85], but very few woks have been devoted to mass transfer phenomena in such geometries. Zhang [86] carried out CFD modelling of fluid flow and mass transfer in a cross-corrugated triangular duct by simulating water vapour transport in dry air; correlations of friction factor and Sherwood number with the Reynolds number were proposed.

1.5.2 Boundary layer resistance and net power in RED stacks with profiled-membrane channels

An increasing interest towards the RED technology is noticeable in the recent years, but very few works have been devoted to studying the performance of RED stacks with profiled membranes. As reported in the literature [29], the adoption of ion-conductive spacers improves the system performance in terms of gross power density compared to the use of non-conductive spacers, but of course does not affect the hydraulic loss. First, Brauns [31] proposed the use of profiled membranes for a RED stack. Later, Veerman et al. [19] introduced the concept of “fractal profiled membranes” in order to have short and spacerless reactor channels.

Experimental data on R_{BL} in RED stacks with profiled membranes are obtained by chronopotentiometry. The first real application of profiled membranes to RED is in the experiments by Vermaas et al. [30]. Profiles having a square cross-section arranged and running along the entire channel length were obtained by hot pressing of commercial membranes. The wet ridges were 245 μm for the CEMs and 230 μm for the AEMs and placed at 1 mm of distance. The performance of the stack with these membranes was compared to the performance of the stack with net spacers 240 μm thick. The maximum gross power density of the stack with profiled membranes was found to be only slightly larger than that relevant to the stack with net spacers. In fact, although the profiled

membranes gave an Ohmic resistance decreased by ~30%, they also caused R_{BL} significantly higher (increment of ~175% at the flow rate that maximises net power) due to a poorer mixing promotion. The maximum values of net power were obtained for *Re* ≈ 5 for profiled membranes and *Re* ≈ 2.5 for spacers. In the condition of maximal net power, with respect to the total resistance, R_{BL} was ~36% for profiled membranes and ~12% for spacers. On the other hand, the hydraulic loss was 4 times lower in the stack with profiled membranes, resulting in a net power density increase of 10%. The gross power was reduced by the pumping power by ~13% for profiled membranes and ~20% for spacers, while the difference between the maximum net power obtained and the maximum gross power was ~44% for profiled membranes and ~40% for spacers. The total pressure drop per unit length through the stack with profiled membranes is ~20 times the pressure drop per unit length in an empty channel with infinite streamwise and spanwise extend. In another work [14] (see also section 1.4.2) higher net power densities were theoretically calculated for stacks with profiled membranes compared to stacks equipped with net spacers.

Further experiments are shown in [28], where different channel configurations were tested: two kind of spacers (see section 1.4.2), profiled membranes as those used in the previous work [30] (although here the channel thickness is declared to be 230 μm), and profiled membranes with additional sub-corrugations of triangular shape with height of 50 μm, perpendicular to the fluid flow. Due to the use of wide manifolds, the stack used for these experiments ensured (i) a uniform feed flow distribution over the whole width of the channels without dead zones and thus low non-Ohmic resistances, and (ii) low pressure drop, compared to those measured in [30]. Therefore different performance for the profiled membranes was found compared to the previous experiments [30]. The stack with profiled membranes exhibited the following performance at the maximum net power (obtained for *Re* ≈ 4): non-Ohmic resistances equal to ~31% of the total resistances, low reduction of the gross power due to the pumping power (<5%, but with large experimental errors), difference between the maximal net power obtained and the maximum gross power of ~37%. The total pressure drop per unit length was found only slightly higher (~doubled) than the theoretical one in a finite rectangular channel, due to the improved distribution system. The configuration with sub-corrugations did not exhibit a decrease in non-ohmic resistance because the sub-corrugations employed did

not act as mixing promoters at the low Reynolds numbers typical of RED systems. Also, higher Ohmic resistances and hydraulic friction reduced the gross power and the net power. For a comparison with the performance of the spacers, see section 1.4.2. Here, it can be highlight that, with respect to the normal spacer, the profiled membranes: (i) reduced of ~50% R_{ohm}; (ii) exhibited practically the same non-Ohmic resistances at the low Reynolds numbers that maximize the net power, while at higher flow rates are reduced by the spacers; (iii) reduced drastically pressure drops, which account for ~10%; (iv) increased gross power and net power respectively of ~60% and ~76%.

Another advantage of profiled membranes is a sensitivity to fouling much lower compared to stacks with net spacers [87]. Finally, profiled membranes which do not disturb much the fluid flow can be adopted for short channels in order to exploit entry effects reducing R_{BL} [27] (see section 1.4.2), as well as for decreasing $R_{\Delta C}$ and pressure drop.

1.6 Influence of the distribution system on the RED stack performance

The total pressure drop through the stack from inlet to outlet includes various contributions. In general, it can be divided in: (i) the pressure drop in the distribution/collection system and (ii) the pressure drop in the channel, provided by a spacer or a profiled membrane. Experiments on lab-scale stack show that the measured hydraulic loss per unit length is significantly higher than that one in an empty channel with infinite streamwise and spanwise extent. Data mentioned in section 1.4.2 and 1.5.2 shows that these increments can be of one or even two orders of magnitude, and also that the hydraulic friction in the manifolds is an important contribution and often is even the main one [14, 18-21, 28, 30, 34].

It is important to remark that in all works cited in section 1.4.2 and 1.5.2 the classical plate-and-frame geometry is adopted for the RED stack, and usually a cross-flow configuration for the two solutions is adopted. In almost all these cases, spacers, gaskets (integrated or not integrated) and membranes are punched; therefore the fluid moves along the ducts created by these holes and enters the channels if encounters the spacer or goes on if encounter the gaskets.

According to Veerman et al. [20] the following parts of this kind of stack that contribute to the total pressure drop can be identified: (i) manifolds (intended as external tubing),

(ii) bores through the stack, (iii) spacer-filled part of the compartments near the supply and drain holes and (iv) part of the spacer-filled compartment where a uniform flow can be assumed. In the stack used for these experiments the external tubing was purposely over dimensioned, while the channels formed by the bores were only 3 cm deep; thus the first and the second contribution can be neglected. Conversely, the initial part of the channels around the inlet and outlet holes was expected to be very high. In fact, the feed solutions enter the compartments in radial direction through these holes with relative high fluid velocities compared to the cross-section of the channel with the whole width. This part was referred as "radial spacer resistance". Experiments were performed in a large stack with 50 cells 25 × 75 cm^2 in two operation modes: vertical, i.e. along a short flow path (25 cm), and horizontal, i.e. along a long flow path (75 cm). The trend of the pressure drop as a function of the flow rate was found almost the same for the two configurations, despite the significant difference in the flow path length. With respect to an infinite wide and long empty channel, the total pressure drop per unit length is incremented of 715 times, as highlighted in [19]. These facts demonstrate that the radial spacer resistance is dominant compared to the resistance offered by the channel where the flow can be assumed uniformly distributed.

In the experiments of Veerman et al. [18] (50 cells stack with spacers 200 μm thick) the trend of the total pressure drop (measured outside the stack) as a function of the flow rate is fitted by a parabolic curve and is mainly due to the high losses localized in the manifolds. In fact, pressure measurements in the spacer-filled channels showed a much lower pressure drop [34]. Therefore, the residual pressure losses are caused by distribution/collection system, which amount to 80% of the total one.

The profiled membranes used by Vermaas et al. [30] create empty channels, although with finite width. Even in this case the total pressure drop per unit length was ~20 times than in an infinite wide and long empty channel. In the stack with spacers, the increment is obviously higher (~80 in this work and ~35 in [21]). Only a minor part of this excess is due to the finite width of the profiled-membrane channels. Taking into account of the width (1 mm), the theoretical pressure drop is ~13 times lower than that measured.

Therefore the major excess in hydraulic friction is caused at the inflow and outflow of the compartments, where the flow moves radially with sharp corners and high velocity.

All these findings highlight that some action are needed in order to reduce the pumping power consumption due to the distribution/collection system. For example, it would be recommended to make more inlet and outlet holes.

Pawlowski et al. [33] developed and experimentally validated a model for predicting the total pressure drop inside a RED stack. In the stack design simulated, the partial pressure drops taken into consideration are: in (1) distribution ducts, (2) branches, (3) beams, (4) due to sudden section expansion between the beam and the compartment channel and (5) in the compartment channel (spacer-filled or spacer-less). In lab-scale stacks simulated, the pressure drop in the compartments was dominant, especially for narrow channels and low fluid flow rates. A non-uniform fluid flow distribution among the channels in the investigated stack geometry was due to the pressure drop in the distribution duct and, especially, in the sudden expansion and contraction branches, where the pressure drop is calculated proportional to the squared fluid velocity. For large-scale stacks dimensions with an increasing number of cell pairs (200), the pressure drop in the branches increases (as the total flow rate has to be incremented to maintain the same average flow rate in the channels); moreover, its relative weight can become important as fluid flow rate increases (higher than 2 cm/s) and/or the channel thickness increases (i.e. 0.8 mm), causing a less uniform distribution of flow rate and a reduction of the net power density.

Tanaka [12] applied hydrodynamics equations for laminar flow to an electrodialysis system in order to evaluate the parameters that describe the performance of the stack. The main parameters were: the static head difference between an entrance and an exit of a current-passing section and that of a passageway; the spacer friction factor; the distribution coefficient of solutions flowing into every cell. The solution flow in a stack was classified as: (i) a one-way flow system, where the flow direction in an entrance duct is identical with that in an exit duct; (ii) a two-way flow system, where the flow direction in an entrance duct is opposite to that in an exit duct. It was found that for operating the stack stably by maintaining a more uniform pressure drop between the entrance and the exit ducts and thus a more uniform flow rate distribution, it is preferable to adopt one-way flow system, reduce the pressure drop in the distributor and reduce the number of channels. From the non-equilibrium thermodynamics, the overall mass transport equation was introduced in order to evaluate solution leakage due to pressure difference. In this equation the ionic flux is expressed by the terms of migration, diffusion and leakage of ions, and the volume flux is expressed by the terms

of electro-osmosis, concentration-osmosis and leakage of solutions. The solution leakages were found in both directions, i.e. from a desalting cell to a concentrating cell and *vice versa*, because the pressure in a desalting cell becomes larger in some part and smaller in another part than that in a concentrating cell. These events are caused by non-uniform distributions of linear velocity and friction head in desalting cells. Therefore, ensuring a more uniform distribution of flow rate in the desalting cells of the stack and decreasing the spacer friction factor should suggest the strategies for reducing the solution leakage.

The above literature review emphasizes that the design of the manifolds for the stack is crucial. Among the experimental works on lab-scale RED stacks, Vermaas et al. [28] are the only to having used a completely different design of the stack. The feed solution is supplied by means of a short duct crated by a hole in a PMMA casing, then passes in a manifold of width equal to the channels, and finally enters the compartments. The two solutions are fed in cross-flow configuration. A gasket was at both sides of either spacer or profiled-membrane parallel to the flow direction closes the channel to the other solution. The performance of this stack in terms of non-Ohmic resistances and pumping power was better than the stack used in [30]. In such a system the preferential channelling is avoided, i.e. a uniform feed flow distribution over the whole width of the channels without dead zones is obtained; as a consequence low non-Ohmic resistances occur. Also, the contribution to the total pressure drop due to the manifolds is significantly reduced. In fact, profiled membranes exhibited a pressure drop which is close to the theoretical value in a finite rectangular channel (~doubled). In addition, also the high thickness of the distributor channel could have beneficial effects, favouring a uniform distribution of flow rate among the channels in a stack with several cell pairs.

Summarizing, the geometry of the distribution/collection system can affect significantly pressure drop, flow rate distribution among the channels, flow rate distribution along the width of each channel (preferential channelling and dead zones), with a consequent influence on pumping power, leakage issues, non-Ohmic resistances and thus on the net power achievable.

1.7 Process modelling

1.7.1 Multi-scale approach

An essential element for the optimization of electro-membrane processes is represented by an effective modelling tool, capable to predict with good accuracy the behaviour of the system involving a sustainable computational demand. In fact, the performance improvement and the design of the optimal configuration can be achieved by the support of a suitable process simulator. Nevertheless, building up a comprehensive simulation tool is a very hard task; this is due to complex phenomena which interact each other and occur over several scales. For this reason, the direct simulation of the complete system by one only tool appears to be impossible.

An integrated simulation tool based on a multi-scale modelling approach can be the effective way to address the full problem [88]. Through a structured *separation of scales*, the detailed analysis at small scale on fluid flow and mass transfer inside the channel can be correlated with the membrane modelling, representing the higher scale of investigation (meso-scale). From the simulation of phenomena at small scale the local distribution of the variables within the channel is obtained; therefore, these results are used to develop the constitutive expressions, i.e. the functions correlating the process parameters such as mass transfer coefficient and friction factor with the parameters describing the operating conditions and the channel geometry. At the meso-scale the of the transport through the membrane is treated by means of a suitable mathematical model integrated with the modelling at lower scale; thus the cell pair in a RED stack can be simulated. Finally, a larger spatial domain is investigated, up to the simulation of the whole stack.

In this work, the spatial scale investigated is mainly the small scale inside the RED channels. A literature review of CFD modelling in spacer-filled channels is provided above in section 1.4.1 (along with experimental works). The mass transfer in those works is addressed by means of a convective-diffusive transport equation. In the next section, modelling of mass transfer phenomena in electro-membrane processes, and thus involving the migrative flux, at the small scale of interest for this work is devised.

1.7.2 Modelling of mass transfer in electro-membrane processes

In an electrolytic solution, ions are charged species that interact with each other as well as with the solvent. These interactions are quite complex and difficult to model, but a simple approach lead to the Nernst–Planck equation, the common equation adopted in

the literature to describe the ionic flux. This approach is based on the so-called *principle of independence* of the ionic fluxes: the flux density of a species *i* is determined by its electrochemical potential gradient only, and not by the electrochemical potential gradients of other species. This means that cross-phenomenological coefficients are neglected in the transport equations for ionic species, i.e. there are no short-range interactions among ions. The Nernst–Planck approach is only strictly applicable to dilute solutions, where the probability that two ions get close is relatively small [45]. The flux of the ionic species *i* ($\vec{J}_i$) is expressed as

$$\vec{J}_i = -D_i \vec{\nabla} C_i - D_i z_i C_i \frac{F}{RT} \vec{\nabla} \varphi + C_i \vec{u} \tag{1.11}$$

where, D_i is the ionic diffusion coefficient, C_i is the concentration, z_i is the valence, φ is the electric potential, and $\vec{u}$ is the velocity vector. The total flux of the species *i* is given by the sum of the diffusive, the migrative and the convective fluxes. As well as the flux of mobile ionic species, the complete system of equations describing mass transfer in electrolytic solutions comprises the expressions of mass balance of the components, conservation of mass (continuity equation) and momentum (Navier–Stokes equations), current density and a condition for the net charge density. Usually the local electroneutrality condition is assumed, which states that the local electrical charge density vanishes everywhere

$$\sum_i z_i C_i = 0 \tag{1.12}$$

Actually, the rigorous relationship is the Poisson's equation, which for a medium of uniform dielectric constant ε is

$$\nabla^2 \varphi = \frac{F}{\varepsilon} \sum_i z_i C_i \tag{1.13}$$

The proportionality constant F/ε is quite large (for water $\varepsilon \approx 7.08 \times 10^{-10}$ F/m), so that a negligible deviation from electroneutrality would lead to a considerable deviation from zero of the Laplacian of the electric potential. In other words, an appreciable separation of charge would require prohibitively large electric forces [89]. However, whenever the electric field varies with position there are deviations from local electroneutrality. These deviations occur in the electrical double layer at interfaces IEM-solution and electrode-solution, and are confined in a quite narrow region (1-10 nm [89]). Although they are irrelevant in terms of chemical composition of the solution, they are crucial for the electrical contribution to the electrochemical potential of charged species. For example the space-charge region has a relatively constant and low charge density (typically less than 0.1 eq/m^3) that is essential for sustaining overlimiting current through the boundary layer. Also, at overlimiting current the space-charge region expands beyond the electric double layer from the IEM [90]. For the solution of transport problems in regions of locally charged solution, Poisson's equation is needed. Therefore, the so-called Nernst–Planck–Poisson (NPP) model has been used. Due to the small numerical value of the permittivity of water, the NPP model is classified as a singularly perturbed problem. It is a complicated mathematical problem, but there are several solution methodologies in the literature [90-97].

As the energy required to charge a macroscopic system is very high, and the double layer is confined in a very narrow region, when transport phenomena are investigated at higher scale, normally electrolytic solutions are assumed electrically neutral and the Poisson's equation is replaced by the electroneutrality condition, with a simplification of the mathematical treatment of mass transfer. Several works based on the Nernst–Planck approach and the electroneutrality conditions have been carried out [6, 38, 40, 47, 98-104].

On the other hand, in concentrated solutions an ion is surrounded not only by solvent molecules but also by other ions. In such a situation, short-range interactions become more important, thus additional frictional forces are present. In other words, the accurate description of transport processes in concentrated solutions requires more transport coefficients than those required by the Nernst–Planck approach as well as a more rigorous approach. According with the Stefan–Maxwell approach [45, 89], the basic scheme for the transport equations is the following: *driving force = friction coefficient* × *relative velocity* (see section 2.4.2). Very few examples of application of this approach

on ion exchange systems can be found in the literature [105-107]. Kraaijeveld et al. [105] used the Stefan–Maxwell equations, assuming the electroneutrality condition, in order to model electrodialysis. The followed approach was able to provide a thorough description of the process simulated. However, the model was based on several parameters not easy to get.

Modelling of mass transfer in electro-membrane processes is a very complex topic. Beyond the approach and the consequent equations system adopted, one needs to choose: the domain to be simulated, from the boundary layer between the fluid bulk and the membrane-solution interface up to the real "periodic" unit consisting of the cell pair; the dimensions to which extend the simulation, 1D, 2D or 3D; the components of the convective transport, if it is included. Moreover, the properties of the membranes (resistance, diffusion coefficient of ions, etc...) and the appropriate boundary conditions are important. The complete system consists of a cell pair simulated in 3D, taking into account the three component of the velocity, the channel geometry (e.g. presence of spacers), and the membranes properties. It appears clear that such a system is very difficult to simulate and would require a huge computational effort for an accurate spatial resolution. As a matter of fact, all the works in the literature are based on some simplifying assumptions. 1D or 2D simulations are carried out usually [6, 38, 40, 47, 98-104], convection is considered in some cases [38, 40, 100, 103, 104] and a cell pair is simulated rarely [6].

1.7.3 Modelling of mass transfer in RED

The complete prediction of the performance of a RED stack could be possible only by simulating the entire stack and taking into account all the phenomena involved in the process. However, it would be unsustainable from the point of view of the computational effort, as well as very complex for the phenomenological modelling. Published computational studies of transport phenomena in channels for RED are only few. Brauns [31] used the Lacey [2] approach, based on a simplified concentration polarization layer model, to evaluate the effect of various parameters on electrical power output. However, mass transfer is not addressed directly and the boundary layer thickness is assumed at a given value. In other words, the small scale of the problem is not analysed. The same author refined the analysis by using two-dimensional finite element modelling [108]; the

steady state salt ion flux through the membranes and the corresponding ion concentration distribution within the solution compartments were investigated. In this case, mass transfer inside the channel is addressed (small scale analisys).

Kim et al. [109] carried out a numerical study to investigate power generation by reverse electrodialysis in ion-selective nanochannels placed between two KCl solutions. Mass transfer was treated by the Nernst–Planck equation (without convective transport) coupled with the Poisson equation and by imposing the potential difference between the two reservoirs as boundary condition. The current-potential characteristics of the nanochannels and the power density were calculated. The numerical results indicate that the power density can be maximized by: using the optimal nanochannel length, which can be determined by an equation purposely found; using the nanochannel with the smaller cross-sectional area; coating the nanochannel surface with materials having strongly acidic or basic functional groups in order to increase surface charge density; keeping the concentration difference between two reservoirs as large as possible.

Kim et al. [110] developed a simplified model in order to simulate a RED unit composed by a concentrated channel and a diluted channel fed by pulsatile flows. Empty channels were considered. The diffusion-convection transport of Na^+ was treated in a 2D framework. The membrane domain was not simulated, but the transport of cation across the membrane (only by diffusion) was expressed as boundary conditions. Also, the cation diffusion coefficient in the membrane and the partition coefficients between membrane and solutions were needed. A subsequent work [111] was based on the same modelling approach in order to investigate a RED stack fed in serial configuration, i.e. seawater and fresh water leaving a compartment enter the subsequent one. As the number of cell pairs increases from 1 to 8, the maximum (gross) power decreases, but the maximum energy density increases. The effect of increasing fluid velocity is inverted.

Jeong et al. [112] proposed a more complete numerical model, although still based on several simplifications. A cell pair of empty channels was simulated in 2D; also, membranes were not included in the computational domain, but were modelled by suitable boundary conditions at the membrane-solution interface. The equations system for mass transfer and fluid dynamics comprises: mass conservations of ions, ions flux expressed by the Nernst–Plank equation, current density, electroneutrality condition, Navier–Stokes and continuity equations. The side ends of the domain were placed at half

of the channel width, with the boundary conditions of velocity and concentration gradients equal to zero and a fixed value of electric potential. The latter condition is somehow equivalent to a fixed external load. The effect of solution velocity, compartment width, and membrane resistance on power generation was investigated. Results show that for a given membrane resistance, the net power output can be maximized by optimizing the flow velocity and compartment thickness. The maximal net power density was obtained by a channel width of ~150 μm and a fluid velocity of ~2-4 cm/s. Also, the results from the 2D model and those from the 1D model based on the assumption of uniform concentration in the direction perpendicular to the membranes were compared. The comparison showed that the gross and net power densities can be overestimated when concentration change in the boundary layer is neglected; also, since the concentration field is developing within the (empty) channel, the fluid velocity affect the discrepancies.

A similar but more rigorous model can be found in [113]. A 2D model was developed for a computational domain consisting of a cell pair and a further diluate channel needed for practical reasons in order to impose the proper periodic boundary conditions. Of course, periodic conditions apply only to concentrations and fluxes of species, but not on the electric potential, due to the generation in the RED system. However a suitable function of the software used, allowed the implementation of such conditions. Membranes were part of the computational domain and were characterized by two adjustable parameters obtained by the model calibration with experimental data, i.e. the counterions/co-ions diffusion coefficient and counterions/co-ions mobility for the flux expressed by the Nernst–Planck equation. Also, the electroneutrality condition within the membranes took into account the concentration of the fix charges. Partition coefficients were used to relate the concentration at membrane-side to that at solution-side of the membrane-solution interfaces. At these interfaces, the jump of voltage was calculated as Donnan potential, i.e. by assuming the equilibrium condition between the two phases (the electrochemical potentials of all ions in the two phases are equal); the activity coefficients were assumed equal to 1. Mass transfer and fluid dynamics were solved by the same equations system mentioned above for [112], and the performance of a stack with N cell pairs was evaluated by calculating the current density, the electric potential and the gross power produced (varying the external load). The model was

validated with experimental data. Moreover, stack with either conductive or non-conductive spacers were simulated.

The literature review of the few works carried out so far shows that modelling of RED process is based on unavoidable simplifying assumptions. For example, the choice of simulating a single cell pair hinds the modelling of the distribution system (as well as the electrodic compartments); simulations of the whole channel length are done by 2D modelling, but they can predict only qualitatively the behaviour of the system. Also, characteristic parameters of the membranes are not easy to find, and models calibrated on experimental data provided by specific apparatuses risk to be predictive with non-negligible limitations.

1.8 What is still lacking in the literature?

In the literature, no attempts have been specifically devoted to develop a suitable model for a 3D depth investigation of fluid dynamics and associated phenomena in channels for RED systems. Also, mass transfer of ions is treated on the basis of the Nernst–Planck approach, which is strictly valid for infinitely diluted solutions; conversely, no specific models have been developed so far on the Stefan–Maxwell approach, which describes mass transport by more rigorous equations valid for concentrated solutions. This aspect could be important as concentrated solutions are very promising for enhancing the process performance. Moreover, a specific investigation devoted to geometries such as woven spacer-filled channels and profiled-membrane channels for membrane processes has not been addressed (section 1.4.1 and 1.5.1), although in RED experiments woven spacers are commonly used (reported in section 1.4.2) and profiled membranes appear promising from the few studies performed on them (section 1.5.2). Another significant aspect not yet investigated is the analysis at the low Reynolds numbers typical of RED systems, as the other membrane processes are usually characterized by higher *Re*. Finally, layout configuration and fluid dynamics of the whole stack are issues poorly considered in the numerical studies, but which cannot be neglected.

The present work is focused on the CFD analysis of RED systems in order to provide what is missing in the literature, according to the REAPower project aims (next section) and on the basis of the modelling described in detail in the next chapter.

1.9 The REAPower project

The work of the present PhD falls within the context of the activities of the REAPower (*Reverse Electrodialysis Alternative Power Production*) project [114, 115]. It is an EU-FP7 funded project carried out by an international multi-disciplinary consortium involving universities and private companies (see Figure 1.2). The aim of the project is optimizing the RED technology in order to guarantee its development and spreading. In particular, this project focuses on the power production by RED technology using seawater or brackish water as dilute solution and brine as concentrated solution, which allows reducing strongly the stack electrical resistance and thus increasing the power achievable [116, 117]. There are several sources of water with very high salt concentration: (i) brine from industrial processes like oil drilling, coal mines, textile industry or some food industries; (ii) natural brine from solar ponds in sea salt production facilities, salt mines, or very salty lakes as the Dead Sea, which has salinity over 250 kg/m^3. The first prototype RED plant to generate electricity from brine was installed by REAPower in the sea salt production facilities in Marsala (*Ettore* and *Infersa* saltworks, Sicily, see Figure 1.3), and the maximum gross power achieved so far was produced.

The specific objectives of the project are:

i. To create/select and optimise materials and components tailored to the process requirements, such as membranes, spacers, electrodes and electrolytes;
ii. To optimise the system design by means of a computer modelling tool purposely developed;
iii. To verify the model, and assess the developed materials, components and design through tests on lab-scale;
iv. To evaluate and improve the performance through tests on a prototype fed with real solutions (brine from a salt work);
v. To analyse the economics and assess the perspectives of the technology;
vi. To define the next R&D activities that are needed aiming at an eventual commercialisation of the technology.

The “Università degli Studi di Palermo” (UNIPA) participated as the leader partner for activities on:

i. Selection of redox couples and electrode materials;

ii. Multi-scale modelling and process simulation:
    a. Fluid dynamics and transport phenomena by means of CFD (the object of this PhD);
    b. Development and validation of a process simulator for a RED stack;
    c. Simulation of the prototype unit;
iii. Design, installation and test of the prototype (dire o accennare qui che mi sono occupato un po' anche di questo?)

Also, UNIPA contributed to lab-scale performance testing.

The work carried out within the PhD represents a fundamental part of the project in order to achieve its goals. The CFD analysis of phenomena at small scale is the basis of the modelling activities of the project, carried out by a hierarchical strategy of simulation and aimed at building up a predictive tool for (i) performance evaluation and (ii) design optimization of the RED process.

The REAPower project started in 2010 and terminated in September 2014. As well as the economic evaluation and the analysis of perspectives, the last period of the project was devoted to the activities relevant the prototype tested on site, in the saltworks of Marsala.

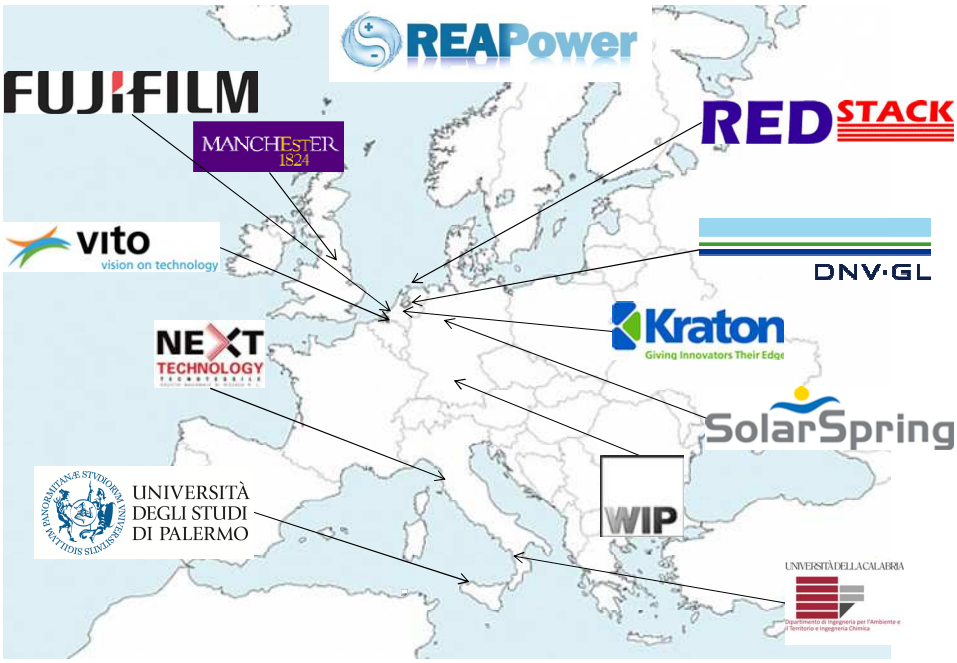

Figure 1.2. The partners of the REAPower project.

Figure 1.3. Installation site of the REAPower prototype pilot plant: *Ettore-Infersa* saltworks facilities in Marsala (Italy, Sicily).

2 MODEL DEVELOPED

Abstract

In reverse electrodialysis (RED), complex phenomena interacting each other over several scales occur, and fluid dynamics is crucial for the process performance. Dealing with the process modelling, which is fundamental for the design and the optimization, is a very complex topic. On the other hand, Computational Fluid Dynamics (CFD) is surely suitable for the simulation of RED systems, as shown by the several literature works on spacer-filled channels for membrane processes. CFD is a powerful technique that studies fluid dynamics and associated phenomena by coupling physical models and numerical methods in computer-based simulations. CFD offers several advantages over the experimental investigation, including the possibility to test many cases with cost effective results, and the effectiveness as predictive tool and the detailed analysis at small scale.

In this work, a 3D CFD modelling tool has been purposely developed for the analysis of fluid flow and mass transfer in RED systems. This model is devised in the framework of a hierarchical simulation strategy of the RED process and is the tool aimed at investigating at small scale thoroughly and effectively spacer-filled and membrane-profiled channels for RED applications. Fluid dynamics and mass transfer phenomena were studied by solving the fluid flow governing equations (Navier–Stokes and continuity) and a transport equation of a binary electrolyte (NaCl) suitable also for concentrated solutions. This electrolyte transport equation was derived from the Stefan–Maxwell approach by assuming the local electroneutrality condition. Simulations of an empty channel showed that the concentration field is greatly controlled by the diffusive transport, while the migrative one had an impact definitely negligible. Therefore, it is shown that mass transfer in RED channels can be dealt simply by a convection-diffusion equation. In the transport equation implemented the migrative term was neglected and the migrative fluxes were simply superimposed with the diffusive ones and reflected in the boundary conditions. A weak non-linearity in the diffusive term, which depends on the concentration itself, makes the transport equation slightly different to an ordinary convection-diffusion equation. Also, the Navier–Stokes equations and the transport

equation were suitably manipulated by adding a source term, in order to simulate a periodic domain.

In fact, the Unit Cell was employed as main approach of the present model, i.e. a periodic repetitive unit of a channel, where fully developed conditions can be assumed, was simulated. Membranes were not included in the computational domain and a single channel was simulated with suitable boundary conditions.

Spacer-filled channels and profiled-membrane channels were simulated. The geometry of spacer-filled channels was built taking into account measurements made by optical microscopy and micrometer; also, the compenetration/compression of filaments were somewhat taken into account in order to reproduce realistic geometries in the simulations. The computational domains were discretized by multi-block grids composed either by hexahedral volumes, for the geometries where this was possible, or by hexahedral-tetrahedral volumes (hybrid grids). The sensitivity analysis of the results to the discretization degree was carefully tested preliminarily, in order to carry out the subsequent simulations with suitable grids for obtaining accurate results along with acceptable computing times.

The commercial software Ansys®-CFX, based on the finite volumes method, was used. The simulations were performed by high-speed computers with a double-hexacore or a double-octacore CPU.

In order to analyse the RED channels performance, the simulation results are then used to calculate synthetic parameters (dimensionless numbers) quantifying pressure drop and mass transfer. The features that a high performance RED channel should possess are identified. CFD data are then used as input information for the higher level of modelling, i.e. the process simulator.

2.1 Introduction

Modelling of electro-membrane processes is a very complex topic (section 1.7.2). The numerical models proposed are based on simplifying assumptions on the domain simulated and on the mathematical description of the phenomena involved. Few works have been devoted specifically to fluid dynamics and mass transfer in RED. Therefore, in the literature various aspects have not been still addressed (section 1.8). This work was carried out in order to investigate these aspects and is part of the activities of the

REAPower project, which pointed to the development of a modelling tool based on the CFD analysis at low scale (section 1.9).

In the next section, a brief description of the peculiarities of the CFD technique is reported. Then, the modelling approach proposed in this thesis is described: modelling strategy, governing equations, computational domain and boundary conditions, model assumptions and numerical details are described here; specific aspects, as cases investigated, grids generated, etc. are contained in the pertinent chapters.

2.2 Computational Fluid Dynamics [118, 119]

CFD is the technique that studies fluid dynamics and associated phenomena by means of numerical methods in computer-based simulations. CFD couples physical models and numerical methodologies, aiming at simulating fluid flows and heat and mass transfer phenomena related to them, using computers to perform modelling, calculations and data processing. CFD arises from the impossibility to solve analytically the governing equations for the fluid motion, except for cases with very simple geometries; thus in most cases of real interest, a numerical approach is required. Physics of any fluid flow is described by the following three fundamental principles:

1) the conservation of mass;
2) the conservation of momentum (Newton's second law);
3) the conservation of energy.

In particular, for a Newtonian fluid (whose viscosity is invariant with the velocity, thus the stress tensor is a linear function of the strain rate tensor) from the principle of conservation of momentum the Navier-Stokes equations are obtained. However, the mathematical equations expressing the three fundamental principles in an infinitesimal volume control are partial differential equations. By means of CFD these equations are discretized and solved numerically in the computational domain with the appropriate initial and boundary conditions, obtaining the distribution in space and time of the fluid dynamics variables (velocity and pressure fields) and associated quantities (solute concentration and temperature fields).

There exist various discretizations methods of the domain. In the finite volume method, commonly used in CFD codes, the domain is divided in many control volumes and the governing partial differential equations are rewritten with integration over the discrete

control volume. Using the Gauss' divergence theorem, volume integrals that contain a divergence term are converted to surface integrals, which are then evaluated as fluxes at the surfaces of the finite volume. Other methods are: finite element, finite difference, spectral element etc. The equation discretization can be done by various schemes and generates an algebraic equation system that can be solved by different iterative numerical methods and algorithms (implicit, semi-implicit or explicit).

CFD applications to problems of more and more detail and sophistication require the manipulation of a huge amount of numbers; thus advances in CFD are related to advances in hardware of high-speed supercomputers equipped with high memory storage capacity. Moreover, during the years several commercial CFD codes have been developed and have found widespread use. Currently CFD is used in research and industry in all fields of application involving fluid mechanics to study all physical and physical-chemical processes whose outcomes are influenced by the flow field. Some examples of application are: fluid dynamics in water bodies, meteorology, aerodynamics (aircrafts, spatial vehicles, cars...), macchine operatrici e motrici (pumps, compressors, and turbines), unit operations, chemical reactors, bioengineering and medicine (blood flows).

CFD offers various advantages over the experimental investigation:

- testing many different cases;
- request for fewer resources of equipment and time with significant cost effective results;
- effectiveness as predictive tool in design and optimization;
- analysing at small scale by providing practically unlimited level of detail of results;
- studying systems under hazardous conditions or whose flow conditions are difficult or impossible to reproduce in experimental model tests.

2.2.1 Steps of CFD modelling

The CFD simulation follows an analysis procedure divided in three phases: pre-processing, solving and post-processing. In the pre-processing is often the most substantial part; it consists of defining the problem to be solved and comprises the following operations:

1. definition and creation of the geometry, i.e. the computational domain;
2. discretization of the domain, i.e. generation of the mesh;
3. definition of the physical model:
    a) equation system;
    b) eventual turbulence model;
    c) boundary conditions;
    d) initial conditions;
    e) fluid properties;
4. definition of the numerical model:
    a) equations discretization scheme;
    b) equations resolution algorithm;
    c) convergence criteria.

Some observations about the discretization of the computational domain are done in the following. The fineness of the mesh has to be suitable to the fluid dynamics regime, the geometry complexity, and the kind of simulation (with turbulence model or not). Hexahedral computational cells are preferable due to: (i) higher accuracy, due to the higher number of faces where the variables are approximated; (ii) higher control of the user during the grid generation; (iii) possibility to use structured grid, i.e. with computational cells identified by indexes, which facilitate the work of the resolution algorithms and the achievement of convergence. Conversely, tetrahedral cells offer higher flexibility and can be used for any domain geometry. When hexahedral meshes cannot be used, hybrid grids with hexahedra and tetrahedra are commonly employed; other polyhedra such as prisms and pyramids are necessary in the interfacial zones. Often it is recommended to increase the discretization degree in the critical zones of the domain, where higher gradients are expected. Moreover, the sensitivity analysis of the results on the discretization degree is useful to find the grid that minimizes the calculation time without affecting the results accuracy (grid independence).

Once defined the pre-processing, the CFD code is used to resolve the equations system. The numerical solution requires very variables computing times that depend on the physical and numerical model and on the computer performance (CPU, RAM). By subdividing the mesh in more partitions, the computational burden is divided among more processors for a parallel run. This speeds up the calculation, but an optimal number

of partition should be set, as an excessive partitioning could slow down the solving due to high communication time among the different processes. Generally, the software user's guide gives instructions on that.

Finally, the results obtained are visualised and analysed in the post-processing. The post-processor provides complete insight into fluid dynamics simulation results predicted. This step is performed by image generation, direct calculations on results data and manipulation of them in external software and datasheet.

2.2.2 Notes on flow regimes and turbulence modelling

In order to solve the flow equations and catch the physical structures of all sizes, the computational grid (spatial discretization) must have cells smaller than the smallest significant structures to be resolved. Also the simulation has to be conducted by using time steps Δt (time discretization) small enough to resolve the time dependent behaviour of the various quantities.

The fluid dynamics regime depends on the domain geometry and the Reynolds number (*Re*, ratio between the inertial and the viscous forces acting on the fluid). In a given geometry, beyond a critical *Re* the fluid flow loses the steadiness and transition conditions are established. Periodic or quasi-periodic regimes can occur, and for higher *Re* fully turbulent conditions are obtained. The turbulent regime is characterized by multi-scale temporal and spatial fluctuations in chaotic conditions.

If *Re* is small enough, the flow is laminar, i.e. viscous forces prevail over the inertial ones avoid the chaotic behaviour. The significant spatial structures of the flow field are then of the same order of magnitude as the physical structures present in the computational domain (duct height, obstacle size, etc.). Also, if the boundary conditions and the forcing terms do not vary with time (or vary in a periodic fashion), the problem has always steady-state or periodic solutions (perhaps following a transient, depending on the initial conditions). Therefore, for laminar flows it is generally possible to attain a sufficient space- and time-resolution, and to obtain computational results which are independent of the particular discretization used, and in good agreement with experimental data.

For higher values of *Re*, the flow becomes turbulent. Turbulence is composed of eddies: patches of zigzagging, often swirling fluid, moving randomly around and about the

overall direction of motion. In turbulent flow, the flow field varies in a non-periodic fashion with time (even for constant boundary conditions), exhibits a sensitive dependence on the initial conditions, and lacks spatial symmetries even if the problem presents geometrical symmetries. The spatial structures identifiable in the flow field ("eddies") cover a wide range of scales which extends from the scale of the physical domain down to that of the "dissipative eddies", in which the kinetic energy of the eddy motion is eventually dissipated into heat by viscous effects. This range of scales increases with the *Re* and, for fully turbulent flows, may include several orders of magnitude. In few words, turbulence is a chaotic, continuum (the smallest scales of turbulence are much larger than any molecular length scale), diffusive, dissipative, three-dimensional phenomenon.

The most renowned interpretation of turbulence is the "energy cascade" by Kolmogorov, enunciated in 1930. The energy cascade process involves a transfer of turbulent kinetic energy (per unit mass), from larger to smaller eddies. Dissipation of kinetic energy to heat through the action of molecular viscosity occurs at the scale of the smallest eddies. It can be imagined that large eddies brake in smaller and smaller eddies till the dissipative scale (named Kolmogorov scale) in which the energy is completely dissipated and thus the existence of turbulent structures of even smaller scale is avoided.

The direct simulation of turbulence captures the smallest physical structures by using computational cells with sizes lower than the Kolmogorov scale (*Direct Numerical Simulation*, DNS). This approach is still possible only for rather simple flow cases at relatively low Reynolds numbers, as it would require too fine grids. An estimation of the number of grid points and of time steps necessary for a DNS follows from considering the Kolmogorov-Obukhov scales of dissipative eddies. It can be demonstrated that the number of grid points must increase as $Re^{9/4}$ and the number of time steps as $Re^{7/8}$. It is evident that the rapid increase of these parameters is an absolute obstacle to the direct simulation of high *Re* turbulent flows, even using eventually high-size and -speed super-computer or clusters. Therefore, DNS provides high quality data that describe in the most precise way physics of the problem and are much more detailed than experimental data, due to the fine spatial and temporal resolution; on the other hand, the computational effort limit the use of DNS, which remains applicable only for

simulations that are not prohibitive and are compatible with the available computational resources.

To overcome this difficulty, turbulence models can be adopted to simplify the resolution of the constitutive equations of fluid flow through appropriate filters. Two basic approaches to turbulence modelling have been followed so far. The Large Eddy simulation (LES) operates a spatial filtering, while the Reynolds-Averaged Navier-Stokes Equations (RANS) applies the concept of time-averaging.

The LES approach is founded on the theory that the small scales of turbulence possess universal features that do not depend on the geometry examined, while the large scales, which transport the turbulent energy, have specific characteristics affected by the geometry. Thus, in LES the large eddies are resolved accurately and the small scales are simulated by a subgrid-scale model. By applying a filtering operator, a variable can be expressed as the sum of the resolved component and the unresolved fluctuation. The governing equation are written with the by replacing the variables with the sums of resolved and unresolved components. Therefore the filtered equations contain additional terms that depend on the unresolved fluctuations and have dimensions of stresses (subgrid terms). These terms have to be approximately modelled in terms of large-scale (resolved) quantities in order to close the turbulence problem. A vast amount of LES work has been based on *gradient diffusion* models in which, by analogy with the molecular stresses, subgrid stresses (or at least their deviatoric components) are assumed to be proportional to the large-scale strain rate by the subgrid viscosity (Boussinesq's hypothesis). Then the sub-grid model closes the system. By far the most popular sub-grid model is that first introduced by Smagorinsky, which relates the subgrid viscosity to the resolved strain rate and the filter width. However, the capability of any subgrid model to capture the effect of unresolved fluctuations increases with the grid resolution. Therefore, large-eddy simulations give the best results if very fine grids are used. As a consequence, large-eddy simulation is usually more computationally demanding than the more traditional Reynolds-averaging approach.

Reynolds-averaging is by far the more common approach to turbulence modelling and is based on the time mean of the generic flow quantity. As in the LES, the variables are replaced in the governing equations with the sum of the resolved component and the unresolved fluctuation. Thus, the RANS containing extra terms (turbulent stresses) are obtained. The set of equations that gives the Reynolds stresses as a function of the time-

averaged variables represents the turbulence model. There are two main classes of turbulence models for the mathematical closure problem: (i) *gradient-diffusion* models (e.g. k-ε model), computing the "*eddy viscosity*"; (ii) *direct* models (e.g. Reynolds Stress Model, RSM), expressing directly each of the Reynolds stresses. The gradient-diffusion models are the most used. In these models the Reynolds stresses are assumed to be proportional to the resolved strain rate by the eddy viscosity. The eddy viscosity is related to the turbulent kinetic energy and the dissipation rate of the turbulent kinetic energy. Then the problem is closed by adding one or two differential equations: in the former case, the system is closed by the balance equation of the turbulent kinetic energy and an algebraic equation of the dissipation rate of the turbulent kinetic energy as a function of mean values of the flow field; in the latter case, the two balance equations for turbulent kinetic energy and the dissipation rate of the turbulent kinetic energy are adopted.

2.3 Modelling strategy adopted

Pursuing the goals of the PhD, a CFD modelling tool has been purposely developed. This work was carried out in the framework of a hierarchical strategy of simulation (see section 1.7.1), where the modelling is based on an integrated approach that involves the use of CFD and process simulation software (*Computer Aided Process Engineering - CAPE*). The CFD modelling carried out within this work is the first step of a structured simulation tool and represents the support base for the higher levels of modelling in the multi-scale process simulator, which is object of another work [120].

CFD is a powerful tool for a detailed analysis at small scale and for testing a number of different cases; therefore, the simulations are carried out at low scale by a 3D CFD model, in order to investigate thoroughly and effectively spacer-filled and membrane-profiled channels for RED applications. Fluid dynamics and mass transfer phenomena have been studied by solving the fluid flow governing equations (Navier–Stokes and continuity) and a transport equation suitable also for concentrated solutions, of a binary electrolyte (NaCl), derived from the Stefan–Maxwell equations by assuming the local electroneutrality. Preliminary simulations of an empty channel showed that the concentration field is greatly controlled by the diffusive transport, while the migrative one had an impact definitely negligible. Therefore, in the following simulations the

migrative term has been neglected and the migrative fluxes are simply superimposed with the diffusive ones and reflected in the boundary conditions. The transport equation is a convection-diffusion equation, with a weak non-linearity in the diffusive term and an additional term for the simulation of a periodic domain. In fact, the periodic repetitive unit of a single channel has been simulated with suitable boundary conditions (membranes are not included in the computational domain).

Different channel configurations have been investigated: commercial spacers have been simulated and parametric analyses of ideal spacer-filled channels and profiled-membrane channels have been performed. From this modelling approach, the local spatial distribution of the variables of fluid dynamics and mass transfer is obtained; therefore, the effects of channel geometry, flow rate (i.e. Reynolds number) and feeds features on concentration polarization and pumping power are evaluated, providing a detailed analysis of the process parameters. These are synthetic parameters consisting of dimensionless numbers as power number (*Pn*) and Sherwood number (*Sh*) that summarize the results obtained by constitutive expressions, i.e. functional correlations.

The validation of pressure drop results for a couple of spacers was done. Also, simulation results were compared with experimental and CFD data on pressure drop and mass transfer from literature.

Moreover, the effect of the spacer hydrophobicity and the use of a porous medium have been evaluated. Some simulations have been devoted to investigate general aspects from a different scale, in order to assess the effect of the features of an entire stack on the fluid dynamics performance; the contributions of manifolds to the overall pressure loss as well as the effect of stack lay-out and geometry on the flow rate distribution within the channels have been evaluated.

Finally, all data collected provide the input information for the higher level of modelling, the process simulator [120], which does not simulate fluid dynamics and mass transfer. This, in turn, is created by a multi-scale approach, integrated with the sub-model (CFD), which describes the phenomena occurring at higher scales, from the cell pair to the RED stack. This is the tool of the REAPower project (i) for the prediction of the stack performance in terms of net power produced and (ii) for the process optimization.

2.4 Governing equations

2.4.1 Continuity and momentum equations

The governing equations for three-dimensional flow of a Newtonian incompressible fluid are the following continuity and Navier–Stokes equations:

$$\vec{\nabla} \cdot \vec{u} = 0 \tag{2.1}$$

$$\rho \frac{\partial \vec{u}}{\partial t} + \rho \vec{u} \vec{\nabla} \cdot \vec{u} = -\vec{\nabla} p + \mu \nabla^2 \vec{u} \tag{2.2}$$

where $\vec{u}$ is velocity, ρ is density, μ is dynamic viscosity and p is pressure. Laminar steady state simulations were performed as the flow was predicted to be steady at all the flow rates investigated on the basis of preliminary time-dependent simulations.

The density was assumed to be constant since its changes associated with concentration gradients along both the streamwise and the cross-stream directions were estimated to be very small. For the same reason, buoyancy due to concentration gradients was neglected.

2.4.2 Transport equation in concentrated solutions

When highly concentrated solutions are employed, the approach based on the Nernst–Planck equation should not be used, since it is strictly valid only for dilute solutions. The transport equation in concentrated solutions can be derived from the Stefan–Maxwell equation [45, 89]. According with the Stefan–Maxwell approach, the basic scheme for the transport equations is the following: *driving force = friction coefficient × relative velocity*

$$C_i \vec{\nabla} \tilde{\mu}_i = \sum_j K_{ij} \left(\vec{u}_j - \vec{u}_i \right) = RT \sum_j \frac{C_i C_j}{C_T \mathfrak{D}_{ij}} \left(\vec{u}_j - \vec{u}_i \right) \tag{2.3}$$

where C_i and $\tilde{\mu}_i$ are the concentration and the electrochemical potential of species *i*, respectively, K_{ij} are friction coefficients or interaction coefficients, $\vec{u}_i$ is the velocity of species *i*, so that the flux density of species *i* is

$$\vec{N}_i = C_i \vec{u}_i \tag{2.4}$$

C_T is the total concentration:

$$C_T = \sum_i C_i \tag{2.5}$$

where the sum includes the solvent. $\mathfrak{D}_{ij}$ is a diffusion coefficient describing the interaction between species *i* and *j*

$$K_{ij} = RT \frac{C_i C_j}{C_T \mathfrak{D}_{ij}} \tag{2.6}$$

The term $-C_i \vec{\nabla} \tilde{\mu}_i$ in Eq. (2.3) can be regarded as a driving force per unit volume acting on species *i* and causing it to move with respect to the surrounding fluid. The force per unit volume exerted by species *j* on species *i* as a result of their relative motion is expressed as $K_{ij}\left(\vec{u}_j - \vec{u}_i\right)$, that is proportional to the difference between the two species velocities. By Newton's third law of motion (action-reaction law), it results that $K_{ij} = K_{ji}$ or

$$\mathfrak{D}_{ij} = \mathfrak{D}_{ji} \tag{2.7}$$

Such a general approach can be theoretically applied to multi-component (ions) systems, but in turn requires the knowledge of a corresponding large number of transport properties, as the cross diffusivities, that are often unavailable. Therefore the general Stefan–Maxwell approach can be simplified by considering a binary electrolyte that dissociates completely into ν_+ ions of charge number z_+ and ν_- ions of charge number z_- such that $z_+\nu_+ + z_-\nu_- = 0$. The corresponding Stefan–Maxwell transport equations are:

$$C_+\vec{\nabla}\tilde{\mu}_+ = K_{+0}\left(\vec{u}_0 - \vec{u}_+\right) + K_{+-}\left(\vec{u}_- - \vec{u}_+\right) \tag{2.8}$$

$$C_-\vec{\nabla}\tilde{\mu}_- = K_{-0}\left(\vec{u}_0 - \vec{u}_-\right) + K_{+-}\left(\vec{u}_+ - \vec{u}_-\right) \tag{2.9}$$

According with the Hittorf reference frame (relative velocities respect to the solvent) the molar ionic fluxes can be expressed as:

$$\vec{N}_i^H = C_i\left(\vec{u}_i - \vec{u}_0\right) \tag{2.10}$$

In order to calculate the former quantities, it is necessary:

(i) to make use of the local electroneutrality condition:

$$z_+C_+ + z_-C_- = 0 \tag{2.11}$$

(ii) to employ the definition of the current density:

$$\vec{i} = F\sum_i z_i\vec{N}_i = F\sum_i z_i\vec{N}_i^H = Fz_+C_+\left(\vec{u}_+ - \vec{u}_-\right) \tag{2.12}$$

(iii) to introduce the chemical potential gradient of the electrolyte:

$$C\vec{\nabla}\mu_e = C_+\vec{\nabla}\tilde{\mu}_+ + C_-\vec{\nabla}\tilde{\mu}_- \tag{2.13}$$

according to the relation $C_i = \nu_i C$ (resulting from salt dissociation), where C is the concentration of the electrolyte. The above Eqs. (2.8), (2.9), (2.12) and (2.13) can be briefly written in matrix form as:

$$\begin{pmatrix} -K_{+0} & -K_{-0} \\ z_+C_+ & z_-C_- \end{pmatrix}\begin{pmatrix} \vec{u}_+ - \vec{u}_0 \\ \vec{u}_- - \vec{u}_0 \end{pmatrix} = \begin{pmatrix} C\vec{\nabla}\mu_e \\ \vec{i}/F \end{pmatrix} \tag{2.14}$$

which in turn can be inverted to give:

$$\begin{pmatrix} \vec{N}_+^H \\ \vec{N}_-^H \end{pmatrix} = \begin{pmatrix} C_+\left(\vec{u}_+ - \vec{u}_0\right) \\ C_-\left(\vec{u}_- - \vec{u}_0\right) \end{pmatrix} = \frac{1}{K_{+0}+K_{-0}} \begin{pmatrix} -C_+ & K_{-0}/z_+ \\ -C_- & K_{+0}/z_- \end{pmatrix} \begin{pmatrix} C\vec{\nabla}\mu_e \\ \vec{i}/F \end{pmatrix} \tag{2.15}$$

As desired, Eq. (2.15) expresses the flux densities in the Hittorf reference frame as:

$$\vec{N}_i^H = \frac{C_i}{K_{+0}+K_{-0}} C\vec{\nabla}\mu_e + \frac{K_{j0}\vec{i}}{\left(K_{+0}+K_{-0}\right) z_i F} \tag{2.16}$$

from which the molar ionic flux densities can be calculated:

$$\vec{N}_i = C_i\vec{u}_i = -\frac{\nu_i \mathfrak{D} C_T}{\nu RTC_0} C\vec{\nabla}\mu_e + \frac{\vec{i}t_i^0}{z_i F} + C_i\vec{u}_0 \tag{2.17}$$

I II III

where $\nu = \nu_+ + \nu_-$, I is diffusive transport, II is migrative transport and III is convective transport. In particular, for cation and anion:

$$\vec{N}_+ = C_+\vec{u}_+ = -\frac{\nu_+ \mathfrak{D} C_T}{\nu RTC_0} C\vec{\nabla}\mu_e + \frac{\vec{i}t_+^0}{z_+ F} + C_+\vec{u}_0 \tag{2.18}$$

$$\vec{N}_- = C_-\vec{u}_- = -\frac{\nu_- \mathfrak{D} C_T}{\nu RTC_0} C\vec{\nabla}\mu_e + \frac{\vec{i}t_-^0}{z_- F} + C_-\vec{u}_0 \tag{2.19}$$

The diffusion coefficient of the electrolyte, based on a thermodynamic driving force, is

$$\mathfrak{D} = \frac{\nu C x_0 RT}{K_{+0}+K_{-0}} = \frac{\nu \mathfrak{D}_{+0}\mathfrak{D}_{-0}}{\nu_-\mathfrak{D}_{+0}+\nu_+\mathfrak{D}_{-0}} = \frac{\mathfrak{D}_{+0}\mathfrak{D}_{-0}\left(z_+ - z_-\right)}{z_+\mathfrak{D}_{+0} - z_-\mathfrak{D}_{-0}} \tag{2.20}$$

where x_0 is the solvent molar fraction, while the transport numbers (with respect to the solvent velocity in the Hittorf reference frame) are

$$t_+^0 = 1 - t_-^0 = \frac{K_{-0}}{K_{+0} + K_{-0}} = \frac{\nu_- \mathfrak{D}_{+0}}{\nu_- \mathfrak{D}_{+0} + \nu_+ \mathfrak{D}_{-0}} = \frac{z_+ \mathfrak{D}_{+0}}{z_+ \mathfrak{D}_{+0} - z_- \mathfrak{D}_{-0}} \tag{2.21}$$

The driving force for diffusion used in Eqs. (2.18) and (2.19) is the gradient of the chemical potential μ_e of the electrolyte in solution. The diffusion coefficient *D* of the salt which is usually measured is based on a gradient of the concentration and is related to D by

$$D = \mathfrak{D} \frac{C_T}{C_0} \left(1 + \frac{d \ln \gamma}{d \ln m} \right) \tag{2.22}$$

where γ is the mean molal activity coefficient and *m* is the molality. The gradient of chemical potential can be more easily expressed in terms of the concentration gradient

$$\frac{\mathfrak{D}}{\nu RT} \frac{C_T}{C_0} C \vec{\nabla} \mu_e = D \left(1 - \frac{d \ln C_0}{d \ln C} \right) \vec{\nabla} C \tag{2.23}$$

The general expression for the material balance for the species *i* is:

$$\frac{\partial C_i}{\partial t} = -\vec{\nabla} \cdot \vec{N}_i + R_i \tag{2.24}$$

where R_i is the production due to homogeneous chemical reactions in the bulk of the solution. Clearly, no chemical reactions occurs within the feed channels of a RED unit and such a term has not to be taken into account (R_i = 0). On the basis of the electroneutrality assumption, the conservation of charge is:

$$\vec{\nabla} \cdot \vec{i} = 0 \tag{2.25}$$

By including Eqs. (2.17) (divided by v_i) and (2.23) in Eq. (2.24) and by taking also into account Eq. (2.25) the transport equation of the electrolyte is obtained:

$$\frac{\partial C}{\partial t} + \vec{\nabla} \cdot \left(C \vec{u}_0 \right) = \vec{\nabla} \cdot \left[D \left(1 - \frac{d \ln C_0}{d \ln C} \right) \vec{\nabla} C \right] - \frac{\vec{i} \cdot \vec{\nabla} t_i^0}{z_i \nu_i F} \tag{2.26}$$

2.4.3 Implementation of the transport equation in the CFD code

In Eq. (2.26) C is the electrolyte concentration, C_0 is the solvent concentration, $\vec{u}_0$ is the solvent velocity (identified here with the solution velocity $\vec{u}$), D is the diffusion coefficient of the salt, $\vec{i}$ is the current density, t_i^0 is the transport number with respect to the solvent velocity, z_i is the valence (=±1 for NaCl), ν_i is the stoichiometric coefficient of ionic species i (=1 for NaCl), and F is the Faraday constant. Subscript i refers to either cation or anion. Eq. (2.26) includes four terms: the first and second on the left hand side are the transient and advection term, respectively, while the first on the right hand side is the diffusive term. The last term on the right hand side (migrative term) coincides, taking account of the charge conservation condition expressed by $\vec{\nabla} \cdot \vec{i} = 0$, with the divergence of the migrative flux of either species and is nonzero only if either transport number exhibits a spatial gradient. Note that different transport numbers for the two ionic species imply different fluxes, but not different concentrations: since electroneutrality is assumed, concentrations of Na^+ and Cl^- are everywhere the same. For the sake of simplicity, in the present work the additional assumption of equal transport numbers for the two species was also made.

The implementation and the solution of Eq. (2.26) along with suitable initial and boundary conditions allow the distribution of the variable C to be obtained within the computational domain.

Since a CFD simulation cannot deal with phenomena occurring in the electric double layer at the membrane interface (i.e. at the molecular scale) or within the membrane itself, the present modelling procedure cannot directly simulate these features and takes account of them by imposing an electrolyte flux at the fluid-membrane interface as a boundary condition. Thus, the aim of the present CFD modelling is the assessment of local concentration polarization phenomena occurring at a far larger scale than that of the electric double layer.

With respect to an ordinary transport equation, Eq. (2.26) exhibits two sources of additional difficulty: (i) the effective diffusion coefficient varies with concentration, and (ii) a source term containing the current density appears at the right hand side.
(i) As regards the former difficulty the solvent concentration can be written as:

$$C_0 = \frac{\rho - C M_e}{M_0} \tag{2.27}$$

where M is the molar mass and the subscripts "*0*" and "*e*" indicate the solvent (water) and the solute (electrolyte), respectively. By switching to the logarithmic form:

$$\ln C_0 = \ln\left(\frac{\rho(C) - C M_e}{M_0}\right) \tag{2.28}$$

By stating:

$$y = \ln C_0 \tag{2.29}$$

$$x = \ln C \rightarrow C = e^x \tag{2.30}$$

the following expression can be obtained:

$$\begin{aligned} &\frac{d\ln C_0}{d\ln C} = \frac{dy}{dx} = \frac{d}{dx}\left[\ln\left(\frac{\rho\left(C(x)\right) - e^x M_e}{M_0}\right)\right] = \\ &= \frac{M_0}{\rho - e^x M_e}\left(\frac{d\rho}{dC}e^x - M_e e^x\right)\frac{1}{M_0} = \frac{\frac{d\rho}{dC}C - M_e C}{\rho - C M_e} \end{aligned} \tag{2.31}$$

$$1-\frac{d\ln C_0}{d\ln C}=1-\frac{dy}{dx}=1-\frac{\frac{d\rho}{dC}C-M_eC}{\rho-CM_e}=\frac{\rho-CM_e-\frac{d\rho}{dC}C+M_eC}{\rho-CM_e}=$$
$$=\frac{\rho-\frac{d\rho}{dC}C}{\rho-CM_e}=\frac{\rho-C\frac{d\rho}{dC}}{C_0M_0} \qquad (2.32)$$

By locally linearizing $\rho(C)$ as:

$$\rho=aC+b \qquad (2.33)$$

the following simple expression is obtained

$$1-\frac{d\ln C_0}{d\ln C}=\frac{b+\cancel{a\cdot C}-\cancel{C\cdot a}}{C_0M_0}=\frac{b}{\rho-CM_e}=\frac{b}{b+aC-CM_e}=\frac{b}{b+(a-M_e)C} \qquad (2.34)$$

The parameters *a* and *b* were obtained *via* linear regression of the function $\rho = \rho(C)$ [121] in the proximity of the bulk concentration of the solution to be simulated (see section 2.7).

The inconsistency between treating ρ as a constant in Eqs. (2.1)-(2.2) and as a function of *C* in Eq. (2.33) is only apparent: Eq. (2.33) serves the purpose of computing the derivative $d\rho/dC$ which appears in Eq. (2.32) and is necessary to express the diffusivity correction in the transport equation. On the other hand, if variations of *C* across the channel are small (as it is the case here), variations of ρ (and μ) are negligible from the hydrodynamic point of view.

(ii) As regards the latter difficulty, solving Eq. (2.26) in its complete form, which contains the current density $\vec{i}$, would require either additional equations for this quantity or an *a priori* knowledge of its distribution. As they are linear dependent, Eqs. (2.12), (2.18) and (2.19) cannot be employed. The latter situation occurs only in the case of a spacerless channel, where the current density can be assumed to be uniform. Thus, simulations were first carried out in a spacerless channel 400 μm thick, in order to quantify the relative importance of the last term in Eq. (2.26) (migrative term) with respect to the diffusive one (of course, in the empty channel no convective contributions

are present in the direction orthogonal to the membranes). The dependence of the transport number on the concentration was derived from Smits and Duyvis [122]. Figure 2.1 reports the Na^+ transport number as a function of the NaCl concentration, showing a weak dependence.

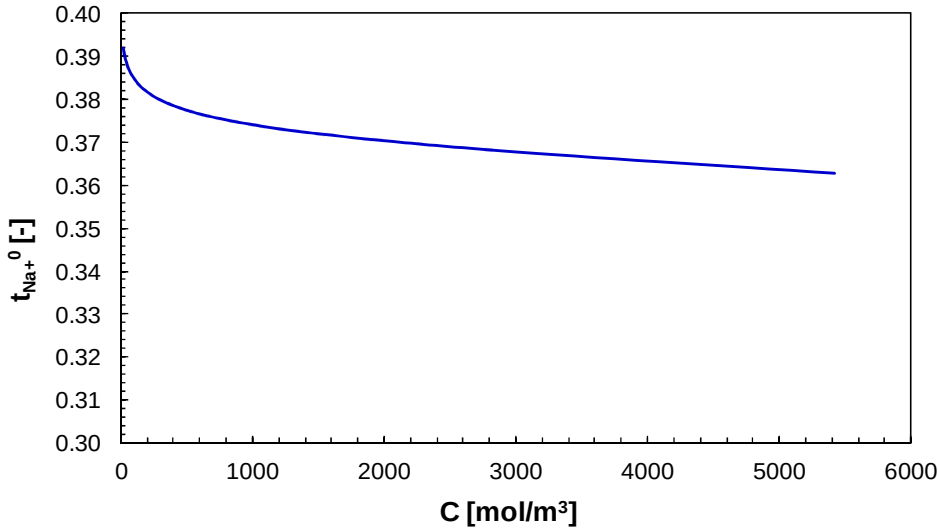

Figure 2.1. Transport number of the sodium ion in NaCl solutions at 25°C [122].

Results showed that the concentration profiles obtained by CFD simulations taking into account the migrative term are practically coincident with those obtained by neglecting it. This evidence is reported in Figure 2.2a for the most unfavourable case (low concentration and high current density), where the migrative term was found to be negligible compared to the diffusive one (Figure 2.2b).

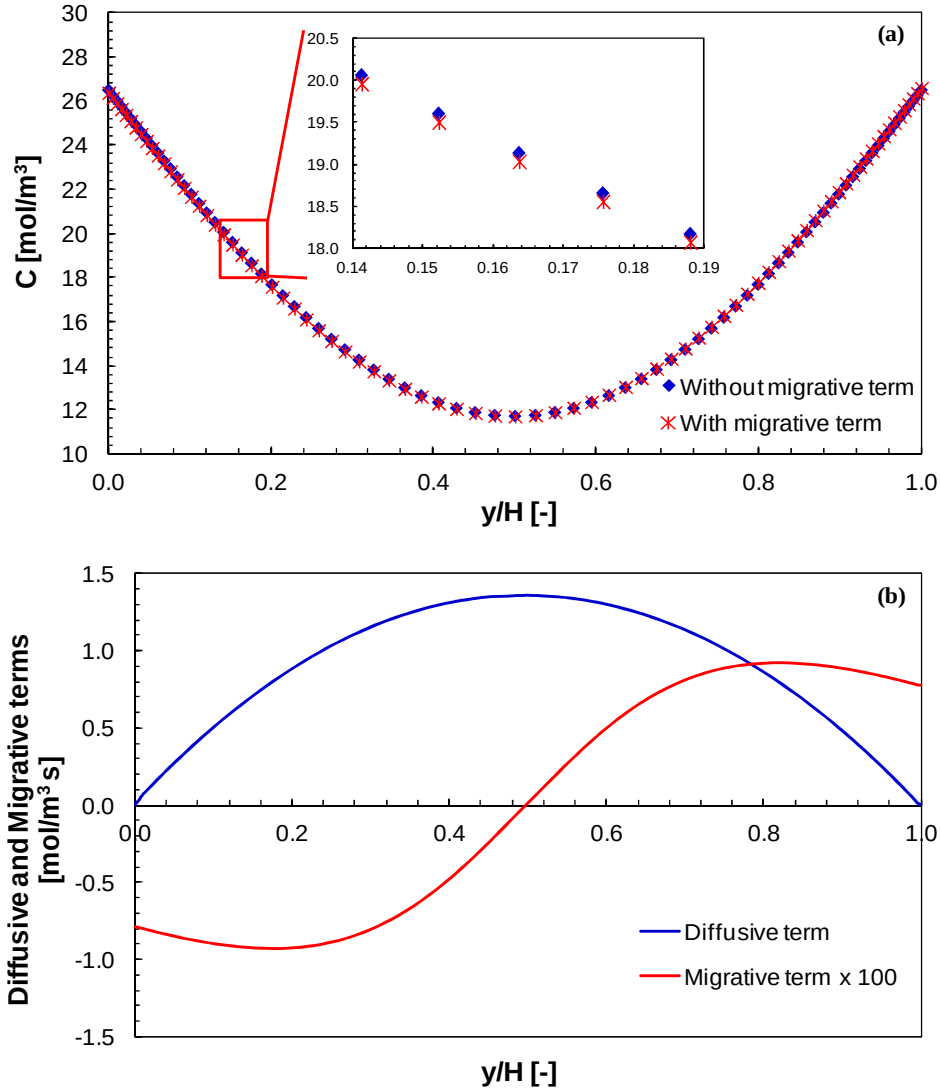

Figure 2.2. Assessment of the contribution of transport equation's migrative and diffusive terms along a monitoring line perpendicular to the membranes for the case of the empty channel fed by Feed3 at w_{ave} = 1.5 cm/s and i = 35 A/m^2. (a) Electrolyte concentration profiles obtained with or without the migrative term; (b) comparison of the contributions of the diffusive and the migrative term. Here, *y/H* represents the *y*-coordinate normalized by the channel thickness *H*.

We stress once more that these findings do not mean that the migrative *flux* is negligible, but only that its *divergence* is negligible. Taking the above results into account, CFD

simulations were carried out by neglecting the last term in Eq. (2.26) and using Eq. (2.34) model the diffusivity correction. Therefore, the equation solved in the CFD simulations is:

$$\vec{\nabla}\cdot\left(C\vec{u}_0\right)=\vec{\nabla}\cdot\left[D\frac{b}{b+\left(a-M_e\right)C}\vec{\nabla}C\right] \tag{2.35}$$

Eq. (2.35) is similar to a standard convection-diffusion transport equation apart from the corrective term which accounts for the dependence of diffusivity on electrolyte concentration.

2.5 Computational domain and boundary conditions

2.5.1 Main approach

Most of the simulations have been carried out by following the approach described in this section.

2.5.1.1 RED channels

Only one channel has been simulated in each CFD simulation, i.e. either the concentrated or the dilute channel, depending on the feed solution concentration. Brine always feeds a concentrated channel, while seawater and river water always feed a dilute channel. The electrolyte flux through the walls representing the membrane-solution interfaces has been imposed. The membranes are not included in the computational domain and the CFD modelling does not take into account phenomena at molecular scale occurring in the electric double layer.

Spacer-filled channels have been simulated; commercial spacers have been studied, and also a parametric analysis of ideal spacers has been carried out (chapter 5). All the spacers studied are composed by two either woven or non-woven filaments. Geometric characterization work, based on optical microscopy and thickness measurements by a micrometer, has been performed for the physical spacers in order accurately to reproduce the same geometries in the numerical simulations. In commercial spacers either a compenetration or a compression of filaments can be observed in the proximity of the

contact areas (ideally points), for overlapped and woven wires respectively; similarly, it can be imagined that the filaments are also compressed in the contact areas (ideally points for woven filaments and lines for overlapped filaments) with the membranes when the spacers are employed in a stack assembled. If *d* is the filament diameter and *h* is the spacer thickness, the quantity *(2d-h)/2d* is found between ~5% and ~18%. These geometrical features were taken into account during the generation of the geometry for the CFD simulations as follows: the filament diameter has been assumed equal to that measured via optical microscopy photographs, and the difference between twice the filament diameter and the spacer thickness was attributed 70% to the overlap region of the filaments and 30% to the filament-membrane contacts. For the ideal spacers simulated in the parametric analysis of chapter 5, *(2d-h)/2d* = 10% is assumed, since this average value was obtained from measurements of the commercial spacers and data by Da Costa et al. [50]. Again, 70% of this quantity has been attributed to the overlap region of the filaments, while 30% to the filament-membrane contacts. Figure 2.3 shows these features.

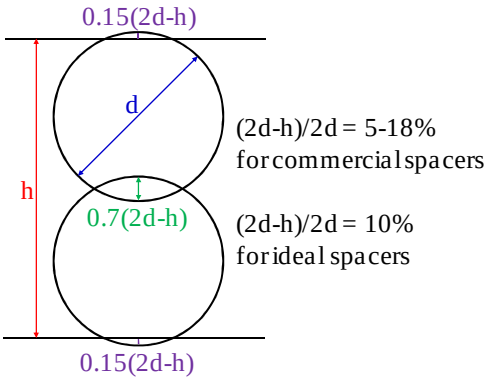

Figure 2.3. Geometric features of the spacers in cross section, assuming that the filaments are parallel).

Ideal profiled-membrane channels made by pillars have been simulated in another parametric analysis (chapter 6). The geometries investigated consist of channels with membranes provided with profiles on one side, which are “pillars” separating the membranes and create the channels for the feed solutions. Two profile shapes have been investigated: (i) square; (ii) circular. The profiles are arranged in a square pitch.

2.5.1.2 Unit Cell and treatment of periodicity

Fully developed flow and concentration fields have been assumed, thus the Unit Cell approach was adopted solving suitably the equations for *periodic* variables. The Unit Cell is the periodic geometric domain of the channel, representing the region far from inlet, outlet and side boundaries, where fully developed fields can be assumed. Simulating such a small domain avoids excessive computational requirements and allows detecting flow features in a very small scale. Several CFD studies can be found in the literature on spacer-filled channels [24, 54, 58-62, 64, 123] and corrugated channels [81, 82, 84, 86] based on this approach, as the fully developed fields are attained after just a few unit cells [55, 63]. As it can be seen in Figure 2.4, different Unit Cells could be devised for the same net spacer. This issue was already investigated by Li and Tung [64] who found the best agreement with experimental data for the case of the Unit Cell type-IV. It is worth noting that the four Unit Cells shown in Figure 2.4 are strictly valid only for spacers with overlapped filaments (and the type II and III are the minimal elementary repetitive units), while for spacers with woven filaments only the Unit Cells type-III and IV can be employed.

Translational periodic boundary conditions have been imposed on the lateral boundaries of the domain consisting of fluid-fluid interfaces. In the *Oxyz* reference frame, the computational domain has been oriented such as the membrane-solution interfaces are perpendicular to the *y* axis. Different flow attack angles, i.e. orientations of the channel with respect to the main flow direction *s*, have been investigated; thus the domain has been rotated around the *y* axis, maintaining the main flow direction *s* fixed and, for convenience, coincident with the *z* axis.

In the Unit Cell approach the Navier–Stokes and the transport equations have to be suitably modified in order to take into account the streamwise variation of pressure and bulk concentration, despite the periodic conditions imposed. In other words, in the Unit Cell approach periodic boundary conditions are imposed to all variables between the inlet and outlet faces; on the other hand, it is necessary to allow for a streamwise variation of (i) pressure (due to frictional losses) and (ii) bulk concentration (due to solute inflow or outflow through the channel walls). This apparent contradiction is managed as follows.

(i) Consider first the hydrodynamic issue, involving pressure. In the fully-developed region of a channel, the static pressure p can be split by definition into a periodic component $\tilde{p}$, whose spatial distribution repeats itself identically in each Unit Cell, and a large-scale component $-K_p z$ which decreases linearly along the main flow direction z with a gradient $K_p=|\mathrm{d}p/\mathrm{d}z|$. By substituting $\tilde{p}-K_p z$ for p in the Navier–Stokes Eqs. (2.2), it is easy to recognize that it can be written as

$$\rho\frac{\partial\vec{u}}{\partial t}+\rho\vec{u}\vec{\nabla}\cdot\vec{u}=-\vec{\nabla}\tilde{p}+\mu\nabla^2\vec{u}+K_p\vec{k} \tag{2.36}$$

in which $\vec{k}$ is the unit vector of the z axis. Eq. (2.36) is similar to Eq. (2.2) but (i) a body force per unit volume (mean pressure gradient) acting along the flow direction z was added to the right hand side, and (ii) the "true" pressure p was replaced by its periodic component $\tilde{p}$. If required, the "true" static pressure p can always be reconstructed from the simulation results as $p=\tilde{p}-K_p z$. Note that the pressure gradient $K_p=|\mathrm{d}p/\mathrm{d}z|$ is imposed as a known constant, while the flow velocity is computed as a result; this is equivalent to imposing not the bulk Reynolds number but the friction Reynolds number which, for a plane channel, can be defined as $Re_\tau = u_\tau(H/2)/(\mu/\rho)$, with $u_\tau = (\tau/\rho)^{1/2}$ (friction velocity) and $\tau = (H/2)|\mathrm{d}p/\mathrm{d}z|$ (mean wall shear stress).

(ii) A similar treatment is adopted for the concentration C. By definition of fully developed conditions, C can be split into a periodic component $\tilde{C}$ and a large-scale component $K_c z$, where the gradient $K_c = (dC/dz)$ can now be either positive (net inflow of electrolyte into the channel) or negative (net outflow of electrolyte from the channel). By substituting $\tilde{C}+K_c z$ for C in Eq. (2.35), after some manipulation the following transport equation is obtained:

$$\vec{\nabla}\left(\tilde{C}\vec{u}_0\right)=\vec{\nabla}\left[D\frac{b}{b+\left(a-M_e\right)\left(\tilde{C}+K_c z\right)}\vec{\nabla}\tilde{C}\right]-K_c w \tag{2.37}$$

The last term at the right hand side is implemented in the code as a source term

$$S = -K_c w = -\frac{\overline{J}^d_{IEM} A}{V} \frac{w}{w_{ave}} \tag{2.38}$$

in which $\overline{J}^d_{IEM}$ is the mean value of the electrolyte flux at walls (imposed in the simulation, see section 2.5.1.3), A is the membrane surface area in a Unit Cell and V is its volume. The quantity $\overline{J}^d_{IEM} A/V$ is the mean value of the source term, while w/w_{ave} represents a local correction. The approach described for the simulation of fully developed conditions has been widely adopted in previous work involving heat or mass transport [81]. Apart from numerical approximations, it guarantees solute mass conservation: the mean value of the bulk concentration (in the proper sense of mass-flow weighted average of C in a cross section) adopted as the initial guess is conserved through the simulation.

Summarizing, the governing equations solved for the Unit Cell are: the continuity Eq. (2.1), the Navier–Stokes Eqs. (2.36) and the transport Eq. (2.37). A body force per unit volume has been set in Eqs. (2.36) as the large-scale component of the streamwise driving pressure gradient, and a source term depending on the large-scale gradient for the concentration has been implemented in Eq. (2.37).

All the boundaries representing the fluid-solid interface (fluid-membrane and fluid-filament) have been set as walls with no-slip conditions (the only exception is represented by simulations in section 3.2, where also free-slip condition on the wires is simulated) and a Neumann boundary condition for the concentration: a uniform diffusive flux has been imposed at the upper and lower walls (see section 2.5.1.3), while the flux has been set to zero at the fluid-filament interfaces (spacer-filled channels) and at the lateral fluid-membrane profile interfaces (profiled-membrane channels).

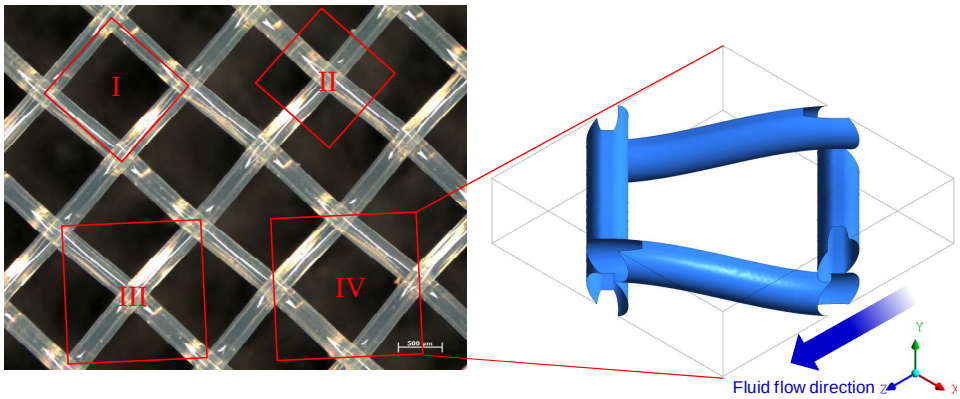

Figure 2.4. Different types of Unit Cell for the spacer. For spacers with woven filaments only the domains III and IV are Unit Cells.

2.5.1.3 Boundary conditions for membrane modelling

The upper and lower surfaces of the domain represent the membrane-solution interfaces. Outgoing or incoming fluxes of the electrolyte were imposed on these walls as discussed below, according to whether the computational domain represents the concentrated or the dilute channel, respectively. From the hydrodynamic point of view, they were treated as impermeable walls with ordinary no slip boundary conditions; this simplifying assumption is coherent with the general assumption of one-way coupling between flow and concentration fields and is justified by the fact that, under the conditions analyzed here, the electrolyte flux in or out of the membrane walls in a single Unit Cell can be estimated never to exceed 10^{-4} times the mass flow rate crossing the same cell.

Since the equation solved is Eq. (2.35), in which only convection and diffusion are explicitly accounted for, the boundary conditions to be set at the fluid-membrane interfaces must involve only diffusive fluxes. Migrative fluxes are not explicitly described by the model because they do not enter concentration balances, but can be deduced from the diffusive ones as described below.

First, note that current density, transport number and migrative flux in the solution in contact with the IEM are related to one another through the following expression

$$\vec{J}_i^m = \frac{t_i^0}{z_i F}\vec{i} \tag{2.39}$$

where $\vec{J}_i^m$ is the migrative flux of species *i*. By regarding the membranes as ideal (i.e., with permselectivity α = 1) the total flux of the co-ion at the membrane-solution interface must be zero. As an example, a cationic exchange membrane is shown in Figure 2.5. Here, it is the total flux of Cl^- at the membrane-solution interface that can be assumed to be zero ($\vec{J}_{-,CEM}^{tot} = 0$). As a consequence, the diffusive and the migrative fluxes of the co-ion must be equal and opposite, and the diffusive flux of co-ion can be written as:

$$\vec{J}_{co,IEM}^d = -\frac{t_{co}^0}{z_{co}F}\vec{i} \tag{2.40}$$

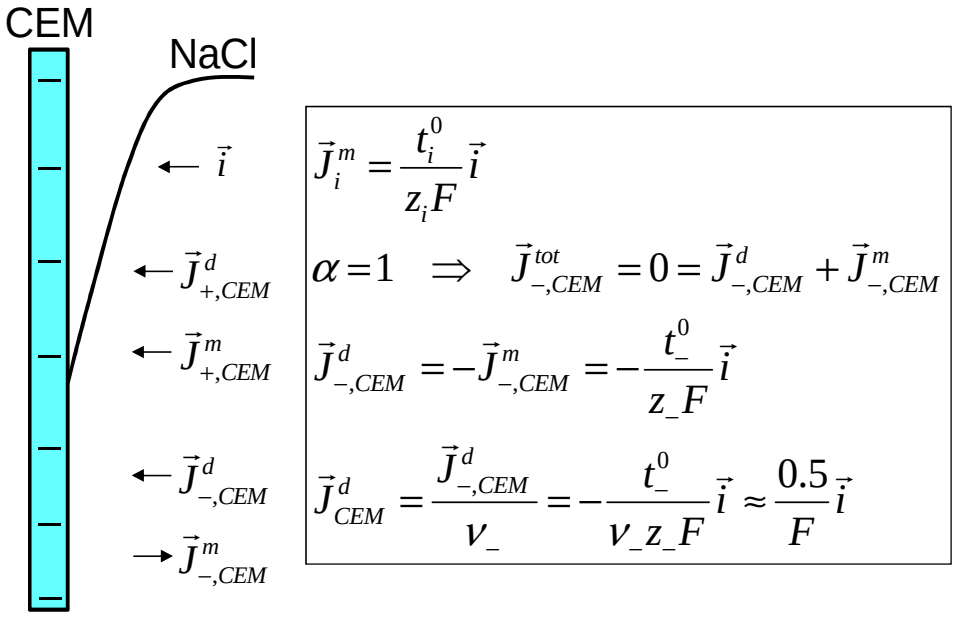

Figure 2.5. Ionic fluxes near the cationic exchange membrane within the concentrated channel, showing the link between diffusive flux and current density.

Taking into account the local electroneutrality condition, the diffusive flux of the electrolyte is $\vec{J}^d = \vec{J}_i^d / \nu_i$, and at the membrane-solution interfaces it can be expressed from Eq. (2.40) as

$$\vec{J}_{IEM}^d = -\frac{t_{co}^0}{\nu_{co} z_{co} F} \vec{i} \tag{2.41}$$

Clearly, for monovalent binary electrolytes such as NaCl, the diffusive fluxes of Na^+, Cl^- and electrolyte are the same ($\nu_+ = \nu_- = 1$, $z_+ = -z_- = 1$).

For NaCl, the transport numbers of cation and anion are slightly different ($t_+^0 \approx 0.4$; $t_-^0 \approx 0.6$). Explicitly accounting for this would lead to two different fluxes to be set on the two membranes, resulting in a larger concentration polarization on one of the membranes and a lower polarization on the opposite one, with related difficulties in the definition of a single polarization coefficient. Here we assumed for simplicity the transport properties of Na^+ and Cl^- to be the same within the solution, so that the corresponding fluxes can be considered equal and a single concentration polarization can be defined. As pointed out by a reviewer, the assumption of equal transport numbers would be more closely satisfied by different electrolytes, e.g. KCl, suggesting that their use would be recommendable in experiments designed to measure polarization.

Note that the assumption of equal transport properties, together with that of negligible gradients of transport numbers, implies that predicted concentration profiles are independent of migration. Eq. (2.41) allows a suitable diffusive boundary condition $\vec{J}_{IEM}^d$ to be deduced from a known current density. A homogeneous flux of electrolyte was imposed. According to the above remarks and to Eq. (2.41), the value implemented was computed from the current density as

$$J_{IEM}^d = \pm \frac{i \cdot 0.5}{F} \tag{2.42}$$

An incoming flux is considered positive (dilute channel), while an outgoing one is considered negative (concentrated channel).

Since Eq. (2.37) includes a concentration-dependent diffusivity, the flux is not linearly dependent on the concentration gradient. Therefore, it may be interesting to carry out simulations at different current densities (i.e. different fluxes). "High" or "low" current densities can be defined with respect to the maximum current density that would be attainable in the absence of non-Ohmic (i.e. concentration-related) losses. For each electrolyte couple, this is a short circuit current, whose assessment requires estimates for (i) the maximum (open circuit) potential associated with that couple (e.g. *BS* or *SR*); (ii) the overall Ohmic resistance of the electrolyte-filled channels; (iii) the Ohmic resistance of the membranes. While estimate (i) can be made with good accuracy, estimates (ii) and (iii) require simplifying assumptions and can only be approximate. Here, we assumed the coupled channels to have the same thickness, neglected the influence of the spacer (which increases the Ohmic resistance of the channel with respect to a void one) and used realistic values for the membrane resistance. Care was taken that, for any given electrolyte couple considered, the value chosen for the current density in the simulations was sufficiently lower than this maximum value. For example, in their RED tests, Tedesco et al. [124] measured values of about 3.7×10^{-4} Ωm^2 for the sum of the Ohmic resistances of anionic and cationic membranes. In channels 280 μm thick (as in the case of the D spacer-filled channel in chapter 4) the short circuit current density would be 237 A/m^2 for brine-seawater (*BS*, E_{OCV} = 0.105 V) and 82 A/m^2 for seawater-river water (*SR*, E_{OCV} = 0.153 V). Of course, higher current densities will be possible if lower-resistance membranes will become available. When different electrolyte couples were compared, the highest current density was limited by the more dilute of the couples (i.e. *SR*, seawater-river water) which is why only values up to 60 A/m^2 were considered.

Some simulations at various current densities in chapter 4 show that the non-linearity of the transport equation has only minimal effects, due to very slight variations of the corrective term of the diffusion coefficient. In fact, the functional dependence of the corrective term of the diffusion coefficient on the concentration is weak; also, the variation of the concentration within the domain is relatively limited, due to the electrolyte fluxes normally involved. For these reasons, the diffusivity correction varies for less than 1% (the values relevant the bulk concentration of the feed are reported in section 2.7). Therefore, the subsequent simulations shown in chapters 4, 5 and 6 are carried out at a fixed value of the current density.

2.5.1.4 Discretization of the Unit Cell

The computational domains have been discretized by multi-block grids composed either by hexahedral volumes, when possible, or by hexahedral-tetrahedral volumes (hybrid grids) when the geometrical complexity of the domain, due to the spacer wires and the periodic cell chosen, has not allowed the discretization with completely hexahedral meshes. However, the hybrid grids built are mainly composed by hexahedral volumes: parallelepipeds have been built around each filament and discretized with tetrahedra, while the rest of the computational domain have been discretized by mapped hexahedral volumes, and some pyramids and wedges have been necessary at the interfaces between the two parts [24]. Hexahedral or hybrid grids are important for the spatial resolution as they provide (i) a greater accuracy for a given number of degrees of freedom, (ii) a better convergence to grid-independent results with respect to fully tetrahedral grids and (iii) results closer to the experimental data [24, 125, 126].

The sensitivity analysis of the results to the discretization degree was carefully tested preliminarily, in order to carry out the subsequent simulations with suitable grids for obtaining accurate results along with acceptable computing times. Various grids were tested by comparing results obtained in terms of global quantities averaged in the whole domain (e.g. the average velocity) and trends of local quantities on lines perpendicular to the walls, for the case of the highest flow rate investigated. As a result, the coarsest grid allowing results being "practically unaffected" (i.e. discrepancies lower than 2% with respect to the finest one) by any grid dependence has been found for all the domains simulated.

2.5.2 Other simulations

Other simulations have been devoted to investigate other specific aspects. Details on these are reported in the pertinent sections. Through an approach very similar to the main one, some simulations have been carried out for a sequence of five unit cells along the flow direction of a spacer-filled channel, aiming at investigating entry effects (Multi-Cell, see section 4.2.2.2). A very different approach has been followed for the analysis of fluid dynamics of a RED system at higher scale. A set of 2D simulations (1 computational cell in the direction perpendicular to the flow) has been purposely

performed on an entire apparatus consisting of a simplified ideal planar stack with 50 channels including the distributor and the collector. Mass transfer is not analysed in these simulations (see section 3.4).

2.6 Numerical details

The continuity, momentum and mass transport equations were discretized and solved in the computational domain with the appropriate boundary conditions by means of the finite volumes method. Various codes were used for the generation and the discretization of the computational domain (CAD, mesh generators). The software package of the code Ansys®-CFX (version 13 or 14) was used for (i) setting the other parameters of the pre-processing (i.e. physical properties of the fluid, boundary conditions, initial conditions, solving parameters and convergence criteria), (ii) solving the problem and (iii) post-processing the results.

As the initial guess, homogeneous values of velocity, pressure and concentration (equal to the feed concentration) were imposed. The *High Resolution* scheme was used for the discretization of the convective terms and shape functions were used for the spatial derivatives of the diffusion terms. A coupled algorithm was adopted to solve for pressure and velocity. All simulations with electrolyte transport were run in double precision.

Convergence was attained after a different number of iterations depending on the specific simulation performed. The convergence criteria were the achievement of stabilized values at the monitor points along with round mean square residuals lower than 1.0e-6 for simulations without electrolyte transport and lower than 1.0e-10 for simulation with electrolyte transport. The simulations were carried out either by a double-hexacore workstation with 2.4 GHz CPU and 48 GB RAM or a double-octacore workstation with 2.6 GHz CPU and 64 GB RAM. The simulations required a variable computing time from some minutes to several hours.

2.7 Feed properties

The features of the feed solutions adopted in the simulations are summarized in Table 2.1. In chapter 3, simulations for pure water at 25°C were carried out for the analysis of fluid dynamics without electrolyte transport.

Various feed concentrations are suitable for the RED process. The REAPower project focuses on the power production by RED technology using seawater or brackish water as dilute solution and brine as concentrated solution, for reducing the Ohmic and non-Ohmic electrical resistance of the stack. For the analysis of mass transfer, it would be interesting to investigate the effect of the fluid properties. In dimensionless terms, this means to investigate the effect of the Schmidt number (*Sc*) on the Sherwood number (*Sh*). On the other hand, the boundary layer resistance, accounting for polarization effects on the actual driving force, decreases as the concentration increases and is even negligible for highly concentrated solutions (see section 1.3.3). Also, the range of variation for *Sc* is moderately narrow for NaCl solutions from very diluted to highly concentrated, as shown in Table 2.1. As a consequence, knowing the effect of *Sc* on *Sh* appears not to be crucial for the RED process. Nevertheless, it can be important for mass transport in spacer-filled channels in other applications. Therefore, in chapter 4 three different NaCl feed solutions at 25°C were simulated: Feed1 at a concentration equal to 5 M, Feed2 at 0.5 M and Feed3 at 0.017 M, representing nearly saturated brine, seawater and river water, respectively. The dependence of *Sh* on *Sc* for one spacer-filled channel configuration was investigated, finding that it was quite weak.

Therefore, it was chosen to perform the subsequent simulations, shown in chapters 5 and 6, only for one solution, the Feed2, i.e. seawater. In fact, a solution with seawater concentration is usually employed as the concentrated feed (coupled with river water as the diluted one), but it can also be fed as the diluate coupled with brine, as proposed within the REAPower project (see section 1.9). Seawater always fed a dilute channel in the simulations, i.e. an electrolyte flux entering through the walls representing the membrane-solution interfaces was imposed. However, once properly normalized, the results have general validity in order to assess concentration polarization phenomena in terms of concentration change from the bulk to the walls.

Notice that the Schmidt number is calculated taking into account the correction of the diffusivity that is equal to 1.1319, 1.0094 and 1.0003 for Feed1, Feed2, and Feed3 respectively. Of course, the major influence of this correction is exerted for the most concentrated solution, while it is practically non-influent for the most diluted one.

The density and viscosity of the solutions were obtained from Green and Perry [121] and Ozbek et al. [127].The diffusivity of NaCl in aqueous solutions was derived from Vitagliano and Lyons [128]. The parameters *a* and *b* of the linear regression of $\rho(C)$ (Eq.

(2.33)) for computing the derivative dρ/dC (in Eq. (2.32)), necessary to express the diffusivity correction in the transport equation, are calculated in the proximity of the bulk concentration of each of the three NaCl aqueous solutions to be simulated. Therefore, three couples of values were employed for the parameters a and b.

Table 2.1. Physical properties of NaCl aqueous solutions and pure water at 25°C.

	Molarity	Density	Viscosity	Diffusivity	Sc*	a**	b**
	C	ρ	μ	D			
Solution	[mol/l]	[kg/m^3]	[Pa s]	[m^2/s]	[-]	[kg/mol]	[kg/m^3]
Feed1 (brine)	5.0	1182.8	$1.659 \cdot 10^{-3}$	$1.580 \cdot 10^{-9}$	784	0.03493	1008.808
Feed2 (seawater)	0.5	1017.2	$9.312 \cdot 10^{-4}$	$1.472 \cdot 10^{-9}$	616	0.03986	997.327
Feed3 (river water)	0.017	997.7	$8.913 \cdot 10^{-4}$	$1.533 \cdot 10^{-9}$	583	0.04127	997.000
Pure water		997.0	$8.899 \cdot 10^{-4}$				

* The Schmidt number is calculated considering the correction of the diffusivity as $Sc = \dfrac{\mu}{\rho D \dfrac{b}{b + (a - M_e)C}}$

** $\rho = aC + b$

2.8 Definitions

The hydraulic diameter of the channel is assumed equal to twice the channel thickness, as in the case of an empty (spacer-less) channel of infinite streamwise and spanwise extend

$$d_{h,void} = 2h \tag{2.43}$$

The Reynolds number was calculated in accordance with

$$Re = \frac{\rho w_{mean,void} d_{h,void}}{\mu} \tag{2.44}$$

where $w_{mean,void}$ is the average velocity along the main flow direction z in a corresponding spacer-less channel, i.e. the superficial velocity [48, 60, 61]. The Fanning friction factor is defined as

$$f = \frac{\Delta p}{\Delta z}\frac{d_{h,void}}{2\rho w_{mean,void}^2} \tag{2.45}$$

where $\Delta p/\Delta z$ is the mean pressure gradient along the main flow direction and coincides with K_p in Eq. (2.36). In this way all the spacers are compared with respect to their reference empty channels, in order to highlight how each spacer modify fluid flow and transport features. The pumping power consumption is evaluated by means of the dimensionless power number, defined as [54]

$$Pn = \mathrm{SPC}\frac{\rho^2 h^4}{\mu^3} = \frac{1}{8} f\, Re^3 \tag{2.46}$$

where SPC is the specific power consumption per unit volume

$$\mathrm{SPC} = \frac{\Delta p}{\Delta z} w_{mean,void} \tag{2.47}$$

The local and average mass transfer coefficients are calculated as

$$k = \frac{J_{IEM}^d}{C_w - \hat{C}_b} \tag{2.48}$$

$$\bar{k} = \frac{J_{IEM}^d}{\bar{C}_w - \hat{C}_b} \tag{2.49}$$

where C_w and $\bar{C}_w$ are the local and averaged wall concentration, and $\hat{C}_b$ is the bulk concentration defined as the mass flow weighted average of the concentration on a cross section of the Unit Cell perpendicular to the main flow direction (e.g. a *x*-*y* plane). The average Sherwood number is calculated as

$$Sh = \frac{\bar{k}\, d_{h,void}}{D_{corr,ave}} \tag{2.50}$$

where $D_{corr,ave}$ is the average value of the term $D\dfrac{b}{b+(a-M_e)\left(\tilde{C}+kz\right)}$ present in Eqs. (2.35) and (2.37) (as mentioned in section 2.5.1.3, the diffusivity correction varies for less than 1%).

It is known that *f* and thus *Pn* depend on the fluid dynamics conditions (i.e. *Re*) and the geometric features of the domain; *Sh* depends on *Re* and geometry as well, but it depends also on the physical properties of the solution (i.e. *Sc*). From dimensional analysis one has

$$f, Pn = f, Pn\left(Re, geometry\right) \tag{2.51}$$

$$Sh = Sh\left(Re, Sc, geometry\right) \tag{2.52}$$

The analysis of performance of the RED channels here investigated was done in terms of pressure drop and mass transfer, by means of dimensionless numbers related by the functions indicated qualitatively in Eqs. (2.51) and (2.52). *f*, *Pn* and *Sh* as functions of *Re* were obtained for a given geometry, while the effect of *Sc* is evaluated for one geometry of spacer-filled channel. Hence, data obtained are valid for a wide range of geometrical features (scaled-up or down), operating conditions and physical properties, and can be easily used for comparison with results from the literature. Moreover the simulation results can be used as input information for the higher level of modelling, i.e. the process simulator. The voltage achievable at the electrodes of a RED stack is affected by polarization phenomena, as the actual driving force depends on the concentrations at the membrane-solution interfaces. Therefore, data to be provided to the process simulator for the calculation of the stack voltage must contain the relationship among the membrane-solution concentration, the bulk concentration and the flux (related to the current density), i.e. the Sherwood number. In order to provide a synthetic parameter (and not the distribution) of *Sh*, it is more suitable the definition of the average mass transfer coefficient given in Eq. (2.49), containing the average value of the wall concentration, although it is different from the usual definition of mean value of the local *k* values. Also this definition is more coherent with the boundary condition of a fixed flux of electrolyte.

Concentration polarization phenomena are usually quantified via polarization factors, defined as the ratio between the bulk and membrane-solution interface concentration. In formulae:

$$\theta^{conc} = \frac{\overline{C}_w^{conc}}{\hat{C}_b^{conc}} \text{ for concentrated channel (brine)} \tag{2.53}$$

$$\theta^{dil} = \frac{\hat{C}_b^{dil}}{\overline{C}_w^{dil}} \text{ for diluted channels (seawater and river water)} \tag{2.54}$$

According to the above definition, θ is always lower than 1, and the higher the θ value, the less significant the polarization effects. On the basis of the definitions given above, it is easy to recognize that θ relevant to a certain flux, corresponding to a current density according to Eq. (2.42), can be calculated from *Sh* and *vice versa*. The polarization effects quantified by θ depend on the flux. Conversely, the mass transfer coefficient is a constant as the flux varies, since the non-linearity of the transport equation is very weak (see chapter 4). In other words, by evaluating *Sh* in one simulation at any current density, the values of θ at any other current density can be calculated. Also, if the dependence of *Sh* on *Sc* is not evaluated for a given channel configuration, from θ (or *Sh*) of the feed solution simulated the calculation of an approximated θ for a different bulk concentration can be easily obtained.

2.9 Conclusions

A CFD model was developed in order to study fluid flow and concentration polarization phenomena in reverse electrodialysis channels. A transport equation suitable also for concentrated solutions was implemented in the CFD code. From the Stefan–Maxwell approach and assuming the local electroneutrality condition, the transport equation of a binary electrolyte (NaCl) can be derived. This equation contains the divergence of the convective, the diffusive and the migrative fluxes.

Respect to an ordinary transport equation, it exhibits two sources of additional difficulty: (i) the effective diffusion coefficient varies with concentration, density and derivative of density as a function of the concentration, and (ii) a migrative term containing the current density appears. As regards the former difficulty, a simple expression is obtained

by locally linearizing $\rho(C)$ in the proximity of the bulk concentration of the solution to be simulated. Therefore the correction term of the diffusivity depends on the parameters of the linear regression and on the concentration. However, the functional dependence on the concentration is weak.

As regards the latter difficulty, solving the transport equation in its complete form, which contains the current density, would require either additional equations for this quantity or an *a priori* knowledge of its distribution. Thus, CFD simulations were first carried out in a spacerless channel, where the current density can be assumed to be uniform, in order to quantify the relative importance of the transport terms (of course, in the empty channel no convective contributions are present in the direction orthogonal to the membranes). Results showed that the concentration profiles obtained by simulations taking into account the migrative term are practically coincident with those obtained by neglecting it. It is important to highlight that these findings do not mean that the migrative *flux* is negligible, but only that its *divergence* is negligible. Therefore, the transport equation of the binary electrolyte derived from the Stefan–Maxwell approach can be brought back to a convection-diffusion equation (with a weak non-linearity in the diffusive term).

The Unit Cell approach was used, based on inlet-outlet periodicity of velocity, pressure and concentration and valid for fully developed conditions. Thus, the Navier–Stokes and the transport equations had to be suitably modified in order to take into account the streamwise variation of pressure and bulk concentration, despite the periodic conditions imposed. By splitting pressure and concentration into a periodic component, whose spatial distribution repeats itself identically in each Unit Cell, and a large-scale component which varies linearly along the main flow direction, the equations for the periodic variables were obtained. In particular, a body force per unit volume was set in the Navier–Stokes equations as the large-scale component of the streamwise driving pressure gradient, and a source term depending on the large-scale gradient for the concentration was implemented in the electrolyte transport equation.

A uniform diffusive flux was imposed at the upper and lower walls, representing the membrane-solution interfaces. Since in the transport equation only convection and diffusion are explicitly accounted for, the boundary conditions to be set at the fluid-membrane interfaces must involve only diffusive fluxes. Migrative fluxes are not

explicitly described by the model because they do not enter concentration balances, but can be deduced from the diffusive ones. Under the assumption of ideal membranes (permselectivity equal to 100%) and transport numbers of ions in solution equal to 0.5, the diffusive flux at the membranes can be correlated to the current density by a very simple expression: the diffusive flux is equal to the current density times 0.5 and divided by the Faraday constant (the valence is 1).

Completely hexahedral grids or hexahedral grids mainly were used for the discretization of the computational domain. Therefore, a good mesh quality was obtained, as hexahedral grids provide (i) a greater accuracy for a given number of degrees of freedom, (ii) a better convergence to grid-independent results with respect to fully tetrahedral grids and (iii) results closer to the experimental data. The grid dependence analysis was carried out for all the domains simulated: various grids were tested for the case of the highest flow rate investigated, thus finding the coarsest grid allowing results being “practically unaffected” by any grid dependence.

From the CFD simulation, the local distribution of the variables within the Unit Cell of the channel is obtained; then, the effects of channel geometry, flow rate (i.e. Reynolds number) and feeds features on pumping power and concentration polarization are evaluated by means of process parameters as power number and Sherwood number that summarize the results. Finally, the functional correlations obtained provide input information for the higher level of modelling, the process simulator, i.e. the tool (i) for the prediction of the RED stack performance in terms of net power produced and (ii) for optimizations of channel configuration and operating conditions.

3 FLUID FLOW BEHAVIOR IN A RED STACK

Abstract

In reverse electrodialysis (RED), as well as in conventional electrodialysis (ED) technology, the process performance can dramatically depend on the stack geometry and internal fluid dynamics conditions: optimizing the system geometry in order to guarantee lower pressure drops and uniform flow rates distribution within the channels is a topic of primary importance.

Although literature studies on CFD analysis and optimization of spacer-filled channels have been recently increasing in number and range of applications, only a few efforts have been focused on the analysis of the overall performance of the process. In particular, the proper attention should be devoted to verify whether the spacer geometry optimization really represents the main factor affecting the overall process performance.

In this chapter, CFD simulations were carried out in order to assess the effects of different parameters on the global process efficiency, such as the choice of spacer material and morphology, and the optimization of feed and blow-down distribution systems. Moreover, experiments were performed in order to validate the CFD prediction of the pressure drop within spacer-filled channels.

Spacer material and morphology can affect fluid dynamics inside each channel. In particular the appropriate choice of net spacer material can influence the slip/no-slip condition of the flow on the spacer wires, thus significantly affecting the channel fluid dynamics in terms of pressure drops. The unit cell approach was adopted to investigate the effect of the different choices on the fluid flow along the channel. Results showed that a completely hydrophobic spacer able to realize free slip conditions can reduce significantly pressure drop.

Also, the possibility of choosing a porous *medium* to substitute the net spacer was theoretically addressed. Such investigation focused on the porosity and the fiber radius required to respect the process constrains of pressure drops and mechanical stability. This analysis highlighted that a feasible porous medium made of small fibers causes pressure drops much larger compared to a typical net spacer.

On the other hand, the overall pressure drop of a RED or ED stack can be considered as resulting from different contributions: the pressure drop relevant to the feed distributor,

the pressure drop inside the channel, the pressure drop in the discharging collector. The choice of the optimal stack geometry is, therefore, strongly related to the need of both minimizing each of the above terms and obtaining the most uniform feed streams distribution among the stack channels. In order to investigate such aspects, simulations were performed on a simplified ideal planar hydraulic circuit of a stack with either 50 spacer-less or 50 spacer-filled channels. Rectangular manifolds being wide as the channels were devised, and such configuration is proved to be able to significantly reduce hydraulic losses. Conversely, in conventional stacks that use small cylindrical ducts a significant contribution of the manifolds to the pressure losses is due to the relatively high velocity of the fluid entering/leaving the channel in radial direction at the inlet/outlet holes. Therefore, improving the design of the manifolds is a crucial topic.

The stack features had a significant influence on the overall process performance. A more homogeneous distribution of flow rates among the channels was obtained by (i) increasing the pressure drops along the channel, (ii) decreasing hydraulic losses in the distributor and (iii) reducing the total flow rate. The adoption of a symmetric feeding system along with an increasing number of inlets/outlets homogenizes the flow rates distribution and decrease the pressure drops.

Experiments by a mono-channel stack in the classical plate-and-frame geometry were performed. Woven spacers 280-480 μm thick were investigated at the flow rates typical of RED channels. Pressure drops were measured with and without the spacer, in order to quantify the effect of inlet-outlet channel and identify the distributed pressure drops due to the woven nets. A fair agreement was found between CFD results and experimental data on hydraulic loss along the channel. Therefore, CFD modelling can be used to evaluate the pressure drops within spacer-filled channels of any customised geometry, representing a powerful cost effective predicting tool.

3.1 Introduction

As thoroughly discussed in chapter 1, the fluid flow features and conditions strongly affect the process performance. The pressure drops along the entire system (including the distributor, the spacer filled channel and the collector) should be minimized in order to reduce the pumping power. On the other hand, the driving force has to be maximized by keeping the concentration polarization as low as possible (e.g. by including a spacer

within the channel). In addition, flow rates distribution within a stack of several cell pairs represents an issue which cannot be neglected. All these aspects confirm the need to investigate the fluid flow of RED apparatuses by a powerful tool as the Computational Fluid Dynamics (CFD).

Most literature works addressing fluid dynamics aspects in spacer-filled channel mainly aim at finding the spacer allowing the best compromise between pressure drop reduction and polarization minimization. Nevertheless, there are many aspects which have been poorly taken into account so far.

- Spacers can be made of different materials: surface-material characteristics influence the sliding of the fluid over the surface thus likely modifying the fluid flow and the relevant pressure drops; in particular, the use of hydrophobic surfaces can increase the slip length and reduce pressure loss. This effect may be not negligible at low overall flow rates (corresponding to the laminar regime) as those typically encountered in RED channels. The only example in the literature concerning spacers for RED is by Jagur-Grodzinski and Kramer [32] that treated the spacer surface and thus obtained a significant reduction of pressure loss (section 1.4.2).
- There are many commercially available porous media which couple a high open porosity with a high mixing promotion: the possibility to substitute a commercial spacer with one of these porous media should be addressed. In particular, a medium of fibres provides a very large number of locations for the membranes thus assuming a “corrugated” aspect. For the case of ED and RED applications this is likely to promote turbulence near their surfaces and consequently reduce concentration polarization phenomena.
- Although the contribute of the spacer geometry and/or the channel features to the process performance cannot certainly be neglected, a not sufficient attention has been paid to verify whether these are the main factors controlling the entire process. In this regard, experimental data highlight that the concentrated pressure drops in the manifolds can play a determinant role in determining the overall loss. In the most common kind of stack geometry, cylindrical ducts created by holes (of spacers, gaskets and membranes) generate high variations of cross-section at the inlet/outlet zones of the channel; thus they determine

high variations of velocity of the fluid entering and leaving the channel, causing high pressure drop in these regions of the stack. Nevertheless, the improvement of the distribution/collection system design can reduce significantly these localized losses [28]. (section 1.6). Moreover, in RED applications the lay-out of the entire stack (distributor-channels-collector) and the relevant flow rate distribution may affect the performance of the process. For example, a non-homogeneous flow rate distribution can determine high residence time in some channels, causing a reduction of the driving force (higher $R_{\Delta C}$, see section 1.3.3).

The present chapter aims at addressing these aspects for the case of a stack devoted to RED applications. In particular, it is devoted to:

- assessing the effect of the spacer material on the pressure drops along the channel;
- evaluating whether a fiber structure porous medium could substitute the most commonly adopted net spacers;
- investigating an entire simplified hydraulic system in order to assess the effect of some parameters (distributor thickness, channels thickness, presence of a spacer, lay-out configuration) on the RED process fluid dynamics. A rectangular configuration of the manifolds with width equal to that of the channels was devised. In fact, this configuration could be suitable to reduce pressure drop compared to the conventional stack configuration, as the distributor width covers that one of the entire channel, thus avoiding sudden expansions/contractions of the fluid vein at the entrance/exit of the channels.

Finally, CFD simulations of spacer-filled channels for RED were carried out in parallel with an experimental campaign by a mono-channel stack focused on the collection of data for model validation on the pressure drop prediction.

Each section of the chapter is devoted to a different aspect among those investigated.

3.2 Effect of net spacers material

3.2.1 Cases investigated

Two different double layer symmetric net spacer topologies were investigated: a commercial spacer made of woven wires and a corresponding ideal spacer made of

overlapped filaments (Figure 3.1). The channel thickness is 380 µm, the filaments have circular cross-section with equal size for both the two layers, the mesh length (distance between two subsequent non-crossing filaments) is 1.1 mm for both the two layers, the angle between two crossing filaments is 90°, and the flow attack angle (angle between the main liquid flow direction and the filaments) is 45°. Notably, the size of these spacers was chosen according to that commonly adopted in small scale electrodialysis plants. The computational domain was generated on the basis of the geometrical features detected by the measurements made on the woven spacer, which is the real one, and the compenetration/compression of filaments were somewhat taken into account (for details see section 2.5.1.1).

The fluid simulated was pure water at 25 °C, whose characteristics are reported in Table 2.1. The pressure drop imposed in the simulations ranges from 500 to 20'000 Pa/m.

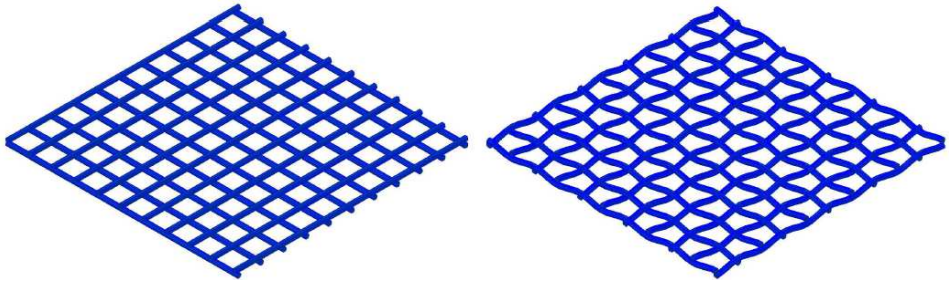

Figure 3.1. Double layer net spacers sketch: (a) overlapped spacer 380 µm thick, (b) woven spacer 380 µm thick.

3.2.2 Governing equations, computational domain and boundary conditions

The fluid flow analysis of the spacer filled channels was performed by simulating the Unit Cell, i.e. assuming fully developed conditions. The modelling approach followed is reported in section 2.5.1. A sketch of one of the unit cells generated is depicted in Figure 3.2. The same Unit Cell sizes were adopted for the two spacer-filled channels. Either no-slip or free-slip conditions were imposed on the wires surfaces in order to assess the effect of the spacer material. The equations system for the periodic domain was adopted, and consists of: the continuity Eq. (2.1), the Navier–Stokes Eqs. (2.36). The body force

per unit volume K_p in Eq. (2.36) was imposed with the effect of the large-scale pressure gradient, allowing the fluid to move within the domain.

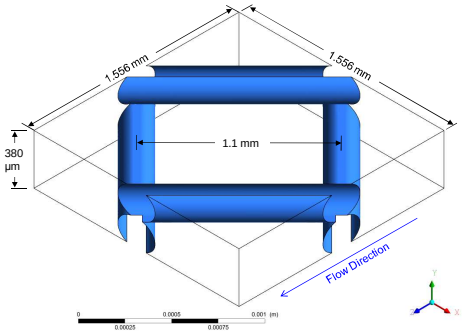

Figure 3.2. Unit cell for the case of the 380 µm thick overlapped spacer.

The two Unit Cells relevant to each spacer-filled channel were discretized by means of hybrid meshes mainly composed by hexahedral elements: because of the geometrical complexities due to the spacer wires, the zones near the filaments were discretized with tetrahedrons while all the rest of the computational volume was discretized with mapped hexahedral elements.

The sensitivity analysis of the results dependence on the discretization degree was performed for the case of the highest fluid velocity investigated for the two spacer-filled channels simulated. On the basis of this analysis, the grids to perform the simulations were chosen. As an example, Figure 3.3 shows the mesh adopted for the case of the woven spacer. The features of the two grids are summarized in Table 3.1.

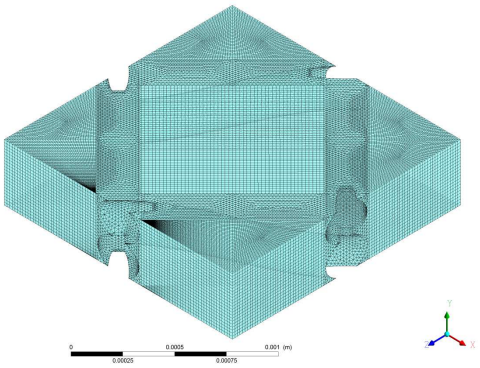

Figure 3.3. Mesh adopted for the case of the 380 μm thick woven spacer.

Table 3.1. Summary of the grids employed to evaluate the effect of the wires slip conditions.

Unit Cell	Number of cells	% of volume discretized with hexahedral cells
woven spacer	~534'000	76.0
overlapped spacer	~519'000	94.3

3.2.3 Results and discussion

Different materials are used to produce commercial spacers (e.g. PET, PP, PA). Materials with different characteristics may influence the system fluid flow patterns. As an example, completely hydrophobic and completely hydrophilic spacers offer a different resistance to the sliding of the water along the wire surfaces. Nevertheless, independently of the material constituting the spacer, the wire surfaces are very often defined as walls with no-slip boundary conditions in the literature. Under turbulent conditions, the effect of this simplification may be considered as being small or even negligible. On the contrary, at the low flow rates corresponding to a laminar regime as those typically employed in RED channels, this influence cannot be passed over.

In order to investigate the spacer material effect, the Unit Cells relevant to the two 380 μm spacer filled channels (i.e. the woven and the overlapped one) were simulated by imposing either no-slip or free-slip boundary conditions on the filaments surfaces. These can be considered as the two opposite conditions at which different materials may lead.

Some different pressure drops were imposed and the corresponding flow rates were provided by the code. The corresponding results are shown in Figure 3.4: the free-slip

condition leads to lower pressure losses for both the two cases as expected because of the viscous stresses reduction. In particular, a large average discrepancy, calculated as $(\Delta P/l_{no\text{-}slip} - \Delta P/l_{free\text{-}slip})/\Delta P/L_{no\text{-}slip}$, can be observed for the two different conditions: for the case of the overlapped spacer it was about 42% while it was about 46% for the case of the woven spacer.

Also, it can be observed that the pressure drops along the channel caused by the woven spacer are fairly higher than those relevant to the overlapped spacer: this average difference is of about 41% and 36% for no-slip and free-slip condition respectively.

According to these findings it can be stated that the spacer material may affect the pressure drop slightly more than the geometric shape thus suggesting that the proper attention should be paid to the choice of the spacer material for RED applications. In particular, the adoption of hydrophobic materials which intrinsically do not hold the water thus reducing wall viscous stresses should be preferable.

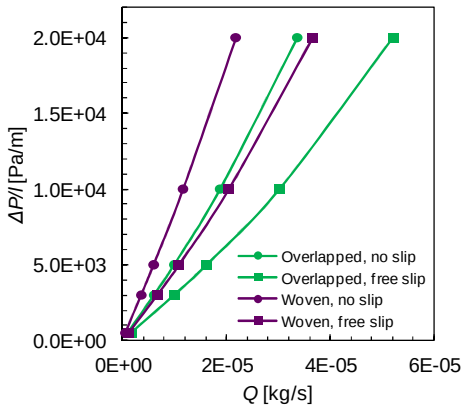

Figure 3.4. Pressure drop per unit length in unit cell for overlapped and woven spacers both with free-slip and no-slip condition on the filament surface. Notably, Q = 1E-05 kg/s in the unit cell corresponds to 38.7 ml/min within a channel 10 cm wide.

Figure 3.4 shows that the relation between water flow rate and pressure drops is linear only at the smallest flow rates. Similarly, the friction factor (f) vs Reynolds number (Re) curves (not reported here) show that f is proportional to Re^{-1} only up to a given flow rate. Despite this lack in linearity at higher flow rates, the flow field regime is however laminar since the velocity vs time trends did not show any chaotic fluctuation in the flow

rate range investigated in the present work. This non-linear behaviour is due to the spacer presence which causes the flow field not to be auto-similar as the flow rates increases. These aspects are discussed in more detail in the next chapters, and in particular in section 4.4 and 5.3.2.

3.3 Porous spacer

A suitable porous medium filled channel would guarantee a good mixing, thus sensibly reducing concentration polarization phenomena. On the other hand, its structure allegedly would yield very large pressure drops. As a consequence, this section is devoted to identify the characteristics that a porous medium must have to provide pressure drops along the channel comparable to those relevant to the formerly presented net spacers (see section 3.2).

There are several analytical methods allowing to relate the microstructure of a porous medium with its permeability. The permeability of a fibrous medium depends on different factors:

- fibers size, e.g. the fibers radius a;
- fibers concentration, usually expressed as solid volume fraction ϕ, or as porosity ε (clearly $\phi = 1-\varepsilon$);
- fibers arrangement.

At a given fiber arrangement the relation between permeability and the other two variables can be expressed as:

$$\frac{k}{a^2} = f(\varphi) \tag{3.1}$$

In accordance with the most commonly adopted theoretical approach [129-135], a porous medium can be ideally considered as a matrix of rods in order to explicit the function $f(\phi)$.

Porous media made of random fibrous structure were already investigated as possible fillers of channels devoted to RED processes [24]. As a consequence, theoretical relations being suitable and valid for this kind of porous media were adopted in the

following. In particular, two different analytical models were employed: the Jackson and James model [131] and the model by Tomadakis and Robertson [135].

According to the first one, the random medium permeability is considered as being equivalent to the permeability of a cubical lattice made of the same material. This results in the following expression for the dimensionless permeability:

$$\frac{k}{a^2} = \frac{3}{20\varphi}(-\ln\varphi - 0.931 + o(\ln\varphi)^{-1}) \tag{3.2}$$

Conversely, Tomadakis and Robertson [135] developed an analytical model based on electrical conduction principles aiming at predicting the permeability of porous media made of random fiber structures. The corresponding relation for the dimensionless permeability was:

$$\frac{k}{a^2} = \frac{\varepsilon}{8(\ln\varepsilon)^2} \frac{(\varepsilon - \varepsilon_p)^{\alpha+2}}{(1-\varepsilon_p)^{\alpha}\left[(\alpha+1)\varepsilon - \varepsilon_p\right]^2} \tag{3.3}$$

where ε is the medium-porosity, ε_p is the percolation threshold, α is a constant. For three-directional random overlapping fiber structures $\varepsilon_p = 0.037$ and $\alpha = 0.661$. Full details can be found in the relevant work [135].

Eqs. (3.2) and (3.3) are plotted in Figure 3.5. As it can be seen, these provide similar dimensionless permeability for solid volume fraction higher than 0.2, while for ϕ lower than 0.1, the lower the ϕ value, the larger the values of dimensionless permeability obtained by the relation by Tomadakis and Robertson [135] with respect to the Jackson and James equation [131].

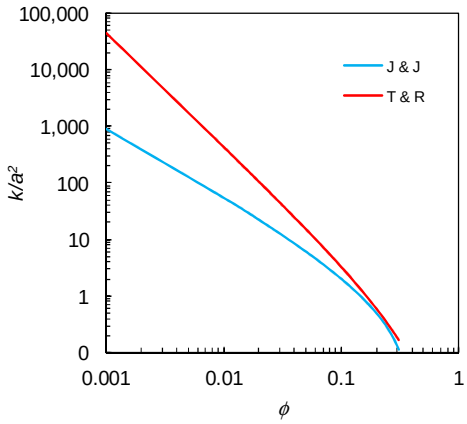

Figure 3.5. Dimensionless permeability as a function of Solid Volume Fraction.

In order to find the characteristics of a fiber structure porous medium providing pressure drops comparable to those relevant to a net spacer, three different fiber radius values (i.e. a_1 = 0.1 μm, a_2 = 1 μm, a_3 = 10 μm) were investigated. The relevant permeability as a function of the porosity is shown in Figure 3.6 for the case of the two former equations.

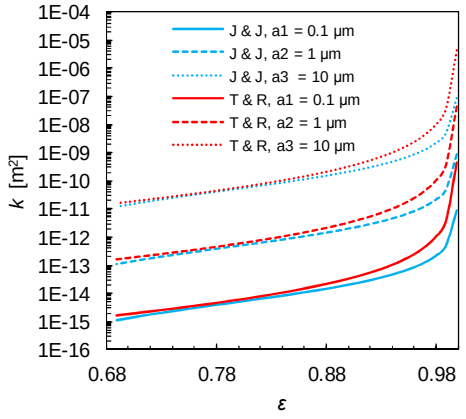

Figure 3.6. Permeability as a function of the porosity for three fiber radius values.

These values were adopted along with a given flow rate $Q = 5 \cdot 10^{-6}$ kg/s and a cross-section $A = 0.38 \cdot 1.556$ mm^2 (equal to the one used in the unit cell CFD simulations) to calculate the corresponding pressure losses by Darcy's law

$$\frac{\Delta p}{l} = -\frac{\mu}{k} u \tag{3.4}$$

where u is the velocity, μ is the dynamic viscosity and k is the permeability. Figure 3.7 shows the obtained pressure drop values. Notably, the pressure drops relevant to the two "completely hydrophilic" spacer (i.e. no-slip condition) filled channels (the woven and the overlapped spacer) are also reported for comparison purposes.

Results show that the lower the fiber radius, the higher the porosity required to provide pressure drops along the channel ΔP_{ch} similar to those relevant to the spacer. As an example, a fiber radius equal to 10 μm would require porosity higher than 95%, while a porous medium made of 1 μm fibers would require values of ε larger than 99%. A low fiber radius and a simultaneous very large porosity are likely to be requirements incompatible with the mechanical stability of the membrane-equipped-channels. On the other hand, ΔP_{ch} comparable with the net spacers may be obtained by employing porous media made of very large fiber radius whose size should be about one hundreds microns thus assuming the same features of a common wire made spacer.

Summarizing, these considerations suggest that a "feasible" porous medium made of small fibers (whose size is lower than typical spacer wire size) allegedly provides pressure drops along the channel much larger than those relevant to a typical spacer thus allegedly being unsuitable for RED applications.

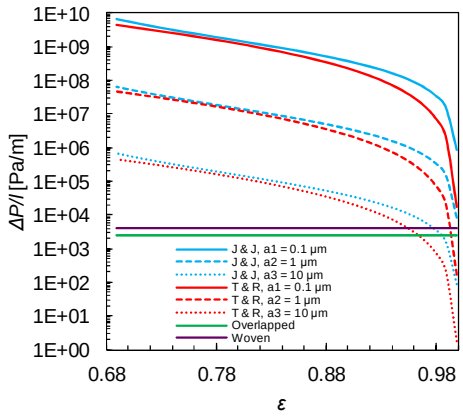

Figure 3.7. Pressure drop as a function of the porosity for three fiber sizes, for a flow rate $Q = 5 \cdot 10^{-6}$ kg/s and a cross-section $A = 0.38 \cdot 1.556$ mm^2.

3.4 Simplified entire stack

3.4.1 Geometrical features

In order to evaluate the contributions of manifolds on the overall pressure loss as well as the effect of stack lay-out and geometry on the flow rate distribution within the channels, an ideal 50-channels stack was devised: it is a "not-cylindrical" stack, where distributor and collector are rectangular channels, with only a computational cell along one direction (*x*-axis) so that it can be somewhat considered as a planar-like (2D) stack. This rectangular configuration could be suitable to reduce pressure drop compared to conventional stacks. The hydraulic circuit of one feed is simulated.

This numerical simplification of the real 3D geometry is adopted in view of its large computational savings: the simulation of an entire 3D stack would require very large computational resources, especially for the case of channels filled with a spacer. However, this simplification can be considered reasonable as the fluid dynamics along the unconsidered direction (*x*-axis) is not crucial for the pressure drop contributions estimation and for the flow rates distribution assessment.

Therefore, only a sheet (along the *x*-axis) of the entire stack was modelled by using a single computational cell along this direction. The channels length was equal to 10 cm. Conversely, two different channel thicknesses were investigated: either 100 μm or 200 μm in accordance with the idea of designing stacks as compact as possible. The distance between two subsequent channels was set to 300 μm for the case of 100 μm channel, while it was 400 μm for the case of the 200 μm channels. Three different distributor thicknesses *s* were simulated: s_1 = 0.2 mm, s_2 = 0.5 mm or s_3 = 1.0 mm. Full details on the 2D stack are shown in Figure 3.8.

The simulations were carried out for a feed with the features of pure water at 25 °C (see Table 2.1).

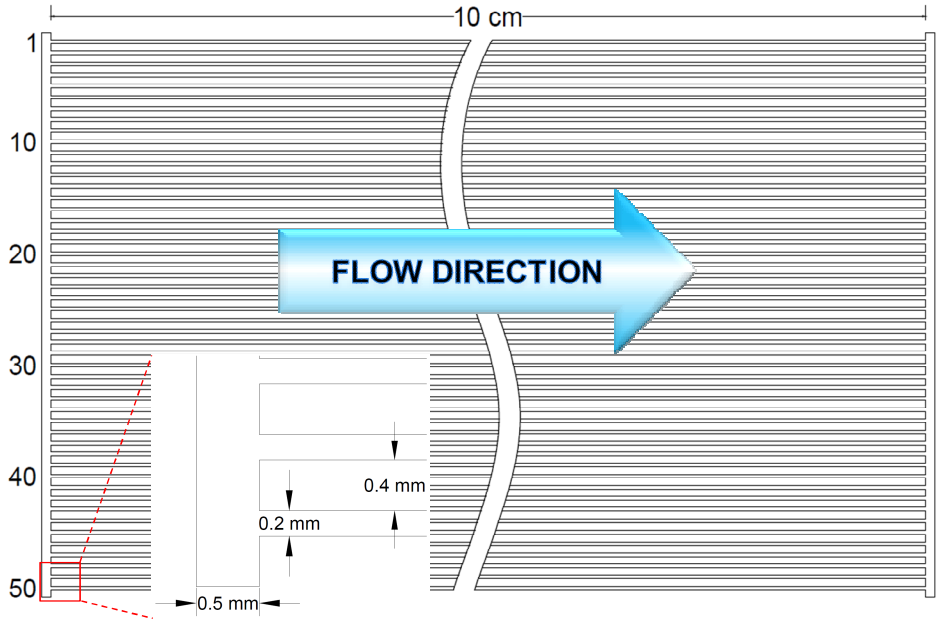

Figure 3.8. 2D geometry stack with 50 channels 200 μm thick and distributor and collector thickness equal to 0.5 mm.

Both empty and spacer-filled channels were investigated: in particular, for the case of the 200 μm channels, the effect relevant to the presence of the woven spacer was addressed. As a consequence, an ideal woven spacer 200 μm thick, similar to the 380 μm one presented previously, was employed in this section. A Unit Cell approach along with a relevant grid dependence analysis was preliminary performed for this spacer. A hybrid mesh of 1'200'000 elements was found to be more than sufficient to avoid any dependence of results on discretization degree.

However, it is not possible to simulate the effect of a spacer in a 2D geometry by considering only a sheet of the spacer. This problem was tackled by filling the channels with a fictitious porous medium able to provide pressure drops along the channel identical to those provided by the presence of the corresponding spacer. More precisely, firstly, the pressure drops along the 200 μm thick spacer-filled channel were evaluated as a function of the flow rates by means of the Unit Cell approach and a relevant $\Delta P/l$ *vs* average u_z (velocity component along the main flow direction) graph was provided (Figure 3.9). Then, these results were fitted by a second order equation composed by two parameters: such two parameters are considered as k and k_{loss} (see Eq. (3.5)) of the

corresponding fictitious porous medium. In fact, in the porous domain the fluid flow is simulated by means a source term corresponding to Darcy's generalized law included in the momentum Eqs. (2.2):

$$\vec{S}_M = -\frac{\mu}{k}\vec{u} - k_{loss}\frac{\rho}{2}u\vec{u} \tag{3.5}$$

where k is the permeability and k_{loss} is the loss coefficient which takes into account the possible deviations from the linear Darcy's law for fluid flow with high Reynolds numbers. The linear term of this expression refers to viscous losses while the quadratic term concerns inertial losses. Notably, the porous media were considered as being isotropic.

Therefore, the system of governing equations was composed by the continuity Eq. (2.1) and the Navier–Stokes Eqs. (2.2), where the source term expressed in Eq. (3.5) was added for the simulation of the fictitious porous domain mimicking the spacer-filled channel.

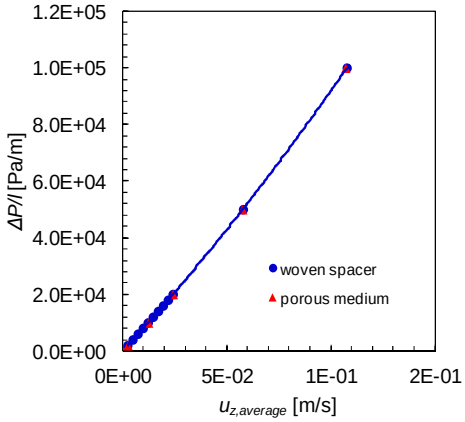

Figure 3.9. Pressure drop per unit length along the unit cell for: woven spacer 200 µm thick and equivalent porous medium.

As far as boundary conditions are concerned, a uniform normal velocity corresponding to the flow rates investigated (see Table 3.2) was set as inlet condition, a pressure equal to the atmospheric one was set as outlet condition, symmetry boundary conditions were

imposed on the surfaces perpendicular to the neglected direction. All other stack surfaces were defined as walls along with no-slip boundary conditions (in the case of channels with porous domain, the channels walls are set with free-slip conditions, as the porous medium dissipates the corresponding spacer-filled channel).

Two different inlet-outlet configurations were investigated:

- a configuration *A* with a single inlet and a single outlet;
- a configuration *B* with two inlets and two outlets.

These two configurations are depicted in Figure 3.10.

Notably, a summary of the different features/conditions investigated for the case of this simplified entire stack are reported in Table 3.2.

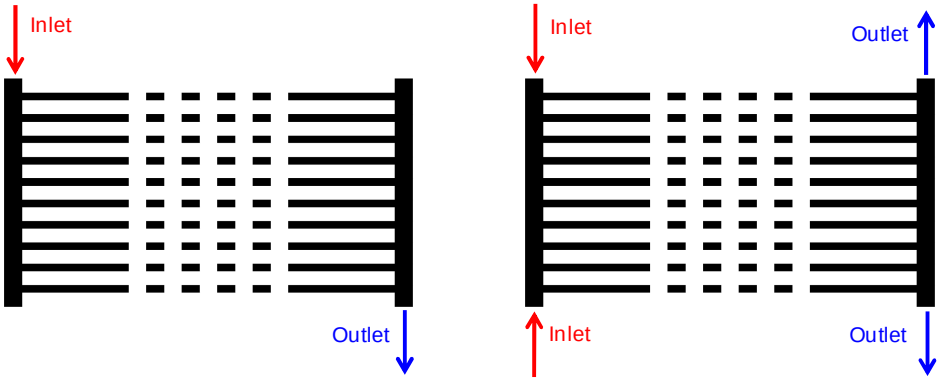

Figure 3.10. The two different inlet-outlet configurations tested: (left) single inlet - single outlet (conf. A); (right) double inlet - double outlet (conf. B).

Table 3.2. Summary of the investigated variables.

Distributor/Collector thickness [mm]		**Channels thickness [µm]**		**Feed configuration**	**Flow rate**	
s_1	0.2	w_1 spacer less	100	A (single inlet and single outlet)	Q_{over-1}	4.00E-06 kg/s(*) 240.7 ml/min(**)
s_2	0.5	w_2 spacer less and spacer filled	200	B (double inlet and double outlet)	Q_{over-2}	2.00E-05 kg/s(*) 1203.6 ml/min(**)
s_3	1.0				Q_{over-3}	4.00E-05 kg/s(*)

						2407.2 ml/min(**)

(*) mass flow rate values within the 2D stack;

(**) the corresponding flow rates within a stack 10 cm wide.

A grid dependence analysis was performed also for the case of the simplified entire stack and it is not presented here for brevity. Quadrilateral areas were adopted for the discretization of the domain (i.e. hexahedral volumes with only one computational cell along the direction not investigated) with a refinement near the walls. The chosen grids range from a minimum of 534'000 to a maximum of 1'365'000 computational elements because of the different geometrical features under investigation. It could appear as surprising that the entire stack requires a grid as fine as those relevant to a singular Unit Cell of the spacer-filled channel. Actually, the channels constituting the stack are either empty or filled with the fictitious porous medium and simulated in 2D, there are no spacers thus resulting in low computational requirements.

3.4.2 Results and discussion

The geometry of the entire stack may significantly affect the RED process performance: as a matter of fact several factors influencing the net power production depend on the stack geometrical features: concentration polarization phenomena, driving force across the membranes, short-cut currents, channels electrical resistance, total pumping power and flow rate distribution are the most crucial among these factors.

In this section, the dependence of *some fluid flow aspects* (i.e. the flow rate distributions within the channels, the overall pressure drop and its different contributions within the stack) on *some of the stack geometrical feature*s (i.e. the distributor, collector and channel size, the presence of the spacer, the feed configuration at three different feed flow rates) is investigated by carrying out a number of CFD simulations on the simplified 50 channels-entire stack.

All the variables and their relevant values investigated are summarized in Table 3.2: notably simulations encompass all the possible combinations of these variable values.

3.4.2.1 Flow rate distribution

The flow rate value within each channel clearly depends on the pressure difference between the distributor and the collector. Thus, the flow rates distribution along the channels can be inferred by the former pressure difference as a function of the Y-coordinate.

In this regard, two lines parallel to the Y-axis were placed in the middle of both the distributor and the collector as it can be seen in Figure 3.11. As an example, the behaviour of the total pressure along these two lines is shown in Figure 3.12 for the simulation case relevant to flow rate $Q_{over\text{-}2}$ = 2E-5 kg/s, distributor/collector thickness s_2 = 0.5 mm, spacer-less channel thickness w_2 = 200 µm. The corresponding collector-distributor pressure differences trend (as a function of the Y-coordinate), which can be inferred from the figure, suggests that the flow rate distribution among the channels is not uniform. The non-uniform distribution is due to the pressured drop in the distributor and collector channels [12, 33]. As a matter of fact, the flow rate shows a minimum which is always relevant to the central channel for the case of the configuration B, while it can vary its position as a function of collector/distributor thickness and overall flow rate for the case of the configuration A.

From Figure 3.12 it appears that the total pressure curves relevant to the configuration B are perfectly symmetric thus suggesting that this configuration leads to a symmetric flow rates distribution along the channels. It is not surprising and in accordance with the geometrical symmetry of this configuration. Compared to the cases investigated by Tanaka et al. [12], the configuration A corresponds to the system I, while the configuration B corresponds to the system II (the flow direction in the distributor is opposite to that in the collector) with doubled inlet and outlet. Since the configuration B has the same effect to halve the number of channels and make the system being symmetric, it appears as the best configuration.

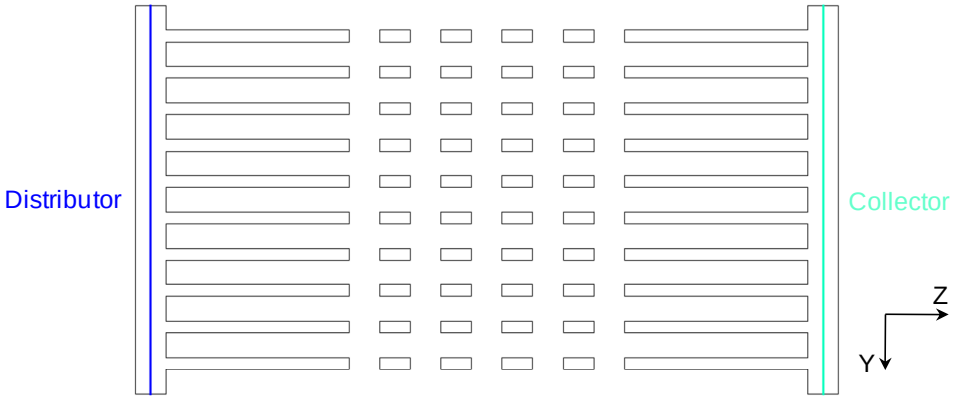

Figure 3.11. Indication of the lines parallel to the Y axis placed in the centre of the distributor and collector.

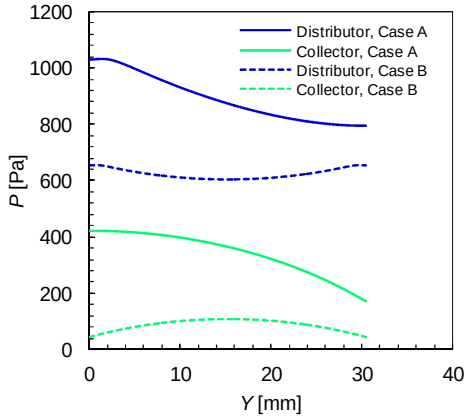

Figure 3.12. Total pressure along two lines parallel to the Y-axis and placed in the middle of the distributor and the collector respectively. Simulation case with flow rate $Q_{over\text{-}2}$ = 2E-5 kg/s, distributor/collector thickness s_2 = 0.5 mm, spacer-less channels thickness w_2 = 200 µm.

Flow rates distribution as a function of all the investigated parameters is provided in Figure 3.13 and Figure 3.14: in particular, the flow rates relevant to some channels only (the first, thirteenth, twenty-sixth, thirty-eighth and fiftieth) are presented.

In Figure 3.13 the dependence of flow rates distribution on channel features and stack configuration is shown. The flow rates distribution relevant to the spacer-less 100 µm channels is the most uniform. For the case of the 200 µm channels, in general the flow rate distribution is poorer and a difference between the spacer-filled and the spacer-less

channel is highlighted. In particular, the presence of a spacer leads to an enhancement of the flow rates distribution uniformity with respect to the corresponding spacer-less channels. This indicates that the higher the pressure drops along the channels (spacer-less 100 µm channel provides the highest pressure drops), the more homogeneous the corresponding flow rates distribution (confirmed by Pawlowski et al. [33]). In fact, with reference to Figure 3.12, as the pressure difference between distributor and collector is the driving force to the water flow inside each channel, a larger distance between pressure curves in these distributor and collector leads to a more uniform distribution of "driving force" in each of the 50 channels, thus to a more uniform flow rates distribution.

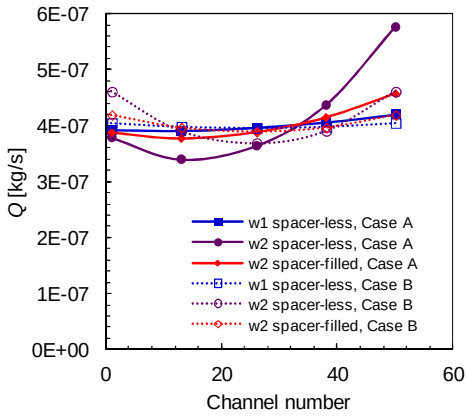

Figure 3.13. Flow rates distribution in some channels (the first, thirteenth, twenty-sixth, thirty-eighth and fiftieth) for the case of flow rate $Q_{over\text{-}2}$ = 2E-5 kg/s, distributor/collector thickness s_2 = 0.5 mm. Notably, Q = 4E-07 kg/s in the 2D stack corresponds to 24.07 ml/min within a stack 10 cm wide.

The effect of the distributor/collector thickness and of total flow rate on the flow rates distribution is presented in Figure 3.14 for the case of the spacer filled channels 200 µm thick.

As regards the effect of the distributor/collector thickness s, the figure shows that a higher s, corresponding to lower pressure losses along the entire stack, results into a better flow rates distribution for both the two configurations. This result is confirmed by the findings of [12, 33]. As far as the pressure drops along the distributor/collector

reduces because of an increase of their thickness, the corresponding total pressure vs Y-coordinate (Figure 3.12) curves tend to flatten thus resulting into more homogeneous pressure differences along Y (i.e. more uniform flow rates distribution).

As far as the influence of the overall flow rate on its distribution degree along the various channels is concerned, results of Figure 3.14 show that an increase of the Q_{over} yields a worse flow rate distribution along the channels, especially for the case of the configuration A, while a very little influence was observed for the symmetric configuration. However, it is worth noting that the effect of the overall flow fate on its distribution along the channels is not significant with respect to the effects relevant to distributor/collector thickness and channel features, thus suggesting that investigations should focus on these last two effects.

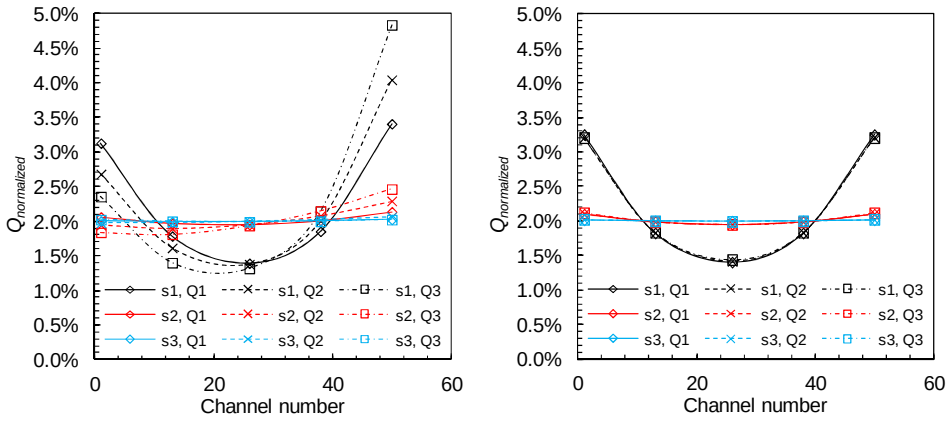

Figure 3.14. Flow rates distribution in some spacer filled channels 200 μm thick (first, thirteenth, twenty-sixth, thirty-eighth and fiftieth). Left: configuration A; right: configuration B.

As previously anticipated and as also observable in Figure 3.13 and Figure 3.14, the employment of the configuration B always leads to a symmetric and more uniform flow rates distribution thanks to its intrinsic geometrical symmetry.

Summarizing, it can be concluded that the flow rate will be distributed more uniformly in stacks characterized by higher pressure drops along the channels (lower channels thickness, presence of spacers) or lower pressure drops along the distributor and collector (case B, higher distributor and collector width).

Notably, the flow rates distribution may affect the total RED process performance: in this regard the results provided by the present CFD simulation were used as input data for a process simulator [124]. In accordance with the results obtained by this process simulator, a bad flow rates distribution leads to a reduction of the power density, especially at low overall flow rates (at high flow rates the driving force in all cell pairs is keep sufficiently high not to affect significantly the overall process performance).

3.4.2.2 Pressure losses along the entire stack

The contribution of the distributor to the overall pressure losses ΔP_{over} was addressed. For the case of the configuration A, this ΔP_{distr} was calculated as:

$$\Delta P_{distr} = P_{in} - P_{50} \tag{3.6}$$

where P_{in} is the total pressure at the inlet surface, while P_{50} is the pressure just afterwards the 50^{th} channel.

Similarly, for the case of the configuration B:

$$\Delta P_{distr} = P_{in} - P_{\min} \tag{3.7}$$

where P_{min} is the minimum total pressure in the distributor, it is achieved midway between the 25^{th} and the 26^{th} channel.

Relevant results and comparison are provided in Figure 3.15. The best fit curve for the trend of ΔP_{distr} as a function of the flow rate is parabolic, but in the range investigated here the curve can be well approximated by a linear function. ΔP_{distr} reduces as the distributor thickness increases as expected. Figure 3.15 shows also that in some cases ΔP_{distr} is of the same order of magnitude of the average pressure drop along the channel ΔP_{ch} (calculated as the arithmetic average of the pressure drop along the various channels) thus suggesting that both the two contributions are important and should be taken into account. In particular, for the case of the stack with the smallest distributor thickness s_1 (i.e. s_1 = 0.2 mm) and the configuration A, ΔP_{distr} is about twice ΔP_{ch}, while they are practically the same for the configuration B. As a difference, in all the other cases ΔP_{ch} corresponds to the main contribution to the overall pressure drops. Also, the

configuration B always leads to ΔP_{distr} being lower than those relevant to the configuration A.

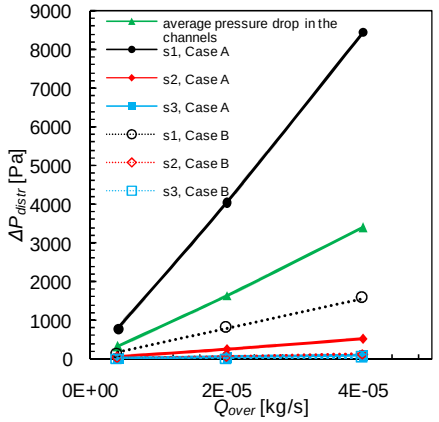

Figure 3.15. Pressure losses along the distributor and average pressure drop along the spacer-filled channel. Notably, Q_{over} = 1E-06 kg/s in the 2D stack corresponds to 60.18 ml/min within a stack 10 cm wide.

Summarizing, in the rectangular stack geometry simulated in this work, where the manifolds are wide as the channels, the pressure drop in the manifolds is shown to be low, unless distributor thickness is very small (i.e. comparable to the channels thickness). Therefore, a real stack designed with wide and sufficiently thick manifolds, can decrease significantly the pressure drop compared to the usual kind of stack with cylindrical ducts generated by holes (see section 3.1).

It should be noted that the model by Pawlowski et al. [33] shows that the geometry of the manifolds can be improved in the common stack configuration with feeding ducts generated by holes; on the other hand, the model is used for prediction of pressure drops in a large-scale stack devised as an industrial electrodialysis unit with channels length of 2 m, where the contribution of the distributed loss along the channel is very high and thus the relative contribution of the distributor/collector system is reduced. Nevertheless, the present CFD results demonstrate that the pressure drop in the manifolds can be dramatically reduced by the alternative geometry simulated here; therefore it is shown to be very promising and suitable for a performance improvement.

On the other hand, it must be highlighted also that in a real stack higher pressure drops concentrated in the manifolds could be expected, because of the ideality of the hydraulic circuit simulated. For instance, it is possible that in real stacks there is not a good alignment of membranes and spacers at the distribution/collection system, causing a more tortuous path of the fluid in the manifolds and a deformation of inlet and outlet cross-sections of the channels. These aspect are obviously neglected in the modelling, thus the "ideal" simulations could actually underestimate the concentrated pressure drops in the manifolds compared to those experimentally measured. Finally, in the experimental tests the proper attention should be paid to the stack assembling, in order to ensure that the stack could resemble as more as possible to the ideal configuration, without deviations that reduce the achievable advantages.

The overall total pressure drops ΔP_{over} (calculated as $P_{in} - P_{out}$) as a function of the overall flow rate is reported in Figure 3.16 for the same cases of Figure 3.15. The trends corresponding to the distributor thickness s_2 and s_3 are similar, since for these two cases, the main contribution to ΔP_{over} is due to the pressure losses along the channel ΔP_{ch}. Conversely, the case relevant to the distributor thickness s_1 exhibits a larger ΔP_{over} because of the main contribution due to the distributor.

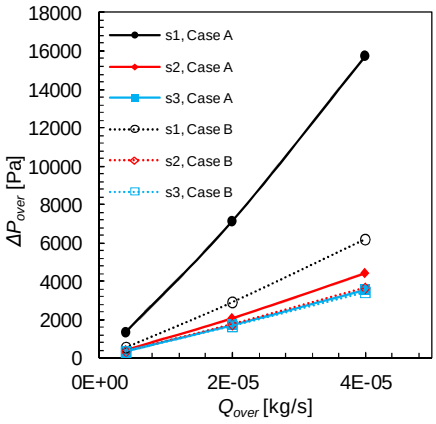

Figure 3.16. Overall total pressure drops along the entire stack for the case of spacer-filled channels. Notably, Q_{over} = 1E-06 kg/s in the 2D stack corresponds to 60.18 ml/min within a stack 10 cm wide.

Figure 3.17 shows that the channel geometrical features (i.e. thickness, spacer presence) also significantly affect ΔP_{over}. In particular, both a decrease of the channel thickness and the presence of a spacer lead ΔP_{over} to increase as expected. Clearly, at a given distributor/collector thickness, the choice of channel geometrical features resulting in larger ΔP_{ch} causes the distributor contribution to ΔP_{over} to be less important. Therefore, whether the pressure drops in the manifolds are reduced by the rectangular geometry along with a suitable thickness, it needs to improve the spacer-filled channel performance that, in addition, should take into account other aspects as concentration polarization phenomena.

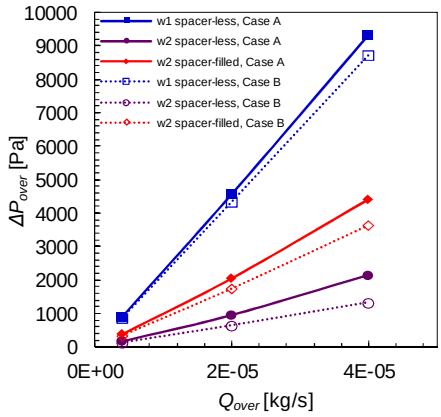

Figure 3.17. Overall pressure drops along the entire stack at a given distributor/collector thickness (s_2 = 0.5 mm). Q_{over} = 1E-06 kg/s in the 2D stack corresponds to 60.18 ml/min within a stack 10 cm wide.

3.5 Validation of pressure drop prediction in spacer-filled channels

3.5.1 Cases investigated

Pressure drop distributed along the channel was investigated for two spacers by CFD simulations and experimental tests, in order to validate the numerical prediction. The spacers were made by woven filaments at 90° with circular cross-section and equal spacing and size for the two layers. One spacer was supplied by Fumatech and is named "blue" spacer (thickness of 480 μm); the other one is supplied by Deukum (thickness of 280 μm) and a picture is shown in Figure 4.1, together with other spacers investigated in chapter 4. In addition, a spacer supplied by Sefar was also simulated for a comparison

with literature data (Sefar Nitex 03-300/51, spacer with woven filaments and thickness of 200 μm).

The computational domain was built considering the measurements made by optical microscopy and micrometer; also, the compression of filaments was taken into account as described in section 2.5.1.1. The features of the spacers are reported in Table 3.3, showing also the angle between the main flow direction and the filaments (the spacers are provided by integrated gasket that imposes the orientation of the filaments with respect to the main flow direction).

Two feed solutions at 25°C were tested: distilled water, and a brine solution of NaCl at concentration of 5 M. The physical properties of the feeds are summarized in Table 2.1. Fluid flow velocities, in the typical range of RED channels, up to ~4.8 cm/s were investigated.

Table 3.3. Geometric features of the spacers investigated and angle between the flow direction and a filament.

Spacer	Filament arrangement	Thickness [μm]	Filament diameter [μm]	Mesh length [μm]	Volume porosity [-]	Angle between filaments [°]	Angle between flow direction and a filament [°]
Blue (Fumatech)	Woven	480	260	1160	0.81	90	45
Deukum	Woven	280	148	809	0.85	90	0
Sefar	Woven	200	122	422	0.77	90	45

3.5.2 Experimental section

3.5.2.1 Mono-channel stack

The experimental apparatus consists of a mono-channel stack in the conventional plate-and-frame geometry. The endplates of a RED stack were used, and the spacer was interposed between two additional rigid plates (that cover the compartments for redox reactions for RED experiments). The plates are transparent (Plexiglas), so that it was easy to detect eventual air bubbles. The solution is fed and discharged by three inlet/outlet holes. The channel thickness was fixed by woven spacers, provided with integrated gasket and inlet/outlet holes. Two different spacers were used, namely Blue and Deukum; their main features are listed in Table 3.3. The hydraulic seal of the stack

is ensured by using threaded rods and nuts, with the suitable tightening. Figure 3.18 shows a schematic representation of the mono-channel stack adopted.

3.5.2.2 Feed solutions

The experiments were performed with (i) distilled water and (ii) an artificial solution of NaCl at concentration of 5 M (brine). Coarse halite crystals with purity of 99% were used. The dissolution was favoured mixing the solution by a stirrer or a submersed pump creating recirculation zones. The solution was then filtered by a cartridge filter and put in a tank.

The feed solution was drawn from a flask and pumped through the stack by a peristaltic pump at different flow rates between 0.87 and 63 ml/min. The solution was fed from below and during the filling phase of the stack, care was taken to make coming out air bubbles that could affect the measurements. Exiting from the stack, the solution was recirculated in the flask at atmospheric pressure at a fixed height over the level of the solution. Figure 3.19 shows the whole experimental apparatus.

3.5.2.3 Measurements and data acquisition

The pressure downstream of the pump was measured by a pressure transducer (Sensortechnics) that generates an electric signal from 0 to 10 V, corresponding to the pressure range 0-2 barg. The pressure transducer was provided with a data logger (National Instruments DAQ NI USB 6210) for detecting and recording measurements continuously. Data were acquired and managed in a pc by the software LabVIEW.

3.5.2.4 Experimental procedure

Pressure drops were measured with and without the spacer, in order to quantify the effect of inlet-outlet channel and identify the distributed pressure drops due to the woven nets.

Due to the small size of the channel and to the stack geometrical characteristics (Figure 3.19), it was not possible to “directly” measure the pressure losses along the channel provided with the spacer: as a matter of fact, only in-out pressure measurements were possible. Therefore, in order to isolate the pressure drops along the spacer-filled channel, an ad-hoc procedure was set up based on the employment of two different channel configurations for the experiments (shown in Figure 3.20):

a) A stack with a full spacer;
b) A stack with a spacer deprived of its central area (10×10 cm^2) which was cut thus resulting in a channel unprovided of spacer (a part from the areas near the inlet and the outlet).

By means of these configurations, two different ΔP were measured (during two separate experiments):

- ΔP_{over} including external loss, distributed spacer filled-channel loss and in-out loss;
- ΔP_{empty} including external loss, distributed empty channel loss and in-out loss.

The distributed pressure drops per unit length within the spacer-filled channel were obtained as

$$\frac{\Delta P_{spacer}}{l} = \frac{\Delta P_{over} - (\Delta P_{empty} - \Delta P_{HP})}{l} \tag{3.8}$$

where ΔP_{HP} is the theoretical distributed loss per unit length in a corresponding spacer-less channel of infinite spanwise and streamwise extent, calculated by means of the Hagen-Poiseuille equation

$$\frac{\Delta P_{HP}}{l} = \frac{12\mu Q}{sb^3} \tag{3.9}$$

where μ is viscosity, Q is flow rate, l is channel length, s is channel width and b is channel thickness.

All measurements were performed in duplicate in order to evaluate the influence of the assembly conditions (torque applied manually to the nuts, spacer alignment) and verify the riproducibility. Discrepancies below 7% were found. The mean values of these duplicates were calculated and are reported in the results of section 3.5.4.

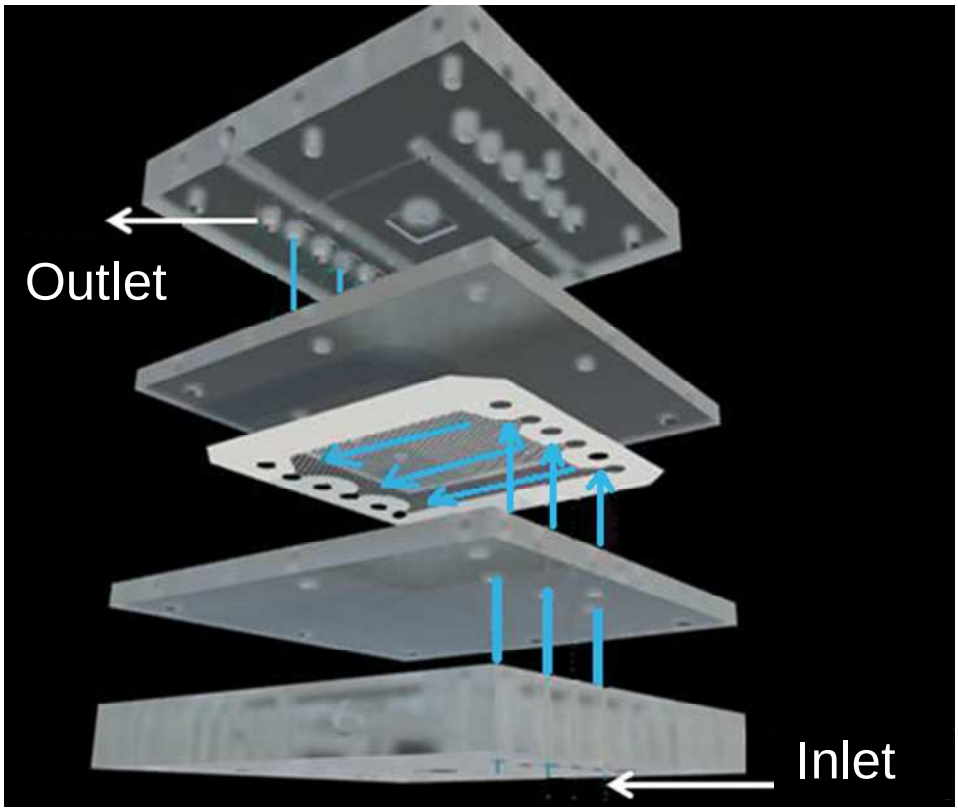

Figure 3.18. Stack with one channel adopted for the experimental measurements of pressure drops.

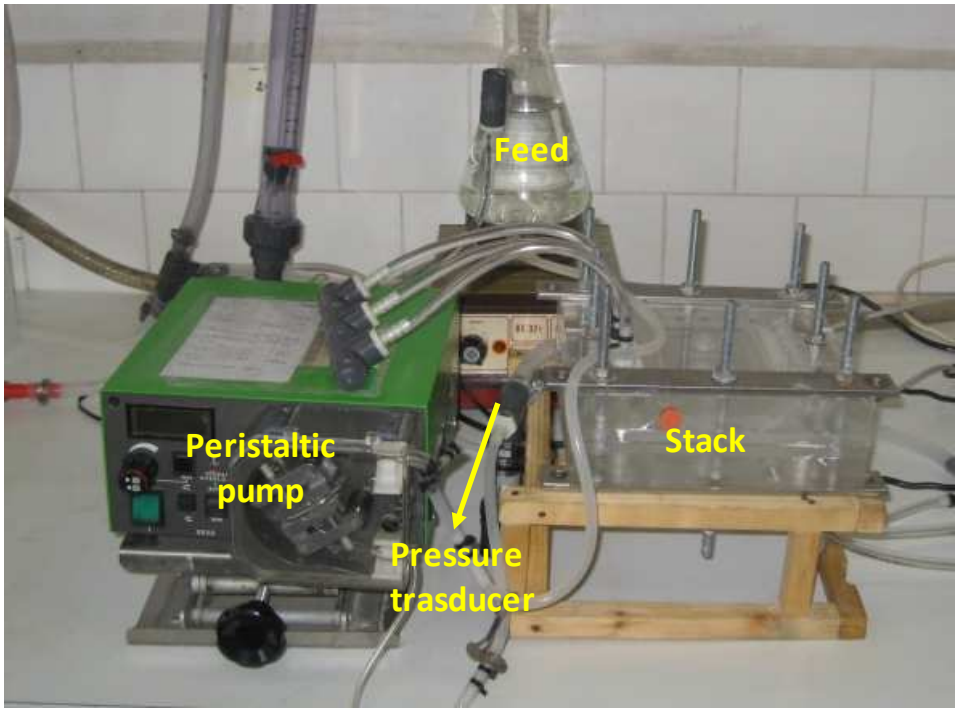

Figure 3.19. Experimental apparatus for the pressure drops measurements.

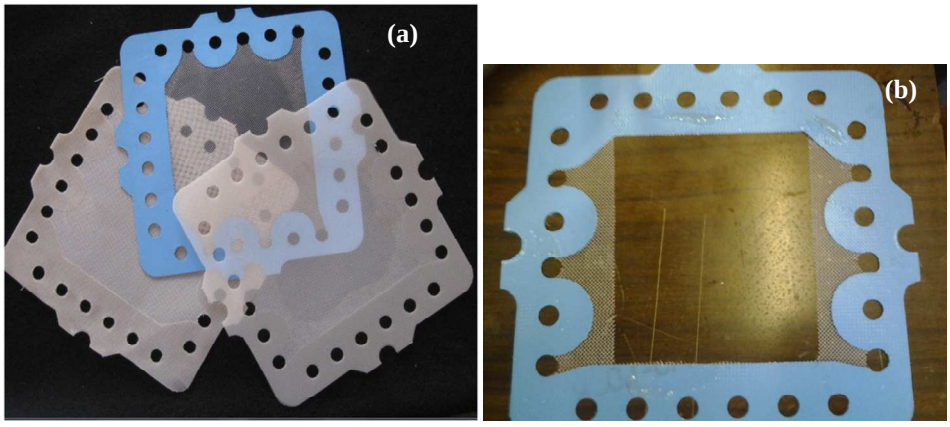

Figure 3.20. Full spacer (a) and spacer deprived of the central area (b).

3.5.3 CFD modelling

Fully developed flow conditions were assumed in the simulations, thus the periodic domain was simulated (Unit Cell approach, see section 2.5.1). The governing equations

are the continuity Eq. (2.1) and the Navier–Stokes Eqs. (2.36) with the body force per unit volume K_p having the effect of the large-scale pressure gradient, ranging from 0.01 to 0.2 bar/m. Fluid flow velocities up to ~4.8 cm/s were obtained.

The Unit Cells of to two spacer-filled channels were discretized by hybrid meshes mainly composed by hexahedral elements (the regions near the wires were discretized with tetrahedrons) as in the case of section 3.2.2. The sensitivity analysis of the results to the discretization degree was tested preliminarily for the case of the highest pressure gradient imposed. The features of the grids chosen by this analysis and employed to run the various simulations are summarized in Table 3.4.

Table 3.4. Summary of the grids employed to asses pressure drop for the validation.

Unit Cell	Number of cells	% of volume discretized with hexahedral cells
Blue (Fumatech)	~1’126’000	71.4
Deukum	~1’600’000	76.1
Sefar	~1’088’000	62.2

3.5.4 Results and siscussion

Figure 3.21 reports experimental results on overall and distributed pressure drops within that stack fed by distilled water. The distributed losses are not directly measured, but calculated as described in section 3.5.2.4. The distributed pressure drop along the spacer-filled channel is 31% and 53% of the overall pressure loss for the cases of the Deukum and Blue spacers respectively.

Therefore, these experimental results demonstrate that a significant contribution to the pressure drop can be attributed to the manifolds when the conventional stack geometry is used; in fact, it causes relatively high velocities of the fluid entering and leaving the channel in radial direction at the inlet and outlet holes, thus leading to high pressure losses. Again, it can be stressed that improving the design of the manifolds is crucial for the stack performance and that the rectangular configuration investigated by CFD simulation in section 3.4 can be reliable for the aim of reducing significantly the concentrated hydraulic losses.

Now, further supporting data from literature are reported. Vermaas et al. [21] have experimentally investigated the effect of the intermembrane distance and the feeds flow rate on the power density of a RED stack. They adopted a conventional stack comprising five cell pairs with one inlet and one outlet hole per channel, with river water and seawater as diluted and concentrated solutions. One of the spacers adopted (Sefar 03-300/51) was simulated in this work. Figure 3.22 shows the overall average pressure drop over the stack measured in [21] and the distributed pressure drop over the spacer-filled channel obtained from CFD modelling, as a function of the flow rate of a channel per unit width. This comparison shows that $\Delta P_{spacer}/\Delta P_{over}$ = 32%; therefore in this stack configuration the incidence of the two contributions to the overall pressure drop is found comparable to that of the experiments of Figure 3.21.

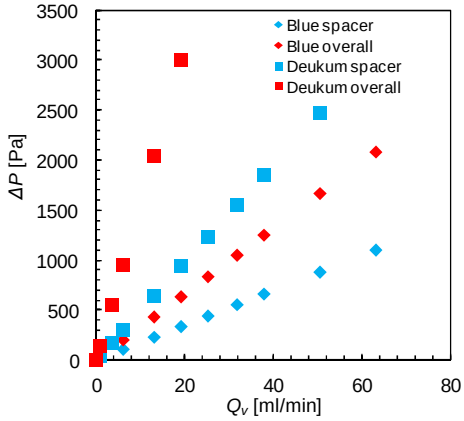

Figure 3.21. Experimental overall and distributed pressure drops along the mono-channel stack.

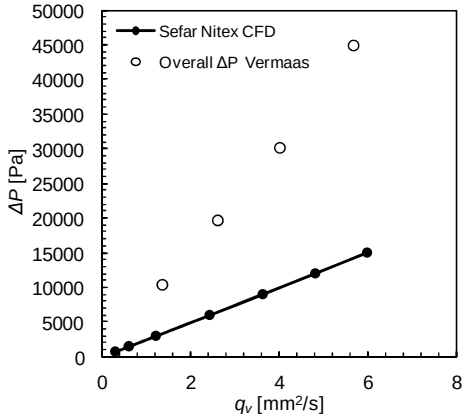

Figure 3.22. Experimental overall pressure drop by Vermaas et al. [21] and distributed pressure drop within Sefar spacer-filled channel from CFD.

Figure 3.23 shows the comparison between experimental data and CFD predictions concerning the distributed pressure drops within the spacer-filled channel, for two spacers (Blue and Deukum) and two different solutions (5 M brine and distilled water). The CFD results are in a fair agreement with the experimental data, although some discrepancies can be observed. In particular, the maximum deviation (~17%) regards the Blue spacer-filled channel fed by brine. It should be mentioned that several factors can cause a deviation between CFD and experimental data. In fact, modelling do not takes into account irregularities in the spacer and it is based on a schematic geometry and on the assumption of fully developed flow conditions. Moreover, the stack tightening may cause different compressions of the spacer, thus modifying the geometry of the channel, with consequent effects on the pressure drop due mainly to the channel thickness.

The validation of the CFD results by experimental data proves that the CFD modelling is a suitable tool to predict the pressure drops within spacer-filled channels of any customised geometry. Moreover, the CFD simulation (i) requires fewer resources in terms of equipment and time compared to the experimental investigation, and (ii) offers the possibility to analyse fluid flow and related phenomena at small scale, by obtaining detailed results that can provide important insights for the system optimization.

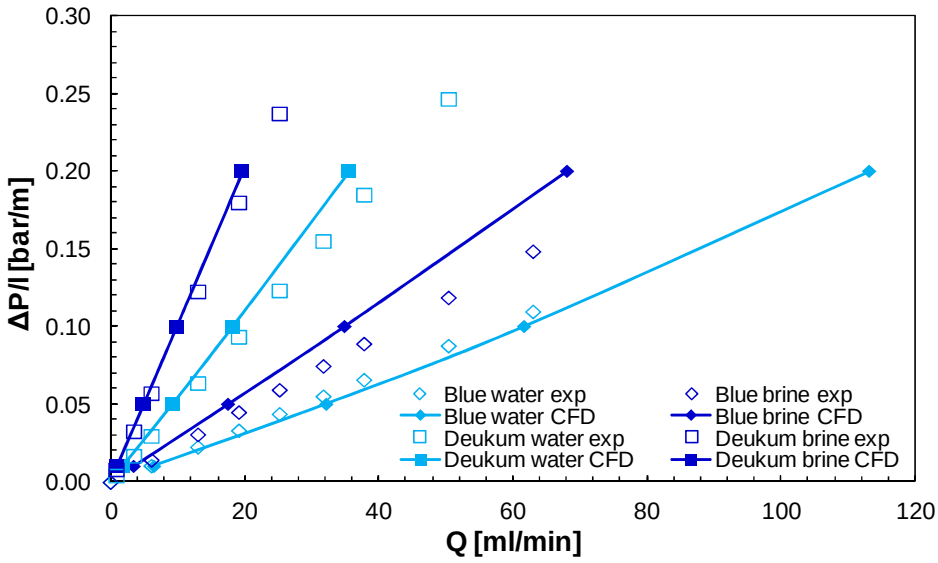

Figure 3.23. Distributed pressure drop as a function of the flow rate in a channel 10 cm wide for Deukum and Blue spacer-filled channels: comparison between CFD and experimental.

3.6 Conclusions

Analysis and CFD simulations of a simplified stack including spacer filled channels for reverse electrodialysis applications were carried out in order to assess the influence of different aspects on the fluid flow performance of the process. Results show that the spacer-geometry optimization may not be the main factor affecting the overall process efficiency.

- At a small scale, the spacer material can affect the sliding conditions of the fluid on the spacer filaments thus modifying the flow field along the channel and the relevant pressure drops. In particular a suitable perfectly hydrophobic material able to avoid any friction between the flowing water and the spacer wires would provide a significant reduction (~40%) of the pressure drops along the channel with respect to a spacer made of a perfectly hydrophilic material providing water-to-filaments no-slip conditions.
- As far as the possibility of adopting a suitable porous medium instead of a net spacer is concerned, a theoretical analysis of porous media characteristics was performed. In particular, two different theoretical approaches (based on the simplification of considering the porous medium as a rods matrix) were adopted

in order to assess the porosity and the fiber radius that a porous medium should have to provide pressure drop in the channel similar to those caused by typical net spacers. A low fiber radius and a simultaneous very large porosity would lead to pressure loss similar to those provided by the spacers, but they are likely to be two slight compatible properties. On the other hand, large fiber radius may also be suitable to accomplish the desired task, but the fiber radius size should be so large that the porous medium shape would become the same of a commercial net spacer. These findings suggest that a feasible porous medium made of small fibers (whose size is lower than typical spacer wire size) allegedly provides pressure drops along the channel much larger than those relevant to a typical net spacer thus likely being unsuitable for RED applications.

- At a larger scale, fluid flow performance depends not only on the channels characteristics, but also on stack geometry and lay out. The dependence of some fluid flow aspects (i.e. the flow rate distributions within the channels, the overall pressure drop and local pressure drops) on some features of the stack (i.e. different distributor, collector and channel size, spacer presence, feed configuration, overall feed flow rate) was investigated by carrying out a number of CFD simulations on a simplified 50 channels-entire stack with rectangular manifolds being wide as the channels. Results indicate that all the parameters considered can affect the stack fluid dynamics.
    - A more homogeneous distribution of liquid flow rates can be obtained by i) increasing the pressure drops along the channel (i.e. decreasing channels thickness and/or adding a spacer), ii) decreasing hydraulic losses in the distributor (i.e. decreasing distributor/collector thickness) and iii) reducing the total flow rate.
    - An analysis of the overall pressure losses along the stack have shown that a fluid flow optimization of a RED apparatus must not focus on channel features only. In fact, a distribution system designed with rectangular geometry was shown to be very effective to decrease dramatically the pressure loss occurring in the manifolds compared to a conventional stack. Also, the reduction of pressure drop in

rectangular manifolds can cause the further advantage of a more uniform distribution of flow rate. On the other hand, several factors of non-ideality can occur in a real stack, as the bad alignment of membranes and spacers, the obstruction by pollution and the mechanical deformation of the stack etc. Therefore, the design of the manifolds is crucial, but the proper attention should be paid also to the stack assembling and operation.

  - The adoption of a symmetric feeding configuration along with an increasing number of inlets/outlets is suggested to provide better flow rates distribution and lower pressure losses although it is intrinsically more complex and expensive by a construction point of view.

- Pressure drops distributed along the spacer-filled channel were investigated by CFD simulations and experimental tests in a mono-channel conventional stack, in order to validate the numerical prediction. Experimental results showed that the pressure drops in the manifolds were ~50-70% of the overall loss through the stack, confirming data from the literature on conventional stacks with cylindrical ducts. Moreover, a fair agreement was found between CFD results and experimental data on distributed pressure drops; this demonstrates that the CFD modelling is a reliable predicting tool to investigate any customised geometry, reducing equipment and time resources compared to the experimental testing, and providing a detailed analysis at small scale of fluid dynamics and associated phenomena, which is very useful for the process optimization.

Beyond the aspects analysed here, concentration polarization phenomena in RED channels represent a prominent feature for the process performance; the next chapter is devoted to the CFD simulation aimed at investigating fluid flow and mass transfer within RED channels.

4 CONCENTRATION POLARIZATION PHENOMENA IN SPACER-FILLED CHANNELS

Abstract

In RED systems, as in most membrane processes, concentration polarization phenomena may affect the theoretical driving force and thus the performance of the process. Operating conditions, including the feed solution flow rate and concentration and the channel geometrical configuration, may greatly influence both the polarization effect and the pumping energy consumption.

In the present chapter CFD simulations are performed to investigate concentration polarization and pressure drop in spacer-filled channels. The transport equation for a binary electrolyte derived from the Stefan–Maxwell equation with the assumption of local electroneutrality is employed. The geometric periodic domain of the channel is simulated, assuming fully developed flow conditions; also, entry effects are investigated in a domain, consisting of a sequence of five unit cells, with inlet-outlet boundaries. Results showed that entry effects are slight and occur only just the first unit cell; thus the Unit Cell approach simulating fully developed flow is shown to be appropriate to represent the conditions that occur in a large part of the channel. Hence, all the subsequent simulations are carried out by the Unit Cell approach.

The influence of flow rate, feeds concentration, current density and spacer features on fluid flow and mass transfer are investigated. Concentration field is slightly affected by the solution properties (Schmidt number), while the *effects* of the concentration polarization were significant at low feed solution concentration (river water), but only secondary at higher concentrations (seawater and brine), even at high current densities; thus different optimization strategies should be employed depending on the feeds concentration.

Different commercial spacers were investigated. Since low Reynolds numbers are typical for RED channels, the fluid flow regime was laminar in all cases; however the fluid flow and concentration fields were significantly affected by the channel geometry, due to the velocity components perpendicular to the membranes induced by the spacer wires. Significant insights on the features that a spacer-filled channel should possess for high efficiency and high current density RED applications were identified. Spacers with

woven filaments were found to be more effective than spacers with overlapped filaments, as they enhance mass transfer at any given pumping power consumption. In spacers with wires at 90°, for any wire arrangement a flow attack angle of 45° results in more efficient mixing compared to the flow direction parallel to one filament. Different angles between the filaments provide similar performance.

4.1 Introduction

As widely discussed in chapter 1, fluid dynamics plays a key role for the RED performance. In fact, the flow and concentration fields affect considerably the stack net power output. In particular, stack geometry, flow rate and feeds properties are the most important parameters that establish these fields within the stack, with effects on concentration polarization phenomena and hydraulic friction. Therefore, fluid dynamics and associated phenomena of mass transport can influence deeply the actual driving force (and thus the actual voltage over the membranes) and the pumping power consumption, and thus the producible net power.

At large scale, the fluid flow behaviour of the stack depends on stack distributor/collector geometry and lay out, as discussed in section 1.6 and analysed by CFD simulations in section 3.4; however, the channels features are crucial for the process performance.

In RED and in many membrane processes with flat sheet and spiral wound modules, net spacers are used as mechanical support between the membranes (thus creating the channel) and mixing promoters (thus reducing the boundary layer resistance) with respect to the empty channel (see section 1.4). A spacer is a polymeric net and can be made with various geometrical features. As shown by results in section 3.2 the geometrical features of the spacer and the hydrophilic/hydrophobic properties of the polymeric material of which it is made can have high influence on pressure drop along the channel.

The aim of this chapter is to assess concentration polarization phenomena within spacer-filled channels for RED applications, by CFD simulation at small scale. This analysis provides insight into the mass transfer phenomena in RED, where an optimisation of channel geometry and operating conditions is crucial for efficiency and economic competitiveness. The CFD model presented in chapter 2, based on the Stefan–Maxwell

equation and the Unit Cell approach, is employed to deal with ion transport in RED channels; therefore, a fully predictive numerical simulation is adopted for the modelling of fluid flow and ion concentration transport, in order to assess the influence of:

- flow rate, i.e. Reynolds number;
- feed properties, with three different NaCl concentration (brine, seawater and river water);
- molar flux through the membranes, i.e. current density;
- spacer-filled channel configuration, including the poorly studied ones involving spacers with woven filaments.

First of all, the entry effects in a spacer-filled channel are evaluated, in order to assess if the assumption of fully developed flow condition and the simulation of the Unit Cell are reliable; then, the other aspects listed above are analysed.

4.2 CFD modelling

4.2.1 Systems under investigation

Different configurations of Reverse Electrodialysis channels were investigated:

i) channels equipped with four different spacers (see Figure 4.1): (A) a diamond spacer 400 μm thick made by woven filaments, supplied by Fumatech; (B) an ideal diamond spacer 400 μm thick with the same sizes, but made by overlapped filaments; (C) a coarser diamond spacer with thickness of 508 μm and overlapped filaments, supplied by DelStar (Naltex); and (D) a spacer with woven filaments and thickness of 280 μm, supplied by Deukum;

ii) an empty (i.e. spacerless) channel (E) with a thickness of 400 μm.

Since industrial or large-scale prototype RED plants do not yet exist, commercial spacers purposely manufactured for this application are not available. All the above spacers are produced for different membrane-based processes (Electrodialysis, Osmosis etc.) or for general purposes (e.g. packaging), and – in lack of more specific spacers – have been adopted by most groups which currently conduct experimental work on RED [21-24] as an alternative to profiled membranes [30]. All the spacers analysed here are similar, apart from the smaller scale (implying lower operational Reynolds numbers), to those

used in Membrane Distillation (MD), on which both experimental [136, 137] and computational work are conducted.

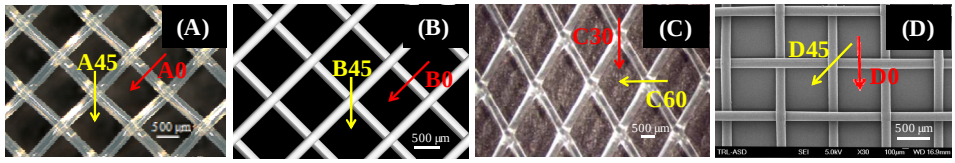

Figure 4.1. Commercial spacers supplied by (A) Fumatech, (C) DelStar (Naltex) and (D) Deukum. (B) is an ideal spacer studied for comparison purposes which does not exist physically. Arrows indicate the different flow directions with respect to the spacer that were investigated.

Only one channel was simulated in each CFD simulation. The geometric construction of the computational domain of spacer-filled channels was based on measurements made by optical microscopy and micrometer; also, the compenetration/compression of filaments were somewhat taken into account in order to reproduce realistic geometries in the simulations (for details see the procedure described in section 2.5.1.1). Table 4.1 summarizes the geometric features of all the spacers investigated, showing also the angle between the main flow direction and the filaments assumed in the simulations. For each spacer two different angles were investigated, as indicated in Figure 4.1 by red and yellow arrows. For the spacers with perpendicular filaments, i.e. Fumatech (A), Deukum (D) and the ideal spacer (B), the flow direction is either parallel to a filament or bisects the angle formed by the filaments; for the DelStar Naltex spacer (C) the flow direction bisects either of the angles formed by the filaments. For convenience, hereafter the test cases studied will be indicated by a letter followed by a number; the letter identifies the spacer (A, B, C or D) while the number specifies the flow incidence angle.

Three different NaCl feed solutions at 25°C were simulated: Feed1 at a concentration equal to 5 M (brine), Feed2 at 0.5 M (seawater) and Feed3 at 0.017 M (river water). The physical properties of the solutions are summarized in Table 2.1.

Fluid flow velocities ranging from 0.1 to 14.3 cm/s were investigated, on the basis of typical residence time and pressure drop constraints on the flow velocities in RED channels. Corresponding values of the Reynolds numbers (defined in Eq. (2.44)) ranged from ~1 to ~125. Notice that the highest value is relevant to the empty channel, as this

configuration allows a higher flow rate for a given pressure drop. The maximum *Re* investigated for the spacer-filled channels is actually ~63.

Some simulations were performed at various current densities in order to investigate the effect of the flux which is not linearly dependent on the concentration gradient, as the transport equation of electrolyte includes a concentration-dependent diffusivity (section 2.5.1.3). Since the non-linearity of the transport equation was shown very weak thus having negligible effects, the subsequent simulations were carried out at a fixed value of the current density (200 A/m^2).

Table 4.1. Geometric features of the spacers investigated and angle between the flow direction and a filament.

Spacer	Configuration	Supplier/ Manufacturer	Filament arrangement	Thickness [μm]	Filament diameter [μm]	Mesh length [μm]	Volume porosity [-]	Angle between filaments [°]	Angle between flow direction and a filament [°]
A	A0 A45	Fumatech	Woven	400	210	1100	0.84	90	0 45
B	B0 B45	(ideal)	Overlapped	400	210	1100	0.84	90	0 45
C	C30 C60	DelStar Naltex	Overlapped	508	312	1960	0.83	60-120	30 60
D	D0 D45	Deukum	Woven	280	148	809	0.85	90	0 45

4.2.2 Governing equations, computational domain and boundary conditions

4.2.2.1 Unit Cell approach

In this chapter the modelling was carried out mainly by following the "main approach" described in section 2.5.1 for defining the computational domain and the boundary conditions. The simulations were carried out on the Unit Cell of the channel, assuming fully developed flow conditions. On the basis of the geometric characterization of the spacers, the computational domains (Unit Cells) were defined as shown in Figure 4.2. The choice of the cell orientation with respect to the spacer wires is largely arbitrary, and is suggested by ease of computational domain build-up. For uniformity, the same Unit

Cell sizes were adopted for the empty channel (not shown in the figure) as for the A and B spacer-filled channels.

The governing equations were the continuity Eq. (2.1), the Navier–Stokes Eqs. (2.36) and the transport Eq. (2.37). The body force per unit volume K_p in Eq. (2.36) was set as the pressure gradient determining the fluid motion. In order to obtain the desired fluid velocity within the channel (w_{ave}), the relationship K_p-w_{ave} was determined by means of preliminary simulations. The source term S depending on the large-scale concentration gradient K_c was implemented in Eq. (2.37). At the upper and lower walls representing the fluid-membrane interfaces a uniform flux of electrolyte was imposed, corresponding to the current density willed according to Eq. (2.42).

The computational domain was discretized by either hexahedral grids for the case of the empty channel or hybrid (hexahedral-tetrahedral) grids for the case of the spacer-filled channels. The use of hybrid meshes was made necessary by the geometrical complexities of the computational domain due to the spacer filaments. However, such grids are mainly composed by hexahedral volumes and contain tetrahedral volumes near the filaments. Details of the hybrid meshes in one half of a cross section are reported in the insets of Figure 4.2.

The grid independence analysis of results was performed for all the channels investigated (not shown for the sake of brevity), thus identifying the suitable meshes for carrying out the simulations whose results are shown and discussed in this chapter. The features of these meshes are summarized in Table 4.2, which also reports the number of control volumes comprised in the channel height H (the number of volumes along a filament diameter is one half of this). Table 4.2 includes also the case of an empty channel.

Table 4.2. Summary of the grids employed.

Unit Cell	Number of cells in height H	Number of cells	% of volume discretized with hexahedral cells
Empty channel	37	~50’000	100
A	22	~500’000	76.0
B	26	~500’000	94.3
C	23	~800’000	78.2

D	28	~1’600’000	76.1

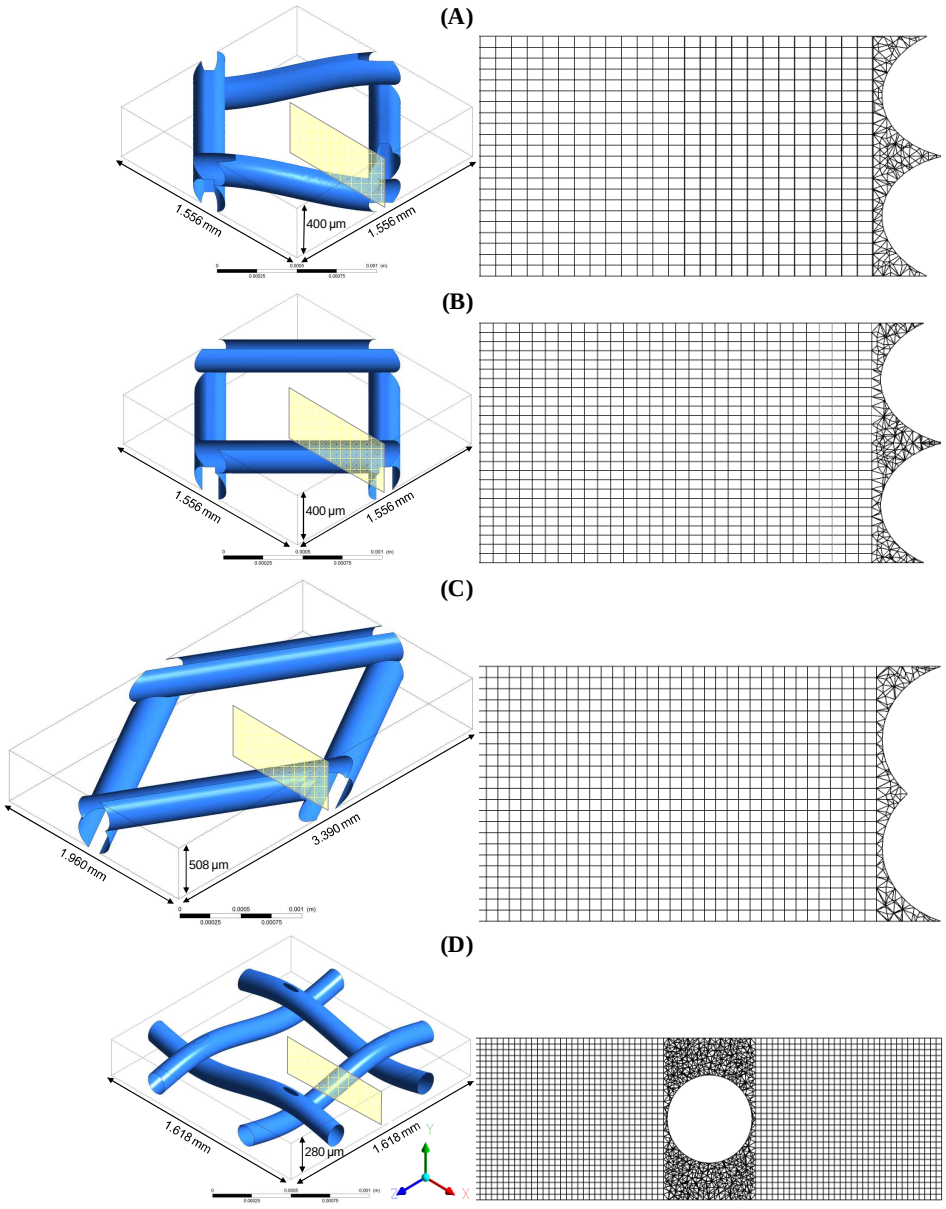

Figure 4.2. Unit Cell geometry for channels filled with spacers (A) through (D). Insets show details of the mesh over one half of a cross section.

4.2.2.2 Multi-Cell approach

A larger domain consisting of a sequence of five *unit cells* along the *z*-direction with Dirichlet inlet conditions and Neumann outlet conditions was also employed aiming at investigating the influence of entry effects (Multi-Cell approach, Figure 4.3). The spacer C30 was used in these simulations. Each Unit Cell of the sequence was discretized by the same number of nodes as in the Unit Cell approach thus resulting in a total number of nodes five times higher.

Boundary conditions were set as in the Unit Cell approach, except for the *inlet* and the *outlet* boundaries, which were set at the beginning and at the end of the sequence of unit cells as fixed flow rate and concentration at the *inlet* and a relative pressure equal to 0 Pa at the *outlet*. Another difference was that in the Multi-Cell approach a variable flux was imposed on the membranes to account for the streamwise variation of the bulk concentration. A correlation akin to the Nernst equation was employed to account for the dependence of the flux on the local concentration:

$$J^{d}_{IEM,MC} = A \ln \frac{C_{ext}}{C_{w}} \tag{4.1}$$

where C_{ext} is the concentration at the external side of the membrane (fixed as uniform concentration), C_w is the local concentration at the membrane-solution interface (wall) and A is a coefficient purposely chosen/set in order to have fluxes similar to those relevant to the Unit Cell simulations for comparison purposes.

The governing equations solved for this domain were the continuity Eq. (2.1), the Navier–Stokes Eqs. (2.2) and the transport Eq. (2.35).

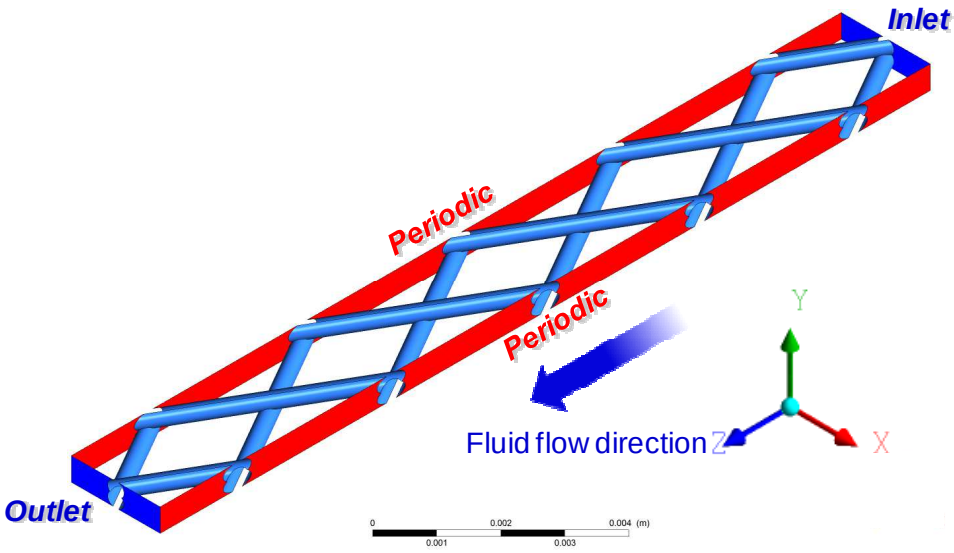

Figure 4.3. Multi-cell domain for the C30 spacer-filled channel.

4.3 Results and discussion

Entry effects are evaluated in section 4.3.1. The influence of several process parameters on concentration polarization phenomena was investigated: feed solution concentration, fluid velocity and current density. Detailed results relevant to a specific configuration (D0) will be presented and discussed in section 4.3.2, while a comparison between the polarization performances of all the configurations investigated will be presented in section 4.4, focusing on the effects of spacer geometry and orientation.

4.3.1 Comparison between Unit Cell and Multi-Cell approach

Some CFD simulations were carried out by adopting the Multi-Cell approach in order to compare the results with those obtained by the Unit Cell approach and assess the importance of entry effects. Among the cases investigated, Figure 4.4 reports results as contours map of the electrolyte flux across the membrane-solution interfaces normalized with respect to the value imposed in the Unit Cell simulation (i.e. $J^d_{IEM,norm} = J^d_{IEM,MC} \big/ J^d_{IEM}$) for the case of the C30 spacer-filled channel fed by Feed2 (seawater) and at w_{ave} = 6.89 cm/s (corresponding to the maximum pressure gradient of 0.1 bar/m within the range here investigated).

As expressed in Eq. (4.1), in the Multi-Cell approach the flux is not assumed to be homogeneous, but it varies depending on the concentration value at the membrane-solution interface. Figure 4.4 shows that the normalized flux does not significantly change from the first to the last cell, i.e. that entry effects are negligible. This is due to two reasons: (i) a very slight decrease of the wall concentration takes place along the *z*-direction; (ii) the logarithmic nature of Eq. (4.1) causes a slight variation of the flux for a given change in wall concentration. These findings highlight the soundness of the simplifying assumption of homogeneous flux imposed in the Unit Cell simulations.

For the same case simulated, Figure 4.5 reports the trends of the normalized flux and the electrolyte concentration at five probe points. It can be observed that entry effects extend over just one cell and they are small and comparable with large-scale trends of the same quantities. Such finding is in accordance with other authors [55, 63], who found a fully developed flow field after a few unit cells.

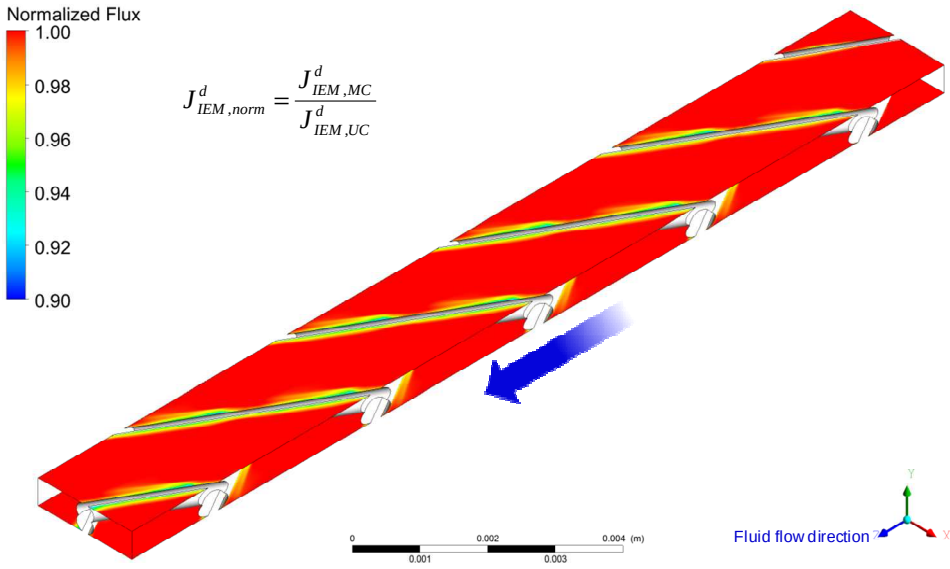

Figure 4.4. Flux at membrane-solution interfaces predicted using the Multi-Cell approach and normalized by the flux imposed on a corresponding Unit Cell domain. C30 spacer-filled channel fed by Feed2 (seawater) at a velocity w_{ave} = 6.89 cm/s (*Re* = 63) and a current density i = 200 A/m^2.

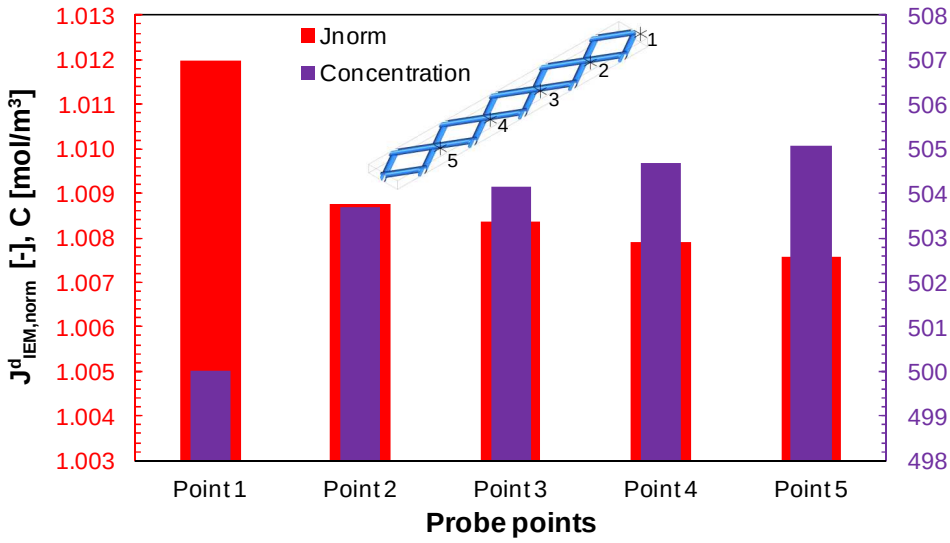

Figure 4.5. Normalized flux and concentration at five probe points within the C30 spacer-filled channel fed by Feed2 (seawater) at velocity w_{ave} = 6.89 cm/s (*Re* = 63) and a current density i = 200 A/m^2.

4.3.2 Influence of feed concentration, velocity and current density on polarization phenomena

An example of the concentration field is reported in Figure 4.6 for the case of the diluted channel fed by Feed3 (0.017 M river water) in a D0 spacer-filled channel, a case purposely chosen the better to visualize polarization phenomena. The quantity shown is the "true" (non-periodic) concentration, i.e. $C = \tilde{C} + K_c z$. Different planes are considered: (a) an *x*-*z* plane located midway between the two membranes, (b) *y*-*z* planes, (c) *x*-*y* planes and (d) the planes representing membrane-solution interfaces (walls).

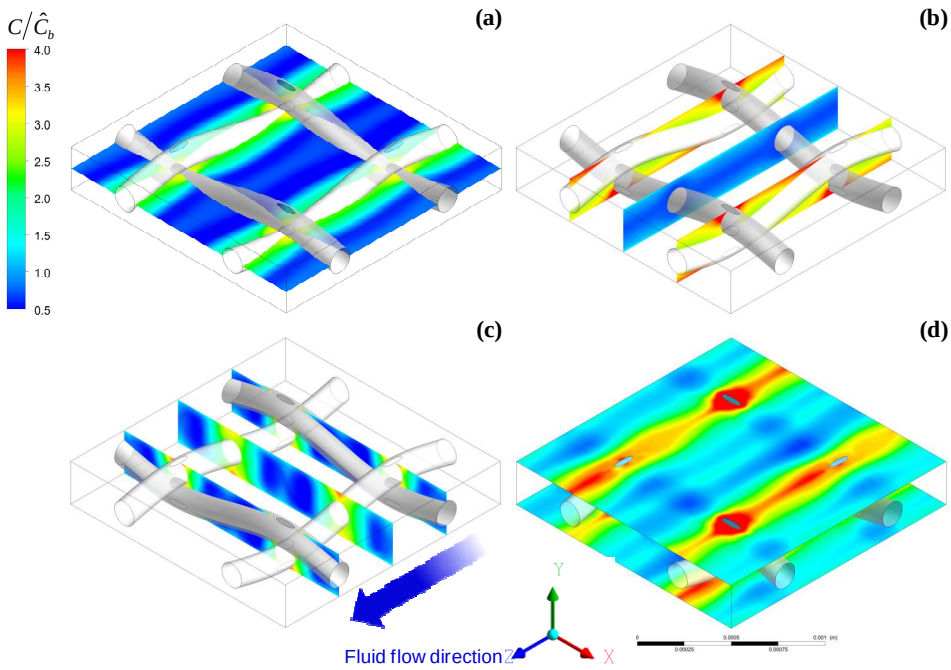

Figure 4.6. Normalized concentration maps on (a) *x*-*z* midplane, (b) *y*-*z* planes, (c) *x*-*y* planes and (d) membrane-solution interfaces for the D0 spacer-filled channel fed by Feed3 (0.017 M river water) at w_{ave} = 1.53 cm/s (*Re* = 8), i = 60 A/m^2.

The figure shows that (i) the presence of the spacer affects the concentration field, (ii) the change of concentration along the main flow direction is negligible, and (iii) the variation of concentration between the central part of the channel and the fluid-membrane interfaces is prominent (i.e., high concentration polarization): compare, for example, the midplane distribution in graph (a) with the wall distribution in graph (d).

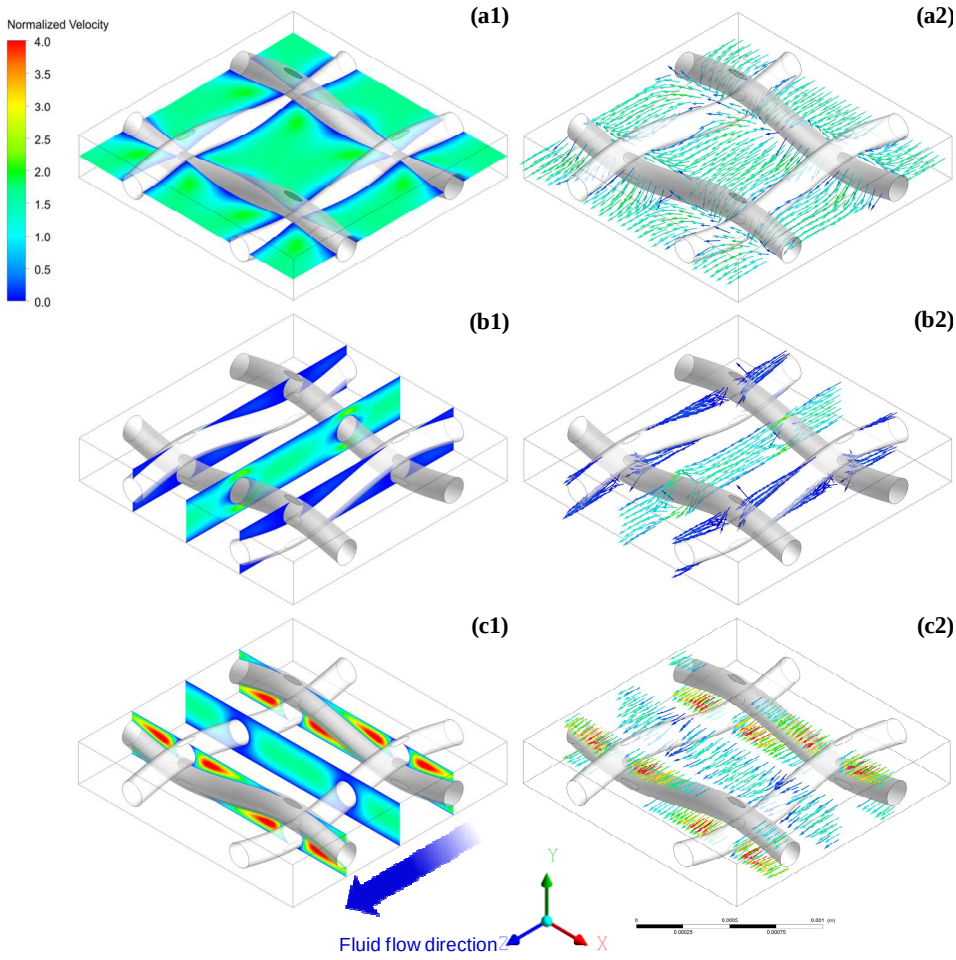

Figure 4.7. Normalized velocity maps and corresponding vector plots on (a) *x*-*z* midplane, (b) *y*-*z* planes and (c) *x*-*y* planes for the D0 spacer-filled channel at w_{ave} = 1.53 cm/s (*Re* = 8).

Velocity maps and vector plots on the same planes of Figure 4.6 are reported in Figure 4.7. As it can be seen, the presence of the spacer wires reduces the section for the passage of the fluid thus resulting in a local increase of the velocity (Figure 4.7-c1). Conversely, low velocity gradients can be observed far from the filaments and domain boundaries in accordance with the low Reynolds number laminar flow regime. Velocity vector plots show that velocity components perpendicular to the membranes are present near the filaments orthogonal to the main fluid flow direction (Figure 4.7-a2,b2). Low velocities with no components perpendicular to the membrane are observed near the

longitudinal filaments, thus resulting in the maximum polarization areas (Figure 4.7d). Velocity vector plots of Figure 4.7-a2,b2 indicate a symmetric flow field without any fluid detachment downstream of the orthogonal filaments, thus confirming the existence of a creeping flow regime.

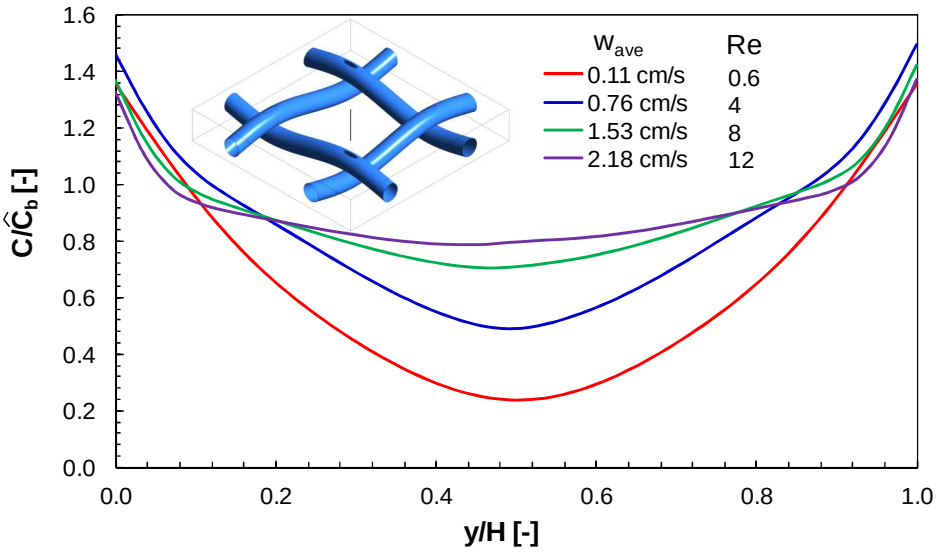

Figure 4.8. Normalized electrolyte concentration profiles along a monitoring line perpendicular to the membranes and placed in the centre of the cell for the case of the D0 spacer-filled channel fed by Feed3 (0.017 M river water) at various mean flow velocities and i = 60A/m^2. Here, y/H represents the y-coordinate normalized by the channel thickness H.

Polarization depends on both mean and local velocities. A first example of the effect of fluid velocity on concentration polarization is provided by Figure 4.8, where the normalized concentration profiles along a line perpendicular to the membranes and placed in the centre of the Unit Cell are shown at different mean fluid velocities. As expected, the mixing enhancement due to the increasing Reynolds number tends to reduce concentration gradients between bulk and membranes.

Figure 4.9 reports the mass transfer coefficient (defined as the ratio between the diffusive flux at the membrane-solution interface, and the wall – to – bulk concentration difference, as a function of the mean fluid velocity for the three feeds. The figure shows that this quantity increases significantly with the flow rate. The fact that the curves at

various current densities (and thus at various fluxes) are practically identical means that the non-linearity of the transport equation, due to the corrective term of the diffusivity depending on the electrolyte concentration, has only minimal effects. In fact, the corrective term of the diffusion coefficient exhibits only small variations within the domain, due to (i) the weak functional dependence on the concentration and (ii) the slight changes of concentration caused by the typical fluxes (current densities) of these systems. As a consequence, the diffusivity correction is found to vary by less than 1%. Curves vary little also with the electrolyte composition; in particular, curves for Feed2 (0.5 M seawater) and Feed3 (0.017 M river water) are almost identical, while only the curve relative to Feed1 (5 M brine) is slightly different (in particular, it starts from a higher value at low flow speed) because of the significantly different physical properties of this solution (e.g. liquid viscosity, Table 2.1).

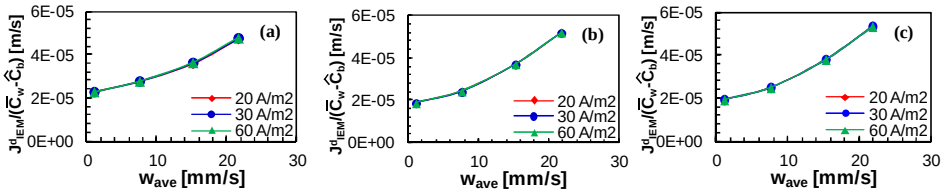

Figure 4.9. Ratio $J_{IEM}^{d}\Big/\left(\overline{C}_w-\hat{C}_b\right)$ as a function of fluid velocity for the D0 spacer-filled channel fed by (a) Feed1 (5 M brine), (b) Feed2 (0.5 M seawater) and (c) Feed3 (0.017 M river water) at various current densities.

In accordance with the Nernst equation, in Reverse Electrodialysis systems, (as better discussed below), the driving force of the process depends on the ratio (and not on the difference) of the concentrations of the two solutions in contact with the membrane. Therefore, notwithstanding very similar values of $\overline{C}_w-\hat{C}_b$ were found for the three feed concentrations, these led to very different effects on driving force. In this regard, it is useful to employ the polarization factor as defined in Eqs. (2.53) and (2.54) to quantify polarization phenomena effect. Figure 4.10 shows the polarization factor as a function of the mean fluid velocity along the main flow direction. The polarization factor is always close to one (θ > 0.96) when either Feed1 (5 M brine) or Feed2 (0.5 M seawater) are simulated, whereas it is significantly lower ($\theta \approx 0.5 \div 0.9$) for the case of Feed3 (0.017 M

river water). Therefore, at a given flow rate and current density, the higher the mean concentration of the feed solution, the higher the polarization factor. Also, the higher the current density (i.e. the higher the flux imposed at the membranes), the lower the value of θ, although such a dependence is crucial only in the case of Feed3 (0.017 M river water). Eventually, Figure 4.10 shows that a higher flow rate of the feed solution corresponds to an enhanced mixing within the channel leading polarization phenomena to decrease. The present findings confirm that polarization phenomena can be reduced by carefully optimizing the fluid dynamics within the stack.

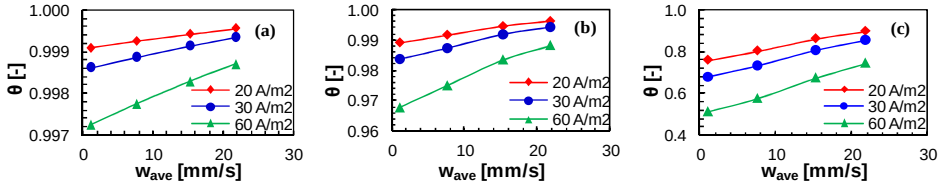

Figure 4.10. Polarization factor as a function of fluid velocity for the D0 spacer-filled channel fed by (a) Feed1 (5 M brine), (b) Feed2 (0.5 M seawater) and (c) Feed3 (0.017 M river water) at various current densities.

The cell potential available in actual operating conditions is lower than the open circuit voltage. Following Vermaas et al. [14], the potential drop across a cell pair can be written as the sum of Ohmic resistances and two non-Ohmic voltage drops, as expressed by Eq. (1.3). Therefore the quantity $E_{OCV} - \eta_{BL}$ indicates how much polarization phenomena affect the obtainable potential by reducing E_{OCV}.

For the case of a monovalent binary electrolyte, considering the standard Nernst equation and assuming that the mean activity on the two interfaces of a channel are equal, this "corrected" potential in a cell pair can be estimated as:

$$E_{OCV} - \eta_{BL} = 2\alpha_m \frac{RT}{F}\left[\ln\left(\frac{\hat{C}_b^{conc}}{\hat{C}_b^{dil}}\right) + \ln\left(\theta^{conc}\theta^{dil}\right) + \ln\left(\frac{\overline{\gamma}_w^{conc}}{\overline{\gamma}_w^{dil}}\right)\right] \tag{4.2}$$

where α_m is the mean permselectivity of the ionic exchange membranes, $\hat{C}_b$ is the bulk concentration of the electrolyte, $\overline{\gamma}_w$ is the activity coefficient averaged over the plane

corresponding to the membrane-solution interface, θ is the polarization factor as defined by Eqs. (2.53) and (2.54), the superscripts *conc* and *dil* refer to the concentrated and diluted channel respectively.

Figure 4.11a reports as functions of the average fluid velocity w_{ave} the quantity $E_{OCV} - \eta_{BL}$, calculated by Eq. (4.2), for the D0 spacer, i = 60 A/m^2 and two electrolyte couples: (i) Feed1-Feed2 (brine-seawater, *BS*) and (ii) Feed2-Feed3 (seawater-river water, *SR*). The mean permselectivities were assumed to be $\alpha_{m,BS}$ = 0.775 and $\alpha_{m,SR}$ = 0.96 [124] and the temperature T = 298 K. The activity coefficients are calculated on the basis of the Pitzer equation [138]. The uncorrected E_{OCV} is also reported for comparison purposes and, of course, does not vary with w_{ave}. These results show that (i) E_{OCV} is larger for *SR* than for *BS*; (ii) the voltage drop η_{BL} due to polarization effects is larger for *SR* than for *BS*; and (iii) the corrected voltage over a cell pair $E_{OCV} - \eta_{BL}$ is higher for *SR* than for *BS* (up to 25% in the range of w_{ave} investigated). This is due to the higher bulk concentrations ratio and mean permselectivity for *SR* conditions. On the other hand, however, the term $\ln\left(\overline{\gamma}_w^{conc} / \overline{\gamma}_w^{dil}\right)$ corresponds to a potential enhancement only in the case of *BS* conditions, where there is also a negligible effect of polarization phenomena, while it represents a detrimental contribution for *SR* conditions. Finally, it should be stressed that higher power densities are obtained under *BS* conditions because of the much lower resistance of the dilute solution, as confirmed by results obtained by multi-scale modelling simulation [115].

Although quantitative comparisons with experimental data are not currently possible, it may be interesting to compare the present results on a qualitative and order-of-magnitude basis with chronopotentiometry results obtained by Vermaas et al. for similar solutions, geometries and spacers [21]. For example, for the *SR* electrolyte couple flowing in channels of height H = 200 μm equipped with commercial Sefar 03-300/51 net spacers, Vermaas et al. report a boundary layer areal resistance of ~7.5 Ω cm^2 at w_{ave} = 5 mm/s and ~5 Ω cm^2 at w_{ave} = 20 mm/s. Figure 4.11a shows that the boundary layer voltage drop η_{BL} for the *SR* couple in channels of a similar height (H=280 μm) equipped with comparable D0 spacers under a current density i=60 A/m^2 is ~0.03 V at w_{ave} = 5 mm/s and ~0.015 V at w_{ave} = 20 mm/s. The corresponding R_{BL} are 5 Ω cm^2 and 2.5 Ω cm^2, respectively, values which are at least of the correct order of magnitude.

A boundary layer efficiency can be defined as

$$\chi_{BL} = \frac{E_{OCV} - \eta_{BL}}{E_{OCV}} = \frac{\ln\left(\frac{\hat{C}_b^{conc}}{\hat{C}_b^{dil}}\right) + \ln\left(\theta^{conc}\theta^{dil}\right) + \ln\left(\frac{\overline{\gamma}_w^{conc}}{\overline{\gamma}_w^{dil}}\right)}{\ln\left(\frac{\hat{C}_b^{conc}}{\hat{C}_b^{dil}}\right) + \ln\left(\frac{\overline{\gamma}_w^{conc}}{\overline{\gamma}_w^{dil}}\right)} \tag{4.3}$$

and is plotted in Figure 4.11b as a function of w_{ave} for the same cases. The relative reduction of E_{OCV} is negligible for *BS* at all the flow rates considered, while for *SR*, in which the low Feed3 concentration (0.017 M) is present on the diluate side, there is a significant reduction of the voltage (up to ~25%); the beneficial effect of raising the flow velocity is evident for this case. Of course, since the physico-chemical parameters of the various solutions do not differ significantly, a larger relative importance of polarization (i.e., a low χ_{BL}) for dilute solutions is to be expected.

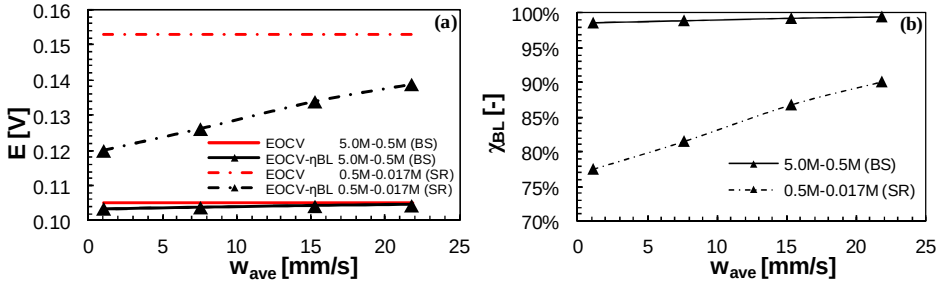

Figure 4.11. D0 spacer filled channel under Feed1-Feed2 (5 M brine-0.5 M seawater) and Feed2-Feed3 (0.5 M seawater-0.017 M river water) conditions at a current density i = 60 A/m^2. (a) open circuit voltage (uncorrected and corrected for polarization effects); (b) boundary layer efficiency.

4.4 Comparison of different spacer geometries

The effect of spacer geometry and orientation on polarization phenomena was also investigated. As an example, Figure 4.12 shows concentration contours over the Unit Cell boundaries for all the configurations investigated here having Feed2 (0.5 M seawater) as the dilute solution at a current density of 200 A/m^2. All cases are characterized by a pressure drop per unit length of 0.01 bar/m (imposed term K_p in Eq.

(2.36)), but differ in the mean flow speed w_{ave} and in the bulk Reynolds number *Re* due to the different geometry. Values of w_{ave} and *Re* are indicated besides each figure.
This figure shows that (i) the presence of the spacer strongly modify the concentration field compared to the spacer-less channel; (ii) not only the spacer geometry, but also its orientation can lead to completely different concentration fields; (iii) polarization is higher near the spacer wires where fluid velocities are allegedly lower; (iv) an angle of 45° between the spacer wires and the main fluid flow direction seems to provide lower concentration polarization.

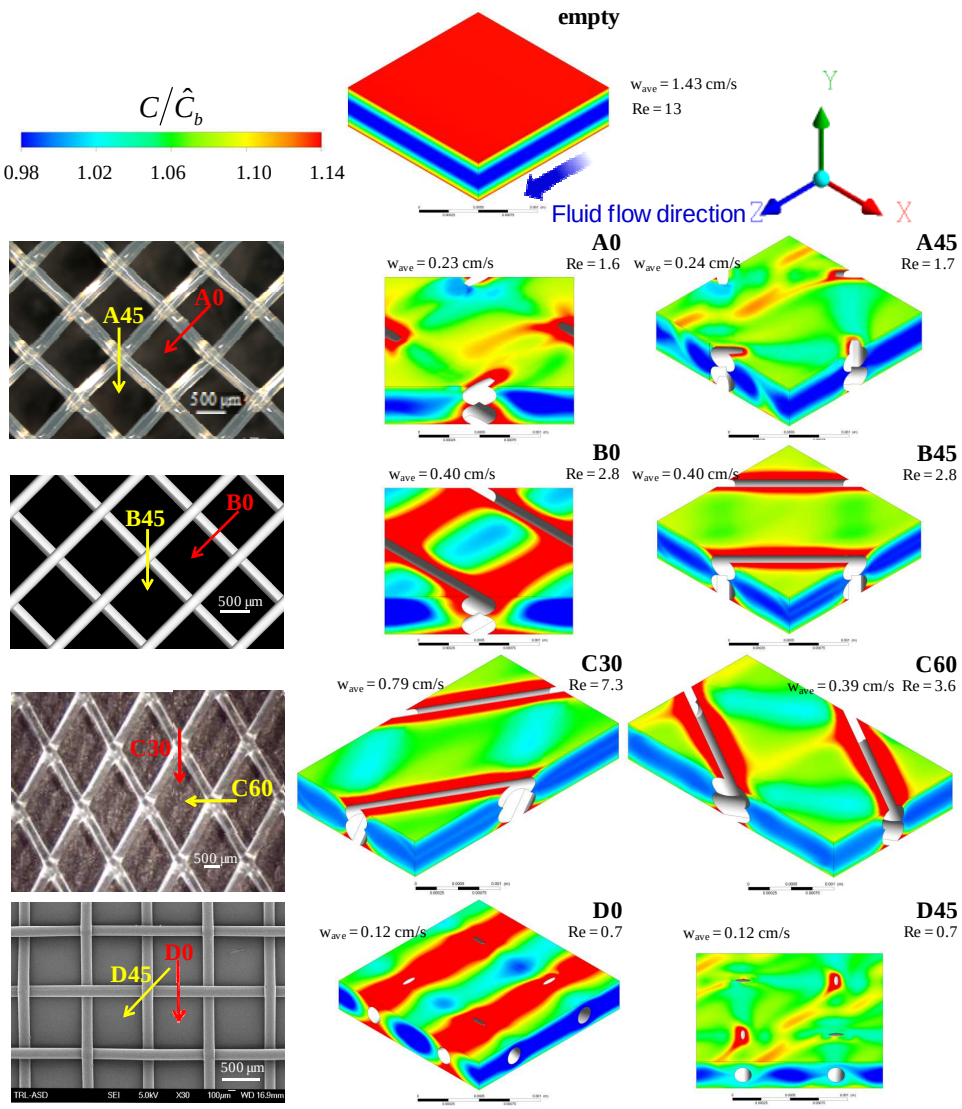

Figure 4.12. Normalized concentration distribution for empty channel, A0, A45, B0, B45, C30, C60, D0 and D45 spacer-filled channels fed by Feed2 (0.5 M seawater) at a current density i = 200 A/m^2 and a pressure drop per unit length K_p = 0.01 bar/m. The Reynolds numbers and mean fluid speed obtained are indicated besides each image.

The dependence of the Fanning friction factor on the Reynolds number was studied in order to better characterize the fluid dynamic behaviour of the spacer-filled channels under investigation. The friction factor is defined in Eq. (2.45). Results are reported in

Figure 4.13. Clearly, the inclusion of any spacer leads the friction factor to strongly increase with respect to the spacer-less channel. No effect of the spacer orientation on the *f-Re* trend was found for the spacers A, B and D, whose angle between subsequent filaments is 90°. In this regard, Shakaib et al. [63] found a difference of 12% in the pressure drops provided by two different orientation of a diamond spacer for Reynolds numbers quite higher than those investigated in the present work.

A different behaviour is exhibited by the two orientations of the spacer C whose angles between the filaments are of 60°-120°: the C30 orientation provided pressure losses far lower (about one half) than the configuration C60, because (i) in the C30 configuration the fluid encounters fewer filaments per unit length, and (ii) the lower angle between the main flow direction and the filaments results in a lower resistance to the flow [62]. We found a comparable behaviour in experiments involving similar but larger-scale spacers for membrane distillation [137]. Similar experimental findings were also reported by Da Costa et al. [139]. This large difference in pressure drops would have significant impact on the choice of the spacer orientation in commercial RED applications.

As far as the comparison of the different spacers is concerned, the woven arrangement provides higher pressure drops than the overlapped one (see spacer A and B). Fumatech and Deukum spacers (A and D respectively) have similar geometrical features, in particular they are woven spacers with a ratio mesh length/spacer length so similar that an analogous dependence of f on Re was found. Notwithstanding the spacer C60 is characterized by overlapped wires, it provides Fanning factors comparable to those provided by the woven spacers A and D. Conversely, the other configuration of the same spacer (i.e. C30) guarantees pressure losses lower than those provided by spacer B.

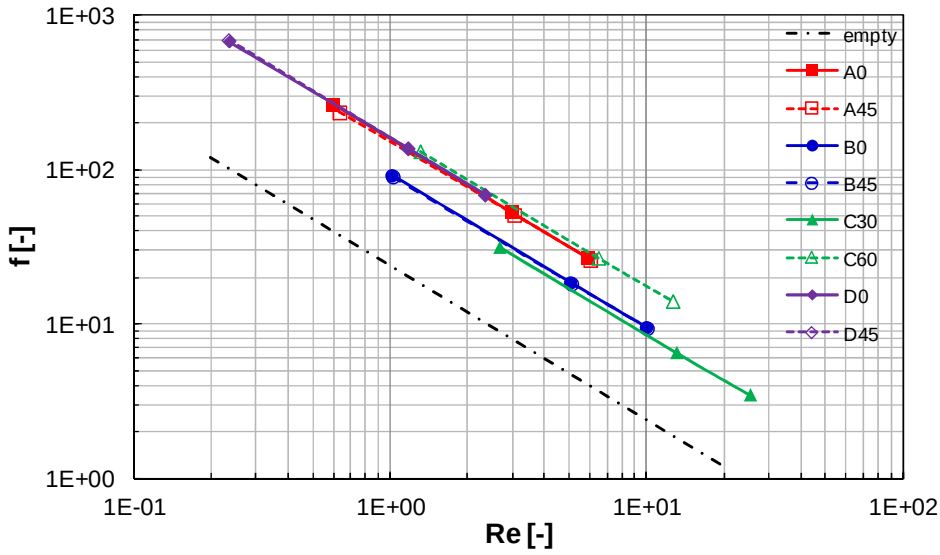

Figure 4.13. Fanning friction factor as a function of Reynolds number for all channels investigated, fed by Feed1.

Notably, for all the spacer-filled channels investigated *f* roughly shows a Re^{-1} trend, thus confirming the existence of a self-similar flow regime (creeping flow), at least at the lowest Reynolds numbers. Only at the highest *Re* (e.g. spacer C) some discrepancies from this trend can be observed. This occurrence is not due to turbulence (the Reynolds number is far too low for that, and the present numerical solutions gave perfectly steady-state results), but to a loss of self-similarity of the fluid flow field: the presence of the spacer causes secondary flows in the cross section of the channel whose relative intensity increases with the flow rate. Such hypothesis is supported by evidence reported in Figure 4.14, where quite different normalized velocity distributions can be observed at two different Reynolds numbers for the case of the spacer configuration C30. This is the reason why a tenfold increase in the pressure drop per unit length leads to a slightly lower (~ninefold) increase in mean flow speed and Reynolds number (this last from 7.3 to 63.3), showing that the pressure drop increases more than linearly with the flow rate.

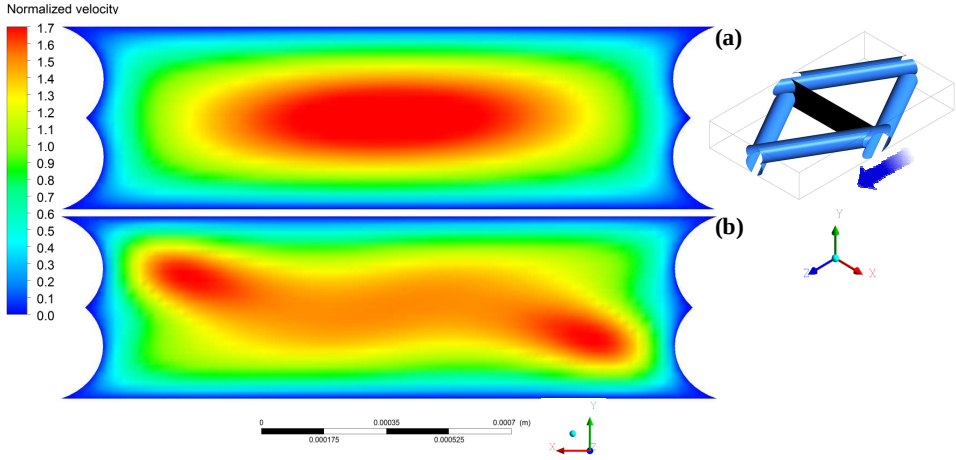

Figure 4.14. Normalized velocity maps on the *x-y* middle plane, for the C30 spacer-filled channel fed by Feed2 at a pressure drop per unit length (a) K_p = 0.01 bar/m (*Re* = 7.3, w_{ave} = 0.79 cm/s) and (b) K_p = 0.1 bar/m (*Re* = 63.3, w_{ave} = 6.89 cm/s).

A quantitative comparison among the cases investigated in terms of concentration polarization is shown in Figure 4.15 which reports the polarization factor as a function of the Reynolds number. It show all the channel configurations fed by Feed1 (5 M brine) or Feed2 (0.5 M seawater) at a current density of 200 A/m^2. In the empty channel θ is constant with *Re*, because the flow is perfectly steady and parallel so that mixing does not occur and only the *z*-component of velocity is present. Conversely, as expected, a performance enhancement can be observed as *Re* increases (i.e. as inertial terms overcome viscous ones) when a spacer is included within the channel: its presence produces velocity components perpendicular to the membrane surfaces, whose relative importance increases as the flow rate increases. Results of Figure 4.15 confirm what reported in literature on diamond spacers with overlapped filaments: (i) for the spacer B a mass transfer enhancement is obtained when the fluid flow direction bisects the angle between the filaments [63]; (ii) the configuration C60 leads to an improved mixing with respect to the configuration C30 [139].

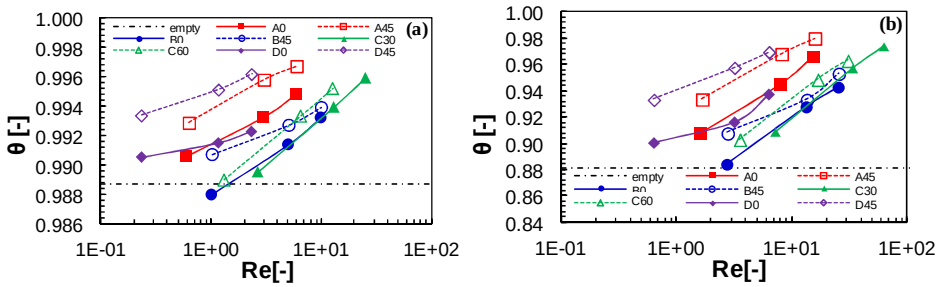

Figure 4.15. Polarization factor as a function of the Reynolds number for all channels investigated, fed by (a) Feed1 (5 M brine) and (b) Feed2 (0.5 M seawater) at a current density i = 200 A/m^2.

However, referring to the pumping power consumption necessary to achieve a certain θ value is the best way to suitably compare the various spacer performance and infer the process efficiency. In order to quantify such efficiency, various authors have adopted a dimensionless power number Pn [54, 62, 140] defined in Eq. (2.46). The polarization factor θ as a function of the power number Pn for the investigated spacers is reported in Figure 4.16. Clearly, high θ with low Pn is the preferable condition. Notably, this figure concerns only Feed1 (5 M brine) and Feed2 (0.5 M seawater). Feed3 (0.017 M river water) is not reported for brevity since very similar considerations can be inferred for the three feeds.

By comparing Figure 4.13 with Figure 4.16 some considerations can be made: notwithstanding the spacer orientation does not provide substantial differences in pressure drops (see spacers A, B and D) on the one hand, on the other hand it leads to very different polarization factors. In particular, spacer configurations with the flow attack angle of 0° provide θ lower than those obtainable in the corresponding 45° configurations. This occurs because convection perpendicularly to the membranes is disadvantaged when the fluid is parallel to a filament array. Such findings are in accordance with those by Li et al. [54] and Shakaib et al. [63], although they studied only overlapped spacer at Pn values quite higher (>10^5) than those investigated in the present work. As far as the filament array arrangement is concerned, results show that the woven spacers guarantee θ higher than the overlapped ones at a given Pn value. This is not surprising since at the lowest flow rates investigated, the woven arrangement forces the whole fluid volume to move up and down continuously thus (i) providing

significant velocity components perpendicular to the membranes and (ii) avoiding the presence of stagnant zones. Conversely, the overlapped arrangement at the lowest Reynolds numbers investigated here does not provide an efficient mixing since a part of the fluid move along the longitudinal filaments without practically encountering any obstacles, while many calm zones take place between the filaments perpendicular to the main flow direction. This occurrence explains why polarization factors lower than the one relevant to the empty channel can be obtained at the lowest flow rates. As regards spacer C, being an overlapped spacer it generally provides low θ values. When the two different orientations of this spacer are compared, one may observe that the higher pressure drops provided by C60 (Figure 4.13) at any given *Re* are counterbalanced by the higher θ (Figure 4.15).

Finally, results of Figure 4.16 confirm that polarization effect is negligible when Feed1 (brine) is flowing in the channel even at very high current densities and low flow rates. In the case of Feed2 (seawater), concentration polarization effect is still very low but of higher significance, while for less concentrated solutions it can play a key role (see Figure 4.10). These findings suggest that, when concentrated solutions are adopted, the channel geometry should be optimized taking into account other aspects such as pressure drop, residence time, electrical resistance, etc. Conversely, when diluted solutions are employed, a proper attention should be paid to polarization phenomena effects which can dramatically affect the driving force and thus the efficiency of the process. In such cases, a woven arrangement and a flow attack angle of 45° appears to be the best performing configuration for a spacer-filled channel in high efficiency (high current densities) RED applications, among those presently investigated.

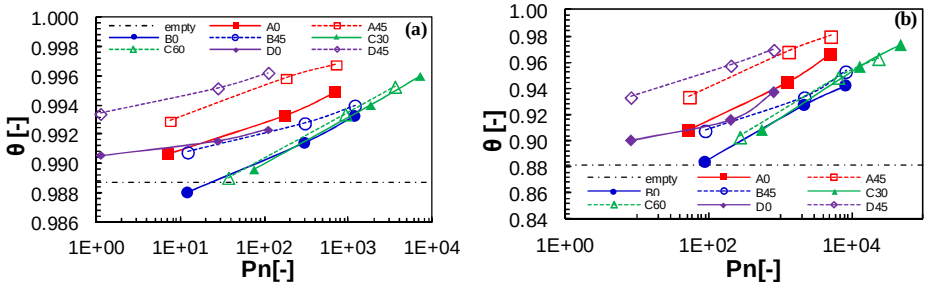

Figure 4.16. Polarization factor as a function of pressure drop for all channels investigated, fed by (a) Feed1 and (b) Feed2 at a current density i = 200 A/m^2.

4.5 Conclusions

The CFD model developed in this thesis (described in chapter 2) was employed in order to study concentration polarization phenomena in reverse electrodialysis channels equipped with net spacers. A transport equation suitable also for concentrated solutions was implemented in the CFD code to analyse the electrolyte transport. Two different simulation approaches were adopted: the less computationally demanding Unit Cell approach based on inlet-outlet periodicity of velocity, pressure and electrolyte concentration, valid for fully developed conditions, and the Multi-Cell approach consisting in simulating five consecutive Unit Cells along the main flow direction and imposing standard inlet-outlet boundary conditions. This latter approach (i) highlighted that entry effects are small and are confined to the first unit cell and (ii) showed the reliability of the simplifying assumption of homogeneous flux imposed in the Unit Cell simulations; therefore most CFD simulations were carried out by adopting the Unit Cell approach.

The dependence of polarization phenomena on various parameters was thoroughly addressed:

- Polarization phenomena are slightly affected by the solution features (Schmidt number), but polarization *effects* greatly decrease as the solution concentration increases, as the voltage established over the membrane depends on the *ratio* of the solutions concentrations. In particular, they are important for river water, barely significant for seawater, and practically negligible for brine.
- The higher the current density imposed, the lower the polarization factor θ (i.e. the higher the polarization effects). However, even at high current densities stacks fed by brine and seawater do not exhibit significant polarization effects (especially on the brine side).
- The diffusivity correction varies by less than 1%, because the functional dependence on the concentration is weak and the variation of the concentration within the domain is relatively limited, due to the electrolyte fluxes normally involved. Hence, the non-linearity of the transport equation was shown to be weak and to have negligible effects.
- Although the fluid flow regime was laminar for all cases investigated, fluid flow was found to strongly affect polarization phenomena. This is due to the

non-similarity of the flow field at the various flow rates and to the presence of velocity components perpendicular to the membranes. Factors promoting fluid mixing within the channel (e.g. the presence of a net spacer and the increase of feed flow rate) were found to enhance the polarization factor, although, on the other hand, they also lead to increased pressure drops. Of course, no effect of flow rate on polarization phenomena was observed for the empty channel where no velocity component perpendicular to the membrane is present.

- As regards the spacer configuration, for the flow rates range investigated here, spacers with woven arrays of filaments were found to provide higher θ at any given normalized pumping power Pn with respect to overlapped arrays. In spacers with wires at 90°, for any wire arrangement a flow attack angle of 45° results in more efficient mixing compared to the 0° case. Different angles between the filaments do not provide different $\theta - Pn$ trends.

Finally, on the basis of all these findings it is worth observing that for the concentrated solutions feeds investigated here (which represent seawater and brine), where concentration polarization effects do not appear to be crucial, other factors should drive the optimization strategy, such as the influence of channel thickness and geometry on the compartment Ohmic resistance, the pressure drop, the plugging potential within the channel and the residence time in the stack.

A limitation of the results presented here is that – for the time being – they lack a proper validation against experimental data. Unfortunately, the current state of the art in reverse electrodialysis experiments is not such that a quantitative validation of simulation results like the present ones can be hoped for. This is partly due to this being a young field: the resources dedicated to it so far are not very large, and often the investigators have focused on general system performance and not on individual effects such as concentration polarization. Polarization losses are inevitably superimposed to (often larger) Ohmic losses both in the fluids and in the membranes and to other sources of irreversibility, which makes their assessment a difficult task requiring focused investigations. Hopefully, these will become available in the near future.

All the results and conclusions presented should be regarded as a way to obtain some important preliminary insights on the optimization of RED systems (including also fluid

dynamics and mass transfer aspects), while a more thorough study on the spacer configuration is reported in the next chapter.

5 PARAMETRIC ANALYSIS OF WOVEN AND NON-WOVEN SPACER-FILLED CHANNELS

Abstract

Concentration polarization phenomena and pressure drop affect strongly the power output obtainable through reverse electrodialysis (RED); therefore the channel geometry is a fundamental operating parameter for the system optimization. Woven spacers are commonly commercialised and adopted for RED experiments, and exhibit some potential benefits, such as better mixing and lower shadow effect; however, they are not suitably investigated in literature so far.

In this chapter, CFD simulations were carried out to predict fluid flow and mass transfer in spacer-filled channels for RED applications. The modelling approach is based on a transport equation obtained from the rigorous Stefan–Maxwell equation along with the assumptions of binary electrolyte and local electroneutrality. Periodic boundary conditions were adopted to simulate a fully developed flow.

A parametric analysis for different spacer geometries was carried out: woven (*w*) and non-woven (overlapped, *o*) spacers with filaments at 90° were simulated, with different pitch to height ratios (*l*/*h*), at various Reynolds numbers typical of RED channels, and with two different orientations (α0 and α45).

Simulation results show how the parameters investigated influence flow field, pressure drop and mass transfer, thus suggesting the features that a spacer should have in order to obtain high process performance. The spacer causes (i) velocity components perpendicular to the main flow direction, but also (ii) calm regions with poor mixing in proximity of the filaments. As a consequence, the spacer-filled channels can have higher concentration polarization (less mixing) at low flow rates than the empty channel, despite the pressure drop are higher (till to ~20 times). Only the configuration *w*-α45 has features that avoid the presence of the poorly mixed zones near the wires.

The filament arrangement was found to be a crucial feature, as the *w*-spacers established flow fields fully different, raising pressure drop, but also enhancing mixing. Moreover, higher Sherwood numbers for any given pumping power were obtained for the *w*-arrangement. The effects of flow attack angle and filament spacing are more complex as the Reynolds number varies and are different for the two filament arrangements.

However, among the cases investigated here, the configuration that provides the best mixing conditions is *w-l/h2-α45*, both for any given Reynolds number and pumping power.

5.1 Introduction

The channel configuration is a prominent feature of a RED stack for fluid dynamics and mass transfer, and thus for the net power achievable. The flow and the concentration fields within the channel determine distributed pressure drop and concentration polarization phenomena. Therefore the channel geometry has a significant influence on the pumping power consumption and on the boundary layer resistance, as argued in chapter 1.

Woven spacers are commonly used in the experimental campaigns for RED applications (section 1.4.2 reports several examples). With respect to spacers with overlapped filaments, woven spacers reduce the shadow effect on the membrane; moreover, the woven arrangement appears to be more suitable in promoting mixing, as shown in the simulations in chapter 4 that provide some preliminary important insights on the spacers performance. On the other hand, in the wide literature pertinent the study of fluid flow, pressure drop and mass transfer in spacer-filled channels for membrane processes, the investigation of woven spacers is not addressed. The only example found in the literature is by Li et al. [55], where also two commercial spacers with woven filaments are analysed in experimental tests. However, no CFD modelling has been performed so far on this kind of geometries.

In this chapter, 3D CFD simulations of channels with woven and non-woven spacers for RED applications are carried out. Fluid flow and mass transfer are predicted through the CFD modelling tool described in chapter 2, based on the Stefan–Maxwell equation and on the Unit Cell approach. The aim of the study is the channel geometry optimization in the suitable range of Reynolds numbers (*Re*) for RED, by means of the performance characterization of some kinds of spacers, including those ones poorly investigated with woven filaments. A parametric analysis was performed in the numerical simulations, by varying the wires arrangement, the pitch to height ratio, the channel orientation and *Re* in spacers with crossing filaments arranged at 90°.

5.2 CFD modelling

5.2.1 Systems under investigation

A net spacer can be made by a variety of geometries on the basis of: filament shape/arrangement, angle between crossing filaments, number of layers, filament spacing and filament size. Other features as deformability and wettability are related to the material. Also, fluid dynamics and mass transfer within a spacer-filled channel depends strongly on the flow attack angle, i.e. the relative orientation of the spacer with respect to the main flow direction.

The cases investigated in this work, are spacers diamond-type with: angle between crossing filaments of 90°, circular cross-section of filaments, equal spacing and size for the two filaments. With regard to the wires arrangement, woven and non-woven (overlapped) spacers are simulated; in particular, woven spacers are commonly adopted but not suitably investigated in literature. The geometrical features which identify the two kind of spacers simulated are the distance between two not-crossing filaments (l) and the height of the channel (h), or more simply the ratio l/h. Three different values were simulated: l/h = 2, 3, 4. The channel height was h = 0.306 mm.

A single channel was simulated in each CFD simulation. In order to reproduce geometries similar to those of commercial spacers, in the simulations the features of compenetration/compression of the filaments were taken into account as described in section 2.5.1.1.

Two different flow attack angles (α) were investigated: the flow direction is either parallel to a filament (α = 0°) or bisects the angle formed by the filaments (α = 45°). Figure 5.1 shows an example of real spacers with overlapped and woven wires at 90°, also indicating the mesh length and the main flow direction.

The parametric analysis was carried out for four values of Reynolds number (Eq. (2.44)): Re = 1, 4, 16, 64. This represents a quite wide range, since the maximum Re investigated here is relatively high for the thin channels typical of RED stacks. For example, for a channel 500 μm thick this corresponds to a superficial velocity of about 6 cm/s.

Summarizing, the parametric analysis was carried out in spacers with crossing filaments at 90° for two wire arrangements (woven and non-woven spacers), three pitch to height ratio, two flow attack angles, and four Re. All cases investigated are reported in Table 5.1. For convenience, each case studied is identified by a code where the first letter

indicates the overlapped (*o*) or woven (*w*) arrangement of filaments, and *l/h* and *α* are reported with their respective values.

In the case *o-α0*, the vertical plane parallel to the main flow direction is a symmetry plane. For all the other channel configurations, this is an antisymmetry plane. In laminar regime these features are reflected on the flow and concentration fields. Imagining the domain divided in two part by the said plain, in the case *o-α0* the fields in one half of the domain are obtained by rotating the other half around a central vertical axis; while in the other cases the fields in one half of the domain are obtained by rotating the other half around a central axis parallel to the main flow direction.

The effect of the Schmidt number (*Sc*) on the Sherwood number (*Sh*) was shown to be weak for NaCl solutions in chapter 4. Moreover, at high concentrations the polarization effects are not significant, thus it is not important to know the exact value of *Sh*. Therefore, here the fluid simulated is only the Feed2, i.e. an aqueous solution of NaCl at a concentration of 0.5 M (seawater) at 25 °C. The physical properties of the solution are reported in Table 2.1.

The current density was set at 200 A/m^2. In chapter 4 the non-linearity of the transport equation (Eq. (2.37)), due to the diffusivity correction term containing the concentration itself, was shown to be very weak, so that simulating different values of the current density is not needed. Moreover, results are assessed in dimensionless form by means of the Sherwood number, thus the absolute value of the flux is not important.

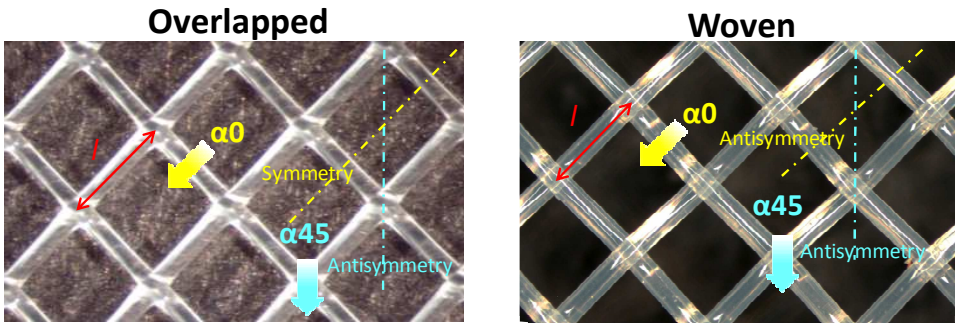

Figure 5.1. Spacers geometries investigated. Arrows indicate the different flow directions with respect to the spacer that were investigated. Lines indicate the projection of the symmetry and antisymmetry planes.

Table 5.1. Cases investigated.

Case/code	Filaments arrangement	*l/h* [mm]	*α* [°]	*Re* [-]
o-l/h2-α0	overlapped	2	0	1, 4, 16, 64
o-l/h3-α0	overlapped	3	0	
o-l/h4-α0	overlapped	4	0	
o-l/h2-α45	overlapped	2	45	
o-l/h3-α45	overlapped	3	45	
o-l/h4-α45	overlapped	4	45	
w-l/h2-α0	woven	2	0	
w-l/h3-α0	woven	3	0	
w-l/h4-α0	woven	4	0	
w-l/h2-α45	woven	2	45	
w-l/h3-α45	woven	3	45	
w-l/h4-α45	woven	4	45	

5.2.2 Governing equations, computational domain and boundary conditions

The simulations of this chapter were performed by following the "main approach" of the present work described in section 2.5.1. Assuming fully developed flow conditions, the Unit Cell of the channel was simulated. The computational domains were created on the basis of the geometric features and the assumptions on the compenetration/compression of filaments in their contact areas and in the contact areas with the walls, as described in section 2.5.1.1. Figure 5.2 shows an example of Unit Cell adopted for the two kind of spacer-filled channels simulated in this chapter. The choice of the cell type (allocation with respect to the spacer wires) is arbitrary [64]; nevertheless, in both spacer-filled channels the minimum repetitive volume is considered and in the case of the overlapped wires the choice is suggested by the possibility to building up an almost completely hexahedral grid. Remembering that the flow direction is fixed along the *z*-axis, the Unit Cells shown in Figure 5.2 are oriented such as the flow attack angle is $\alpha = 45°$.

The governing equations for the periodic domain were implemented: the continuity Eq. (2.1), the Navier–Stokes Eqs. (2.36) and the transport Eq. (2.37). The body force per unit volume K_p in Eq. (2.36) was set with the effect of the large-scale pressure gradient. Preliminary simulations were carried out in order to find the relationship K_p-*Re*, so that in the subsequent ones K_p has been set in order to achieve the desired *Re* (1, 4, 16, 64). The source term *S* depending on the large-scale concentration gradient K_c was implemented in Eq. (2.37). A uniform flux of electrolyte, corresponding to the current density according to Eq. (2.42), was imposed at the upper and lower walls representing the fluid-membrane interfaces.

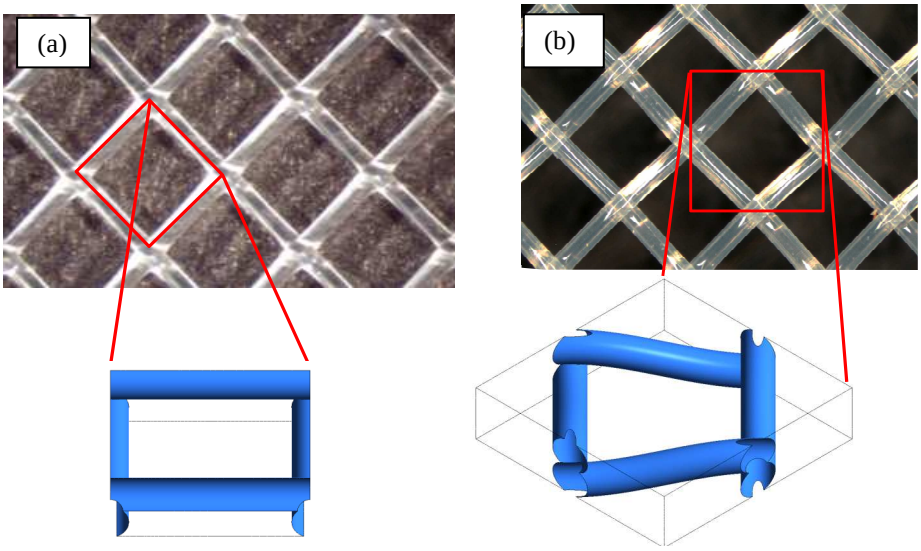

Figure 5.2. Unit Cell geometry for (a) overlapped and (b) woven spacer-filled channels. The cases shown are with *l*/*h* = 3.

The computational domain of the overlapped spacer-filled channels was discretized by multi-block grids composed almost 100% by hexahedral elements (only a part < 1% of domain is meshed by tetrahedra, pyramids and wedges, see Table 5.2). This kind of discretization was possible because of the spacer geometry and the Unit Cell type chosen, as well as the subdivision of the domain in 48 sub-volumes. For the woven spacer-filled channels, multi-block hybrid grids, mainly composed by hexahedral elements, were created, due to geometrical complexities. In particular, the zones around

the filaments were discretized by tetrahedra (this percentage of the domain is indicated in Table 5.2), the other parts of the computational domain were discretized with hexahedral volumes.

The sensitivity analysis of the results to the discretization degree was performed (results not reported for the sake of brevity). Therefore it was possible to identify the size of the computational cells which guarantees the independence of results on the discretization degree along with a very good accuracy in the spatial resolution (gradients and curvatures) and a computational effort compatible with the available computing and time resources. A mesh size equal to 0.006 mm, corresponding to 51 control volumes in the channel thickness (h = 0.306 mm), was chosen for the simulations reported in this chapter.

The grids obtained contain a number of computational cells ranging from ~$4 \cdot 10^5$ to ~$6 \cdot 10^6$ depending on the specific geometry simulated. Of course, the number of computational cells increases by increasing l/h, and is higher for the woven spacer-filled channels because the domain volume is higher and discretized with a not negligible tetrahedral portion. Figure 5.3 reports enlarged details of the meshes in one half of a cross section (at 45° with respect to the filaments). The mesh features are summarized in Table 5.2.

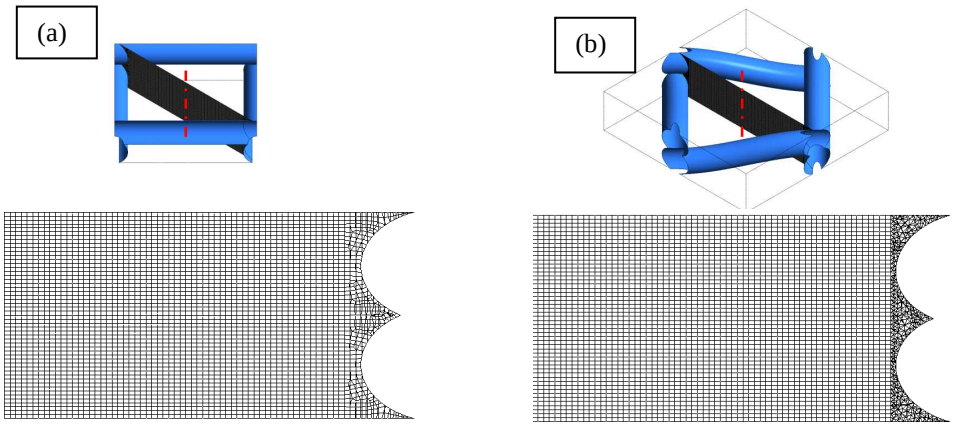

Figure 5.3. Details of the mesh over one half of a cross section of the Unit Cell for (a) overlapped and (b) woven spacer-filled channels. The cases shown are with l/h = 3.

Table 5.2. Summary of the grids employed.

Unit Cell	Number of cells in height *h*	Number of computational cells	% of domain discretized with hexahedral cells
o-l/h2	51	421’042	>99
o-l/h3		1’050’986	>99
o-l/h4		1’922’001	>99
w-l/h2		1’657’319	66.3
w-l/h3		3’397’154	77.2
w-l/h4		5’756’552	82.8

5.3 Results and discussion

Simulations results are presented and discussed in this section. Section 5.3.1 reports results relevant to fluid flow, section 5.3.2 is relevant to pressure drop, section 5.3.3 is devoted to mass transfer, and finally section 5.3.4 compares results with available CFD and experimental data from the literature. For the sake of brevity, streamlines and mass transfer coefficient maps are shown for some cases simulated, by highlighting the effect of some parameters in specific configurations; conversely, the graphs relevant to the global variables *Re*, *f*, *Pn* and *Sh*, report all the cases investigated, so that the effect of all parameters is shown. For convenience, all cases are indicated by an identification code, as reported in Table 5.1.

5.3.1 Fluid flow

Figure 5.4 reports 2-D streamlines on the *y-z* midplane for the case *o-l/h3-α0* at different *Re*. The fluid enters the Unit Cell from below a transverse filament, then occupies the channel for the whole height and finally is forced to come out from below the subsequent transverse wire. At low *Re* the presence of creeping flow conditions can be observed, as the flow field is symmetric without any flow separations downstream of the orthogonal filaments. At higher *Re* the symmetry feature disappears and a detachment of the fluid stream from the filaments occurs. Below the upper wall in proximity to the transverse wires, the streamlines are characterized by stagnation areas; by increasing *Re*, a slow laminar vortex downstream the transverse filaments is developed, and the rectilinear part of the streamlines is shortened, i.e. the relative importance of the vertical

components of velocity increases (as expected). Also, Figure 5.4 refers to the medium filament spacing investigated (*l/h3*), but, by increasing *l/h* of the cases *o-α0* (figure not shown for the sake of brevity), the longer the rectilinear parts of the streamlines, shorter the laminar vortex at the maximum *Re* (for *o-l/h2-α0* it goes from filament to filament, while for *o-l/h4-α0* is about 1/4*l*).

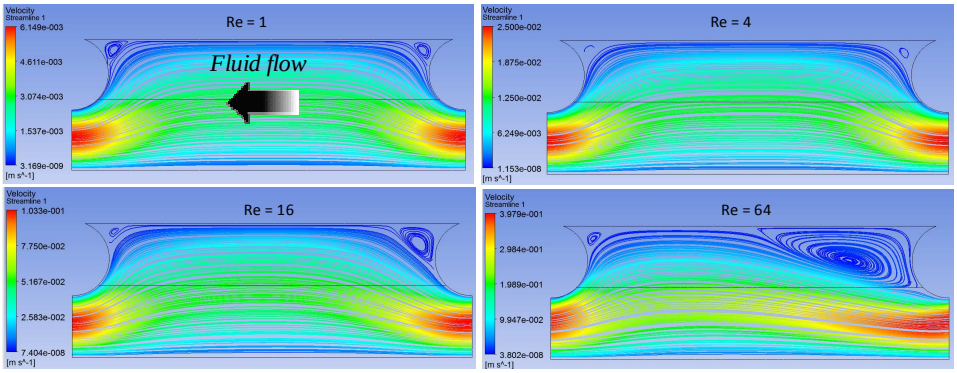

Figure 5.4. Streamlines on the *y-z* midplane for *o-l/h3-α0* at *Re* = 1, 4, 16, 64.

Figure 5.5 reports the streamlines for the same filament shape and the other flow attack angle (case *o-α45*), at *Re* = 4 at increasing *l/h* values. Crossing the periodic domain, the fluid veins are divided: some of them remain confined in its own half-channel (upper or lower), the others move towards the other half-channel. In particular, the closer the flow veins to a wall (upper or lower), the more they tend to remain in their half-channel and move more slowly, although with curved sigmoidal trajectories. On the contrary, the fluid in the central part of the channel (along the height, *y*-axis) moves mainly along a 3D zigzag flow path passing to the other half-channel. For lower values of *l/h* the fluid has a higher tendency to proceed along its half-channel, while for higher values of *l/h*, having the possibility to move along narrower curves, an increasing part of fluid goes towards the other half-channel. The flow rate has an opposite effect with respect to the mesh length, but the range of *Re* here investigated has only a slight influence on the streamlines, thus it is not shown. These findings confirms as reported in the literature Karode and Kumar [53] and Shakaib et al. [62]. Moreover, streamlines are not observed near the upper and lower walls in proximity of the filaments, thus suggesting the existence of calm regions in these locations.

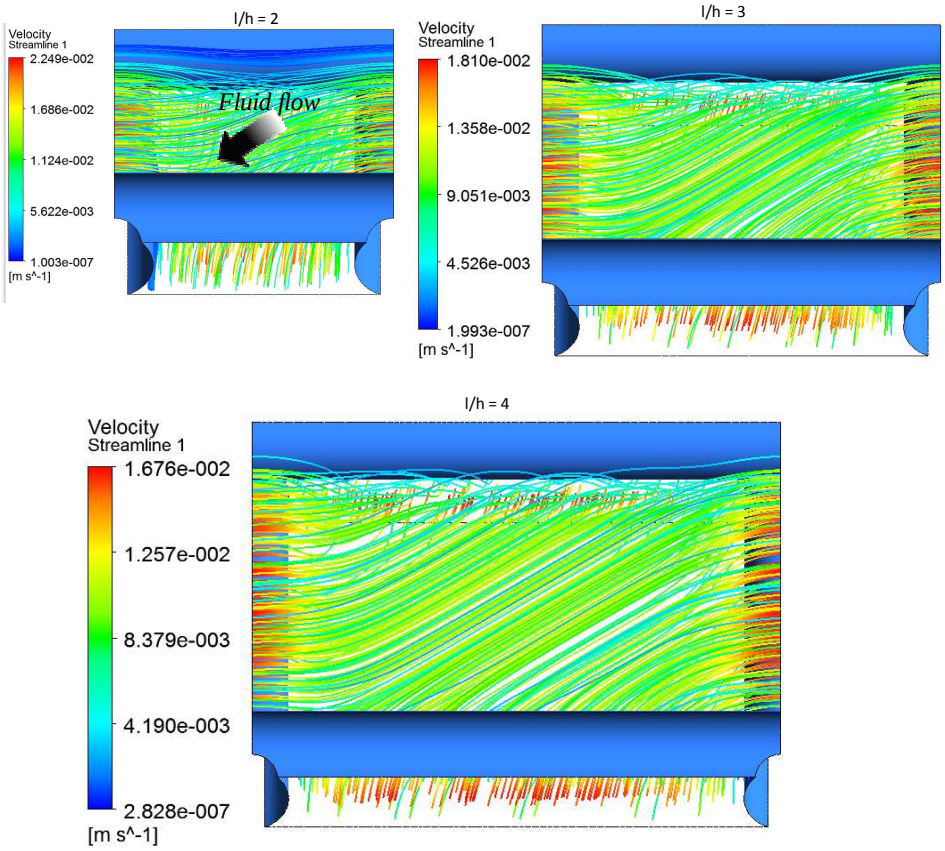

Figure 5.5. Streamlines for *o-α45* at *Re* = 4 at *l/h* = 2, 3, 4.

A flow field sensibly different is established when a woven spacer fills the channel. It can be observed in Figure 5.6, where the streamlines for the case *w-l/h3-α0* are reported at increasing *Re*. Along the longitudinal wires, calm regions are generated where the fluid flows slowly. In all the remaining part of the channel the fluid trajectories are determined by the curvilinear transversal filaments arranged alternately; along the main flow direction, in correspondence of a transversal wire the fluid fillet that encounters more space in the upper part of the channel, then at the next transverse filament finds more space in the lower one and *vice versa*. Therefore, a part of fluid moves up and down also with some lateral displacements, while the other always remains either in the superior or in the inferior part of the channel. Notice that no differences can be appreciably observed between the two lowest *Re*, thus confirming a self-similar flow regime (creeping flow). As *Re* increases, the streamlines are more curvilinear and follow

less the filaments boundary (more detachment). When the obstacles are more distant (i.e. *l/h* is higher), the curvature of the trajectories is reduced and "rectilinear" parts are longer (figure not shown for brevity).

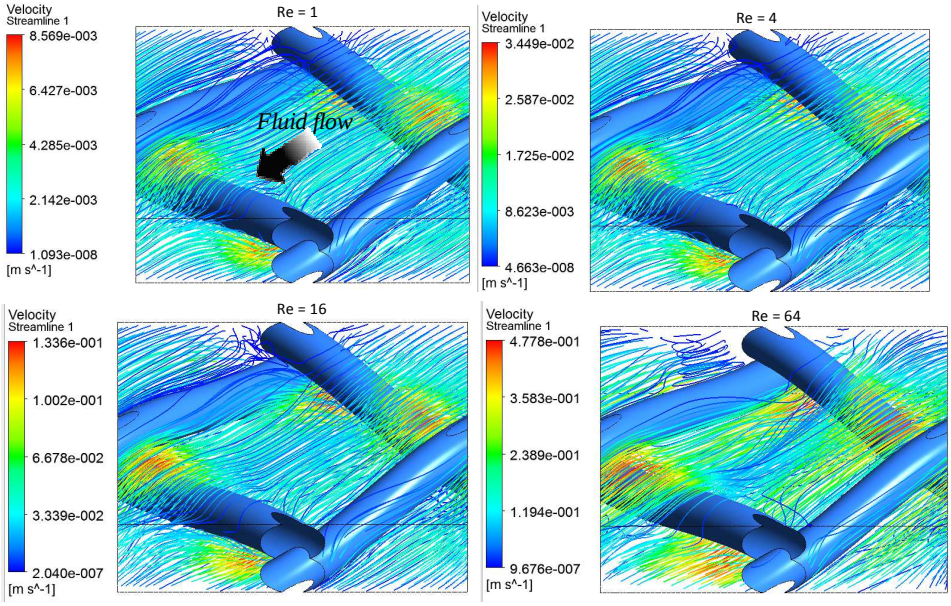

Figure 5.6. Streamlines for *w-l/h3-α0* at *Re* = 1, 4, 16, 64.

Changing the flow attack angle (case *w-α45*) the woven filaments arrangement and their orientation with respect to the main flow direction are such as to give rise to the most complex flow field among the cases investigated here (Figure 5.7). This configuration is the only one without any stagnant regions, and it forces the fluid to move along intricate trajectories with both vertical and lateral movements. This flow pattern is suitable for achieving a high mixing degree. As *l/h* increases, the streamlines are less curved, thus a lower mixing is observed. Increasing *Re* causes the streamlines to be more curved, to follow less the filament arrangement, and to assume an *x*-shape in the central part of the domain (figure not shown for brevity).

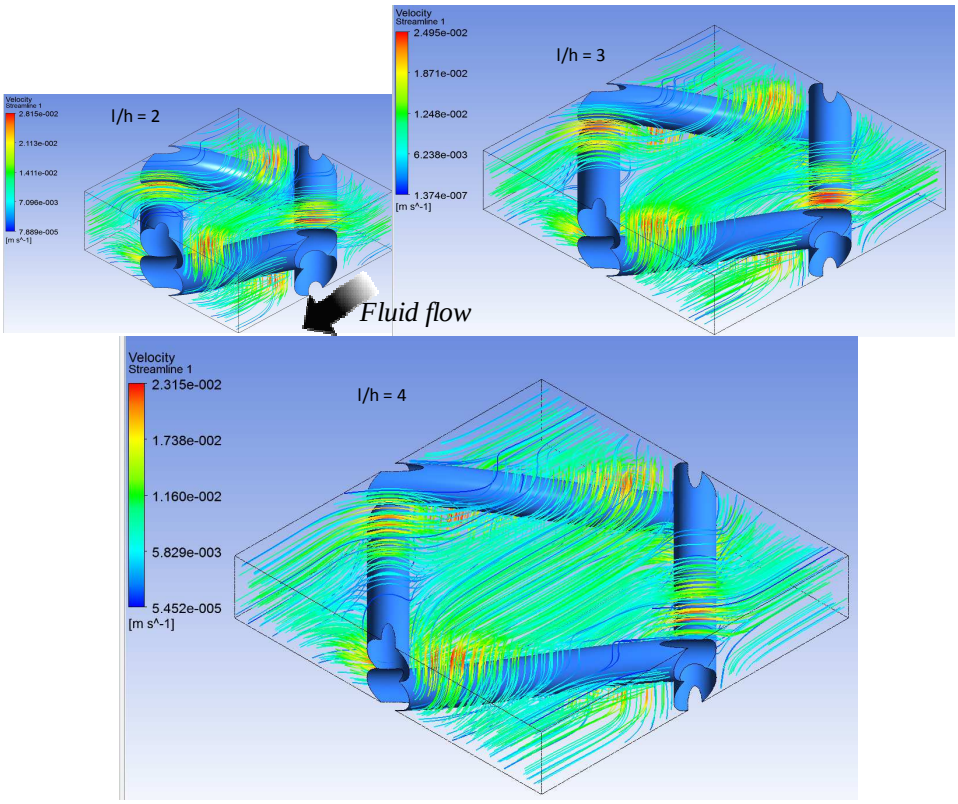

Figure 5.7. Streamlines for *w-α45* at *Re* = 4 at *l/h* = 2, 3, 4.

As mentioned above, the case *o-α0* is the only one where the vertical plane parallel to the main flow direction (*y-z* midplane) is a symmetry plane, thus the flow field is symmetric with respect to it. In the other channel configurations, the *y-z* midplane is a plane of geometric antisymmetry, thus the flow field is antisymmetric.

Summarizing all these results, the effect of the parameters investigated on the flow field, and in particular on the streamlines, can be inferred. In general, the presence of a spacer causes velocity components perpendicular to the main flow direction. The streamlines are more curved on average within the domain as *Re* increases and *l/h* reduces. The filament shape determines flow fields completely different for both α investigated, but the woven spacer guarantees a better mixing with respect to the overlapped one. For the overlapped shape, the two flow attack angles generate very different flow fields: in both cases (*o-α0* and *o-α45*) the fluid accomplishes movements in the two directions perpendicular to the main flow direction; but in the case *o-α0* the lateral motion is

confined inside the unit cell due to the filaments parallel to the main flow direction, while in the case *o-α45* some fluid particles follow the filament direction and thus remain in their half-channel (along the height), and some fluid particles move towards the other half-channel along zigzag flow paths, with a predominance of the formers when *l/h* reduces and *Re* increases. For the channels with woven filaments the common features are that the flow particles move up and down and laterally, and that the streamlines present a rectilinear part at low *Re* and high *l/h*. On the other hand, different *α* results in some important differences: the main is that the case *w-α45* is characterized by more displacements in lateral direction and absence of stagnant areas. This is a prominent feature, which makes the case *w-α45* the best configuration for mixing, as shown in section 5.3.3.

5.3.2 Pressure drop

The Fanning friction factor as a function of the Reynolds number for all the cases investigated is reported in Figure 5.8. The curves can be well interpolated by power laws as [48-50, 53, 55, 60, 61]

$$f = ARe^{n} \tag{5.1}$$

In a more detailed analysis, at the lowest *Re* $n = -1$ indicating for all cases the presence of a creeping (self-similar) flow regime. As *Re* increases, the exponent *n* deviates slightly from -1, as it can be observed by the increasing discrepancy with respect to the empty channel ($f = 24/Re$). This is due to the slight but increasing inertial effects induced by the spacers: the fluid is forced to move more chaotically (onset of secondary flows), so that the flow fields lose the self-similar feature as *Re* rises. Of course, no turbulence occurs in the range of *Re* here investigated.

The power number trend as a function of *Re* can be interpolated by a power function as

$$Pn = BRe^{m} \tag{5.2}$$

where $B = A/8$ and $m = 3 + n \approx 2$ (see definitions in section 2.8). The charts of *Pn vs. Re* are not shown for the sake of brevity. Table 5.3 reports the correlations obtained for all the channel configurations.

In order to better compare quantitatively the cases investigated, the charts in Figure 5.9 show *f* normalized with respect to that in an empty channel (24/*Re*). Of course, this quantity corresponds to the *Pn* normalized with respect to that in an empty channel ($3Re^2$). The spacer-filled channels exhibit significant increments of pressure drops with respect to the spacer-less channel, providing *f* from ~3 to ~20 times higher. Also, these increments become higher as *Re* increases.

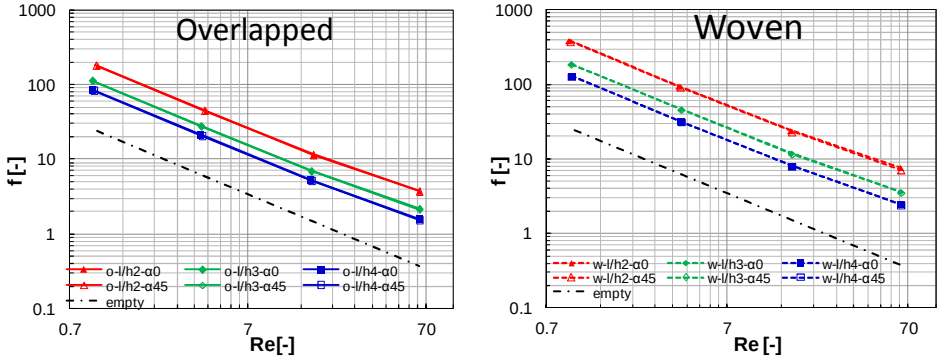

Figure 5.8. Friction factor as a function of Reynolds number for all cases simulated.

Table 5.3. Correlations of the friction factor and the power number as a function of the Reynolds number.

Case/code	*f* [-]	*Pn* [-]
o-l/h2-α0	$168.378Re^{-0.933}$	$21.047Re^{2.067}$
o-l/h3-α0	$100.874Re^{-0.939}$	$12.609Re^{2.061}$
o-l/h4-α0	$76.566Re^{-0.949}$	$9.571Re^{2.051}$
o-l/h2-α45	$168.483Re^{-0.933}$	$21.060Re^{2.067}$
o-l/h3-α45	$101.114Re^{-0.942}$	$12.639Re^{2.058}$
o-l/h4-α45	$76.744Re^{-0.952}$	$9.593Re^{2.048}$

w-l/h2-α0	$340.181Re^{-0.930}$	$42.523Re^{2.070}$
w-l/h3-α0	$172.692Re^{-0.941}$	$21.586Re^{2.059}$
w-l/h4-α0	$119.234Re^{-0.946}$	$14.904Re^{2.054}$
w-l/h2-α45	$341.145Re^{-0.944}$	$42.643Re^{2.056}$
w-l/h3-α45	$172.548Re^{-0.947}$	$21.569Re^{2.053}$
w-l/h4-α45	$119.267Re^{-0.950}$	$14.908Re^{2.050}$

The flow attack angle α effect is irrelevant at these *Re*, notwithstanding it influences deeply the flow field. The only exception is the case of the woven arrangement along with the minimum filament spacing (*w-l/h2*), which reveals an effect of α, but small and limited to the highest *Re*. In other words, when the flow is creeping or at least when the viscous stresses are predominant on the inertial ones, α does not affects the hydraulic loss; on the contrary, when *Re* is sufficiently high some effects are expected, which here begin to be visible only for case *w-l/h2*.

The filament spacing *l/h* has remarkable effects, especially for the *w*-arrangement. Of course, as *l/h* increases, pressure drop is reduced and approaches that one of the empty channel. Figure 5.9 shows the increments of pumping power from *l/h4* to *l/h3* and *l/h2*. It is evident that the pitch is a fundamental parameter in determining the pumping consumption.

Moreover, the filaments arrangement has a significant influence. *W*-arrangement requires a pressure drop increased on average by 106%, 67% and 54% with respect to the *o*-shape, for *l/h* = 2, 3, 4 respectively. Thus, it is worth noting that (i) passing from the overlapped to the woven filaments, the hydraulic loss is dramatically increased, and that (ii) the arrangement has a greater influence as the pitch decreases.

The effect of the filament arrangement is not surprising; in fact woven wires offer a larger area of fluid-solid interface for the friction, as the fluid particles can pass both above and below the obstacle, while for overlapped one they can pass only through one side. Also, higher velocity gradients at the walls are obtained in the woven spacer-filled channel. Finally, the components of velocity orthogonal to the main flow direction are more important, thus increasing the inertial effects on pressure drop.

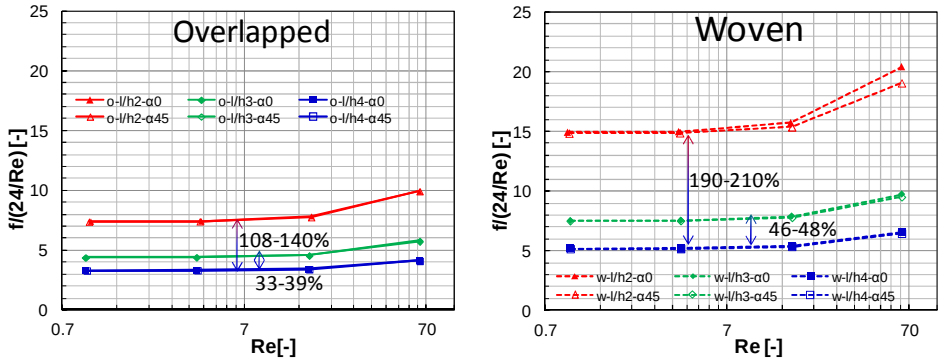

Figure 5.9. Friction factor normalized by that pertaining to an empty channel (24/*Re*) as a function of the Reynolds number for all cases simulated.

5.3.3 Mass transfer

Figure 5.10 reports the distribution of the mass transfer coefficient normalized by the average value ($k / \bar{k}$) on the upper wall for the case *w-α45* by varying *Re* and *l/h*. These maps are reported as an example of the effect of the two parameters (*Re* and *l/h*) on *k*, and are pertaining to the configuration which offers the best performance, as it will be discussed below. The maps reported in the figure are similar, thus indicating that the two parameters here analysed do not affect significantly the normalized distribution of the mass transfer coefficient; conversely, the other parameters have a stronger influence, as highlighted below (Figure 5.11). As either *Re* increases or *l/h* reduces, the standard deviation of the normalized *k* increases, with the gain of higher maximum values. Also, a different location of the maximum values can be observed by varying either *Re* or *l/h*. This effect is very remarkable at the highest *Re* (64). Between the two lowest *Re* the maps are only slightly different, thus indicating that the concentration fields begin to lose the self-similarity feature.

As expected, as *Re* increases, a mixing enhancement is obtained, i.e. $\bar{k}$ increases, due to the convective motions orthogonal to the main flow direction. Moreover, an increase of $\bar{k}$ is obtained as the pitch reduces. Notice that the configuration *w-α45* is the only one, among the cases investigated here, that exhibits a mixing enhancement for all *Re* by reducing *l/h*, as shown better in Figure 5.12 (for the sake of brevity only the results

relevant to one *Re* are reported in Figure 5.10). This effect of the filament spacing confirms what inferred from the streamlines results (Figure 5.7).

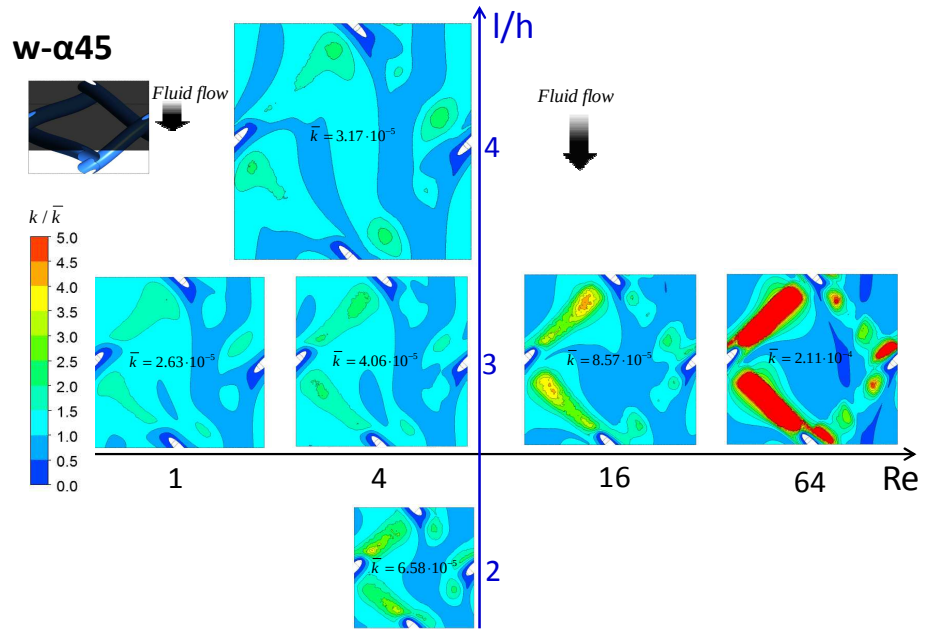

Figure 5.10. Maps of the local mass transfer coefficient normalized by the average value on the upper wall for the case *w-α45* by varying *Re* and *l/h*.

In

Figure 5.11 the distribution of the local mass transfer coefficient normalized by the average value ($k / \bar{k}$) on the walls is reported for evaluating the effect of filaments arrangement and flow attack angle at a fixed value of *l/h* and *Re*. Of course, the symmetry/antisymmetry features mentioned above are observable also for the concentration field. Therefore the maps on the upper and lower walls are exactly antisymmetric (i.e. are equivalent each other if overturned) for all cases, apart from *o-α0*: in this case both the two maps are symmetric, but different between each other.

Figure 5.11 shows that the spacer filaments arrangement and the spacer orientation have a strong impact on the *k* distribution. It is worth noting the presence of areas with low mass transfer coefficients (thus high concentration polarization) in correspondence of calm regions with low fluid velocities in proximity of the filaments. These areas,

detrimental for mixing, are located in proximity of the longitudinal wires for the case *w-α0* and near both the filament layers for the overlapped spacer (*o-α0* and *o-α45*). The configuration *w-α45* is the only one able to avoid this disadvantageous effect of the filaments (see Figure 5.7). This feature, combined with a complex flow field with significant vertical and lateral velocity components, favours mixing thus giving rise to the highest $\bar{k}$ for the case *w-α45*.

By comparing the cases *w-α45* and *w-α0*, higher $\bar{k}$ are obtained for the former case and this is found for all *l/h* and *Re*. Also, different distributions of *k* can be observed, but both show the maximum values of *k* in the proximities of two filaments (the transversal ones for *w-α0*). The filament arrangement gives rise to completely different distributions of *k* for both *α* investigated. However, the woven spacers lead to a mixing degree greater than the corresponding overlapped spacer, especially in the case of *α45*. Finally, from Figure **5.11** the effect of *α* on the maps for *o*-arrangement is evident, but a similar $\bar{k}$ is obtained.

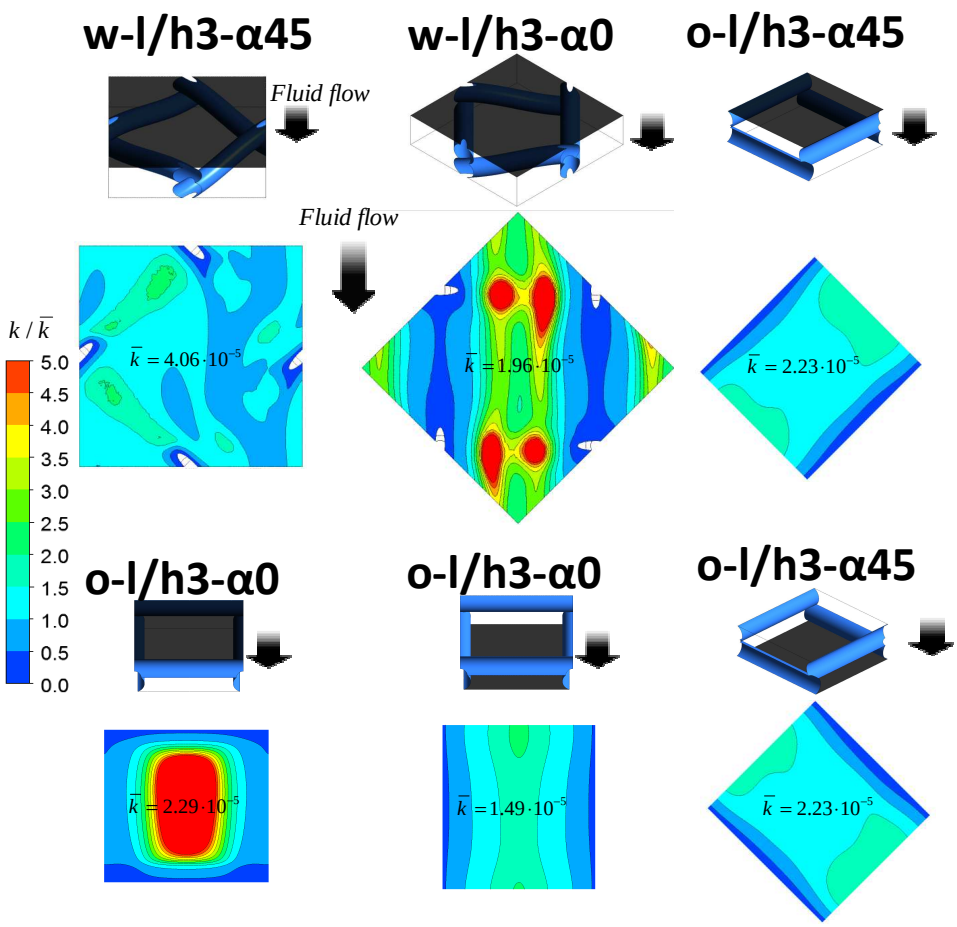

Figure 5.11. Maps of the local mass transfer coefficient normalized by the average value on the upper and lower walls for the two filaments arrangement (*o* and *w*) and the two flow attack angles (*α0* and *α45*) at *l/h3* and *Re* = 4.

Figure 5.12 reports *Sh* as a function of *Re* for all cases simulated. The charts show also *Sh* for fully developed (no entry effects) laminar flow within an empty channel of infinite streamwise and spanwise extension. It is evident that the presence of a spacer affects strongly mass transfer phenomena. At very low *Re*, mixing is not favoured in the spacer-filled channels, due to the calm regions caused by the filaments which are detrimental for the mass transfer, especially for *α0*. As a consequence, the spacer-filled channels can exhibit *Sh* even lower than the empty channel [141]. On the other hand, as *Re* increases, much higher *Sh* can be attained; in fact increased inertial fluid flow

phenomena come into play, thus promoting a mixing degree enhancement. Each channel configuration is characterized by a specific cut-off value of *Re* beyond which mass transfer performance is better than the empty channel. In the case *w-α45* this occurs at *Re* close to 0, in the other cases for higher values, but however always at *Re* lower than 7.

All the curves of Figure 5.12 have positive concavity directed upwards, due to the range of *Re* here investigated. As far as the influence of the parameters, the filament spacing has a clear effect for all *Re* only in the case *w-α45*: in particular, *Sh* is reduced as *l/h* increases. For *w-α0* this occurs only at the highest Reynolds numbers; for *o*-arrangement the dependence of *Sh* on *l/h* is not so significant.

The flow attack angle plays an important role in determining mass transfer for the *w*-arrangement, although it has very slight effects on pressure drops: for all *Re* and *l/h*, a mixing promotion is achieved when the fluid bisects the angle between crossing filaments, i.e. the configuration *w-α45* implies *Sh* higher than the case *w-α0*; on the other hand, the discrepancies between the two woven spacer-filled channels appear to be lower at high *Re*. For the *o*-arrangement the effect of *α* is more complex as *Re* varies, but however slighter: *Sh* for the configurations *o-α45* tends to be higher than for *o-α0*, but very similar values are found at *Re* = 16 (confirming results shown in section 4.4), where even an inversion can be observed.

The filament arrangement is shown to be a key parameter for mass transport. Results show that the *w*-arrangement allows to achieve a mixing enhancement with respect to the *o*-arrangement, notwithstanding at low *Re* the performance is very similar for *α0*; in particular, higher *Sh* are obtained for the *w*-arrangement at all *Re* and *l/h* unless one case (*w-l/h2-α0* at *Re* = 4).

All these results are in accordance with what was discussed about the results pertinent the effect of the channel features on fluid flow and mass transfer coefficient distribution. Finally it is worth noting that for any given *Re* the configuration which guarantees the best mixing conditions is *w-l/h2-α45*.

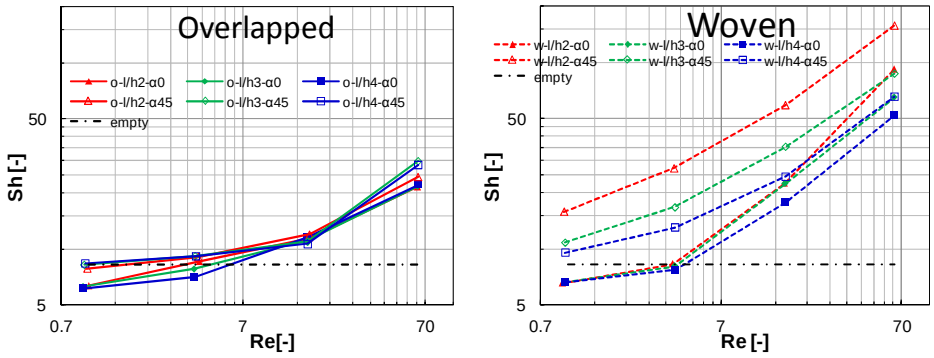

Figure 5.12. Sherwood number as a function of the Reynolds number for all cases simulated.

Figure 5.13 shows *Sh* as a function of *Re* for the *o-α0* cases simulated, where the two walls have a different behaviour, as discussed above. With respect to the main flow direction, the *high* wall touches the transverse filaments and the *low* wall touches the longitudinal filaments. Apart from the minimum *Re* investigated, the flow pattern within the channel enhances mass transport at the *high* wall rather than in the *low* wall (see streamlines in Figure 5.4). Interestingly, the trend of *Sh* is not monotonic with *Re* for the *low* wall. Moreover *Sh* reduces in this wall as *l/h* increases, but at the highest *Re* investigated values practically equal are obtained for the three pitches. At *Re* = 4, also at the *high* wall *Sh* is reduced by increasing *l/h*, but then the tendency is inverted, obtaining however similar values as *l/h* varies.

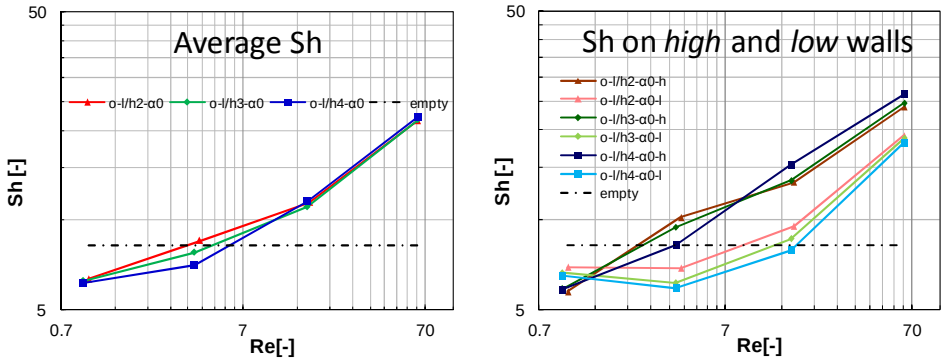

Figure 5.13. Sherwood number as a function of the Reynolds number for the *o-α0* cases simulated.

Figure 5.14 shows *Sh* as a function of *Pn* for all cases simulated; thus it summarizes the combined effect of all the parameters investigated on pressure drop and mass transfer. By comparing these data with those reported in Figure 5.12, similar considerations on the spacers performance can be inferred. As a difference, the pitch has not a significant effect for the configuration *w-α0*, especially at high *Pn*; for the *o*-arrangement the dependence of *Sh* on *l/h* is still not so significant, but however is increased at high *Pn*.
For any given pumping consumption, *w-l/h2-α45* is again the configuration providing the best performance in terms of mixing degree. Actually, the identification of the best channel configuration in a RED stack should take into account also other parameters affecting the net power producible.

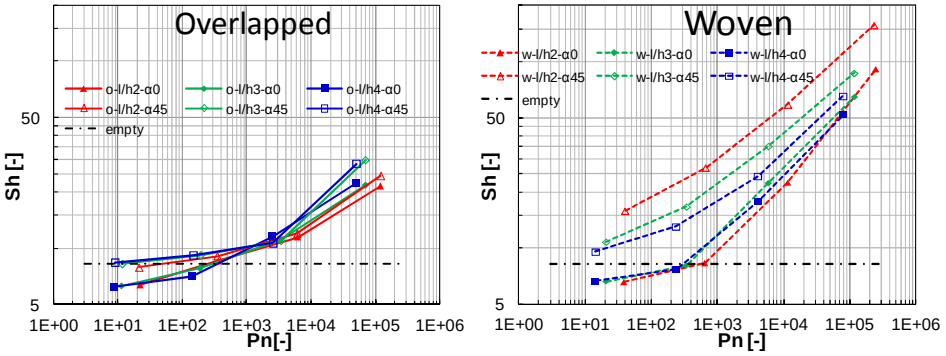

Figure 5.14. Sherwood number as a function of the Power number for all cases simulated.

5.3.4 Comparison with CFD and experimental data from the literature

As seen in section 5.3.2, the curves *f-Re* and *Pn-Re* can be fitted with good approximation in the range of *Re* here investigated by means of the typical power laws adopted in the literature. On the other hand, the effect of *Re* on *Sh* is more complex for all geometries. The correlations *Sh-Re* and *Sh-Pn* are often reported in the literature in the form of power laws, but these functions are not suitable for the present data due to the different range of *Re* here investigated. All the curves of Figure 5.12 and Figure 5.14 have concavity directed upwards. The trend of *Sh* in a wide range of *Re* (and thus *Pn*) starting from values relatively low emerges from simulations and experiments carried out in the literature [48, 54, 55, 141]: it can be supposed with an horizontal asymptote

for *Re* approaching zero, an increasing part (as that shown in the figures mentioned above) up to attaining the unsteady flow, an inflection, an asymptote and finally a rectilinear part in the fully turbulent regime (logarithmic graph).

Detailed comparisons with literature data are shown in the next charts of this section. The variables are calculated according to the definitions reported by the references. First the present results are compared with data by Li et al. [54, 55]. In these manuscripts there are some differences: the filament diameter is exactly equal to half the channel height ($d = h/2$), $Sc = 1278$, the boundary condition at the walls is $C_w = 0$ and the average mass transfer coefficient is calculated as the mean value of the local *k*. Also, there are no details on the grids adopted. For the comparison of *Sh*, it is assumed proportional to $Sc^{0.4}$ [61]. In Figure 5.15 results on *Pn* for two overlapped spacers are reported with data from Figure 16 in [54] and Figure 11 in [55]. The two series with *l/h4* in [54] are coincident in the first part ($Re_{Li} < 140$), so one series is extrapolated and is valid for the two α. The experimental data of Figure 11 in [55] for *α45* appear to be wrong, as the series, reporting also CFD results from the previous paper, is strangely too distant from the series relevant to the case *α0*, thus here is not reported. As well as a qualitative confirmation of the results (α irrelevant on *Pn* under a certain *Re*, *Pn* increase as *l/h* reduces), a good quantitative agreement is found.

Figure **5.16** shows a comparison with CFD results from Figure 8 and 9 in [54] and experimental results from Figure 12 in [55]. For the curves relevant to the cases with *l/h4* it appears that they can be linked up well; for the case *l/h2* the agreement is lower. However, the effect of the parameters is found to be qualitatively the same. Figure 5.17 reports a comparison between the present CFD results and the only data found in literature for woven spacers (experimental mass transfer results from Figure 13 in [55]). The present CFD results overestimate slightly *Sh*, but a similar behaviour of the spacers is shown; in fact, *α45* exhibits *Sh* higher than *α0* and the two curves approach as *Pn* increases.

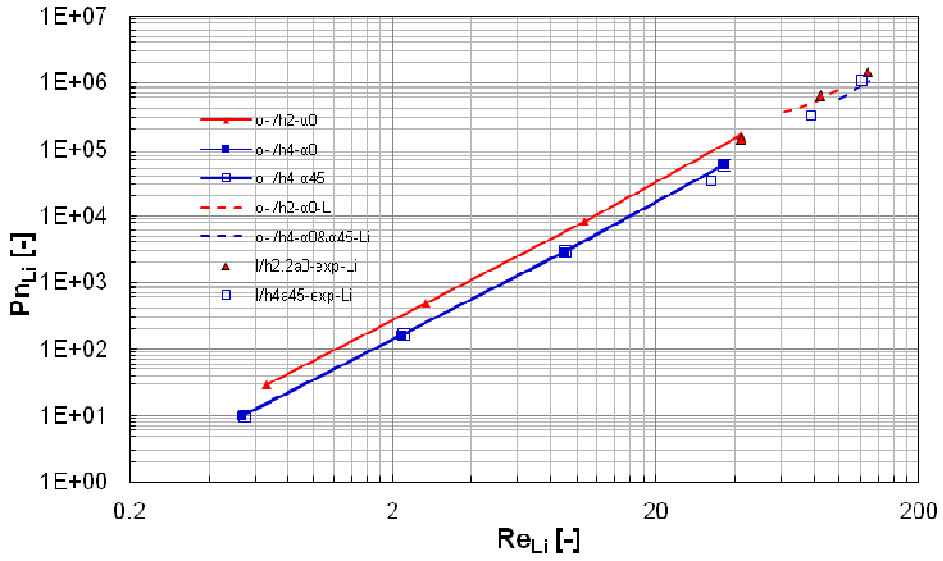

Figure 5.15. Power number as a function of Reynolds number for some cases simulated. Comparison with results of Li et al. [54] (CFD) and [55] (experimental).

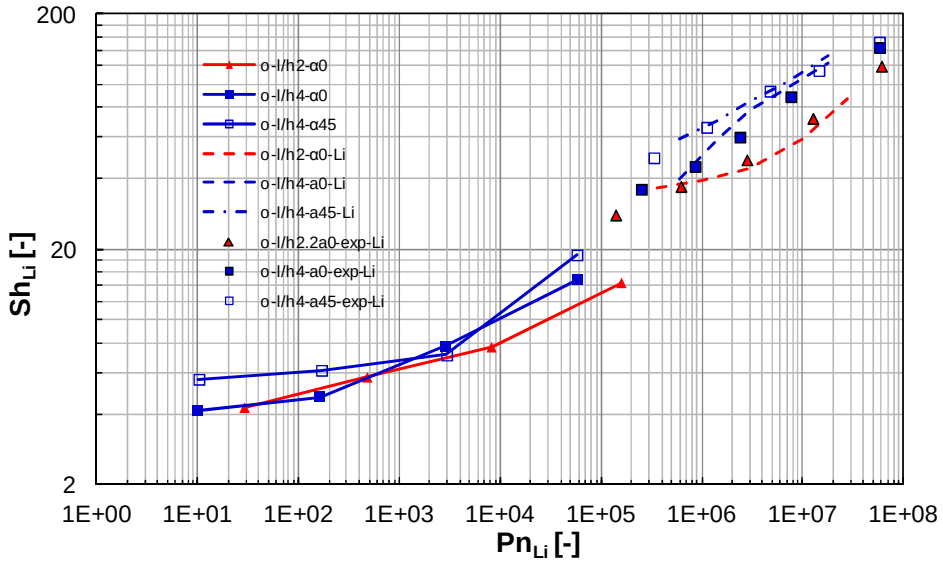

Figure 5.16. Sherwood number as a function of Power number for some cases simulated. Comparison with results of Li et al. [54] (CFD) and [55] (experimental).

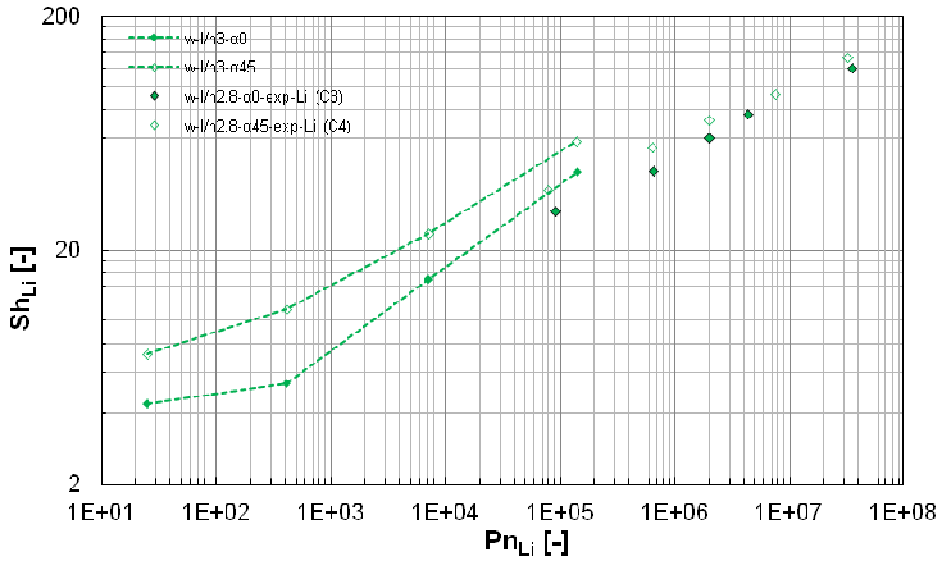

Figure 5.17. Sherwood number as a function of Power number for some cases simulated. Comparison with results of Li et al. [55] (experimental).

Another comparison is performed with the results by Koutsou et al. [60, 61], obtained by DNS CFD simulations and experiments. As a difference with respect to the present simulations, in these papers $d = h/2$, the dependence of *Sh* on *Sc* is studied, grid elements are ~300,000 in [60] and from 540,000 to 1,000,000 in [61], the boundary condition at the walls is a fixed concentration, a spatially averaged value of the local time-averaged mass transfer coefficient *k* is calculated. Figure 5.18 shows a comparison in terms of dimensionless pressure drop with the correlations obtained from literature numerical results (Table 2 in [60]). Since there is a gap in the two range of *Re* investigated, a direct comparison is not possible. However, the effect of increasing *l/h* is found to be a reduction of pressure drop, and the slope of the curves is expected lower as *Re* increases (unsteadiness), thus one can guess that the curves could link up reasonably. Nevertheless, the simulations of [60] seem to overestimate the hydraulic friction, as in Figure 14a of that manuscript an increment of about 35% with respect to experiments can be observed; also similar discrepancies are found with respect to experimental data of Schock and Miquel [49] reported in the same figure, and higher discrepancies in Figure 18 with Li et al. [55]. Figure 5.19 reports *Sh* as a function of *Re* for the same cases of Figure 5.18. CFD and experimental correlations from Table 4 and 5 in [61] are

reported. Also in this case there is a gap which does not allow a direct comparison; however it is confirmed that the filament spacing does not affect strongly *Sh*, and taking into account the slope of the curves, similar values can be supposed at the same *Re*. Figure 5.19 shows also not negligible discrepancies between CFD and experimental data of [61], and in Figure 27 of [61] a fair agreement with the results of Li et al. [55] is shown, although with a different dependence of *Sh* on *Pn*.

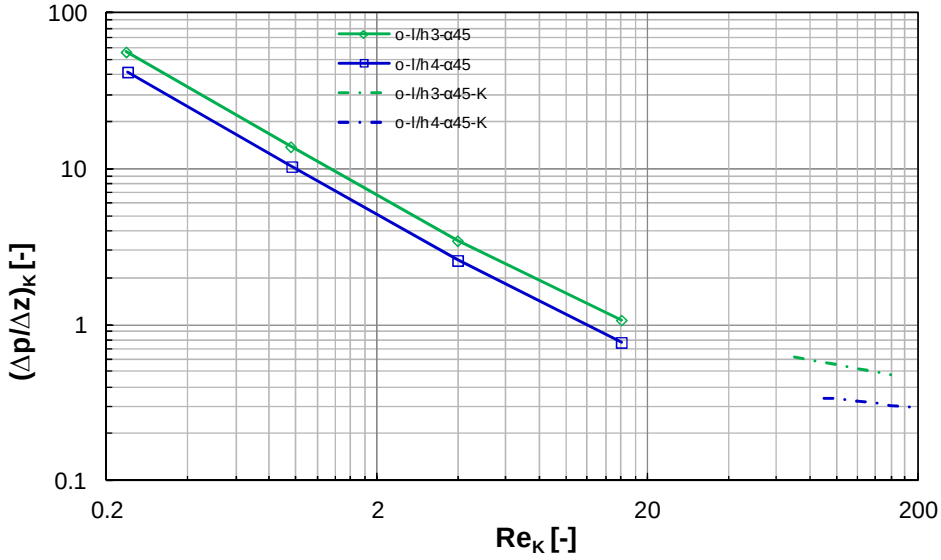

Figure 5.18. Dimensionless pressure drop as a function of Reynolds number for some cases simulated. Comparison with results of Koutsou et al. [60] (CFD).

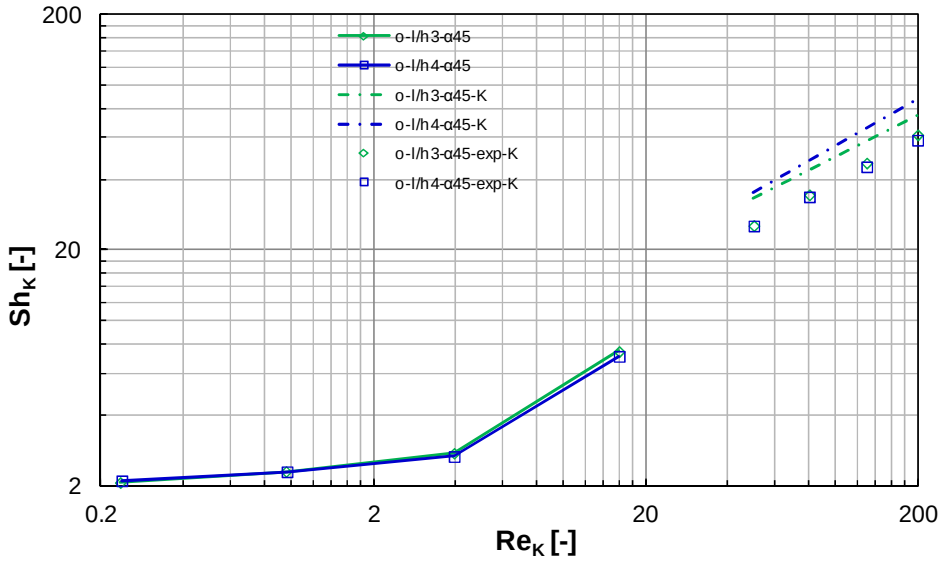

Figure 5.19. Sherwood number as a function of Reynolds number for some cases simulated. Comparison with results of Koutsou et al. [61] (CFD and experimental).

Another thorough CFD analysis of non-woven spacer-filled channels is by Shakaib et al. [62, 63]. In their papers, trends with *Re* are not shown, but only values at a fixed *Re* higher than the maximum studied in this manuscript, and often in dimensional form without the indication of the channel height. Therefore, no charts for comparison are made here, but some important results on spacers with overlapped filaments are reported in order to verify eventually the agreement with the simulations results of this work. The simulations from these papers confirm that pressure drop reduces as the filament spacing increases for all flow attack angles, while a slight effect of α is found. For example, in Table 3 of [63] only an increment of 7.1, 14.0 and 3.4% is obtained from *α0* to *α45* for *l/h2*, *l/h3* and *l/h4* respectively, but for a *Re* beyond the highest investigated here (Re_S = 125, corresponding to *Re* ≈ 166 for *l/h4*). On the other hand, an effect of α on pressure drop is reasonable at higher *Re*, where higher inertial effects occur. Moreover, in Figure 12 of [62] acceptable agreement with Koutsou et al. [60] and better agreement with the experiments of Li et al. [55] for pressure drop is shown. Table 3 in [63] reports also mass transfer coefficients. These data confirm that (i) the angle *α45* enhances mass transfer for all *l/h* values with respect to *α0* (in the present simulations it is found for all *Re* apart from *Re* = 16), and (ii) for *α45* the sequence for mass transfer coefficient is *l/h3* > *l/h4* >

l/h2 (found in the present simulations at the highest *Re* investigated). Finally, a certain agreement is found with experimental data of Li et al. [55] on mass transfer, showing a difference within 30%.

The analysis of this section highlights that literature data show in general a qualitative agreement, with not negligible discrepancies among different authors and between numerical and experimental results.

5.4 Conclusions

CFD simulations of fluid flow and mass transfer in spacer-filled channels for reverse electrodialysis were carried out. The effect of the spacer-to-channel configuration was assessed in a parametric analysis, where woven (*w*) and non-woven (*o*, overlapped) spacers with crossing filaments arranged at 90° were simulated, with different pitch to height ratios (*l/h* = 2, 3, 4), two different flow directions (parallel to a filament, i.e. *α0*, and bisecting the angle formed by the filaments, i.e. *α45*) and at various Reynolds numbers (1, 4, 16, 64).

The flow regime is found to be steady in all cases. The vertical plane parallel to the main flow direction is a plane of geometric antisymmetry for all channel configurations except for the case *o-α0*, where it is a symmetry plane; therefore the flow and concentration fields are either antisymmetric or symmetric with respect to this plane. The presence of a spacer causes velocity components perpendicular to the main flow direction, but calm regions with low fluid velocities and poor mixing (low *k*) are generated in proximity of the filaments. These areas are located in proximity of the longitudinal wires for the case *w-α0* and near both the filament layers for the two overlapped spacer configurations. Only in the case *w-α45* the filaments do not cause this drawback. At low *Re* creeping flow conditions are observed. As *Re* increases, increasing inertial effects are induced by the spacer, i.e. the fluid is forced to move more chaotically by the onset of secondary flows, so that the flow fields lose the self-similarity, and a mixing enhancement is obtained. The pumping power (*Pn*) is proportional to Re^m, where *m* is slightly larger than 2. *Pn* values from ~3 to ~20 times higher than the spacer-less channel are obtained. Also, these increments become higher as *Re* increases. The curves *Sh-Re* have concavity directed upwards in the range of *Re* here investigated. The spacer-filled channels can offer mass transfer performance better than the empty channel beyond a specific cut-off

value of *Re*. In the case *w-α45* this occurs for *Re* close to 0, in the other cases for higher values, but however for *Re* lower than 7. Then, as *Re* increases, *Sh* much higher are attained. All parameters affect the normalized distribution of *k* on the walls, but filament arrangement and *α* are the main.

- As *l/h* reduces, the streamlines are more curved on average (opposite effect of *Re*) and *Pn* is increased especially for the *w*-arrangement (increments up to 210% from *w-l/h4* to *w-l/h2*). The filament spacing has a clear effect on *Sh* for all *Re* only in the case *w-α45*; in particular, *Sh* is reduced as *l/h* increases. For *w-α0* this occurs only at the highest *Re*. For *o*-arrangement the dependence of *Sh* on *l/h* is not so significant.
- The filament arrangement is a key parameter. The *w*-arrangement establishes flow fields fully different, raising pressure drop, but favouring mixing. *W*-spacers require *Pn* increased on average by 106%, 67% and 54% with respect to the *o*-spacers, for *l/h* = 2, 3, 4 respectively. Notably the influence is greater as the pitch decreases. The effect of the filament arrangement is due to fact that woven wires offer larger area for the friction, velocity gradients at the walls and inertial effects. Also, the *w*-arrangement allows a significant mixing enhancement, although at low *Re* the performance is very similar for *α0*.
- *α* influences deeply the flow field. In the case *o-α0* the lateral motion is confined inside the unit cell, while in the case *o-α45* some fluid particles follow the filament and thus remain in their half-channel, and some fluid particles move towards the other half-channel along 3D zigzag flow paths, with a predominance of the formers when *l/h* reduces and *Re* increases. For the *w*-arrangement the streamlines present a rectilinear part at low *Re* and high *l/h*, but the case *w-α45* shows more displacements in lateral direction and absence of stagnant areas with respect to the case *w-α0*. This is a prominent feature which makes the case *w-α45* the best configuration for mixing. However, *α* does not affect pressure drop (only the case *w-l/h2* exhibits a small effect of *α* at the highest *Re*), probably because the viscous stresses are predominant on the inertial ones at these *Re.* The configuration *w-α45* implies *Sh* higher than the case *w-α0* for all *Re* and *l/h*, but the discrepancies are lower at high *Re*. For the *o*-arrangement the effect of *α* is more complex but slighter as *Re* varies: *Sh* for

the configurations *o-α45* tends to be higher than for *o-α0*, but very similar values are found at *Re* = 16.

The trends *Sh-Pn* are qualitatively the same as *Sh-Re*. As a difference, the pitch has not a significant effect for the configuration *w-α0*, especially at high *Pn*; for the *o*-arrangement the dependence of *Sh* on *l/h* is still not so significant, but however is increased at high *Pn*.

The present results show that the channel features have a strong impact on process performance. For all *Re* and all *Pn*, the highest *Sh* values are obtained by the configuration *w-l/h2-α45*. The woven spacers, not yet investigated up to now, are very promising: mixing is enhanced by complex flow fields with significant vertical and lateral motions, especially for the case *w-α45* where calm regions are absent. Therefore the proper attention should be paid in the choice of the spacer configuration, and woven spacers deserve further studies.

A satisfactory agreement was found with the literature, although the comparison is not easy due to the range of *Re* investigated, the presence of very few data on woven spacers and the differences observed among the various studies.

Finally, alternative channel geometries, beyond those investigated here, could improve the process performance. Among the various possibilities, profiled-membrane channels are very interesting and are object of the CFD simulations of the next chapter.

6 PROFILED-MEMBRANE CHANNELS

Abstract

Channel geometry strongly influences fluid flow and thus crucial phenomena such as pressure drop and concentration polarization in reverse electrodialysis (RED). Profiled membranes are an alternative to the more commonly adopted net spacers and offer a number of advantages: avoiding the use of non-conductive and relatively expensive materials, reducing hydraulic losses and increasing the active membrane area. However, they are poorly investigated in literature.

In this chapter, CFD simulations were performed to predict the fluid flow and mass transfer behaviour in channels with profiled membranes for RED applications. In particular, channels equipped with pillars were simulated. The influence of the channel configuration on fluid flow and concentration polarization was assessed by means of a parametric analysis for different profile geometries. In particular, the effects of channel geometry (shape, size and pitch of profiles) and orientation (fluid flow direction) at various Reynolds numbers (*Re*) were investigated.

The Unit Cell approach along with periodic boundary conditions was adopted to simulate fully developed boundary conditions. A transport equation, valid also for concentrated solutions, obtained from the rigorous Stefan–Maxwell equation along with the assumptions of binary electrolyte and local electroneutrality, was implemented.

Simulation results show that the presence of pillars in the channel modifies significantly the flow and concentration field, although they do not generate velocity components perpendicular to the membranes. In the geometries investigated here the pumping power consumption is much lower than in a conventional net spacer and very close to that of the empty channel, while calm zones are generated by the profiles, which may accentuate polarization phenomena at the low *Re* usual for RED.

The interaction of the various parameters investigated produces complex effects on fluid dynamics and transport phenomena, thus suggesting how the channel geometry could be optimized.

6.1 Introduction

The channel features of a RED stack affect strongly the process performance, since they have an influence on Ohmic resistances, non-Ohmic resistances and pumping power.

Together with flow rate and feed properties, the channel features determine fluid dynamics within the channels, which is crucial for the net power producible by the stack (see chapter 1).

Net spacers are usually adopted in RED stacks as mechanical support for the membranes, as in electrodialysis stacks and many other membrane processes. However, profiled membranes are an alternative option that exhibits some interesting peculiarities and thus some advantages over the spacer-filled channel: (i) reduction of Ohmic resistances, (ii) elimination of the spacer shadow effect and increase of the membrane active area, (iii) reduction of the friction factor (see section 1.5). Nevertheless, only very few experimental works have been devoted to the application of these kinds of geometries in RED, and no CFD simulations have been carried out so far on them.

Therefore, after the analysis of spacer-filled channels carried out in chapter 4 and 5, in this chapter the CFD modelling have been extended to the simulation of channels with profiled membranes for RED stacks. The model developed in this thesis (chapter 2) based on the Stefan–Maxwell equation and on the Unit Cell approach, was adopted for the simulations. By predicting fluid flow and mass transfer, the specific aims of this study are: (i) understanding the behaviour of such geometries with respect to empty channels and spacer-filled channels; (ii) verifying if they can enhance process efficiency and economic competitiveness. In particular, the influence of the channel geometry (shape, size and pitch of profiles) and orientation (fluid flow direction) is assessed via parametric analysis at Reynolds numbers typical of RED applications.

6.2 CFD modelling

6.2.1 Systems under investigation

The geometries investigated here consist of channels with membranes provided with profiles on one side, obtainable by hot pressing [30]. The profiles are “pillars” that separate the membranes and create the channels for the feed solutions (Figure 6.1).

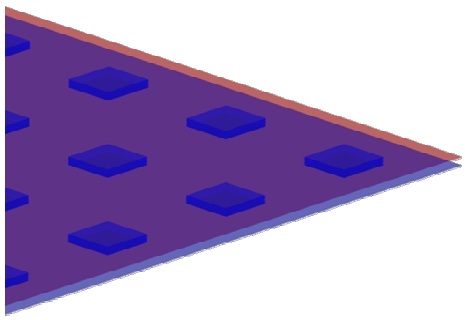

Figure 6.1. Sketch of a profiled-membrane channel. Red and blue colours indicate the upper and lower IEMs, respectively. Profiles are obtained from the lower membrane.

As schematically shown in Figure 6.2, two profile shapes were investigated: (i) square and (ii) circular. The profiles are arranged in a square pitch. The geometrical features of the simulated systems are: (i) the size of the profiles l (edge or diameter), (ii) the distance between two profiles (pitch) L and (iii) the height of the channel h. Corrugated membranes would involve lower pressure drops than spacer-filled channels, allowing eventually the use of thinner channels, which can be a good option to reduce the electrical resistance of the stack; therefore, the present modelling is focused on thin channels of height h = 160 μm. The parametric analysis was carried out on three different values of both profiles size and pitch: l = 0.75, 1.00, 1.50 mm; L = 2, 3, 4 mm. Only one channel was simulated in each CFD simulation, as done for the spacer-filled channels in chapters 4 and 5.

Two different main flow directions were investigated: (i) parallel to one edge of the square pitch of the profiles (flow attack angle α = 0°), (ii) along the diagonal of the square pitch (flow attack angle α = 45°). The influence of profile shape and flow attack angle was investigated only for l = 1 mm and L = 3 mm; then, for the circular shape and the flow attack angle of 45°, the influence of l at a fixed value L = 3 mm and the influence of L at a fixed value l = 1 mm were assessed (L/l = 2, 3, 4) (see Table 6.1). For convenience, each case simulated is indicated by an identification code: the first letter indicates the square (*s*) or circular (*c*) shape of profiles; then, l, L and α are reported with their respective values. For instance, the case *s-l1-L3-α45* indicates square profile, size l = 1 mm, pitch L = 3 mm and flow attack angle α = 45°.

For comparison purposes a spacer-filled channel was also simulated (Figure 6.2c). This spacer was made by woven filaments with angle of 90° and mesh length of 462 μm, and is 160 μm thick; the fluid attack angle chosen was 45°, since such configuration was found to offer performance better than other spacers (see chapter 4). In dimensionless terms (*l*/*h*), the spacer here considered coincides with the commercial D spacer (configuration D45).

Moreover, an empty flat (i.e. spacerless) channel with the same thickness was simulated as a reference case. The empty channel should be regarded as an ideal condition, since a certain "spacer" separating the membranes is compulsory.

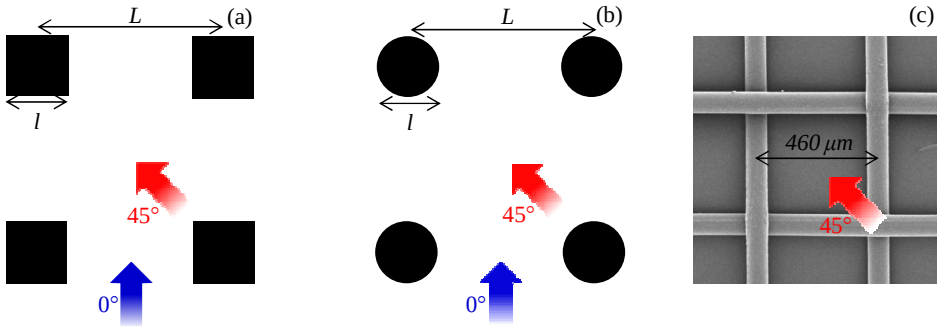

Figure 6.2. Sketches of the two profile geometries simulated (a-b). The woven wire spacer is also shown for comparison (c).

Table 6.1. Profile configurations and Reynolds numbers investigated.

Case	Shape	*l* [mm]	*L* [mm]	*α* [°]	*Re* [-]
s-l1-L3-α0	square	1	3	0	0.5, 2, 8, 32
s-l1-L3-α45	square	1	3	45	0.5, 2, 8, 32
c-l1-L3-α0	circular	1	3	0	0.5, 2, 8, 32
c-l1-L3-α45	circular	1	3	45	0.5, 2, 8, 32
c-l1-L2-α45	circular	1	2	45	8
c-l1-L4-α45	circular	1	4	45	8
c-l0.75-L3-α45	circular	0.75	3	45	8
c-l1.5-L3-α45	circular	1.5	3	45	8

The simulations presented here were performed on the Feed2, i.e. an aqueous solution of NaCl 0.5 M (typical concentration of seawater) at 25°C, whose physical properties are indicated in

Table **2.1**. The effect of the Schmidt number (*Sc*) on the Sherwood number (*Sh*) for NaCl solutions was found weak in chapter 4 . Moreover, at high concentrations the polarization factor θ is near 1, i.e. the polarization effects are scarcely significant, thus it is not important to know the exact value of *Sh*.

The current density was set at 200 A/m^2 (over the total area of upper and lower walls) in all the simulations. In chapter 4 was shown that the corrective term of the diffusion coefficient which confers a non-linearity to the transport equation (Eq. (2.37)), has negligible effects, so that simulating different values of the current density is not necessary.

6.2.2 Governing equations, computational domain and boundary conditions

The present CFD simulations are based on the modelling approach described in section 2.5.1. The periodic domain of the channel, named Unit Cell, was simulated assuming fully developed flow and concentration fields. The Unit Cell for the profiled-membrane channels was built up by joining the centres of four profiles (see Figure 6.3a). A totally equivalent domain would be that indicated in Figure 6.3b. Figure 6.4 shows an example of Unit Cell chosen for the two profile shapes and for the spacer-filled channel investigated in the present chapter.

The governing equations implemented for the periodic domain were: the continuity Eq. (2.1), the Navier–Stokes Eqs. (2.36) and the transport Eq. (2.37). The body force per unit volume K_p in Eq. (2.36) was set in order to force the fluid to move (effect of the large-scale pressure gradient). The relationship K_p-*Re* was found by preliminary simulations; then K_p was set in order to achieve a range of Reynolds numbers between 0.5 and 32. The maximum value investigated is relatively high for this kind of applications; the corresponding fluid velocity is around 0.1 m/s. However, an important feature of profiled-membrane channels is a lower friction factor, which allows operating at higher Reynolds numbers compared to those typical of spacer-filled channels. The source term

S depending on the large-scale concentration gradient K_c was implemented in Eq. (2.37). A Neumann boundary condition was set for the concentration at the walls: a homogeneous diffusive flux, corresponding to the current density according to Eq. (2.42), was imposed at the upper and lower walls, while the flux is set to zero at the lateral walls (fluid-membrane profile interfaces). The latter assumption was done considering that an ion close to the membrane profile would cross solution and membrane more easily than profile and membrane, especially for highly conductive solutions and profiles with a high *l*/*h* ratio. Furthermore, the ionic current across the membrane profiles is expected to be so low due to their small area, that its contribution to the overall current is negligible.

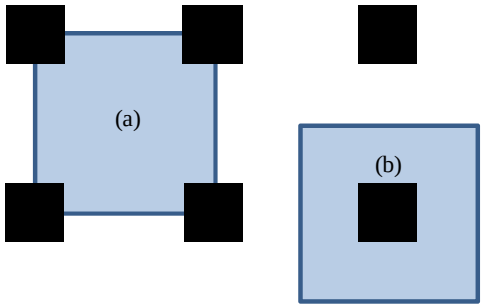

Figure 6.3. Possible equivalent Unit Cells. Type (a) was chosen in the present work.

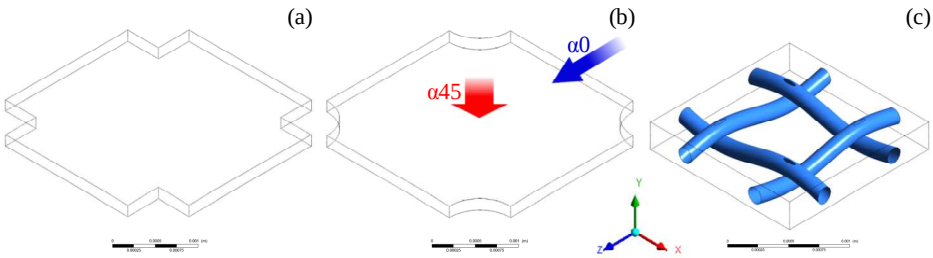

Figure 6.4. Unit Cell geometry for (a) *s-l1-L3* channel, (b) *c-l1-L3* channel and (c) spacer-filled channel.

Multi-block hexahedral grids were used for the discretization of the computational domain. The size of the computational cells employed along the thickness of the channel (i.e. h = 160 μm) was chosen to be the half of the sizes imposed along the other two

directions thus resulting into a grid much finer in the direction perpendicular to the membranes. A refinement was also set towards these walls. A grid independence analysis was performed and the parametrical study was conducted using grids still providing grid independent results. More precisely, various grids were tested, generated by setting a number of divisions of the channel thickness ranging from 10 to 60; the comparison of the results established a grid independence for meshes with a minimum number of divisions of the thickness equal to 30 (vertical element size equal to 5.33 μm). Therefore this size was chosen for carrying out all the simulations reported in the present chapter. It results into grids with a number of computational cells ranging from ~$1 \cdot 10^6$ to ~$4 \cdot 10^6$ depending on the specific pitch to height ratio.

A hybrid hexahedral-tetrahedral grid was generated for the case of the spacer-filled channel (~$1.6 \cdot 10^6$ of computational cells) as described in detail in section 4.2.2.1. Figure 6.5 shows enlarged details of meshes employed for two profiled-membrane channels and for the spacer-filled channel.

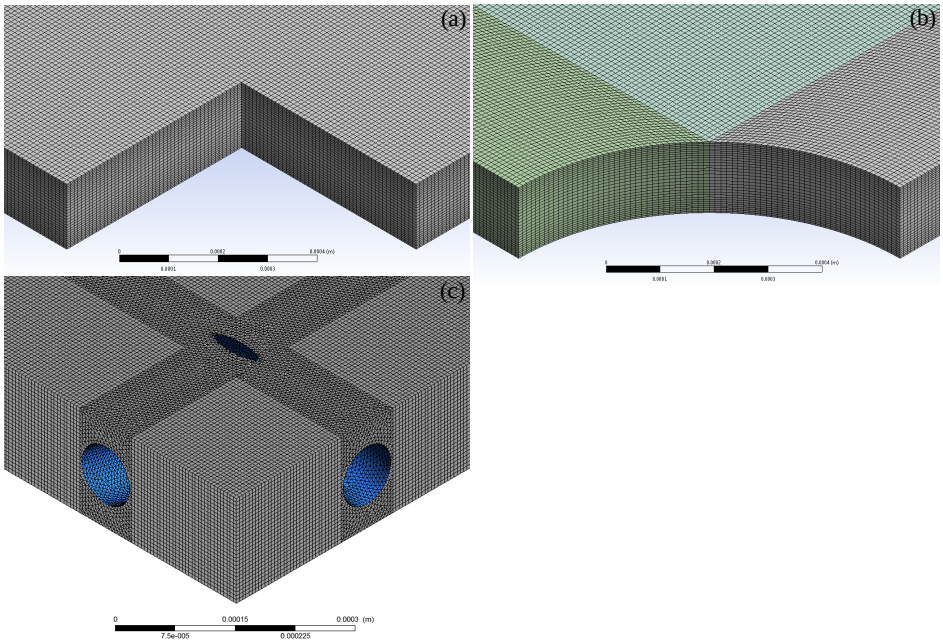

Figure 6.5. Discretization of the Unit Cell for (a) *s-l1-L3* channel, (b) *c-l1-L3* channel and (c) spacer-filled channel.

6.3 Results and discussion

In this section, simulation results are presented and discussed by analyzing the effect of geometric parameters and fluid dynamic conditions on fluid flow and mass transfer. In section 4.3.2 the effect of profile shape, flow attack angle and Reynolds number is investigated for l = 1 mm and L = 3 mm (cases *l1-L3*). Then, in section 6.3.2, the parametrical analysis is focused on the effect of profile size l and pitch L while the other parameters are kept fixed; in particular, for the circular shape, the flow attack angle *α45*, and Re = 8, the effect of three values of l (*l0.75*, *l1*, *l1.5*) for the pitch *L3* and three values of L (*L2*, *L3*, *L4*) for the size *l1* is assessed, so that the ratios L/l = 2, 3, 4 are investigated (see Table 1.1).

6.3.1 Influence of profile shape, flow attack angle and Reynolds number

6.3.1.1 Velocity and concentration fields

Figure 6.6 reports contour plots of the streamwise velocity component u_s (normalized by $u_{s,ave}$) on a *x-z* plane placed at mid-height, for cases *l1-L3* at Re = 8 ($u_{s,void} \approx$ 2.3 cm/s, a typical value for RED channels). The profiles are full-thickness obstacles which influence the fluid motion, so that the flow field deviates significantly from that relevant to a corresponding empty channel. Clearly, the absence of velocity components perpendicular to the membranes is a prominent feature of profiled-membrane channels. The cross-section of the channel is periodically reduced by the obstacles, thus resulting in a velocity increase between two profiles, especially close to the obstacles themselves. At the same time, low-velocity wake zones can be recognized both downstream of each obstacle and in the stagnation areas just upstream of the next obstacle. This is more evident for the *α0* cases. Circular shaped obstacles provide a velocity distribution more uniform than square obstacles due to the lack of sharp edges. The velocity field is characterized by a saddle shape strongly influenced by the attack angle. For the *α0* cases, in the central part of the unit cell there is a minimum along the flow direction and a maximum in the direction perpendicular to it, while this feature is inverted for the *α45* cases.

The streamlines are affected by the obstacles and follow their boundary in the region close to them, as highlighted by the velocity vector plots in Figure 6.7. No flow separation is observed, which indicates the presence of a creeping flow regime.

Figure 6.8 reports maps of the local polarization factor $\theta = \hat{C}_b / C_w$ on one of the walls for the same cases of Figure 6.6 and Figure 6.7. In the *α0* cases, the θ distribution is highly non-uniform. The lowest θ values correspond to regions of high wall concentration, associated with low mass transfer coefficients, and are observed in the calm regions between two profiles along the main flow direction and all around the profiles. On the contrary, high θ values are observed in the central region; note that local values of $\theta > 1$ are compatible with $\theta_{ave} < 1$. The case *α45* results in a much more homogeneous distribution of concentration, leading to higher average polarization factors (i.e. less polarization effects).

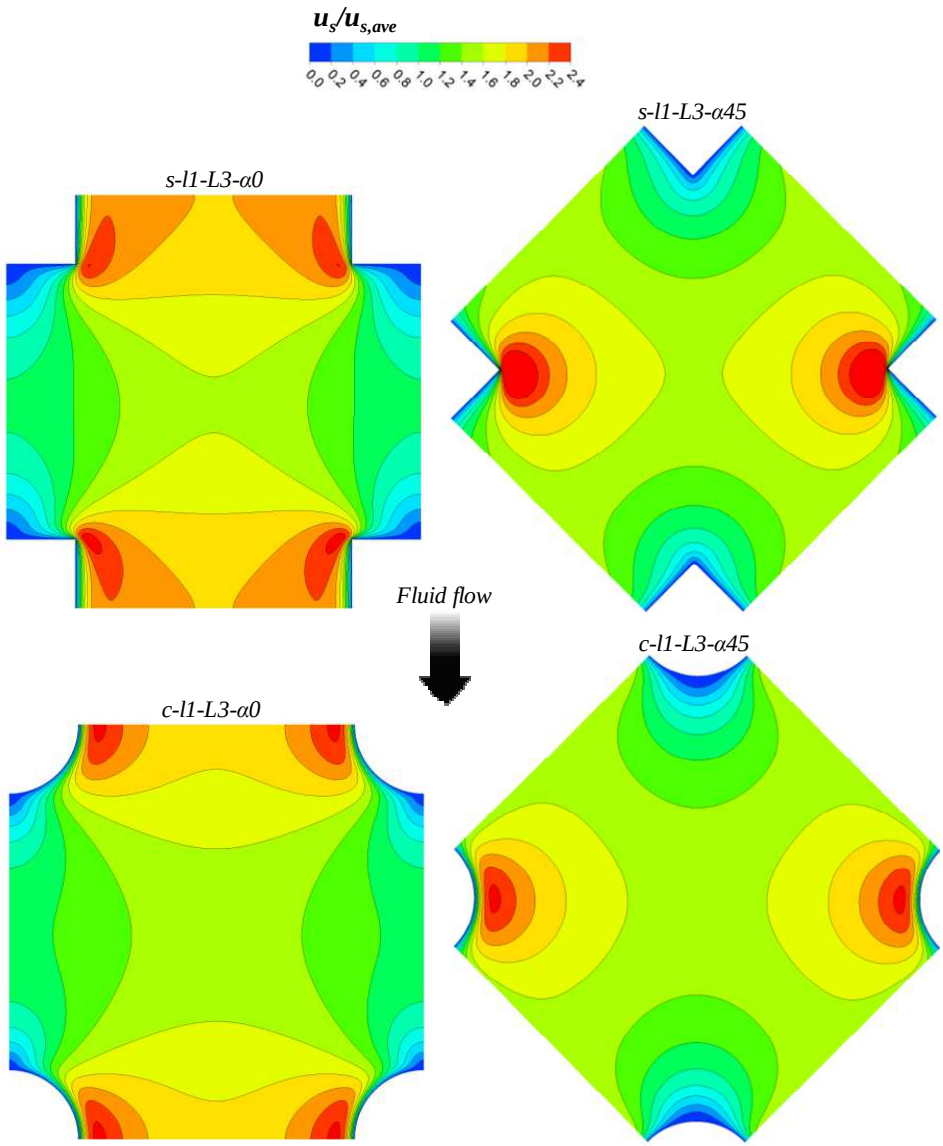

Figure 6.6. Maps of the normalized streamwise velocity component on the *x-z* midplane for *s-l1-L3-α0*, *s-l1-L3-α45*, *c-l1-L3-α0* and *c-l1-L3-α45* channels at *Re* = 8.

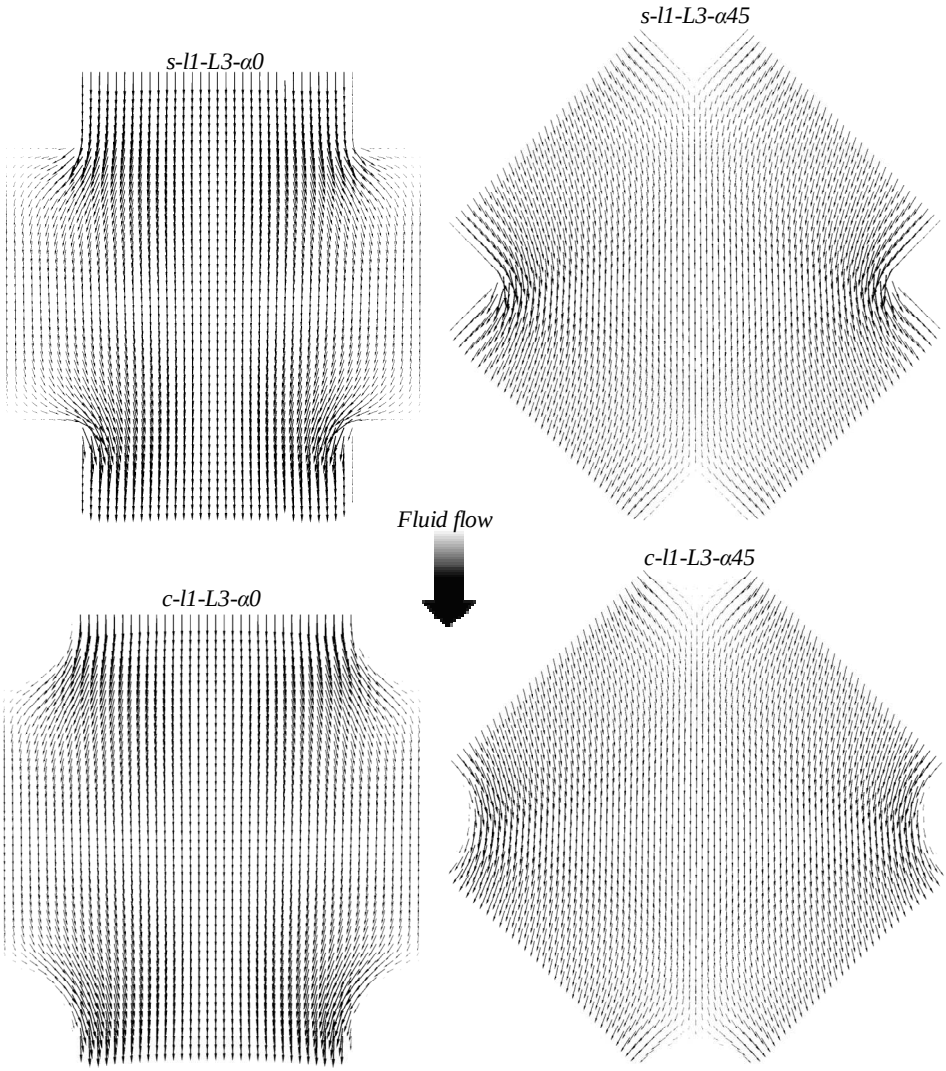

Figure 6.7. Velocity vector plots on the *x-z* midplane for *s-l1-L3-α0*, *s-l1-L3-α45*, *c-l1-L3-α0* and *c-l1-L3-α45* channels at *Re* = 8.

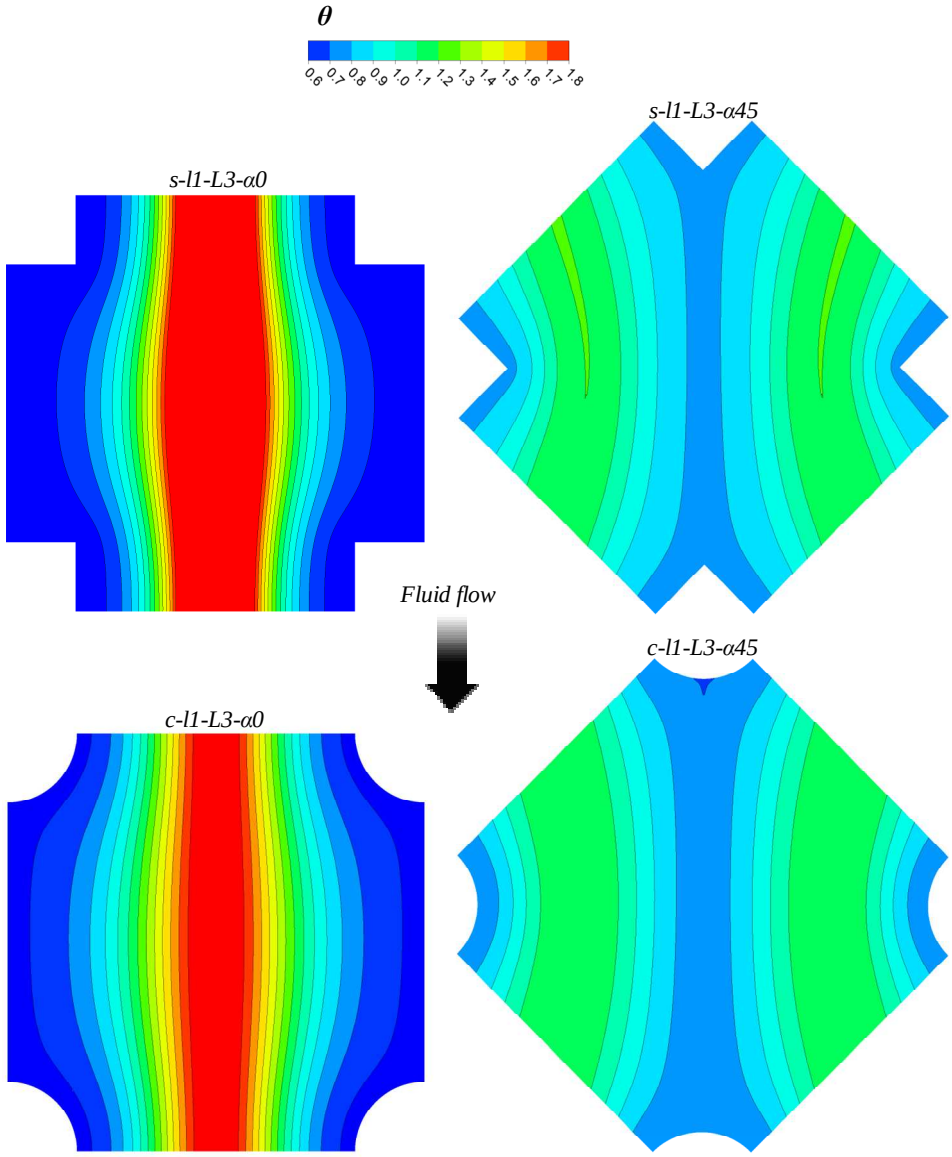

Figure 6.8. Maps of the local polarization factor $\theta = \hat{C}_b / C_w$ on one of the fluid-membrane interfaces for *s-l1-L3-α0*, *s-l1-L3-α45*, *c-l1-L3-α0* and *c-l1-L3-α45* channels at *Re* = 8.

In order to show how the flow dynamics conditions affect concentration polarization, Figure 6.9 reports concentration profiles in the direction perpendicular to the membranes for cases *c-l1-L3-α0* (a) and *c-l1-L3-α45* (b) at various *Re*. The concentration is averaged

in each plane parallel to the walls and normalized by its bulk value. Notwithstanding the absence of a velocity component perpendicular to the walls, a significant reduction of the normalized mean concentration at the walls (i.e. a significant increase of $\theta_{ave} = \hat{C}_b / \overline{C}_w$) is obtained at higher *Re*. The influence of *Re* is more evident for α = 0°. For low *Re*, the lowest $\overline{C}_w$ values (i.e. highest θ_{ave} values) are obtained for α = 45°, while for the highest *Re* (32) the distributions are very similar for the two angles. The same profiles are practically obtained at *Re* = 0.5 and *Re* = 2, due to self-similar creeping flow distributions at very low Reynolds numbers. For higher *Re*, the curve shape varies because of the lack in self-similarity of the fluid flow and concentration fields caused by the presence of the profiles within the channel [24, 142]. Note that in Figure 6.9 concentration values are simple area averages and are everywhere larger than the bulk concentration, which is a mass flow average, due to the influence of low-speed, high-concentration regions; as expected from the velocity maps in Figure 6.6, this effect is much more evident for α = 0° and low Reynolds numbers.

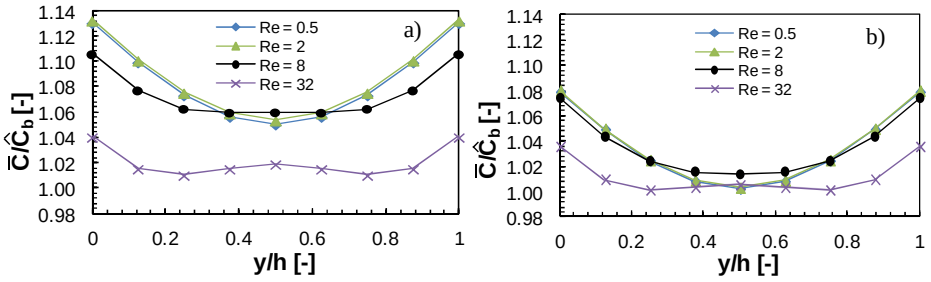

Figure 6.9. Normalized area-averaged electrolyte concentration in the direction perpendicular to the membrane-solution interfaces at various *Re* for channels (a) *c-l1-L3-α0* and (b) *c-l1-L3-α45* .

6.3.1.2 Global parameters

In Figure 6.10 the Fanning friction factor (see Eq. (2.45)) is reported as a function of the Reynolds number for the *l1-L3* cases. *f* is normalized with respect to that in an empty channel (24/*Re*). Unlike net spacers, the membrane profiles investigated here lead only to slight increments of pressure drops with respect to the empty channel, mainly due to the associated area restriction. It is worth noting that the flow attack angle has practically no effect for the circular shape and only a small effect, limited to the highest *Re*, for the

square shape, notwithstanding it affects heavily the flow field (see Figure 6.6 and Figure 6.7). This means that, especially for the circular profile shape, overall pressure drop is the sum of the individual pressure drops across each obstacle and thus depends only on the number of obstacles per unit area, which, of course, does not depend on the flow attack angle. On the contrary, the obstacle shape has a more significant influence; the square shape implies a friction factor ~8% higher than the circular one. Note that, in the present range of *Re*, the friction factor for the net spacer-filled channel is ~6 times higher than in the empty channel. Up to $Re \approx 10$, the friction factor for the profiled geometries can be interpolated by power functions as

$$f = ARe^{-1} \tag{6.1}$$

For the empty channel $A = 24$. For the profiled-membrane channels $A \approx 29.6$ (circular obstacles) and $A \approx 32.0$ (square obstacles). At higher *Re* the exponent in Eq. (6.1) begins to deviate from -1, since the obstacles induce slight but increasing inertial effects, generating flow fields which do not remain self-similar as *Re* increases.

The pumping power consumption represents a fundamental factor affecting the process efficiency as it determines the net power producible by the stack. Therefore, a more effective comparison of RED channels can be done by considering the dimensionless power number *Pn*, defined in Eq. (2.46). This quantity is reported in Figure 6.11 as a function of the Reynolds number for (i) *l1-L3* cases, (ii) empty and (iii) spacer-filled channels.

The relationship *Pn-Re* can be expressed by an equation in the form

$$Pn = BRe^{m} \tag{6.2}$$

where $B = A/8$ and $m \approx 2$. Compared to the empty channel, the profiled-membrane channels provide an increment in *Pn* of about 23% and 33%, respectively, for the circular and square shape, while the spacer-filled channel requires a pumping power increase of ~5.7 times. The square shape requires a pumping power about 8% larger than the circular shape. Notably, the flow attack angle is irrelevant for the profiled-membrane channels, as discussed above with regard to *f*.

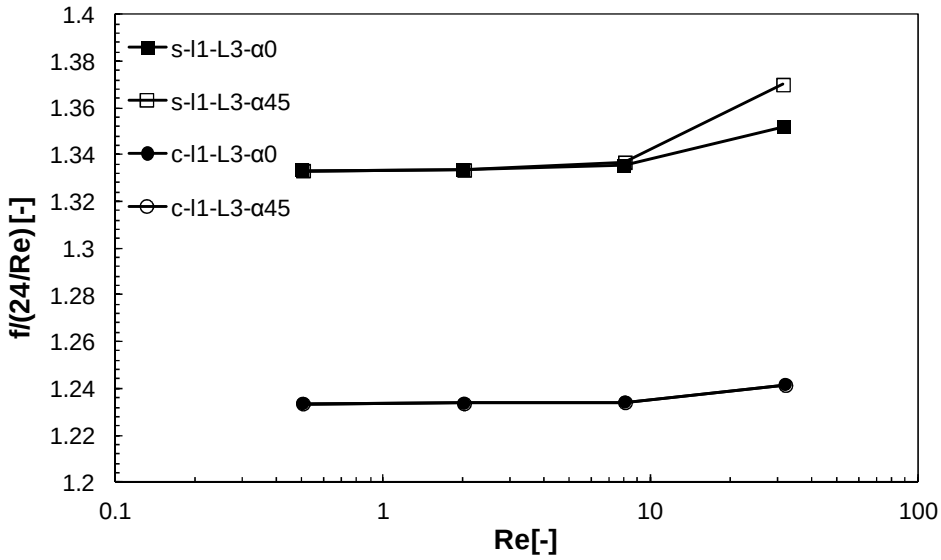

Figure 6.10. Fanning friction factor normalized by that pertaining to an empty channel (24/*Re*) as a function of the Reynolds number for *l1-L3* profile configurations.

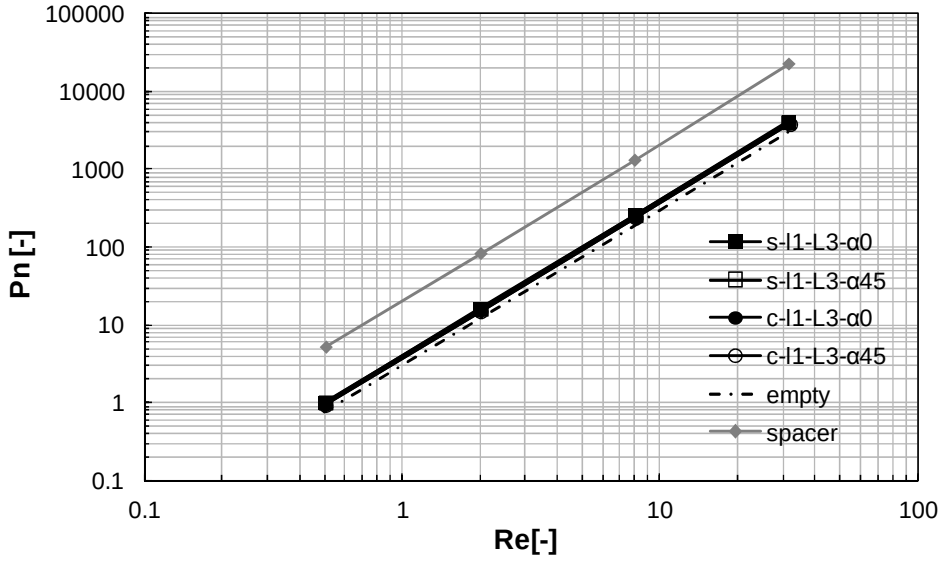

Figure 6.11. Dimensionless power number as a function of Reynolds number for *l1-L3*, empty and spacer-filled channels.

The results obtained regarding the average polarization factor defined in Eq. (2.54) are reported in Figure 6.12 which shows θ_{ave} as a function of *Re* for the cases *l1-L3*. Clearly, due to geometric symmetry and imposed equal fluxes, θ_{ave}-values for upper and lower walls are equal. In the empty channel, self-similar parallel flow is present at all *Re*, thus resulting in a θ_{ave}-value independent of the Reynolds number. In the profiled-membrane channels, a significant increase of θ_{ave} can be observed as *Re* increases beyond ~4 (creeping flow regimes), due to the increased inertial fluid flow phenomena favouring a mass transfer enhancement.

It is worth observing that profiled-membrane channels offer performance even worse than the empty channel at low *Re*. This is due to the regions of high polarization (low θ) which arise streamwise between two profiles and around the profiles, as discussed above (Figure 6.8). At higher *Re*, the mean polarization factor is higher for the profiled-membrane channels. Analogous considerations can be inferred by plotting θ_{ave} against the Power Number *Pn* (Figure 6.13): there exists a cut-off value of *Pn*, depending on the specific profiled geometry, beyond which profiled membranes become more efficient than the empty channel.

In the range of *Re* investigated, the spacer-filled channel simulated here is the configuration yielding the maximum θ_{ave}. A large mass transfer enhancement is obtained because the woven arrangement of the spacer wires gives the fluid significant velocity components perpendicular to the walls, whose relative importance increases as the flow rate increases. Moreover, the flow attack angle *α45* avoids the presence of stagnant zones.

By comparing the different profile configurations considered in Figure 6.12 and Figure 6.13, it can be observed that the flow attack angle affects significantly mass transport, although it has only slight effects on pressure losses. As highlighted above, high polarization regions occur within the system for the case *α0*, thus leading to a lower θ_{ave}. The shape of the profiles seems to affect polarization phenomena more in the case *α0*, where the circular shape allows a higher θ_{ave}; on the contrary, very similar θ_{ave}-values are obtained for the two shapes in the case *α45*. However, at high *Re* all the configurations provide a similar performance. Therefore, channel geometry and orientation might have a significant effect on polarization phenomena, but their relative importance depends on the flow rate.

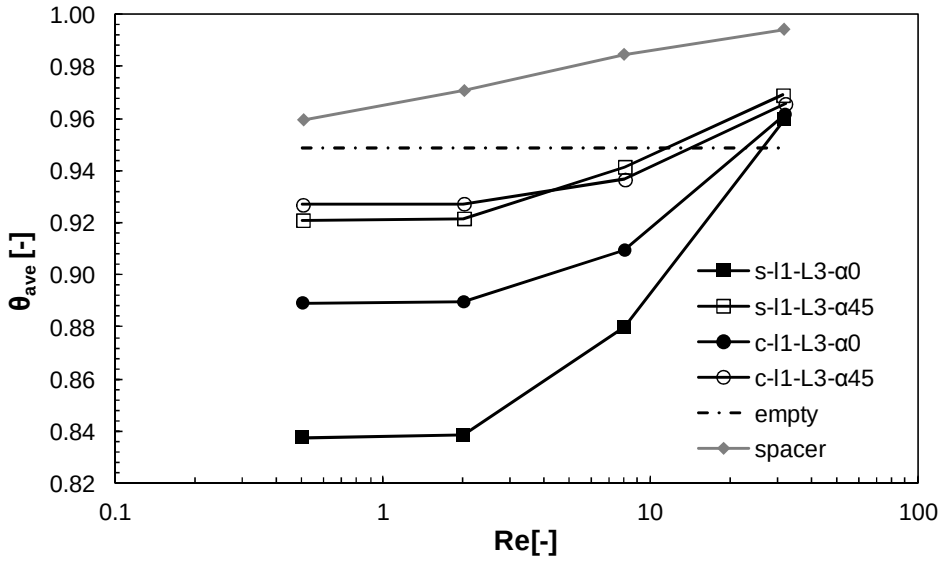

Figure 6.12. Average polarization factor θ_{ave} as a function of the Reynolds number for *l1-L3*, empty and spacer-filled channels.

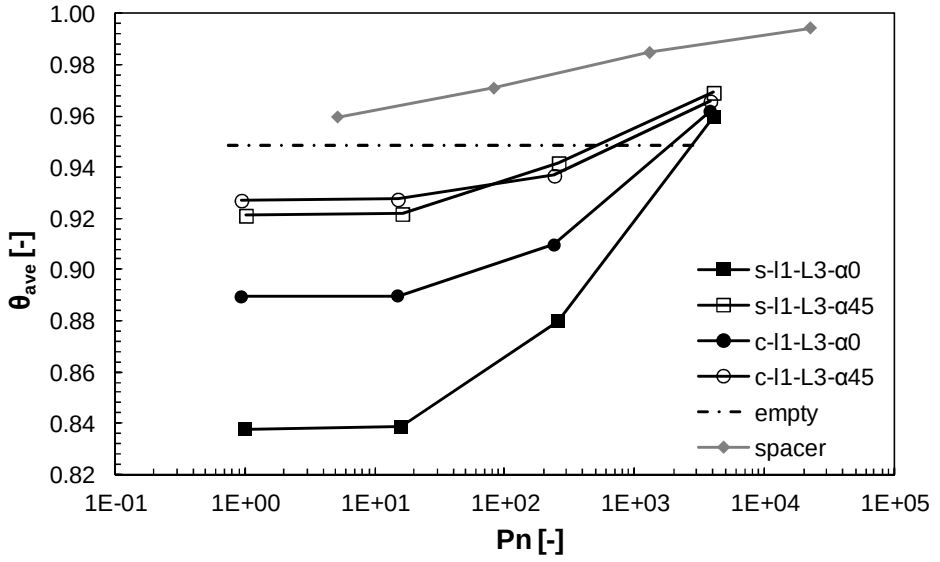

Figure 6.13. Average polarization factor θ_{ave} as a function of the dimensionless power number for *l1-L3*, empty and spacer-filled channels.

6.3.2 Influence of size and pitch

6.3.2.1 Velocity and concentration fields

In this section the effects of the size l and pitch L of the profiles is analysed (L/l = 2, 3, 4). For simplicity, the comparison is restricted to the circular shape, the flow attack angle $\alpha 45$ at Re = 8. Figure 6.14 and Figure 6.15 show normalized streamwise velocity maps and corresponding vector plots on an x-z plane placed at mid-height. Note that all configurations are represented to the same geometrical scale. At the fixed value of the size $l1$, increasing L the effects are: (i) a more homogeneous velocity field, i.e. a larger portion of the plane exhibits velocities close to the average; (ii) velocity vectors more aligned to the main flow direction s, i.e. a less tortuous flow path. Similarly, at the fixed value of the pitch $L3$, the reduction of l provides practically the same effects. Summarizing, similar flow fields are found for the geometries with the same L/l ratio ($l1$-$L2$ with $l1.5$-$L3$, $l1$-$L4$ with $l0.75$-$L3$). This shows that the influence of the L/h or l/h ratios is only minor.

The local polarization factor θ on one of the walls is reported in Figure 6.16. Note that the scale of θ in this figure was kept equal to that adopted in Figure 6.8 although the present variation range is much more limited. Therefore, the central map in Figure 6.16 identical to that reported in Figure 6.8 for the same configuration (c-$l1$-$L3$-$\alpha 45$). As L increases, a slightly less uniform distribution of θ is obtained; conversely, as l decreases, only a smaller variation of θ distribution is found, but the trend is inverted.

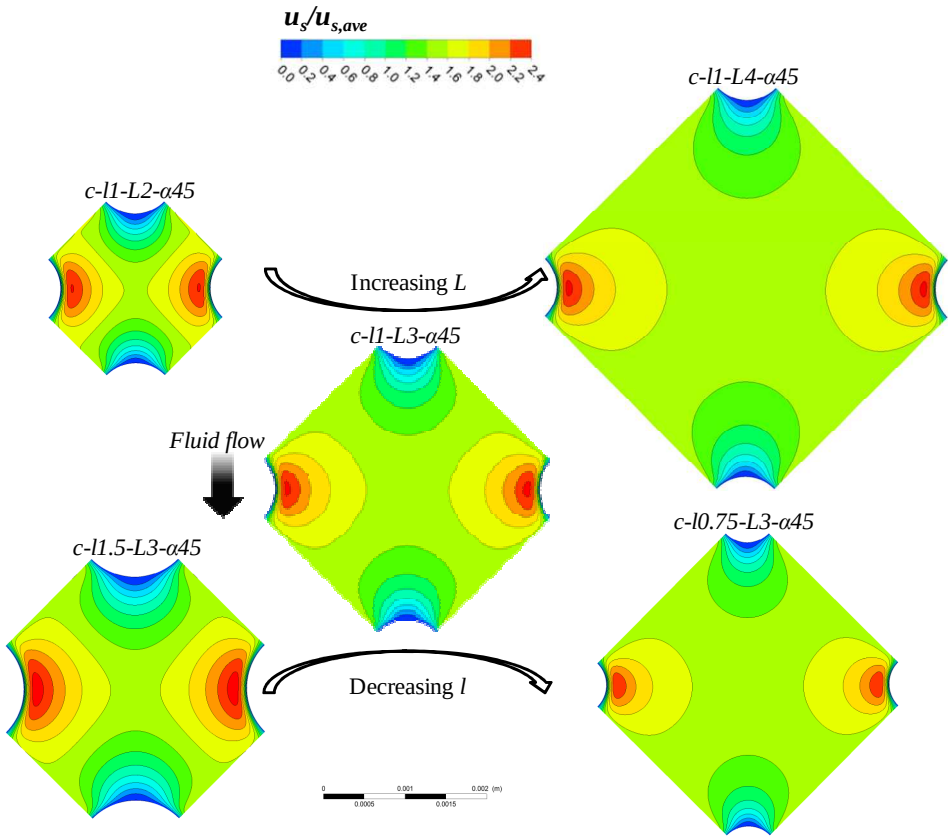

Figure 6.14. Maps of the normalized streamwise velocity component on the *x*-*z* midplane for *c-l1-L2-α45*, *c-l1-L4-α45*, *l1-L3-α45*, *l1.5-L3-α45* and *l0.75-L3-α45* channels at *Re* = 8.

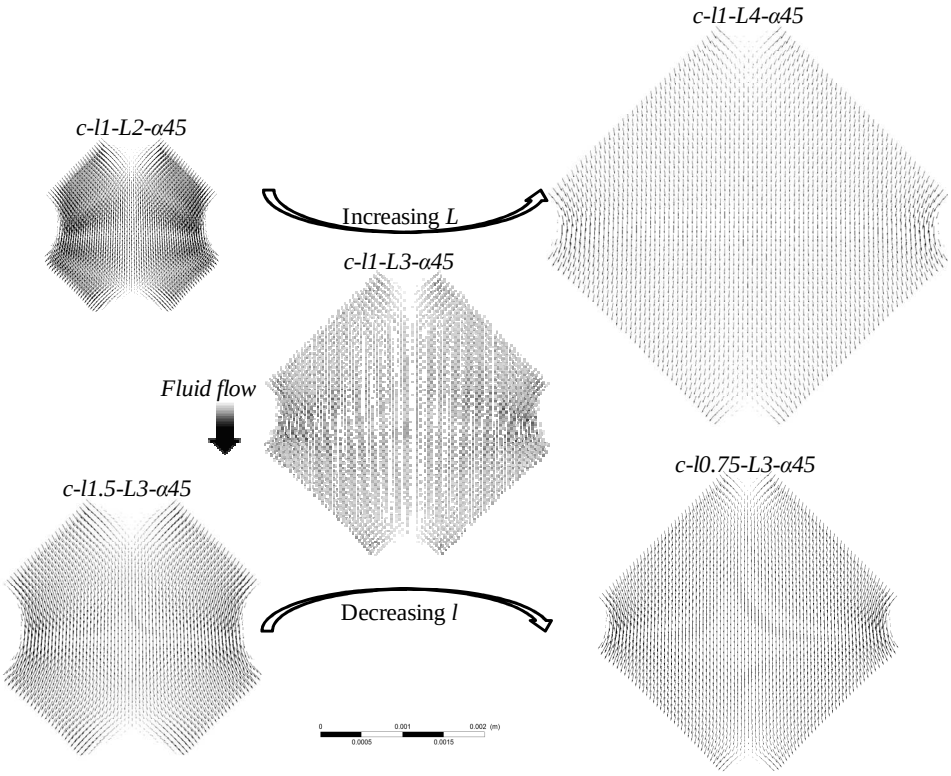

Figure 6.15. Velocity vector plots on the *x-z* midplane for *c-l1-L2-α45*, *c-l1-L4-α45*, *l1-L3-α45*, *l1.5-L3-α45* and *l0.75-L3-α45* channels at *Re* = 8.

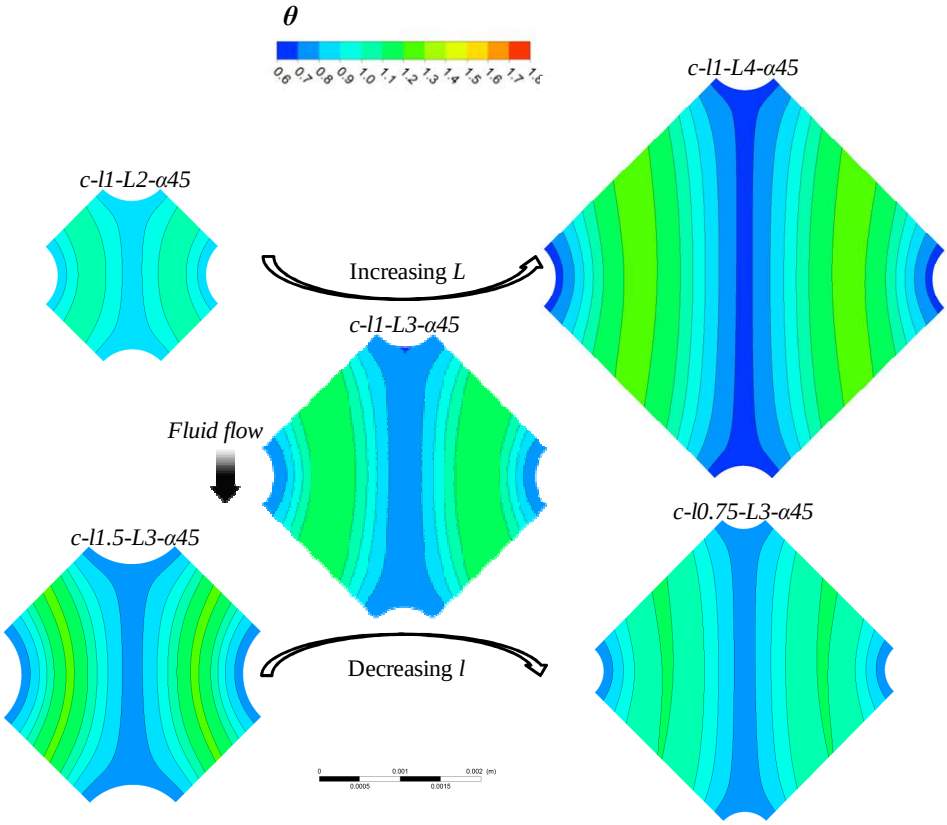

Figure 6.16. Maps of the local polarization factor $\theta = \hat{C}_b / C_w$ on one of the fluid-membrane interfaces for *c-l1-L2-α45*, *c-l1-L4-α45*, *l1-L3-α45*, *l1.5-L3-α45* and *l0.75-L3-α45* channels at *Re* = 8.

6.3.2.2 Global parameters

The dependence of the friction factor *f* on *l* and *L* is shown in Figure 6.17. Here, *f* is normalized by the value relevant to an empty channel (24/*Re*) and is reported as a function of *L/l*. As *L/l* increases, hydraulic friction is reduced and tends to attain the value relevant to the empty channel, both in the case of increasing pitch *L* and in the case of decreasing size *l*. For a given value of *L/l*, the absolute value of the two parameters has a negligible impact; in fact, the maximum discrepancy is just of 3%, obtained for *L/l* = 2. This confirms again the small importance of the *L/h* and *l/h* ratios.

When *L/l* decreases, an increasing rate of increment of the friction coefficient can be observed compared to the empty channel (up to +62% for the case *c-l1-L2-α45*), while it

remains noticeably lower than that exhibited by the spacer-filled channel (~6.8·24/*Re*). Note that, for a fixed *Re*, the power number *Pn* defined by Eq. (2.46) is proportional to *f* as *L*/*l* varies, so that it is not reported here.

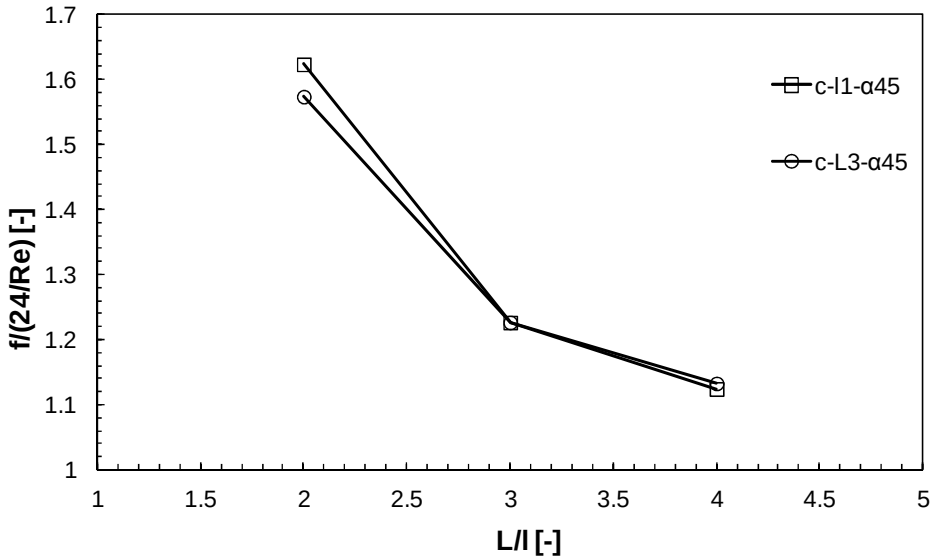

Figure 6.17. Fanning friction factor normalized by that pertaining to an empty channel (24/*Re*) as a function of the profile pitch-to-size ratio for *c-α45* channels at *Re* = 8.

Figure 6.18 shows the dependence of the mean polarization factor θ_{ave} on *L* and *l*. As *L*/*l* varies, two different behaviours are found on the basis of the absolute value of *L* and *l*. For increasing *L* and fixed *l*, lower θ_{ave}-values are obtained. Conversely, when *l* decreases, for a fixed *L*, θ_{ave} increases. Among the cases investigated, the maximum θ_{ave} is achieved for *c-l1-L2-α45* which is also the case of with the highest *f* (Figure 6.17).
Clearly, a trend asymptotically approaching the θ_{ave}-value of the empty channel is expected for $L/l \rightarrow \infty$. With respect to the spacer-filled channel, mixing remains less favoured for the present low *Re* (8); however, as shown by Figure 6.12 and Figure 6.13, values of θ_{ave} higher than in the empty channel are obtained for higher Reynolds numbers.

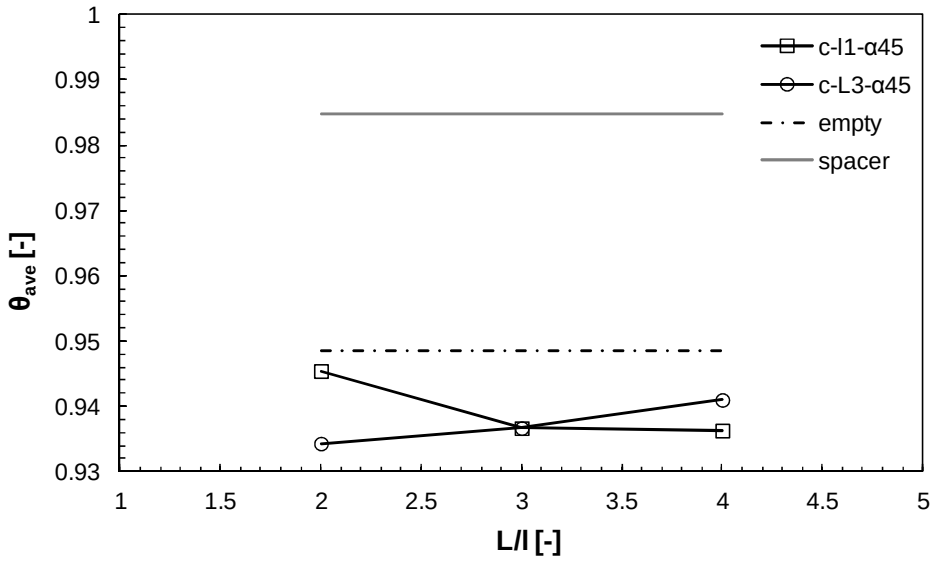

Figure 6.18. Average polarization factor θ_{ave} as a function of the profile pitch-to-size ratio for *c-α45* channels at *Re* = 8. Empty and spacer-filled channels are also reported for comparison.

6.4 Conclusions

CFD simulations of channels with profiled membranes for RED, not yet investigated up to now, were carried out. The profiles were "pillars" that create the channels for the feed solutions. The effect of various parameters of the channel configuration on fluid flow and mass transfer was assessed. Velocity and concentration fields highlight the presence of calm zones of high polarization near the profiles and in the part of the channel comprised between two consecutive profiles along the main flow direction. This kind of geometries, does not generate velocity components perpendicular to the membranes. At low Reynolds numbers (*Re*) a creeping flow regime is present; as *Re* increases, inertial effects arise, thus causing a non self-similarity of the flow field which, in its turn, (i) enhances the rate of increase of the pumping power consumption (*Pn*) with *Re* and (ii) favours mass transfer enhancement.

The flow attack angle α has an important role in determining velocity and concentration fields: the velocity distribution in a midplane parallel to the walls exhibits a saddle shape with features inverted from $\alpha = 0°$ to $\alpha = 45°$; a more uniform distribution of concentration is obtained in the case of $\alpha = 45°$. With regard to the global parameters, it has practically irrelevant effects on *Pn*, especially for the circular profiles and low

Reynolds numbers; also, higher average polarization factors θ_{ave} (lower polarization effects) are found in the case of the flow attack angle $\alpha = 45°$ for both shapes.

The shape of the profiles is found to affect velocity and concentration fields very slightly, and an increment of 8% in *Pn* is caused by the square shape respect to the circular one. Circular profiles give rise to a better mixing than square ones for $\alpha = 0°$ while the influence of shape on polarization is minimal for $\alpha = 45°$. Anyhow, at higher *Re* ($\geq$32) a similar θ_{ave} is achieved regardless shape and α.

A parametric analysis, focused on the effect of profile size *l* and pitch *L* in circular profiles and at $\alpha = 45°$, shows that increasing *L*/*l* (2, 3, 4) leads to a less tortuous flow path, a more homogeneous velocity distribution, and a reduction of *Pn* with very similar effects caused both by the increase in *L* and by the decrease of *l* (i.e. less "filled" channel). On the contrary, the concentration field and the average polarization factor vary in a different way as a function of the two parameters *L* and *l*: as *L* increases (2, 3, 4 mm) with *l* = 1 mm, the local polarization field is less uniform and θ_{ave} decreases; as *l* decreases (1.5, 1, 0.75 mm) with *L* = 3 mm, a slightly more uniform θ distribution is found and θ_{ave} increases.

Profiled-membrane channels provide a power number *Pn* comparable with that relevant to the empty channel, (maximum increment ~62% for the configuration *c-l1-L2-α45*) in the range of the flow rates investigated. Mass transfer is disadvantaged by calm zones with high local polarization, so that, at low *Re*, θ_{ave}-values even worse than that pertaining to the empty channel are obtained. However, beyond a cut-off value of *Re* $\approx$ 10-20, depending on the configuration, mixing is better than that offered by the empty channel, whose performance is independent of *Re*.

Compared to a high-performance net spacer-filled channel, *Pn* was found to be about 5 times lower in the profiled-membrane channels. On the other hand, mixing is improved by adopting a net spacer. Nevertheless, θ_{ave}-values (of spacer-filled and profiled-membrane channels) tend to get closer at high *Re* and profiled-membrane channels promise to offer even better performance at higher *Pn*.

Finally, it should be stressed that the θ_{ave}-values found in this work are quite close to 1 for seawater, but they can be much lower for more diluted solutions. In fact, polarization effects greatly increase as the solution bulk concentration decreases, becoming prominent for solutions as brackish or river water. Although the *difference* of concentration between bulk and membrane-solution interface is similar at various bulk

concentrations (at a given current density), very different effects on the driving force can be obtained, quantified by the polarization factor which represents the *ratio* of bulk and interface concentration.

However, the results of the present work confirm that the fundamental feature of channels generated by profiled membranes is a significant reduction of pumping costs with respect to spacer-filled channels. Also, suitable profiled membrane geometry and Reynolds number can lead to a comparable reduction of polarization phenomena, which, combined with advantages as lower electrical resistance, higher membrane active area and lower costs, makes the profiled-membrane channels a promising alternative for the optimization of the RED process. Finally, this study lays the groundwork for assessing performance of profiled-membrane channels, which offer endless geometric possibilities.

CONCLUSIONS AND FUTURE PERSPECTIVES

The present thesis is devoted to the Computational Fluid Dynamics (CFD) analysis of reverse electrodialysis (RED) systems. Fluid dynamics and associated mass transfer phenomena were studied, giving a scientific contribution to the stack design and optimization and the evaluation of the most effective operating conditions. In order to fill some main gaps in the literature, the following activities were carried out:

(i) developing a CFD modelling tool;

(ii) investigating RED channels and influence of feed flow rate and features;

(iii) simulating the hydraulic circuit of a stack;

(iv) validating the simulation results.

(i) A 3D CFD model was devised for the detailed analysis at small scale of RED channels in the framework of a hierarchical simulation strategy of the process. From the Stefan–Maxwell approach and assuming the local electroneutrality condition, the transport equation of a binary electrolyte (NaCl), suitable also for concentrated solutions, can be derived. Preliminary simulations of an empty channel showed that the concentration field is greatly controlled by the diffusive transport, while the migrative one had an impact definitely negligible. Therefore, it was shown that mass transfer in RED channels can be dealt simply by a convection-diffusion equation. As a consequence, the transport equation was implemented without the migrative term and the migrative fluxes were simply superimposed with the diffusive ones and reflected in the boundary conditions (a a single channel was simulated and membranes are not included). The diffusive term depends on the concentration itself, but this non-linearity had negligible effects (the diffusivity correction varied by less than 1%). Also, the Navier–Stokes equations and the transport equation were suitably manipulated, in order to simulate a periodic domain, where fully developed conditions can be assumed.

(ii) Low Reynolds numbers (*Re*) typical of RED were analysed. In these conditions, as the Schmidt number (*Sc*) increases, the Sherwood number (*Sh*) increases more at higher *Re*; also, polarization *effects* greatly decrease as the solution concentration increases, as the voltage over the membrane depends on the *ratio* of the solutions activities. In particular, they are important for river water, barely significant for seawater, and practically negligible for brine. Thus different optimization strategies should be employed depending on the feeds concentration.

Different channel configurations were investigated, including geometries not simulated so far: commercial spacers, and customised spacers and profiled-membrane channels in parametric analyses. The spacers were with crossing filaments at 90° with either woven (*w*) or overlapped (*o*) arrangement; also a spacer with overlapped filaments at 60°-120° was simulated; profiled-membrane channels were devised by pillars in square pitch.

The flow regime was found to be steady. The symmetry/antisymmetry geometric features were reflected on flow and concentration fields. Calm regions with low velocities and poor mixing were created by the obstacles (wires or pillars). At low *Re* the flow regime was creeping. As *Re* increases, inertial effects were induced by the obstacles, i.e. the fluid is forced to move more chaotically (secondary flows), thus the flow fields lose the self-similarity; therefore a mixing enhancement is obtained and the rate of increase of the pumping consumption (power number, *Pn*) with *Re* increases (*Pn* proportional to Re^m, where *m* is slightly larger than 2). All the channel configurations were found able to provide *Sh* values higher than the empty channel beyond a cut-off value of *Re*, despite they exhibit always larger pressure drop. The curves *Sh*-*Re* have positive concavity directed upwards in the range of *Re* investigated here.

Different angles between overlapped filaments may provide different performance; nevertheless, the filament arrangement was found to be the crucial feature for the flow and concentration fields. Woven spacers were found to be more effective than the overlapped ones, as they enhance mass transfer by complex flow fields with significant vertical and lateral motions at any given *Pn*. The effects of flow attack angle and filament spacing are more complex as *Re* varies and are different for the two wires arrangements. However, in spacers with wires at 90°, for any wire arrangement a flow attack angle of 45° results in more cost effective mixing compared to the flow direction parallel to one filament. The configuration that provides the best mixing conditions both for any given *Re* and *Pn* was the woven spacer with pitch to height ratio of 2 (the minimum investigated) and flow attack angle of 45°.

Simulations with the free-slip condition, achievable in completely hydrophobic materials, showed reduced pressure losses (by ~44%); thus also the use of special spacer materials might be a reliable way to optimize the process.

A theoretical evaluation of the possibility of choosing a porous medium in place of the net spacer revealed that a feasible porous medium made of small fibers causes much larger pressure drops.

In the profiled-membrane channels, the pillars modified significantly the flow and concentration fields, although they did not generate velocity components perpendicular to the membranes. The effects that arise from the interaction of the various geometrical parameters were complex. However, these configurations exhibited *Pn* being much lower than a net spacer-filled channel and very close to that of the empty channel; on the other hand calm zones generated by the profiles may accentuate polarization phenomena with respect to the empty channel at the usual low *Re* for RED. Nevertheless, at high *Re* profiled membranes promise to offer performance closer to that of spacers.

(iii) An analysis at larger scale of the stack was performed. 2D simulations were carried out on a simplified hydraulic circuit of a stack with 50 channels, equipped with improved manifolds in rectangular geometry and being wide as the channels. The results showed that a fluid flow optimization of a RED apparatus must not focus on channel features only. In fact, the rectangular distribution system was shown to be very effective to decrease dramatically the pressure loss compared to a conventional stack with small cylindrical ducts.
A more homogeneous distribution of flow rates among the channels can be obtained by increasing the pressure drops along the channel, decreasing hydraulic losses in the distributor and reducing the total flow rate. The adoption of a symmetric feeding system and a larger number of inlets and outlets is suggested to even the flow rates distribution and decrease the pressure losses.

(iv) Pressure drop measurements were performed. A fair agreement was found between CFD simulation results and experimental data on hydraulic loss along the channel. Moreover, simulation results were compared with experimental and CFD data on pressure drop and mass transfer from literature and a satisfactory agreement was found. Therefore, the CFD modelling was shown to be a reliable predicting tool to investigate any customised geometry, offering the advantages of a cost effective and detailed analysis at small scale, which is very important for the system optimization.

CFD model outcomes and next steps

The present CFD modelling is the first step of a structured simulation tool and represents the support base for the higher levels of modelling in the multi-scale process simulator

[120]. The performance of RED systems depends on other factors, as well as *Pn* and *Sh*. In fact residence time, electrical resistance, solutions adopted, channel deformation, spacer shadow effect, etc., and the effective sizes of the spacers, affect the net power.

Thus, the CFD results are used as input data for the process simulator, in order to find the optimal channel configuration and operative conditions.

To this aim, a thorough investigation of the effect of the angle between crossing filaments and of the channel orientation would be helpful. The woven spacers, here investigated for the first time in the literature, have shown to be the very promising, and thus deserve more detailed studies. Moreover, the investigation could be extended to particular geometries, e.g. multilayer spacers, twisted spacers, spacers with various cross-sections etc.

On the other side, profiled-membrane channels exhibit an interesting behaviour, and suitable geometry and *Re* could lead to a mixing degree comparable to net spacers. These aspects combined with advantages as lower electrical resistance, higher membrane active area and lower costs, make the profiled-membrane channels a very promising alternative. Interestingly, profiled-membrane channels are not investigated at all in the literature, although they offer countless geometric possibilities. Therefore a more in depth investigation is advisable for assessing the influence of geometrical parameters and also analysing the fluid/membrane interaction when electric/ionic currents are involved.

With this respect, a “multi-physics” model could be suitable for accounting for local phenomena at the membrane-fluid interface, membrane deformation, presence of multivalent ions, modelling of membranes etc. Therefore, a process simulator coupled with CFD/multi-physics results could eventually identify the optimal channel configuration and operating conditions, reducing the ideality of the prediction.

Notation

a	Slope of the function $\rho\ (C)$ obtained via linear regression [kg mol^{-1}]
A	Coefficient in the equation for f as a function of Re [-]
b	Intercept of the function $\rho\ (C)$ obtained via linear regression [kg m^{-3}]
B	Coefficient in the equation for f as a function of Pn [-]
C	Molar concentration of electrolyte [mol m^{-3}]
$\tilde{C}$	Periodic molar concentration of electrolyte [mol m^{-3}]
$\hat{C}_b$	Bulk concentration of electrolyte [mol m^{-3}]
C_w	Local molar concentration of electrolyte in the membrane-solution interfaces [mol m^{-3}]
$\overline{C}_w$	Mean molar concentration of electrolyte in the membrane-solution interfaces [mol m^{-3}]
D	Measured diffusion coefficient of electrolyte [m^2 s^{-1}]
d	Filament diameter [m]
$D_{corr,ave}$	Average corrected diffusion coefficient [m s^{-2}]
$d_{h,void}$	Hydraulic diameter of the spacer-less channel [m]
f	Fanning friction factor [-]
F	Faraday's constant [C mol^{-1}]
h	Channel thickness [m]
i	Current density [A m^{-2}]
J_{IEM}^{d}	Diffusive flux of electrolyte at the membrane-solution interface [mol m^{-2} s^{-1}]
$\overline{J}_{IEM}^{d}$	Mean diffusive flux at the membranes-solution interface [mol m^{-2} s^{-1}]
k	Mass transfer coefficient [m s^{-1}]
$\overline{k}$	Average mass transfer coefficient [m s^{-1}]
K_c	Concentration gradient along the main flow direction [mol m^{-4}]
l	Mesh length [m]
m	Exponent to Re in the equation for Pn [-]
M_e	Molar mass of electrolyte [kg mol^{-1}]
n	Exponent to Re in the equation for f [-]
p	Pressure [Pa]

$\tilde{p}$	Periodic component of pressure [Pa]
$\vec{P}$	Body force per unit volume [Pa m^{-1}]
Pn	Power number
Re	Reynolds number [-]
Sc	Schmidt number [-]
Sh	Sherwood number [-]
S	Area of membrane-solution interfaces [m^2]
SPC	Specific power consumption [Pa s^{-1}]
t	Time [s]
$\vec{u}$	Velocity of solution [m s^{-1}]
V	Volume of a Unit Cell [m^3]
w	Velocity component along the flow direction *z* [m s^{-1}]
w_{ave}	Average velocity along *z* in the unit cell [m s^{-1}]
$w_{mean,void}$	Average velocity along *z* in a corresponding spacerless channel [m s^{-1}]
x	Cartesian position coordinate [m]
y	Cartesian position coordinate [m]
z	Cartesian position coordinate [m]
$\Delta p/\Delta z$	Mean pressure gradient along the main flow direction [Pa m^{-1}]

Greek letters

α	Flow attack angle [°]
μ	Dynamic viscosity of solution [Pa s]
ρ	Solution density [kg m^{-3}]

Abbreviations

CFD	Computational Fluid Dynamics
ED	Electrodialysis
RED	Reverse electrodialysis

References

[1] G.L. Wick, W.R. Schmitt, Prospects for renewable energy from sea, Mar. Technol. Soc. J., 11 (1977) 16-21.
[2] R.E. Lacey, Energy by reverse electrodialysis, Ocean Eng., 7 (1980) 1-47.
[3] R.E. Pattle, Production of elctric power by mixing fresh and salt water in hydroelectric pile, Nature, 174 (1954) 660.
[4] P. Długołęcki, P. Ogonowski, S.J. Metz, M. Saakes, K. Nijmeijer, M. Wessling, On the resistances of membrane, diffusion boundary layer and double layer in ion exchange membrane transport, J. Membr. Sci., 349 (2010) 369-379.
[5] V. Geraldes, V. Semião, M.N. Pinho, Hydrodynamics and concentration polarization in NF/RO spiral-wound modules with ladder-type spacers, Desalination, 157 (2003) 395-402.
[6] Y. Kim, W.S. Walker, D.F. Lawler, Electrodialysis with spacers: Effects of variation and correlation of boundary layer thickness, Desalination, 274 (2011) 54-63.
[7] H.-J. Lee, H. Strathmann, S.-H. Moon, Determination of the limiting current density in electrodialysis desalination as an empirical function of linear velocity, Desalination, 190 (2006) 43-50.
[8] E. Nagy, E. Kulcsára, A. Nagy, Membrane mass transport by nanofiltration: Coupled effect of the polarization and membrane layers, J. Membr. Sci., 368 (2011) 215-222.
[9] S.S. Sablani, M.F.A. Goosen, R. Al-Belushi, M. Wilf, Concentration polarization in ultrafiltration and reverse osmosis: a critical review, Desalination, 141 (2001) 269-289.
[10] H. Strathmann, Electrodialysis, a mature technology with a multitude of new applications, Desalination, 264 (2010) 268-288.
[11] A. Tamburini, A. Cipollina, S. Al-Sharif, M. Albeirrutty, L. Gurreri, G. Micale, M. Ciofalo, Assessment of temperature polarization in membrane distillation channels by liquid crystal thermography, Desalin. Water Treat., in press, DOI: 10.1080/19443994.2014.957916 (2014).
[12] Y. Tanaka, Pressure distribution, hydrodynamics, mass transport and solution leakage in an ion-exchange membrane electrodialyzer, J. Membr. Sci., 234 (2004) 23-39.
[13] M. Tedesco, A. Cipollina, A. Tamburini, I.D.L. Bogle, G. Micale, A simulation tool for analysis and design of Reverse Electrodialysis using concentrated brines, Chem. Eng. Res. Des., in press, DOI: 10.1016/j.cherd.2014.05.009 (2014).
[14] D.A. Vermaas, E. Guler, M. Saakes, K. Nijmeijer, Theoretical power density from salinity gradients using reverse electrodialysis, Energy Procedia, 20 (2012) 170-184.
[15] H. Strathmann, Ion-exchange membrane separation processes, first ed., Elsevier, Amsterdam, 2004.
[16] P. Długołęcki, K. Nijmeijer, S.J. Metz, M. Wessling, Current status of ion exchange membranes for power generation from salinity gradients, J. Membr. Sci., 319 (2008) 214-222.
[17] J.W. Post, H.V.M. Hamelers, C.J.N. Buisman, Energy recovery from controlled mixing salt and fresh water with a reverse electrodialysis system, Environ. Sci. Technol., 42 (2008) 5785-5790.
[18] J. Veerman, M. Saakes, S.J. Metz, G.J. Harmsen, Reverse electrodialysis: Performance of a stack with 50 cells on the mixing of sea and river water, J. Membr. Sci., 327 (2009) 136-144.
[19] J. Veerman, M. Saakes, S.J. Metz, G.J. Harmsen, Reverse electrodialysis: A validated process model for design and optimization, Chem. Eng. J., 166 (2011) 256-268.

[20] J. Veerman, M. Saakes, S.J. Metz, G.J. Harmsen, Electrical power from sea and river water by reverse electrodialysis: a first step from the laboratory to a real power plant, Environ. Sci. Technol., 44 (2010) 9207-9212.
[21] D.A. Vermaas, M. Saakes, K. Nijmeijer, Doubled power density from salinity gradients at reduced intermembrane distance, Environ. Sci. Technol., 45 (2011) 7089-7095.
[22] O. Scialdone, A. Albanese, A. D'Angelo, A. Galia, C. Guarisco, Investigation of electrode material - Redox couple systems for reverse electrodialysis processes. Part II: Experiments in a stack with 10-50 cell pairs, J. Electroanal. Chem., 704 (2013) 1-9.
[23] O. Scialdone, C. Guarisco, S. Grispo, A. D'Angelo, A. Galia, Investigation of electrode material - Redox couple systems for reverse electrodialysis processes. Part I: Iron redox couples, J. Electroanal. Chem., 681 (2012) 66-75.
[24] A. Tamburini, G. La Barbera, A. Cipollina, M. Ciofalo, G. Micale, CFD simulation of channels for direct and reverse electrodialysis, Desalin. Water Treat., 48 (2012) 370-389.
[25] A. Daniilidis, D.A. Vermaas, R. Herber, K. Nijmeijer, Experimentally obtainable energy from mixing river water, seawater or brines with reverse electrodialysis, Renew. Energy, 64 (2014) 123-131.
[26] P. Długołęcki, A. Gambier, K. Nijmeijer, M. M. Wessling, Practical potential of reverse electrodialysis as process for sustainable energy generation, Environ. Sci. Technol., 43 (2009) 6888-6894.
[27] S. Pawlowski, P. Sistat, J.G. Crespo, S. Velizarov, Mass transfer in reverse electrodialysis: Flow entrance effects and diffusion boundary layer thickness, J. Membr. Sci., 471 (2014) 72-83.
[28] D.A. Vermaas, M. Saakes, K. Nijmeijer, Enhanced mixing in the diffusive boundary layer for energy generation in reverse electrodialysis, J. Membr. Sci., 453 (2014) 312-319.
[29] P. Długołęcki, J. Dąbrowska, K. Nijmeijer, M. Wessling, Ion conductive spacers for increased power generation in reverse electrodialysis, J. Membr. Sci., 347 (2010) 101-107.
[30] D.A. Vermaas, M. Saakes, K. Nijmeijer, Power generation using profiled membranes in reverse electrodialysis, J. Membr. Sci., 385-386 (2011) 234-242.
[31] E. Brauns, Salinity gradient power by reverse electrodialysis: effect of model parameters on electrical power output, Desalination, 237 (2009) 378-391.
[32] J. Jagur-Grodzinski, R. Kramer, Novel process for direct conversion of free energy of mixing into electric power, Ind. Eng. Chem. Process Des. Dev., 25 (1986) 443-449.
[33] S. Pawlowski, J.G. Crespo, S. Velizarov, Pressure drop in reverse electrodialysis: Experimental and modeling studies for stacks with variable number of cell pairs, J. Membr. Sci., 462 (2014) 96-111.
[34] M.H. Dirkse, W.K.P. van Loon, J.W. Post, J. Veerman, J.D. Stigter, G.P.A. Bot, Extending potential flow modelling of flat-sheet geometries as applied in membrane-based systems, J. Membr. Sci., 325 (2008) 537-545.
[35] J. Veerman, R.M. de Jong, M. Saakes, S.J. Metz, G.J. Harmsen, Reverse electrodialysis: Comparison of six commercial membrane pairs on the thermodynamic efficiency and power density, J. Membr. Sci., 343 (2009) 7-15.
[36] D.A. Vermaas, M. Saakes, K. Nijmeijer, Early detection of preferential channeling in reverse electrodialysis, Electrochim. Acta, 117 (2014) 9-17.

[37] J.-H. Choi, J.-S. Park, S.-H. Moon, Direct measurement of concentration distribution within the boundary layer of an ion-exchange membrane, J. Colloid Interface Sci., 251 (2002) 311-317.
[38] Y. Tanaka, Concentration polarization in ion-exchange membrane electrodialysis. The events arising in an unforced flowing solution in a desalting cell, J. Membr. Sci., 244 (2004) 1-16.
[39] O.V. Grigorchuk, V.I. Vasil'eva, V.A. Shaposhnik, Local characteristics of mass transfer under electrodialysis demineralization, Desalination, 184 (2005) 431-438.
[40] V.A. Shaposhnik, O.V. Grigorchuk, E.N. Korzhov, V.I. Vasil'eva, V.Y. Klimov, The effect of ion-conducting spacers on mass transfer - numerical analysis and concentration field visualization by means of laser interferometry, J. Membr. Sci., 139 (1998) 85-96.
[41] V.A. Shaposhnik, V.I. Vasil'eva, O.V. Grigorchuk, Diffusion boundary layers during electrodialysis, Russ. J. Electrochem., 42 (2006) 1202–1207.
[42] V.A. Shaposhnik, V.I. Vasil'eva, O.V. Grigorchuk, The interferometric investigations of electromembrane processes, Adv. Colloid Interface Sci., 139 (2008) 74-82.
[43] J.O.M. Bockris, A.K.N. Reddy, M.E. Gamboa-Aldeco, Modern Electrochemistry 2A, second ed., Kluwer Academic Publishers, New York, 2000.
[44] C. Forgacs, N. Ishibashi, J. Leibovitz, Polarization at ion exchange membranes in electrodialysis, Desalination 10 (1972) 181-214.
[45] K. Kontturi, L. Murtomäki, J.A. Manzanares, Ionic transport processes in electrochemistry and membrane science, Oxford University Press Inc., New York, 2008.
[46] H.-J. Lee , F. Sarfert, H. Strathmann, S.-H. Moon, Designing of an electrodialysis desalination plant, Desalination, 142 (2002) 267-286.
[47] K.S. Spiegler, Polarization at ion exchange membrane-solution interfaces, Desalination, 9 (1971) 367-385.
[48] M.S. Isaacson, A.A. Sonin, Sherwood number and friction factor correlations for electrodialysis systems, with application to process optimization, Ind. Eng. Chem. Proc. Des. Dev., 15 (1976) 313-321.
[49] G. Schock, A. Miquel, Mass transfer and pressure loss in spiral wound modules, Desalination, 64 (1987) 339-352.
[50] A.R. Da Costa, A.G. Fane, D.E. Wiley, Spacer characterization and pressure drop modelling in spacer filled channel for ultrafiltration, J. Membr. Sci., 87 (1994) 79-98.
[51] J. Schwinge, D.E. Wiley, D.F. Fletcher, Simulation of the flow around spacer filaments between channel walls. 1. Hydrodynamics, Ind. Eng. Chem. Res., 41 (2002) 2977-2987.
[52] J. Schwinge, D.E. Wiley, D.F. Fletcher, Simulation of the flow around spacer filaments between channel walls. 2. Mass-Transfer Enhancement, Ind. Eng. Chem. Res., 41 (2002) 4879-4888.
[53] S.K. Karode, A. Kumar, Flow visualization through spacer filled channels by computational fluid dynamics I. Pressure drop and shear rate calculations for flat sheet geometry, J. Membr. Sci., 193 (2001) 69-84.
[54] F. Li, W. Meindersma, A.B. de Haan, T. Reith, Optimization of commercial net spacers in spiral wound membrane modules, J. Membr. Sci., 208 (2002) 289-302.
[55] F. Li, W. Meindersma, A.B. de Haan, T. Reith, Experimental validation of CFD mass transfer simulations in flat channels with non-woven net spacers, J. Membr. Sci., 232 (2004) 19-30.

[56] Y. Tanaka, Limiting current density of an ion-exchange membrane and of an electrodialyzer, J. Membr. Sci., 266 (2005) 6-17.
[57] J. Balster, I. Pünt, D.F. Stamatialis, M. Wessling, Multi-layer spacer geometries with improved mass transport, J. Membr. Sci., 282 (2006) 351-361.
[58] V.V. Ranade, A. Kumar, Fluid dynamics of spacer filled rectangular and curvilinear channels, J. Membr. Sci., 271 (2006) 1-15.
[59] L.C. Santos, V. Geraldes, S. Velizarov, J.G. Crespo, Investigation of flow patterns and mass transfer in membrane module channels filled with flow-aligned spacers using computational fluid dynamics (CFD), J. Membr. Sci., 305 (2007) 103-117.
[60] C.P. Koutsou, S.G. Yiantsios, A.J. Karabelas, Direct numerical simulation of flow in spacer-filled channels: Effect of spacer geometrical characteristics, J. Membr. Sci., 291 (2007) 53-69.
[61] C.P. Koutsou, S.G. Yiantsios, A.J. Karabelas, A numerical and experimental study of mass transfer in spacer-filled channels: Effects of spacer geometrical characteristics and Schmidt number, J. Membr. Sci., 326 (2009) 234-251.
[62] M. Shakaib, S.M.F. Hasani, M. Mahmood, Study on the effects of spacer geometry in membrane feed channels using three-dimensional computational flow modeling, J. Membr. Sci., 297 (2007) 74-89.
[63] M. Shakaib, S.M.F. Hasani, M. Mahmood, CFD modeling for flow and mass transfer in spacer-obstructed membrane feed channels, J. Membr. Sci., 326 (2009) 270-284.
[64] Y.L. Li, K.L. Tung, CFD simulation of fluid flow through spacer-filled membrane module: selecting suitable cell types for periodic boundary conditions, Desalination, 233 (2008) 351-358.
[65] S.M. Mojab, A. Pollard, J.G. Pharoah, S.B. Beale, E.S. Hanff, Unsteady laminar to turbulent flow in a spacer-filled channel, Flow turbul. combust., 92 (2014) 563-577.
[66] J. Schwinge, D.E. Wiley, D.F. Fletcher, A CFD study of unsteady flow in narrow spacer-filled channels for spiral-wound membrane modules, Desalination, 146 (2002) 195-201.
[67] D. Dendukuri, S.K. Karode, A. Kumar, Flow visualization through spacer filled channels by computational fluid dynamics-II: Improved feed spacer designs, J. Membr. Sci., 249 (2005) 41-49.
[68] F. Li, W. Meindersma, A.B. de Haan, T. Reith, Novel spacers for mass transfer enhancement in membrane separations, J. Membr. Sci., 253 (2005) 1-12.
[69] J. Schwinge, D.E. Wiley, A.G. Fane, Novel spacer design improves observed flux, J. Membr. Sci., 229 (2004) 53-61.
[70] A. Shrivastava, S. Kumar, E.L. Cussler, Predicting the effect of membrane spacers on mass transfer, J. Membr. Sci., 323 (2008) 247-256.
[71] P. Xie, L.C. Murdoch, D.A. Ladner, Hydrodynamics of sinusoidal spacers for improved reverse osmosis performance, J. Membr. Sci., 453 (2014) 92-99.
[72] S. Wardeh, H.P. Morvan, CFD simulations of flow and concentration polarization in spacer-filled channels for application to water desalination, Chem. Eng. Res. Des., 86 (2008) 1107-1116.
[73] D.E. Wiley, D.F. Fletcher, Computational fluid dynamics modelling of flow and permeation for pressure-driven membrane processes, Desalination, 145 (2002) 183-186.
[74] D.E. Wiley, D.F. Fletcher, Techniques for computational fluid dynamics modeling of flow in membrane channels, J. Membr. Sci., 211 (2003) 127-137.
[75] V.I. Zabolotskii, S.A. Loza, M.V. Sharafan, Physicochemical properties of profiled heterogeneous ion-exchange membranes, Russ. J. Electrochem., 41 (2005) 1185-1192.

[76] K. Scott, J. Lobato, Mass transfer characteristics of cross-corrugated membranes, Desalination, 146 (2002) 255-258.
[77] D.W. Hall, K. Scott, R.J.J. Jachuck, Determination of mass transfer coefficient of a cross-corrugated membrane reactor by the limiting-current technique, Int. J. Heat Mass Transf., 44 (2001) 2201-2207.
[78] V.V. Nikonenko, N.D. Pismenskaya, A.G. Istoshin, V.I. Zabolotsky, A.A. Shudrenko, Description of mass transfer characteristics of ED and EDI apparatuses by using the similarity theory and compartmentation method, Chem. Eng. Process., 47 (2008) 1118-1127.
[79] C. Larchet, V.I. Zabolotsky, N. Pismenskaya, V.V. Nikonenko, A. Tskhay, K. Tastanov, G. Pourcelly, Comparison of different ED stack conceptions when applied for drinking water production from brackish waters, Desalination, 222 (2008) 489-496.
[80] J. Balster, D.F. Stamatialis, M. Wessling, Membrane with integrated spacer, J. Membr. Sci., 360 (2010) 185-189.
[81] M. Ciofalo, J. Stasiek, M.W. Collins, Investigation of flow and heat transfer in corrugated passages - II. Numerical simulations, Int. J. Heat Mass Transf., 39 (1996) 165-192.
[82] J.H. Doo, M.Y. Ha, J.K. Min, R. Stieger, A. Rolt, C. Son, Theoretical prediction of longitudinal heat conduction effect in cross-corrugated heat exchanger, Int. J. Heat Mass Transf., 55 (2012) 4129-4138.
[83] A.G. Kanaris, A.A. Mouza, S.V. Paras, Flow and Heat Transfer Prediction in a Corrugated Plate Heat Exchanger using a CFD Code, Chem. Eng. Technol., 29 (2006) 923-930.
[84] M.A. Mehrabian, R. Poulter, Hydrodynamics and thermal characteristics of corrugated channels: computational approach, Appl. Math. Model., 24 (2000) 343-364.
[85] M. Ciofalo, I. Di Piazza, J. Stasiek, Investigation of flow and heat transfer in corrugated-undulated plate exchangers, Heat Mass Transfer, 36 (2000) 449-462.
[86] L.Z. Zhang, Convective mass transport in cross-corrugated membrane exchangers, J. Membr. Sci., 260 (2005) 75-83.
[87] D.A. Vermaas, D. Kunteng, M. Saakes, K. Nijmeijer, Fouling in reverse electrodialysis under natural conditions, Water Res., 47 (2013) 1289-1298.
[88] A.J. Karabelas, M. Kostoglou, C.P. Koutsou, Modeling of spiral wound membrane desalination modules and plants – review and research priorities, Desalination, 356 (2015) 165-186.
[89] J.S. Newman, Electrochemical Systems, second ed., Prentice Hall, Englewood Cliffs, 1991.
[90] Y. Kim, W.S. Walker, D.F. Lawler, The Painlevé equation of the second kind for the binary ionic transport in diffusion boundary layers near ion-exchange membranes at overlimiting current, J. Electroanal. Chem., 639 (2010) 59-66.
[91] A. Golovnev, S. Trimper, Steady state solution of the Poisson–Nernst–Planck equations, Phys. Lett. A, 374 (2010) 2886-2889.
[92] J.J. Jasielec, R. Filipek, K. Szyszkiewicz, J. Fausek, M. Danielewski, A. Lewenstam, Computer simulations of electrodiffusion problems based on Nernst–Planck and Poisson equations, Comp. Mater. Sci., 63 (2012) 75-90.
[93] J. Lim, J. Whitcomb, J. Boyd, J. Varghese, Transient finite element analysis of electric double layer using Nernst–Planck–Poisson equations with a modified Stern layer, J. Colloid Interface Sci., 305 (2007) 159-174.

[94] J.A. Manzanares, W.D. Murphy, S. Mafé, H. Reiss, Numerical simulation of the nonequilibrium diffuse double layer in ion-exchange membranes, J. Phys. Chem., 97 (1993) 8524-8530.
[95] M.A.-K. Urtenov, E.V. Kirillova, N.M. Seidova, V.V. Nikonenko, Decoupling of the Nernst-Planck and Poisson equations. Application to a membrane system at overlimiting currents, J. Phys. Chem. B, 111 (2007) 14208-14222.
[96] V.M. Volgin, A.D. Davydov, Ionic transport through ion-exchange and bipolar membranes, J. Membr. Sci., 259 (2005) 110-121.
[97] V.I. Zabolotskii, J.A. Manzanares, S. Mafé, V.V. Nikonenko, K.A. Lebedev, Steady-state ion transport through a three-layered membrane system: a mathematical model allowing for violation of the electroneutrality condition, Russ. J. Electrochem., 38 (2002) 819-827.
[98] R.Q. Fu, T.W. Xu, W.H. Yang, Z.X. Pan, A new derivation and numerical analysis of current-voltage characteristics for an ion-exchange membrane under limiting current density, Desalination, 173 (2005) 143-155.
[99] K.A. Lebedev, V.V. Nikonenko, V.I. Zabolotskii, M. Metaye, I.V. Kovalev, Ion transport in a three-layered ion-exchange membrane: a mathematical model, Russ. J. Electrochem., 38 (2002) 688-697.
[100] V.V. Nikonenko, N.D. Pismenskaya, E.I. Belova, P. Sistat, P. Huguet, G. Pourcelly, C. Larchet, Intensive current transfer in membrane systems: Modelling, mechanisms and application in electrodialysis, Adv. Colloid Interface Sci., 160 (2010) 101-123.
[101] P. Sistat, G. Pourcelly, Steady-state ion transport through homopolar ion-exchange membranes: an analytical solution of the Nernst–Planck equations for a 1:1 electrolyte under the electroneutrality assumption, J. Electroanal. Chem., 460 (1999) 53-62.
[102] P. Sistat, G. Pourcelly, Chronopotentiometric response of an ion-exchange membrane in the underlimiting current-range. Transport phenomena within the diffusion layers, J. Membr. Sci., 123 (1997) 121-131.
[103] Y. Tanaka, Concentration polarization in ion-exchange membrane electrodialysis—the events arising in a flowing solution in a desalting cell, J. Membr. Sci., 216 (2003) 149-164.
[104] Z. Yu, W. Admassu, Modeling of electrodialysis of metal ion removal from pulp and paper mill process stream, Chem. Eng. Sci., 55 (2000) 4629-4641.
[105] G. Kraaijeveld, V. Sumberova, S. Kuindersma, H. Wesselingh, Modelling electrodialysis using the Maxwell–Stefan description, Chem. Eng. J., 57 (1995) 163-176.
[106] P.N. Plntauro, D.N. Bennion, Mass transport of electrolytes in membranes. 1 Development of mathematical transport model, Ind. Eng. Chem. Fundam., 23 (1984) 230-234.
[107] H. Wesselingh, P. Vonk, G. Kraaijeveld, Exploring the Maxwell–Stefan description of ion exchange, Chem. Eng. J., 57 (1995) 75-89.
[108] E. Brauns, Finite elements-based 2D theoretical analysis of the effect of IEX membrane thickness and salt solution residence time on the ion transport within a salinity gradient power reverse electrodialysis half cell pair, Desalin. Water Treat., 51 (2013) 6429-6443.
[109] D.-K. Kim, Numerical study of power generation by reverse electrodialysis in ion-selective nanochannels, J. Mech. Sci. Technol., 25 (2011) 5-10.
[110] K.S. Kim, W. Ryoo, M.-S. Chun, G.-Y. Chung, S.O. Lee, Transport analysis in reverse electrodialysis with pulsatile flows for enhanced power generation, Korean J. Chem. Eng., 29 (2012) 162-168.

[111] K.S. Kim, W. Ryoo, M.-S. Chun, G.-Y. Chung, Simulation of enhanced power generation by reverse electrodialysis stack module in serial configuration
Desalination, 318 (2013) 79-87.
[112] H.-I. Jeong, H.J. Kim, D.-K. Kim, Numerical analysis of transport phenomena in reverse electrodialysis for system design and optimization, Energy, 68 (2014) 229-237.
[113] F. Santoro, Modelling and optimization of the reverse electrodialysis process, in: Dipartimento di Ingegneria Chimica, Gestionale, Informatica e Meccanica, Università degli studi di Palermo, Palermo, 2014.
[114] http://www.reapower.eu/, in.
[115] M. Tedesco, A. Cipollina, A. Tamburini, G. Micale, J. Helsen, M. Papapetrou, Reapower - Use of desalination brine for power production through reverse electrodialysis, Desalin. Water Treat., in press, DOI: 10.1080/19443994.2014.934102 (2014).
[116] E. Brauns, Towards a worldwide sustainable and simultaneous large-scale production of renewable energy and potable water through salinity gradient power by combining reversal electrodialysis and solar power?, Desalination, 219 (2008) 312-323.
[117] E. Brauns, An alternative hybrid concept combining seawater desalination, solar energy and reverse electrodialysis for a sustainable production of sweet water and electrical energy, Desalin. Water Treat., 13 (2010) 53-62.
[118] J.D. Anderson, Computational fluid dynamics. The basics with applications, McGraw-Hill, 1995.
[119] G. Comini, Fondamenti di termofluidodinamica computazionale, Second ed., SGE, 2004.
[120] M. Tedesco, Reverse electrodialysis: advanced modelling and scale-up, in: Dipartimento di Ingegneria Chimica, Gestionale, Informatica e Meccanica, Università degli studi di Palermo, Palermo, 2015.
[121] D.W. Green, R.H. Perry, Perry's Chemical Engineers' Handbook, eighth ed., McGraw-Hill, New York, 2007.
[122] L.J.M. Smits, E.M. Duyvis, Transport numbers of concentrated sodium chloride solutions at 25°, J. Phys. Chem., 70 (1966) 2747-2753.
[123] A. Tamburini, G. La Barbera, A. Cipollina, G. Micale, M. Ciofalo, CFD prediction of scalar tranport in thin channels for reverse electrodialysis, Desalin. Water Treat., in press (2014).
[124] M. Tedesco, A. Cipollina, A. Tamburini, W. van Baak, G. Micale, Modelling the Reverse ElectroDialysis process with seawater and concentrated brines, Desalin. Water Treat., 49 (2012) 404-424.
[125] D. Molyneux, N. Bose, Escort tug at large yaw angle: comparison of CFD predictions with experimental data, Trans.Royal Inst. Naval Arch. Part B Int. J. Small Craft Tech., 150 (2008) 41-60.
[126] H.I. Oguntade, G.E. Andrews, A. Burns, D. Ingham, M. Pourkashanian, CFD predictions of single row film cooling with inclined holes: influence of hole outlet geometry, in: Proceedings of the ASME Turbo Expo, 2010, pp. 1371-1385.
[127] H. Ozbek, J.A. Fair, S.L. Phillips, Viscosity of aqueous sodium chloride solutions from 0 - 150°C, in, University of California, Berkeley, 2010.
[128] V. Vitagliano, P.A. Lyons, Diffusion coefficients for aqueous solutions of sodium chloride and barium chloride, J. Am. Chem. Soc., 78 (1956) 1549-1552.
[129] J.E. Drummond, M.I. Tahir, Laminar viscous flow through regular arrays of parallel solid cylinders, Int. J. Multiphase Flow, 10 (1984) 515-540.

[130] J. Happel, Viscous flow relative to arrays of cylinders, AIChE J., 5 (1959) 174-177.
[131] G.W. Jackson, D.F. James, The permeability of fibrous porous media, Can. J. Chem. Eng., 64 (1986) 364-374.
[132] A.S. Sangani, A. Acrivos, Slow flow past periodic arrays of cylinders with application to heat transfer, Int. J. Multiphase Flow, 8 (1982) 193-206.
[133] E.M. Sparrow, A.L. Loeffler, Longitudinal laminar flow between cylinders arranged in regular array, AlChE J., 5 (1959) 325-330.
[134] L. Spielman, S.L. Goren, Model for predicting pressure drop and filtration efficiency in fibrous media, Environ. Sci. Technol., 2 (1968) 279-287.
[135] M.M. Tomadakis, J.T. Robertson, Viscous permeability of random fiber structures: Comparison of electrical and diffusional estimates with experimental and analytical results, J. Compos. Mater., 39 (2005) 163-188.
[136] A. Tamburini, G. Micale, M. Ciofalo, A. Cipollina, Experimental analysis via Thermochromic Liquid Crystals of the temperature local distribution in Membrane Distillation modules, Chem. Eng. Trans., 32 (2013) 2041-2046.
[137] A. Tamburini, P. Pitò, A. Cipollina, G. Micale, M. Ciofalo, A Thermochromic Liquid Crystals image analysis technique to investigate temperature polarization in spacer-filled channels for membrane distillation, J. Membr. Sci., 447 (2013) 260-273.
[138] K.S. Pitzer, Thermodynamics of electrolytes. I. Theoretical basis and general equations, J. Phys. Chem., 77 (1973) 268–277.
[139] A.R. Da Costa, A.G. Fane, D.E. Wiley, Spacer characterization and pressure drop modelling in spacer-filled channels for ultrafiltration, J. Membr. Sci., 87 (1994) 79-98.
[140] J. Liu, A. Iranshahi, Y. Lou, G. Lipscomb, Static mixing spacers for spiral wound modules, J. Membr. Sci., 442 (2013) 140-148.
[141] G.A. Fimbres-Weihs, D.E. Wiley, Numerical study of two-dimensional multi-layer spacer designs for minimum drag and maximum mass transfer, J. Membr. Sci., 325 (2008) 809-822.
[142] L. Gurreri, A. Tamburini, A. Cipollina, G. Micale, M. Ciofalo, CFD prediction of concentration polarization phenomena in spacer-filled channels for reverse electrodialysis, J. Membr. Sci., 468 (2014) 133-148.